



HAL
open science

Coherent interferometric imaging in fluid dynamics

Etienne Gay

► **To cite this version:**

Etienne Gay. Coherent interferometric imaging in fluid dynamics. General Mathematics [math.GM].
Université Paris Cité, 2019. English. NNT : 2019UNIP7029 . tel-02334698v2

HAL Id: tel-02334698

<https://theses.hal.science/tel-02334698v2>

Submitted on 18 Nov 2020

HAL is a multi-disciplinary open access archive for the deposit and dissemination of scientific research documents, whether they are published or not. The documents may come from teaching and research institutions in France or abroad, or from public or private research centers.

L'archive ouverte pluridisciplinaire **HAL**, est destinée au dépôt et à la diffusion de documents scientifiques de niveau recherche, publiés ou non, émanant des établissements d'enseignement et de recherche français ou étrangers, des laboratoires publics ou privés.

Université de Paris
École doctorale Sciences Mathématiques de Paris Centre ED386

THÈSE

présentée par

Etienne Gay

pour l'obtention du grade de

Docteur de l'Université de Paris

Discipline	Sciences Mathématiques
Spécialité	Mathématiques Appliquées
Laboratoires d'Accueil	Dépt. Aérodynamique, Aéroélasticité, Acoustique ONERA LPSM (UMR 8001) Université Paris-Diderot

**Coherent interferometric imaging
in fluid dynamics**

Présentée et soutenue publiquement le 19 septembre 2019 devant la commission d'examen
composée de :

M. Xavier Blanc	Professeur Université Paris-Diderot	Examineur
M. Josselin Garnier	Professeur École Polytechnique	Directeur de Thèse
M. Frédéric Magoulès	Professeur CentraleSupélec	Rapporteur
Mme Agnès Maurel	Directrice de Recherche CNRS	Président
M. Philippe Pouliguen	Responsable Innovation AID DGA	Examineur
M. Éric Savin	Ingénieur ONERA	Co-directeur de Thèse
Mme Chrysoula Tsogka	Professeur University of California at Merced	Rapporteur

Thèse numéro : DAAA 19096
Châtillon

PhD thesis

Specialty: Applied Mathematics

Host laboratories: ONERA/DAAA & LPSM Paris-Diderot University

by

Etienne Gay

Imagerie par interférométrie cohérente en dynamique des fluides

Résumé

La présente recherche vise à développer des algorithmes d'imagerie par interférométrie cohérente (CINT) pour localiser des sources et des réflecteurs dans des applications impliquant des écoulements. L'imagerie CINT s'est avérée efficace et statistiquement stable dans des milieux inhomogènes au repos, où les techniques classiques d'imagerie, telles que la migration de Kirchhoff (KM), peuvent éventuellement échouer en raison de leur manque de robustesse statistique. Nous visons à étendre ces méthodes aux milieux en mouvement inhomogènes, car elles concernent l'aéroacoustique, l'acoustique atmosphérique et sous-marine, la propagation des infrasons, voire l'astrophysique. Dans ce rapport de thèse, nous abordons à la fois le problème direct de la modélisation de la propagation des ondes acoustiques dans un écoulement ambiant hétérogène et aléatoire, et le problème inverse de la recherche de la position de sources ou de réflecteurs par l'algorithme CINT mis en œuvre avec les traces des ondes acoustiques qui ont traversé l'écoulement.

Mots-clefs: *Imagerie par interférométrie cohérente, ondes acoustiques, écoulement aléatoire.*

Coherent interferometric imaging in fluid dynamics

Abstract

The present research is aimed at developing coherent interferometric (CINT) imaging algorithms to localize sources and reflectors in applications involving fluid flows. CINT imaging has been shown to be efficient and statistically stable in quiescent cluttered media where classical imaging techniques, such as Kirchhoff's migration (KM), may possibly fail due to their lack of statistical robustness. We aim at extending these methods to inhomogeneous moving media, for it has relevance to aero-acoustics, atmospheric and underwater acoustics, infrasound propagation, or even astrophysics. In this thesis report we address both the direct problem of modeling the propagation of acoustic waves in a randomly heterogeneous ambient flow, and the inverse problem of finding the position of sources or reflectors by the CINT algorithm implemented with the traces of the acoustic waves that have travelled through the flow.

Keywords: *Coherent interferometry imaging, acoustic waves, random flow.*

Remerciements

Je tiens à remercier ici toutes les personnes qui ont contribué, de près ou de loin, à la réalisation de ce travail de thèse.

Je souhaite remercier mes deux Directeurs de thèse, Josselin Garnier et Éric Savin pour leur disponibilité, leur aide et leurs conseils. Ils sont pour beaucoup dans la qualité de ce travail notamment pour la rédaction de ce mémoire. Enfin je voudrais leur adresser un dernier remerciement pour m'avoir donné l'occasion d'effectuer cette thèse à l'ONERA sur ce sujet passionnant.

Mes remerciements vont ensuite vers Agnès Maurel qui a accepté de présider ma soutenance et aux deux rapporteurs, Chrysoula Tsogka et Frédéric Magoulès. Je remercie également Xavier Blanc et Philippe Poulinguen, qui ont accepté de participer au jury de la soutenance, pour l'intérêt qu'ils ont porté au sujet.

Grâce à l'ONERA et au département DAAA j'ai pu effectuer ce travail de recherche dans de bonnes conditions. Je remercie Vincent Couaillier pour m'avoir accueilli dans son unité, je voudrais aussi remercier Christophe Peyret, pour le temps qu'il a su me consacrer, et Luc Bonnet pour son enthousiasme et la qualité de son travail. Je tiens aussi à témoigner ma reconnaissance à tous les membres de l'unité NFLU pour leur sympathie et leur accueil chaleureux.

Je voulais prendre le temps de remercier l'entreprise VO2 Group qui m'a accueilli à la suite de mes trois ans de thèse et où j'ai pu finir ce travail, et en particulier Florent Daversin pour sa compréhension.

Enfin je tiens à remercier tous mes proches pour leur soutien pendant la durée de cette thèse. À tous ceux qui ont été présent dans les moments difficiles. Mes pensées vont vers ma famille et plus particulièrement à mes parents à qui je dédie cette thèse.

Introduction

The purpose of imaging techniques is to estimate the location of one or more sources and/or reflecting structures with a passive or an active array of sensors, respectively. Coherent INTERferometry (CINT) shall be considered for imaging in cluttered media from the time traces of echoes recorded at a remote array [77]. Here clutter means that the propagation medium (*e.g.* water, turbulent flow, stratified flow...) is perturbed by inhomogeneities that are unknown and cannot be estimated in detail. Its main effect is to induce large delay spread, or coda, to the recorded time traces in regimes where significant multiple scattering of the acoustic waves by the clutter occurs. In the envisaged applications, the size of the targets to be imaged and the typical correlation lengths of the clutter shall be comparable to the carrier wavelength of the probing pulses. In this work we are more particularly interested in the propagation of acoustic waves in a stratified, heterogeneous flow and the possible localization of sources by these wave fields using the CINT approach. It is therefore understood that we are not interested in the amplitudes when we talk about imaging techniques and more specifically about CINT. Although the developments are focused on applications to aeroacoustics and/or underwater acoustics, this technique has a clear dual feature. Indeed, it has potential direct extensions in *e.g.* structural health monitoring, seismic or medical imaging among others [93], provided of course that the relevant space-time scales have been correctly adjusted. More particularly, we have in mind the experiments carried on by Candel *et al.* [41–43] more than forty years ago at the low speed open wind tunnel of the Von Karman Institute. It offers a 3 m initial jet diameter and a maximum flow velocity of $60 \text{ m}\cdot\text{s}^{-1}$ in an anechoic environment whereby acoustic reflections are partially suppressed. A sound source is placed inside the free jet and the acoustic field transmitted by the shear flow is explored at the outer of the jet. This typical configuration is illustrated by the sketch of Fig. 1 where S is the position of the source, P is the position of a microphone, 0 is the position of the trailing edge of the jet duct, and U_1 and U_2 are the high and low-speed side free-stream velocities respectively. A photo of DGA’s CEPRA 19 facility is also displayed, since it is very much similar to the experimental setup described in [41–43]. As the acoustic waves travel through the turbulent mixing layer and shear flow they are convected, refracted and scattered resulting in a change of directivity, phase and amplitude modulation, and a spectral re-distribution of the acoustic energy over a band of (sufficiently high) frequencies around the tone frequency of the source—the so-called “spectral broadening” or “haystacking” effect in the literature; see *e.g.* [1, 16] and references therein. It is illustrated for example by the far-field power spectral density (PSD) of the pressure field recorded at the outside of the jet, which exhibits side lobes induced by the turbulent structures of the flow and a progressive energy decrease afterwards. The results obtained by Candel *et al.* [41] are shown on Fig. 2, where the PSD of the scattered pressure field for different values of the tone frequency f_0 of the acoustic source are displayed. A

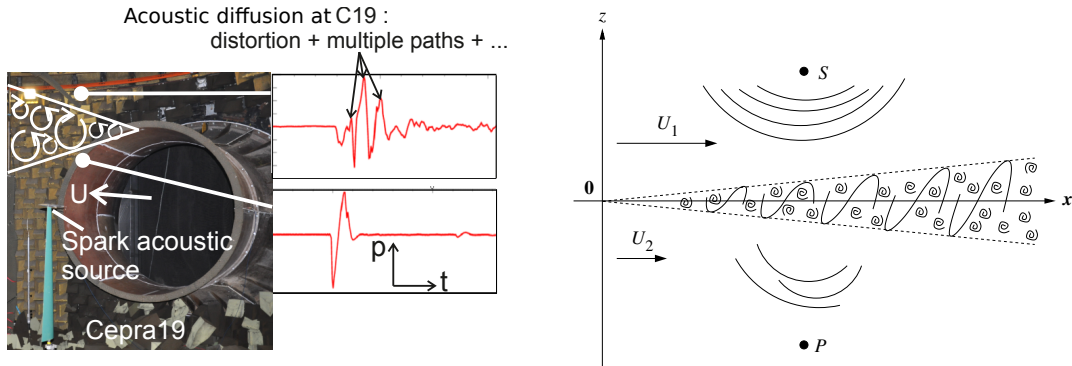


Figure 1 – *Anechoic wind tunnel with open-jet test section (nozzle exit $\varnothing = 2\text{-}3\text{ m}$, $U_1 \leq 100\text{ m/s}$); the configuration at CEPR19 [50] (left) and a sketch of the experiment (right).*

Large Eddy Simulation (LES) consisting in calculating only the larger scales of both the turbulent flow and the acoustic field, and using a dedicated model for the smaller scales, has been recently presented in [16]. These results are displayed on Fig. 2 as well. In the mean time numerous theoretical and numerical studies have been carried on to both understand the main physical phenomena in acoustic wave propagation in shear layers, and simulate the interaction between acoustic waves and turbulent flows. Several of them are reviewed in [1, 16, 35, 36, 49, 67, 107] and references therein, among many other works. Our aim in this research is twofold:

- First, one intends to develop analytical models of acoustic wave propagation in stratified random flows to obtain the main features of the transmitted waves and their PSD (direct problem); these models should be able to describe the aforementioned spectral-broadening effect and PSD shapes.
- Second, one intends to use the previous results to develop a CINT imaging technique in shear flows to localize acoustic sources from these waves, for applications in aeroacoustics and underwater acoustics for example (inverse problem).

In both instances we rely on some existing theoretical results on the propagation of waves in stratified media [25, 35, 36, 72, 74, 76, 107] and extend these analyses to the consideration of a convective flow, possibly with random characteristics.

CINT imaging is based on the back-propagation of local space-time empirical cross-correlations of the array data, namely the recorded pressure fields at the near free-surface of an half-space or a random slab [72, 74, 75]. Imaging of sources or reflectors in smoothly varying background media is efficiently done with Kirchhoff [20], or reverse-time migration [120] when the background velocity is known or can be estimated. In cluttered environments however, Kirchhoff migration does not work well since it produces images with speckles which are difficult to interpret. These images are also statistically unstable, in the sense that they depend on the realization of the clutter. This is because the phases of the measured waves are shifted with respect to the deterministic, unperturbed phase in the presence of the unknown clutter. Consequently, when these recorded data are numerically back-propagated in a homogeneous or smoothly varying medium, the phase terms do not compensate each other at the source location, resulting in instability and loss of resolution in the image. The original idea of CINT is to correct this effect by considering empirical

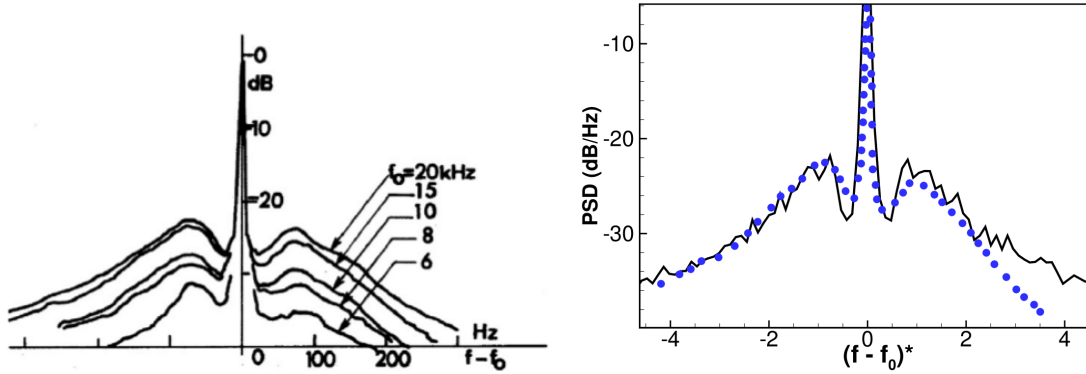


Figure 2 – Power spectral density (PSD) of the scattered pressure field at the outside of the turbulent mixing layer ($M \approx 0.2$, $Re \approx 1200$); experimental results after [41] (left) and numerical simulation (–) compared to experiments (•) for $f_0 = 15$ kHz after [16] (right).

cross-correlations of the data. Indeed, considering recorded data for nearby frequencies and nearby locations of the receivers, their random phase shifts remain similar, or in a way, correlated. Consequently, if the space and frequency correlations (products) between these data are formed, the random phase shifts roughly cancel each other. In such a case, the back-propagation of these products in a smoothly varying medium should be statistically stable. Thus the CINT imaging function assembles pairs of receivers and frequencies for which the corresponding recorded data are presumably coherent, and removes those pairs that do not bring any information. This strategy introduces some crucial cut-off parameters, namely the decoherence length and the decoherence frequency. They are defined as the limits beyond which coherence between the data at pairs of frequency and locations are considered as lost. At this stage, the approach however raises the difficulty of estimating these windowing (cut-off) parameters, which are in fact related to the clutter. Consequently, an adaptive version of the CINT algorithm has been proposed [26, 27], that estimates the decoherence parameters during the image construction process by optimization of an objective function quantifying the quality of the image in formation. This approach has shown to be very efficient in the localization of point sources and reflectors in cluttered media, but the results presented in the open literature have been limited to two-dimensional, motionless media to our knowledge.

Outline of the thesis

In Chapter 1 we review several results of the literature concerning acoustic wave propagation and imaging in quiescent and moving random media. In Sect. 1.1 we summarize the basic setting of acoustic wave propagation in a stationary ambient flow starting from the Navier-Stokes equations, and write in this context the linearized Euler's equations in Sect. 1.1.1, Lighthill's equation in Sect. 1.1.2, and Lilley's equation in Sect. 1.1.3. We also present a global form of the problem of acoustic wave propagation in a layered medium in Sect. 1.1.4. Then important definitions of the autocorrelation function and the power spectral density of a stationary stochastic process are recalled in Sect. 1.2. After that random media or flows are considered in Sect. 1.3. We present the experimental context of wave

propagation in an anechoic open jet wind in Sect. 1.3.1, and then we describe in Sect. 1.3.2 the Born approximation, an approach often used to solve wave propagation problems in random media or random flows. We finish this section by presenting two other approaches, the ODA theory in Sect. 1.3.3 and the radiative transfer theory in Sect. 1.3.4. The end of this first chapter shows numerical methods used for the simulation of acoustic wave propagation in random flows in Sect. 1.4, and introduces the CINT imaging technique and its context in Sect. 1.5.

In Chapter 2 two models of acoustic wave propagation in random stratified flows are developed. In Sect. 2.1 we extend the analysis presented in Sect. 1.1.1 to the case of an unsteady inhomogeneous flow. In Sect. 2.2 we specialize further on the results seen in Sect. 1.1 to the case where the ambient quantities do not depend any longer on the vertical coordinate. We obtain a fully explicit integral representation of the transmitted pressure field. In Sect. 2.3 we turn back to the horizontally stratified case considering random perturbations of the ambient bulk modulus. Again, we obtain a fully explicit integral representation of the transmitted pressure in terms of a random transmission coefficient of which moments are thoroughly characterized. In Sect. 2.4 we consider the situation where the ambient flow velocity is randomly perturbed and obtain an explicit form of the power spectrum of the transmitted pressure field. We can recover by our approach the experimental results of [41–43], at least qualitatively.

The CINT imaging algorithm is developed in Chapter 3. After presenting the problem in Sect. 3.1.1, we introduce the standard Kirchhoff migration technique in Sect. 3.1.2, the CINT imaging technique in the absence of a flow in Sect. 3.1.3, and propose a modification of these algorithms to account for the flow. Then we describe the numerical method (the discontinuous Galerkin finite element method implemented in the code SPACE [60]) and the numerical setup in Sect. 3.2. We validate our solver in a homogeneous medium at rest and then we reproduce the results of the literature [24, 27] with the case of a random medium at rest in Sect. 3.3. Finally we treat the cases of a random medium subjected to a homogeneous speed in Sect. 3.4.1 and then subjected to a random speed in Sect. 3.4.2 to compare KM and CINT in the presence of a flow. Finally we obtain some results for the case of imaging through a turbulent jet calculated by CFD in Sect. 3.5.

Contents

Introduction	7
1 Acoustic waves in quiescent and moving random media	13
1.1 Acoustic waves in a stationary flow and quiescent layered medium	13
1.1.1 Linearized Euler equations	13
1.1.2 Lighthill equation	16
1.1.3 Lilley equation	18
1.1.4 Acoustic waves in quiescent layered media	19
1.1.5 Acoustic waves in randomly heterogeneous media	21
1.2 Autocorrelation function and power spectral density	22
1.3 Acoustic waves in random media and random flows	23
1.3.1 Acoustic scattering in the anechoic open jet wind tunnel measurements	24
1.3.2 The Born approximation	26
1.3.3 The O’Doherty-Anstey (ODA) theory	28
1.3.4 Radiative transfer theory	31
1.4 Numerical simulation methods of acoustic waves in random flows	32
1.5 Source localization in random media	35
1.5.1 Coherent interferometric (CINT) imaging in random media	36
1.5.2 Numerical CINT experiments	39
1.5.3 Correlation-based imaging of moving objects	41
1.6 Conclusion	44
2 Acoustic wave propagation in a random stratified flow	45
2.1 Linearized Euler equations about an unsteady inhomogeneous flow	45
2.2 Acoustic waves in an homogeneous flow	48
2.2.1 Modes of wave propagation	49
2.2.2 Integral representation of the pressure field	50
2.3 Acoustic waves in a stratified flow with random bulk modulus	55
2.3.1 Integral representation of the pressure field	56
2.3.2 Characterization of moments	59
2.3.2.1 Transmission coefficient	59
2.3.2.2 Stationary-phase method	61
2.4 Acoustic waves in a stratified flow with random velocity	64
2.4.1 Transmitted fields with fluctuations of the ambient flow velocity . .	65
2.4.2 Computation of the power spectral density	70
2.4.3 Stationary-phase method	73

2.4.4	Numerical example	77
2.5	Conclusion	78
3	Coherent interferometry in a random flow	81
3.1	Imaging functionals in random moving media	81
3.1.1	Model problem	81
3.1.2	Reverse-time and Kirchhoff migration	83
3.1.3	Coherent interferometric imaging	86
3.2	Discontinuous Galerkin method for Euler equations	88
3.2.1	Euler equations DG solver (CFD)	88
3.2.2	Linearized Euler equations DG solver (CAA)	90
3.2.3	Spatial discretization and functional basis	91
3.2.4	Boundary conditions	93
3.2.5	Time discretization	93
3.3	Imaging in a motionless random medium	93
3.3.1	Model setup	93
3.3.2	Mesh	95
3.3.3	Active imaging	95
3.3.4	Passive imaging	97
3.4	Imaging in a moving random medium	99
3.4.1	Active imaging in a random medium moving at a uniform velocity	100
3.4.2	Active imaging in a random medium moving at a random velocity	101
3.5	Passive imaging through a synthetic turbulent jet flow	105
3.5.1	Model setup	105
3.5.2	Imaging setup	107
3.5.3	Mesh for the CFD and CAA computations	108
3.5.4	Flow calculation	108
3.5.5	Refraction compensation mechanism	109
3.5.6	Imaging of the sources	109
3.6	Conclusion	110
	Conclusions and perspectives	115

Chapter 1

Acoustic waves in quiescent and moving random media

In this chapter we will present the framework in which the work done during these three years of research is inscribed. After introducing several models of acoustic wave propagation in quiescent and moving ambient media, we will focus on the experiments carried out in the 70s by Candel and his co-workers around the scattering of acoustic waves by a turbulent shear layer. Then we will present several numerical methods to simulate the propagation of acoustic waves in random flows, and more particularly the simulation of these experiments. Finally, we will present some work done on source localization in quiescent random media that inspired us in the context of a possible generalization to randomly heterogeneous flows.

1.1 Acoustic waves in a stationary flow and quiescent layered medium

First, we introduce the notations as well as the context of the fluid mechanics equations that we consider. We also present several models of acoustic wave propagation in quiescent and moving media, such as stationary flows.

1.1.1 Linearized Euler equations

We start by considering the Navier-Stokes equations for a compressible fluid flow. The mass, momentum, and energy conservation equations for that flow read:

$$\begin{aligned}\frac{d\rho}{dt} &= -\rho \nabla \cdot \mathbf{v} + m, \\ \rho \frac{d\mathbf{v}}{dt} &= \nabla \cdot \boldsymbol{\sigma} + \rho \mathbf{f}, \\ \rho T \frac{ds}{dt} &= \boldsymbol{\tau} : \nabla \mathbf{v}^T - \nabla \cdot \mathbf{q} + \rho Q,\end{aligned}\tag{1.1}$$

where:

$$\frac{d}{dt} = \frac{\partial}{\partial t} + \mathbf{v} \cdot \nabla$$

is the convective derivative with $\nabla = (\frac{\partial}{\partial x}, \frac{\partial}{\partial y}, \frac{\partial}{\partial z})$, $\mathbf{A} : \mathbf{B} = \text{Tr}(\mathbf{A}\mathbf{B}^T) = \sum_{ij} A_{ij}B_{ij}$ is the tensor scalar product of second order tensors \mathbf{A} and \mathbf{B} , $\boldsymbol{\tau} : \nabla \mathbf{v}^T = \sum_{ij} \tau_{ij} \frac{\partial v_i}{\partial r_j}$, and:

- $\mathbf{v}(\mathbf{r}, t)$ is the fluid velocity, $\varrho(\mathbf{r}, t)$ the density, $T(\mathbf{r}, t)$ the temperature, $s(\mathbf{r}, t)$ the specific entropy, and $\mathbf{q}(\mathbf{r}, t)$ the heat flux vector at the position $\mathbf{r} = (x, y, z)$ and time t ;
- $\boldsymbol{\sigma}(\mathbf{r}, t) = -p(\mathbf{r}, t)\mathbf{I} + \boldsymbol{\tau}(\mathbf{r}, t)$ is the stress tensor, \mathbf{I} is the identity matrix, $p(\mathbf{r}, t)$ is the (static) fluid pressure, $\boldsymbol{\tau}(\mathbf{r}, t)$ is the viscous stress tensor;
- $m(\mathbf{r}, t)$ is the specific mass source per unit time, $\mathbf{f}(\mathbf{r}, t)$ is the force per unit mass exerted on the fluid (neglecting gravity), and $Q(\mathbf{r}, t)$ is the heat production per unit mass.

For an ideal fluid in which there is no friction ($\boldsymbol{\tau} = \mathbf{0}$), no heat conduction ($\mathbf{q} = \mathbf{0}$), and no heat production ($Q = 0$), these conservation equations then read as the Euler equations:

$$\begin{aligned}\frac{d\varrho}{dt} &= -\varrho \nabla \cdot \mathbf{v} + m, \\ \frac{d\mathbf{v}}{dt} &= -\frac{1}{\varrho} \nabla p + \mathbf{f}, \\ \frac{ds}{dt} &= 0.\end{aligned}\tag{1.2}$$

This shows that the flow is isentropic (*i.e.* each fluid particle has constant entropy), and by the equation of state $p = p^\#(\varrho, s)$:

$$\frac{dp}{dt} = c^2 \frac{d\varrho}{dt}, \quad c^2(\varrho, s) = \left. \frac{\partial p^\#}{\partial \varrho} \right|_s,\tag{1.3}$$

where c is the adiabatic speed of sound. For a perfect gas for example, the equation of state $p\varrho^{-\gamma} = C$ along particle paths, where the constant C may differ for each particle in isentropic flows, yields $c^2 = \gamma p/\varrho$. The foregoing Euler equations are linearized about an unperturbed, stationary flow for which the pressure, fluid velocity, and fluid density do not depend on time. They are denoted by $p_0(\mathbf{r})$, $\mathbf{v}_0(\mathbf{r})$ and $\varrho_0(\mathbf{r})$ respectively, such that:

$$\begin{aligned}(\mathbf{v}_0 \cdot \nabla) \varrho_0 &= -\varrho_0 \nabla \cdot \mathbf{v}_0, \\ (\mathbf{v}_0 \cdot \nabla) \mathbf{v}_0 &= -\frac{1}{\varrho_0} \nabla p_0, \\ (\mathbf{v}_0 \cdot \nabla) p_0 &= c_0^2 (\mathbf{v}_0 \cdot \nabla) \varrho_0.\end{aligned}\tag{1.4}$$

Here c_0 stands for the sound velocity not influenced by the waves. Linearization consists in considering that the actual flow is a perturbation (ϱ' , \mathbf{v}' , p') of the stationary flow generated by the mass m and force \mathbf{f} injected to the fluid:

$$\begin{aligned}\varrho(\mathbf{r}, t) &= \varrho_0(\mathbf{r}) + \varrho'(\mathbf{r}, t), \\ \mathbf{v}(\mathbf{r}, t) &= \mathbf{v}_0(\mathbf{r}) + \mathbf{v}'(\mathbf{r}, t), \\ s(\mathbf{r}, t) &= s_0(\mathbf{r}) + s'(\mathbf{r}, t), \\ p(\mathbf{r}, t) &= p_0(\mathbf{r}) + p'(\mathbf{r}, t), \\ c^2(\mathbf{r}, t) &= c_0^2(\mathbf{r}) + (c^2)'(\mathbf{r}, t).\end{aligned}$$

The primed quantities p' , \mathbf{v}' , ϱ' , and $(c^2)'$ are the acoustic pressure, fluid velocity, density, and speed of sound, respectively, of which non-linear contributions to the Euler equations

above are assumed negligible. In other words, these quantities are first-order increments of the zero-th order stationary quantities. They satisfy the following linearized Euler equations (LEE):

$$\begin{aligned}\frac{d\rho'}{dt} + (\mathbf{v}' \cdot \nabla)\rho_0 &= -\rho' \nabla \cdot \mathbf{v}_0 - \rho_0 \nabla \cdot \mathbf{v}' + m, \\ \frac{d\mathbf{v}'}{dt} + (\mathbf{v}' \cdot \nabla)\mathbf{v}_0 &= \frac{\rho'}{\rho_0^2} \nabla p_0 - \frac{1}{\rho_0} \nabla p' + \mathbf{f},\end{aligned}\tag{1.5}$$

with the convective derivative modified to:

$$\frac{d}{dt} = \frac{\partial}{\partial t} + \mathbf{v}_0 \cdot \nabla.$$

The linearized equation of state reads:

$$\frac{dp'}{dt} + \mathbf{v}' \cdot \nabla p_0 = c_0^2 \left(\frac{d\rho'}{dt} + \mathbf{v}' \cdot \nabla \rho_0 \right) + (c^2)' \mathbf{v}_0 \cdot \nabla \rho_0.\tag{1.6}$$

Assume first that in the absence of perturbations (waves) the fluid is at rest, *i.e.* $\mathbf{v}_0 = \mathbf{0}$. Then $\nabla p_0 = \mathbf{0}$ and:

$$\begin{aligned}\frac{\partial \rho'}{\partial t} &= -\nabla \cdot (\rho_0 \mathbf{v}') + m, \\ \frac{\partial \mathbf{v}'}{\partial t} &= -\frac{1}{\rho_0} \nabla p' + \mathbf{f},\end{aligned}\tag{1.7}$$

with:

$$\frac{\partial p'}{\partial t} = c_0^2 \left(\frac{\partial \rho'}{\partial t} + \mathbf{v}' \cdot \nabla \rho_0 \right)$$

from the linearized equation of state. The operators $\frac{\partial}{\partial t}$ and $\nabla \cdot$ commute (whereas $\frac{d}{dt}$ and $\nabla \cdot$ do not in general), hence the non-homogeneous acoustic wave equation reads [18]:

$$\frac{1}{c_0^2} \frac{\partial^2 p'}{\partial t^2} - \rho_0 \nabla \cdot \left(\frac{1}{\rho_0} \nabla p' \right) = \frac{\partial m}{\partial t} - \rho_0 \nabla \cdot \mathbf{f}.\tag{1.8}$$

If the background flow velocity \mathbf{v}_0 is a non vanishing constant, then $\nabla p_0 = \mathbf{0}$ again and $\mathbf{v}_0 \cdot \nabla \rho_0 = 0$. $\frac{d}{dt}$ and $\nabla \cdot$ can be commuted in this particular case, yielding the convected wave equation [21]:

$$\frac{d}{dt} \left(\frac{1}{c_0^2} \frac{dp'}{dt} \right) - \rho_0 \nabla \cdot \left(\frac{1}{\rho_0} \nabla p' \right) = \frac{dm}{dt} - \rho_0 \nabla \cdot \mathbf{f}.\tag{1.9}$$

This equation can be written as:

$$L(p'; \mathbf{w}_0) = S(\mathbf{w}_0),\tag{1.10}$$

with:

$$\begin{aligned}L(p'; \mathbf{w}_0) &= \frac{d}{dt} \left(\frac{1}{c_0^2} \frac{dp'}{dt} \right) - \rho_0 \nabla \cdot \left(\frac{1}{\rho_0} \nabla p' \right), \\ S(\mathbf{w}_0) &= \frac{dm}{dt} - \rho_0 \nabla \cdot \mathbf{f},\end{aligned}\tag{1.11}$$

where $\mathbf{w}_0 = (\mathbf{v}_0, \rho_0, c_0)$. We will see later that other models can be written as above, and in Sect. 1.3.2 we show how we can solve this form of equation.

1.1.2 Lighthill equation

In Lighthill's work [94,95], a subsonic turbulent airflow of relatively small spatial extent \mathcal{V} embedded in a uniform quiescent atmosphere, is considered. Such a situation arises for example for the flow in a jet, which is the main application we have in mind in this work. The speed of sound c_0 , pressure p_0 , and density ϱ_0 in this atmosphere (denoted with a subscript 0) are constant. The so-called Lighthill's acoustic analogy consists in realizing that at large distances from the turbulent region \mathcal{V} , the density fluctuations $\varrho' = \varrho - \varrho_0$, where ϱ is the density of the real fluid and ϱ' is not necessarily a first-order term with respect to ϱ_0 , ought to behave like acoustic waves in this atmosphere. Thus they should satisfy an homogeneous wave equation:

$$\frac{1}{c_0^2} \frac{\partial^2 \varrho'}{\partial t^2} - \Delta \varrho' = 0, \quad (1.12)$$

away from \mathcal{V} . To show this, Lighthill rearranged the equations governing the density fluctuations in the real fluid in the form of Eq. (1.12) appropriate to a uniform acoustic atmosphere at rest, which coincide with the real fluid outside the turbulent region \mathcal{V} . His derivation is done as follows. In the absence of source, the mass conservation and balance of momentum of Eq. (1.1) also read, in their Reynolds form:

$$\begin{aligned} \frac{\partial \varrho}{\partial t} + \nabla \cdot (\varrho \mathbf{v}) &= 0, \\ \frac{\partial(\varrho \mathbf{v})}{\partial t} + \nabla \cdot (\varrho \mathbf{v} \otimes \mathbf{v} - \boldsymbol{\sigma}) &= \mathbf{0}. \end{aligned} \quad (1.13)$$

Here $\mathbf{a} \otimes \mathbf{b}$ is the usual tensor product of vectors \mathbf{a} and \mathbf{b} such that $(\mathbf{a} \otimes \mathbf{b})_{ij} = a_i b_j$ in Cartesian coordinates. Applying ∂_t to the first equation, $\nabla \cdot$ to the second, and subtracting $c_0^2 \Delta \varrho$ and recalling that $\boldsymbol{\sigma} = -p\mathbf{I} + \boldsymbol{\tau}$, one obtains the Lighthill equation:

$$\frac{\partial^2 \varrho}{\partial t^2} - c_0^2 \Delta \varrho = \nabla \otimes \nabla : \mathbf{T} \quad (1.14)$$

where $\mathbf{T}(\mathbf{r}, t)$ is the Lighthill tensor [94,95]:

$$\mathbf{T} = \varrho \mathbf{v} \otimes \mathbf{v} - \boldsymbol{\tau} + (p - c_0^2 \varrho) \mathbf{I}, \quad (1.15)$$

and $\nabla \otimes \nabla : \mathbf{A} = \sum_{i,j} \partial_i \partial_j A_{ij}$.

In terms of the pressure and density fluctuations $p' = p - p_0$ and $\varrho' = \varrho - \varrho_0$, respectively, about that steady atmosphere (which again are not necessarily first-order terms), and ignoring from now on the viscous stresses $\boldsymbol{\tau}$,¹ one has:

$$\frac{\partial^2 \varrho'}{\partial t^2} - c_0^2 \Delta \varrho' = \nabla \otimes \nabla : \mathbf{T}', \quad (1.16)$$

with:

$$\mathbf{T}' = \varrho \mathbf{v} \otimes \mathbf{v} + (p' - c_0^2 \varrho') \mathbf{I}. \quad (1.17)$$

1. The ratio of the Reynolds stress terms $\varrho \mathbf{v} \otimes \mathbf{v}$ to the viscous stress terms $\boldsymbol{\tau}$ is of the order of magnitude of the Reynolds number $\text{Re} = \frac{\|(\varrho \mathbf{v} \cdot \nabla) \mathbf{v}\|}{\|\nabla \cdot \boldsymbol{\tau}\|}$, which is usually large in aerodynamic noise applications.

Eq. (1.16) is derived without any approximation and is true for an arbitrary fluid motion. It has the same form as the wave equation governing the acoustic field produced by a quadrupole source $S = \nabla \otimes \nabla : \mathbf{T}'$ in a non-moving ambient medium—the atmosphere. Thus there is an exact analogy (Lighthill’s acoustic analogy) between the density variations that occur in any real flow, and the density fluctuations that would arise in a quiescent homogeneous atmosphere with speed of sound c_0 and a quadrupole source distribution of strength \mathbf{T}' [79]. In addition the latter vanishes outside the region of extent \mathcal{V} of the turbulent flow, so that Eq. (1.16) reduces to Eq. (1.12) outside \mathcal{V} . Indeed, there the velocity field \mathbf{v} is reduced to the small sound motions and it appears quadratically in Lighthill’s tensor; and heat conduction effects, which causes departures of p' from $c_0^2 \rho'$, are very small.

We now turn to the Lighthill tensor \mathbf{T}' in Eq. (1.17) and its possible simplifications. The second term $p' - c_0^2 \rho'$ pertains to the heterogeneities of the speed of sound, which are induced by temperature fluctuations. This term vanishes in isentropic subsonic flows (assuming no combustion occurs either), but for hot jets temperature gradients are important and the local speed of sound varies significantly from the ambient speed of sound c_0 . The first term $\rho \mathbf{v} \otimes \mathbf{v}$ (the impulse or fluctuating Reynolds stresses) pertains to the heterogeneities of the flow, and is often approximated by $\rho_0 \mathbf{v} \otimes \mathbf{v}$ upon assuming that the density fluctuations ρ' are negligible within the moving fluid; this approximation is adopted in [81, 94, 95] and in the discussion below. In particular, it is argued in *e.g.* [94] that it is valid at low Mach number $M \equiv \frac{|\mathbf{v}|}{c_0}$ and provided that any difference in temperature between the flow and the atmosphere is due to kinetic heating or cooling.

Next, a sound wave propagating in the surrounding atmosphere is assumed to be incident upon the turbulent flow. In this situation the fluid particle velocity is written $\mathbf{v}(\mathbf{r}, t) = \mathbf{v}_0(\mathbf{r}, t) + \mathbf{v}'(\mathbf{r}, t)$, where \mathbf{v}_0 is the turbulent flow velocity in the absence of acoustic field, and \mathbf{v}' is the velocity perturbation induced by the presence of the incident sound wave. In this setting $\mathbf{v}_0(\mathbf{r}, t) = \mathbf{0}$ whenever $\mathbf{r} \notin \mathcal{V}$. Then adopting the foregoing approximations, that is, temperature variations are small (the jet is at the ambient temperature) and the magnitudes of \mathbf{v}_0 and \mathbf{v}' are small compared to c_0 , the Lighthill tensor on the right-hand side of Eq. (1.16) is:

$$\mathbf{T}' \simeq \rho_0 \mathbf{v}_0 \otimes \mathbf{v}_0 + 2\rho_0 \mathbf{v}_0 \otimes_s \mathbf{v}', \quad (1.18)$$

up to second order terms in \mathbf{v}' . Here $\mathbf{a} \otimes_s \mathbf{b} = \frac{1}{2}(\mathbf{a} \otimes \mathbf{b} + \mathbf{b} \otimes \mathbf{a})$ stands for the symmetric tensor product of vectors \mathbf{a} and \mathbf{b} . Consequently Eq. (1.16) has the form:

$$L(\rho'; \mathbf{w}_0) = S(\mathbf{w}_0), \quad (1.19)$$

where:

$$L(\rho'; \mathbf{w}_0) = \frac{\partial^2 \rho'}{\partial t^2} - c_0^2 \Delta \rho' - 2\rho_0 \nabla \otimes \nabla : (\mathbf{v}_0 \otimes_s \mathbf{v}'),$$

with $\mathbf{w}_0 = (\mathbf{v}_0, \rho_0, c_0)$, and $\mathbf{v}'(\rho')$ is the acoustic velocity field induced by ρ' , and:

$$S(\mathbf{w}_0) = \rho_0 \nabla \otimes \nabla : (\mathbf{v}_0 \otimes \mathbf{v}_0).$$

Eq. (1.19) has the same form as Eq. (1.10) for the convected wave equation, and is solved for a particular model of the background flow velocity \mathbf{v}_0 by a Born approximation alike; see Sect. 1.3.2.

1.1.3 Lilley equation

The analysis in Sect. 1.1.1 is now specialized to the case where \mathbf{v}_0 does not depend on "horizontal" Cartesian coordinates, say x, y , but only on the "vertical" coordinate z . This situation arises in many instances of real media (the ocean, the Earth's crust and atmosphere, some media in technical applications such as jet flows, *etc.*) which can be approximated by layered ones. The case of "horizontally" stratified media is the primary subject of the treatment below. From now on we note $\mathbf{r} = (\mathbf{x}, z)$ where \mathbf{x} stands for the two-dimensional horizontal components of the position vector \mathbf{r} , and z stands for the vertical component. It is further assumed that the background velocity \mathbf{v}_0 of the unperturbed flow is also horizontal:

$$\mathbf{v}_0(\mathbf{r}) = v_{0x}(z)\hat{\mathbf{e}}_x + v_{0y}(z)\hat{\mathbf{e}}_y, \quad (1.20)$$

where $(\hat{\mathbf{e}}_x, \hat{\mathbf{e}}_y, \hat{\mathbf{e}}_z)$ is a Cartesian basis. Then $(\mathbf{v}_0 \cdot \nabla)\mathbf{v}_0 = \mathbf{0}$, $\nabla \cdot \mathbf{v}_0 = 0$, and consequently $\nabla p_0 = \mathbf{0}$, $(\mathbf{v}_0 \cdot \nabla)\varrho_0 = 0$. The linearized Euler equations together with the equation of state read:

$$\frac{d\varrho'}{dt} + \mathbf{v}' \cdot \nabla \varrho_0 = -\varrho_0 \nabla \cdot \mathbf{v}' + m, \quad (1.21a)$$

$$\frac{d\mathbf{v}'}{dt} + v'_z \frac{d\mathbf{v}_0}{dz} = -\frac{1}{\varrho_0} \nabla p' + \mathbf{f}, \quad (1.21b)$$

$$\frac{dp'}{dt} = c_0^2 \left(\frac{d\varrho'}{dt} + \mathbf{v}' \cdot \nabla \varrho_0 \right), \quad (1.21c)$$

where $v'_z = \mathbf{v}' \cdot \hat{\mathbf{e}}_z$ is the vertical component of the acoustic velocity. We may eliminate the horizontal components of \mathbf{v}' from these equations by applying the divergence operator $\nabla \cdot$ to Eq. (1.21b) and the convective derivative $\frac{d}{dt}$ to Eq. (1.21a). By subtracting one from the other and noting the relation:

$$\nabla \cdot \frac{d\mathbf{v}'}{dt} - \frac{d}{dt} \nabla \cdot \mathbf{v}' = \frac{d\mathbf{v}_0}{dz} \cdot \nabla v'_z = \nabla \cdot \left(v'_z \frac{d\mathbf{v}_0}{dz} \right),$$

we get:

$$\frac{d}{dt} \left(\frac{1}{c_0^2} \frac{dp'}{dt} \right) - \varrho_0 \nabla \cdot \left(\frac{1}{\varrho_0} \nabla p' \right) - 2\varrho_0 \frac{d\mathbf{v}_0}{dz} \cdot \nabla v'_z = \frac{dm}{dt} - \varrho_0 \nabla \cdot \mathbf{f}. \quad (1.22)$$

In Eq. (1.22) above v'_z may be eliminated using the projection of Eq. (1.21b) on $\hat{\mathbf{e}}_z$, which yields $\frac{dv'_z}{dt} = -\frac{1}{\varrho_0} \frac{\partial p'}{\partial z} + f_z$ where $f_z = \mathbf{f} \cdot \hat{\mathbf{e}}_z$. Lilley's equation [97] is finally obtained by taking the convective derivative of Eq. (1.22):

$$\begin{aligned} \frac{d}{dt} \left[\frac{d}{dt} \left(\frac{1}{c_0^2} \frac{dp'}{dt} \right) - \varrho_0 \nabla \cdot \left(\frac{1}{\varrho_0} \nabla p' \right) \right] + 2\varrho_0 \frac{d\mathbf{v}_0}{dz} \cdot \nabla \left(\frac{1}{\varrho_0} \frac{\partial p'}{\partial z} \right) \\ = \frac{d^2 m}{dt^2} + 2\varrho_0 \frac{d\mathbf{v}_0}{dz} \cdot \nabla f_z - \varrho_0 \frac{d}{dt} \nabla \cdot \mathbf{f}. \end{aligned} \quad (1.23)$$

The left-hand side is the so-called Pridmore-Brown operator [113]. The Lilley equation is also derived in [79, Chapter 1] for a unidirectional, transversely sheared background flow of the form $\mathbf{v}_0(\mathbf{r}) = v_0(\phi(y, z))\hat{\mathbf{e}}_x$, where ϕ is an arbitrary function of the cartesian coordinates y, z in the crossflow directions. If for example $\phi(y, z) = \sqrt{y^2 + z^2}$ the background flow

remains constant on cylindrical surfaces of radius $r = \phi(y, z)$ and the Lilley equation in cylindrical coordinates (r, θ, x) is:

$$\begin{aligned} \frac{d}{dt} \left[\frac{d}{dt} \left(\frac{1}{c_0^2} \frac{dp'}{dt} \right) - \varrho_0 \nabla \cdot \left(\frac{1}{\varrho_0} \nabla p' \right) \right] + 2\varrho_0 \frac{dv_0}{dr} \frac{\partial}{\partial x} \left(\frac{1}{\varrho_0} \frac{\partial p'}{\partial r} \right) \\ = \frac{d^2 m}{dt^2} + 2\varrho_0 \frac{dv_0}{dr} \frac{\partial f_z}{\partial x} - \varrho_0 \frac{d}{dt} \nabla \cdot \mathbf{f}. \end{aligned} \quad (1.24)$$

We can write this equation as:

$$L(p'; \mathbf{w}_0) = S(\mathbf{w}_0), \quad (1.25)$$

with:

$$\begin{aligned} L(p'; \mathbf{w}_0) &= \frac{d}{dt} \left[\frac{d}{dt} \left(\frac{1}{c_0^2} \frac{dp'}{dt} \right) - \varrho_0 \nabla \cdot \left(\frac{1}{\varrho_0} \nabla p' \right) \right] + 2\varrho_0 \frac{dv_0}{dr} \frac{\partial}{\partial x} \left(\frac{1}{\varrho_0} \frac{\partial p'}{\partial r} \right), \\ S(\mathbf{w}_0) &= \frac{d^2 m}{dt^2} + 2\varrho_0 \frac{dv_0}{dr} \frac{\partial f_z}{\partial x} - \varrho_0 \frac{d}{dt} \nabla \cdot \mathbf{f}, \end{aligned} \quad (1.26)$$

where $\mathbf{w}_0 = (v_0, \varrho_0, c_0)$. Eq. (1.25) has the same form as Eq. (1.10) for the convected wave equation, and is solved for a particular model of the background flow velocity \mathbf{v}_0 by a Born approximation alike; see Sect. 1.3.2.

1.1.4 Acoustic waves in quiescent layered media

Acoustic waves propagating in quiescent layered media have been studied in [71, 72, 74] for example. The situation considered is that of a source \mathbf{f} located at $\mathbf{x}_s = \mathbf{0}$ and $z_s \geq 0$ (for we remind that $\mathbf{r} = (\mathbf{x}, z) = (x, y, z)$ is the position vector where \mathbf{x} stands for the two-dimensional horizontal coordinates and z is the vertical coordinate) emitting a pulse that will pass through an heterogeneous layer of thickness L , located between $z = 0$ and $z = -L$. The signal is recorded at the bottom of the layer at $z = -L$; see Fig. 1.1 for a sketch of this configuration. Here we are first interested by the deterministic case with constant parameters of the layer and we will show how we can randomize the medium in Sect. 1.3.

We consider linear acoustic waves propagating in three spatial dimensions:

$$\begin{aligned} \varrho_0 \frac{\partial \mathbf{v}'}{\partial t} + \nabla p' &= \varrho_0 \mathbf{f}, \\ \frac{1}{K_0} \frac{\partial p'}{\partial t} + \nabla \cdot \mathbf{v}' &= 0, \end{aligned} \quad (1.27)$$

where $K_0 = \varrho_0 c_0^2$ is the bulk modulus. Eq. (1.27) is obtained from Eq. (1.7) with $m = 0$ and using Eq. (1.6). The particular geometry of the problem suggests to use the particular Fourier transform, and its inverse:

$$\hat{\tau}(\omega, \boldsymbol{\kappa}, z) = \iint e^{i\omega(t - \boldsymbol{\kappa} \cdot \mathbf{x})} \tau(t, \mathbf{x}, z) dt d\mathbf{x}, \quad (1.28a)$$

$$\tau(t, \mathbf{x}, z) = \frac{1}{(2\pi)^3} \iint e^{-i\omega(t - \boldsymbol{\kappa} \cdot \mathbf{x})} \hat{\tau}(\omega, \boldsymbol{\kappa}, z) \omega^2 d\omega d\boldsymbol{\kappa}, \quad (1.28b)$$

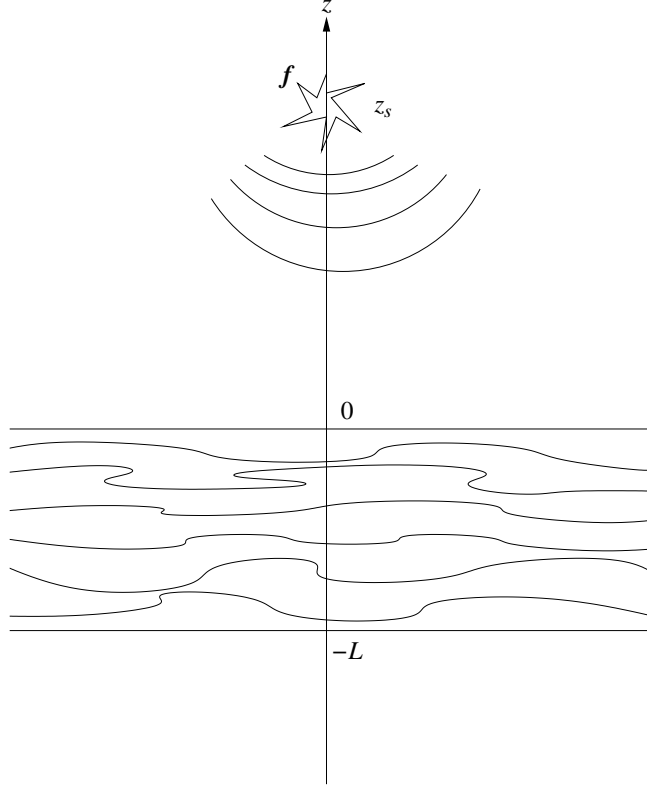


Figure 1.1 – Acoustic waves in a quiescent layered medium of typical thickness L . The emitting sources \mathbf{f} is centered at some $z_s \geq 0$.

for either $\tau = p'$ or $\tau = \mathbf{v}'$. In the Fourier domain the problem (1.27) then reads:

$$\begin{aligned} -i\omega\varrho_0\widehat{\mathbf{v}}'_x + i\omega\boldsymbol{\kappa}\widehat{p}' &= \varrho_0\widehat{\mathbf{f}}_x, \\ -i\omega\varrho_0\widehat{v}'_z + \frac{\partial\widehat{p}'}{\partial z} &= \varrho_0\widehat{f}_z, \\ -\frac{i\omega}{K_0}\widehat{p}' + i\omega\boldsymbol{\kappa} \cdot \widehat{\mathbf{v}}'_x + \frac{\partial\widehat{v}'_z}{\partial z} &= 0, \end{aligned} \tag{1.29}$$

where \mathbf{v}'_x is the projection of \mathbf{v}' on the plan \mathbf{x} and v'_z is the the projection of \mathbf{v}' on the z -axis. We eliminate the terms with $\widehat{\mathbf{v}}'_x$ in (1.29) multiplying the first equation by $\frac{\boldsymbol{\kappa}}{\varrho_0}$ and adding the third:

$$\begin{aligned} \frac{\partial\widehat{v}'_z}{\partial z} - i\omega\left(\frac{1}{K_0} - \frac{|\boldsymbol{\kappa}|^2}{\varrho_0}\right)\widehat{p}' &= \boldsymbol{\kappa} \cdot \widehat{\mathbf{f}}_x, \\ \frac{\partial\widehat{p}'}{\partial z} - i\omega\varrho_0\widehat{v}'_z &= \varrho_0\widehat{f}_z. \end{aligned} \tag{1.30}$$

The source:

$$\mathbf{F}(\mathbf{x}, z) = \begin{pmatrix} \varrho_0\mathbf{f}(\mathbf{x}, z) \\ 0 \end{pmatrix} = \mathbf{F}(\mathbf{x}_s, z_s)\delta(\mathbf{x} - \mathbf{x}_s)\delta(z - z_s). \tag{1.31}$$

generates a forcing term at the point (\mathbf{x}_s, z_s) . We choose $\mathbf{x}_s = \mathbf{0}$ here so $\delta(\mathbf{x} - \mathbf{x}_s) = \delta(\mathbf{x})$.

It will be useful in the Fourier domain because $\widehat{\delta(\mathbf{x})} = 1$. Eq. (1.30) can be reduced to:

$$\mathbf{L}(\widehat{p}', \widehat{v}'_z; \mathbf{w}_0) = \widehat{\mathbf{S}}(\mathbf{w}_0), \quad (1.32)$$

with:

$$\mathbf{L}(\widehat{p}', \widehat{v}'_z; \mathbf{w}_0) = \begin{pmatrix} \frac{\partial \widehat{v}'_z}{\partial z} - i\omega \left(\frac{1}{K_0} - \frac{|\boldsymbol{\kappa}|^2}{\varrho_0} \right) \widehat{p}' \\ \frac{\partial \widehat{p}'}{\partial z} - i\omega \varrho_0 \widehat{v}'_z \end{pmatrix} \quad (1.33)$$

a linear operator with respect to \widehat{p}' and \widehat{v}'_z , and:

$$\widehat{\mathbf{S}}(\mathbf{w}_0) = \begin{pmatrix} \boldsymbol{\kappa} \cdot \widehat{\mathbf{f}}_x \\ \varrho_0 \widehat{f}_z \end{pmatrix} \delta(z - z_s), \quad (1.34)$$

where, in particular, $\mathbf{w}_0 = (K_0, \varrho_0)$ here. Again, Eq. (1.32) can be solved for a particular model of the layer parameters \mathbf{w}_0 by a Born approximation; see Sect. 1.3.2.

1.1.5 Acoustic waves in randomly heterogeneous media

Research on wave propagation in random media has always been motivated by communication and imaging problems. Geosciences were the first to take an intense interest in imaging in random media, typically source and reflector localization [8, 34]. The objective was to better understand the interaction of waves with the medium in order to design and implement new imaging techniques. The characterization of a stratified or porous media, inducing multiple reflections-transmissions is useful in many fields (seismic-volcanic studies, oil industry, construction, ...). The acoustic wave will be separated in two parts, the coherent one, which will undergo a delay and an attenuation, and the incoherent one, so-called coda in seismology, which have random fluctuations. Indeed in the literature, it is shown that the coherent part of the wave experiences a deterministic spreading and a random time shift. As the coherent wave decays exponentially with the propagation distance, the relevant information is carried by the covariance function or second-order moment of the incoherent wave field. These phenomena were originally described by O'Doherty and Anstey in a geophysical context [105]. They were interested in the delay produced by a stratified environment on a signal as well as the attenuation of that induced by multiple reflections-transmissions. Then they were studied mathematically in [2, 56]. The mathematical approach is based on techniques of separation of scales as introduced by George Papanicolaou and his coauthors [8]. One finds that the coherent (mean) wave amplitude decreases with distance traveled since wave energy is converted to incoherent fluctuations. In this context the model presented above in Sect. 1.1.4 can be useful for modeling wave propagation in randomly layered media. Indeed, Alfaro *et al.* [2], Fouque *et al.* [72] or Garnier [74] use this approach assuming that the background properties \mathbf{w}_0 are decomposed into mean properties, and fluctuating parts modeled by zero mean random fields. Inhomogeneities are supposed to be small. In particular for a randomly stratified quiescent medium, K_0 (and possibly ϱ_0) in Eq. (1.32) is randomized in this manner. In Sect. 1.3 we will further detail some models of acoustic wave propagation in random media.

The scattering of acoustic waves by a random flow is also widely studied. In [64–66] or [103, 112] and further works by the same authors, Eq. (1.25) is solved introducing an incident field propagated in the mean background flow, and a scattered field induced by scattering by the fluctuating turbulent velocity. In this model the background flow velocity

\mathbf{v}_0 is randomized by considering its mean part and a fluctuating part, representing the turbulent velocity fluctuations within the flow. An integral representation is derived for that scattered field in the Born approximation, using a Green function-like solution of the Pridmore-Brown operator of which source is constituted by the incident field. As in [64–66], McAlpine and Tester [104] start from Lilley’s equation (see Sect. 1.1.3) and randomize it to study the spectral broadening. The Lighthill equation of Sect. 1.1.2 is solved along the same lines in [81]. In these approaches, the scattered field is thus obtained as a linear function of the turbulent velocity \mathbf{v}_0 (or bulk modulus K_0 as in Sect. 1.1.4). This allows to compute its autocorrelation function and power spectrum, provided that the autocorrelation function and power spectrum of the fluctuations of the turbulent velocity are known. The same approach will be developed in Chapter 2 for the model of a randomly stratified background flow we have considered in this research. The overall analysis is described in Sect. 1.3.2, while in Sect. 1.2 below we recall for completeness the useful definitions and properties of the autocorrelation and spectral density matrices of a random field.

1.2 Autocorrelation function and power spectral density

In the various models outlined above in Sect. 1.1.1 the ambient flow velocity may be written:

$$\mathbf{v}_0 = \underline{\mathbf{v}} + \varepsilon \mathbf{V}, \quad (1.35)$$

where $\underline{\mathbf{v}}$ is the constant mean velocity field, \mathbf{V} is the fluctuating turbulent velocity modeled by a random field with zero mean, and ε is a small scaling factor—typically the turbulence intensity scaling the turbulent kinetic energy of the flow. This model of the ambient flow velocity will be considered in Chapter 2. For this reason we will review here some important definitions of stochastic processes and their correlation which are widely used in this thesis. The random field $(\mathbf{V}(\mathbf{r}, t), (\mathbf{r}, t) \in \mathbb{R}^3 \times \mathbb{R})$ such that $\mathbb{E}\{|\mathbf{V}(\mathbf{r}, t)|^2\} < +\infty, \forall (\mathbf{r}, t) \in \mathbb{R}^3 \times \mathbb{R}$, is characterized as follows. Its autocorrelation function is:

$$\mathbf{R}_{\mathbf{V}}(\mathbf{r}_1, \mathbf{r}_2, t_1, t_2) = \mathbb{E}\left\{\mathbf{V}(\mathbf{r}_1, t_1)\overline{\mathbf{V}(\mathbf{r}_2, t_2)}^\top\right\} \quad (1.36)$$

where $\overline{\cdot}^\top$ is the complex conjugate transpose and \mathbb{E} stands for mathematical expectation. The random field is mean-square stationary if its mean is independent of t —if we talk about time—, *i.e.* $\mathbb{E}\{\mathbf{V}(\mathbf{r}, t)\} = \mathbf{0}$ if the random field is centered—which is the case for us—, and its autocorrelation function depends on the difference of times solely:

$$\mathbf{R}_{\mathbf{V}}(\mathbf{r}_1, \mathbf{r}_2, t_1, t_2) = \mathbf{R}_{\mathbf{V}}(\mathbf{r}_1, \mathbf{r}_2, t_1 - t_2)$$

with $\mathbf{R}_{\mathbf{V}}(\mathbf{r}_1, \mathbf{r}_2, t_1 - t_2)^\top = \mathbf{R}_{\mathbf{V}}(\mathbf{r}_1, \mathbf{r}_2, t_2 - t_1)$. This definition holds for the spatial variables alike. The random field is mean-square homogeneous if its mean is independent of \mathbf{r} , *i.e.* $\mathbb{E}\{\mathbf{V}(\mathbf{r}, t)\} = \mathbf{0}$ if the random field is centered—which is again the case for us—, and its autocorrelation function depends on the difference of positions solely:

$$\mathbf{R}_{\mathbf{V}}(\mathbf{r}_1, \mathbf{r}_2, t_1, t_2) = \mathbf{R}_{\mathbf{V}}(\mathbf{r}_1 - \mathbf{r}_2, t_1, t_2)$$

with $\mathbf{R}_{\mathbf{V}}(\mathbf{r}_1 - \mathbf{r}_2, t_1, t_2)^\top = \mathbf{R}_{\mathbf{V}}(\mathbf{r}_2 - \mathbf{r}_1, t_1, t_2)$. The random field can be mean-square stationary and homogeneous and in this case its autocorrelation function reads:

$$\mathbf{R}_{\mathbf{V}}(\mathbf{r}_1, \mathbf{r}_2, t_1, t_2) = \mathbf{R}_{\mathbf{V}}(\mathbf{r}_1 - \mathbf{r}_2, t_1 - t_2).$$

Thus one has $\mathbf{R}_V(\mathbf{r}_1 - \mathbf{r}_2, t_1 - t_2)^\top = \mathbf{R}_V(\mathbf{r}_2 - \mathbf{r}_1, t_2 - t_1)$. Homogeneous isotropic turbulence is defined by the properties that [13]:

$$\mathbf{R}_V(\mathbf{r}, t) = \overline{\Theta}^\top \mathbf{R}_V(\Theta \mathbf{r}, t) \Theta$$

for any proper rotation Θ , and $\mathbf{R}_V(\mathbf{r}, t) = \mathbf{R}_V(\mathbf{r}, t)^\top$. Furthermore it is shown that in this case $\mathbf{R}_V(\mathbf{r}, t)$ necessarily reads [13, 88, 114]:

$$\mathbf{R}_V(\mathbf{r}, t) = F(r, t) \hat{\mathbf{r}} \otimes \hat{\mathbf{r}} + G(r, t) \mathbf{I}, \quad (1.37)$$

where $r = |\mathbf{r}|$, $\hat{\mathbf{r}} = \frac{\mathbf{r}}{r}$ for $r \neq 0$, and $r, t \rightarrow F(r, t)$ and $r, t \rightarrow G(r, t)$ are even functions. According to the Wiener-Khintchine theorem [100], the necessary and sufficient condition for $\mathbf{R}_V(\mathbf{r}, t)$ to be the correlation function of a mean-square stationary and homogeneous centered random field is that it should be expressible as (see for example [13, §2.4]):

$$\mathbf{R}_V(\mathbf{r}, t) = \frac{1}{(2\pi)^4} \iint e^{-i(\omega t - \mathbf{k} \cdot \mathbf{r})} \Sigma_V(\mathbf{k}, \omega) d\mathbf{k} d\omega, \quad (1.38)$$

where $\mathbf{k}, \omega \rightarrow \Sigma_V(\mathbf{k}, \omega)$ is an Hermitian, non-negative complex matrix function—the power spectral density (PSD) matrix of the random field ($\mathbf{V}(\mathbf{r}, t), (\mathbf{r}, t) \in \mathbb{R}^3 \times \mathbb{R}$). Conversely:

$$\Sigma_V(\mathbf{k}, \omega) = \iint e^{i(\omega t - \mathbf{k} \cdot \mathbf{r})} \mathbf{R}_V(\mathbf{r}, t) d\mathbf{r} dt. \quad (1.39)$$

Since $\int e^{i\omega t} dt = 2\pi\delta(\omega)$, time stationarity and spatial homogeneity implies that:

$$\mathbb{E} \left\{ \widehat{\mathbf{V}}(\mathbf{k}_1, \omega_1) \overline{\widehat{\mathbf{V}}(\mathbf{k}_2, \omega_2)}^\top \right\} = (2\pi)^4 \delta(\mathbf{k}_1 - \mathbf{k}_2) \delta(\omega_1 - \omega_2) \Sigma_V(\mathbf{k}_1, \omega_1), \quad (1.40)$$

and $\Sigma_V(-\mathbf{k}_1, -\omega_1) = \Sigma_V(\mathbf{k}_1, \omega_1)^\top$, where the Fourier transform is defined by:

$$\widehat{\mathbf{V}}(\mathbf{k}, \omega) = \iint e^{i(\omega t - \mathbf{k} \cdot \mathbf{r})} \mathbf{V}(\mathbf{r}, t) d\mathbf{r} dt. \quad (1.41)$$

Now we have seen the main definitions used in this thesis for the autocorrelation function and the power spectral density of a stochastic process.

1.3 Acoustic waves in random media and random flows

Having introduced several models of acoustic wave propagation in homogeneous and heterogeneous flows in Sect. 1.1, and useful definitions for stochastic processes in Sect. 1.2, we present here some models of acoustic wave propagation in random media and random flows. The motivations for considering such models have been outlined in Sect. 1.1.5 in a general context. In this section we more particularly focus on the experiments with acoustic waves in jet flows carried out by Candel *et al.* [41–43], and the approaches that may be used to explain their observations.

1.3.1 Acoustic scattering in the anechoic open jet wind tunnel measurements

Despite the major differences between real and experimental configurations that must be considered during acoustic measurements, anechoic open jet wind tunnels are experimental devices used to approach flight conditions in the laboratory in order to study aeroacoustic characteristics of an aircraft. Indeed, in the experimental configuration, the scale model aircraft, placed in a flow of uniform velocity, is motionless compared to the microphones located in a medium at rest, outside the vein. In a real configuration, the aircraft moves relative to the observer which induces a Doppler effect on the perceived wavelength. During the experimental tests, the differential velocity destabilizes the flow according to the Kelvin-Helmholtz mechanism and causes the formation of a turbulent shear layer. The acoustic waves emitted by the model cross the uniform flow, then the turbulent shear layer before reaching the microphones. In order to characterize the physical phenomena that come into play during the propagation of an acoustic wave, experiments [43, 81] have been conducted by replacing the model with a monochromatic source S of which we know the emission frequency. The acoustic wave emitted by S thus undergoes four effects: the convection of the acoustic wave by the medium; the diffraction of the wave by the orifice of the source; the refraction of the acoustic wave by the average velocity gradient; the diffusion of the acoustic wave by the fluctuations of turbulent velocities of the shear layer. These phenomena come to replace the Doppler effect, present in real flight conditions.

The effects of convection and diffraction have been studied by Candel *et al.* [42] during measurements in the Von Kármán Institute L1 wind tunnel. Their diffraction model makes it possible to take into account the influence of uniform flow on acoustic emission. They also analyzed the effects of refraction on the acoustic propagation thanks to the measurement of the average phase variation (between the electric pulse of the source and the pressure signal received by a microphone outside the jet), outside the jet. The average phase difference evolves linearly as a function of the viewing angle (relative to the direction of flow), independently of the emission circular frequency ω_0 . This shows the geometrical nature of acoustic propagation, confirmed by comparisons between experimentally measured directivity diagrams and diagrams calculated using a geometrical acoustical code for stationary flow. Finally, the refraction induces a spatial redistribution of the amplitude, characterized by a deviation of the acoustic propagation law in $1/d$, where d is the distance between the wavefront and the source. This spatial reorientation of the amplitude and the change of the propagation angles during the crossing of the shear layer has been studied by Amiet [7]. The author expresses the relationships that exist between the initial propagation angle, the angle after refraction, and the propagation angle without the shear layer. He shows that the relationships between the angles do not depend on the thickness of the shear layer, if it is small compared to the distance between the source and the microphone. For the corrections to be valid, however, it is necessary that the microphone source distance is large in front of the wavelength and the dimensions of the source. The amplitude correction depends on the nature of the shear layer (plane or cylindrical). Ahuja *et al.* [4] explained the procedure to take into account the effects of convection and refraction during acoustic measurements in open-jet anechoic wind tunnel. They showed that the level of sound pressure emitted by the source is precisely found, provided that we take into account the change in directivity of the rays and that we apply, at the level of sound pressure received by the microphones located in outside the jet, correction coefficients related to the microphone source distance. The

authors are also interested in potential internal reflections on shear layers. They become important if the direction of the acoustic wave emitted is close to that of the flow. For measurements more or less above the source, they are weak.

The experimental setup used by Candel *et al.* [41] is schematized in Fig. 1.2. S is an

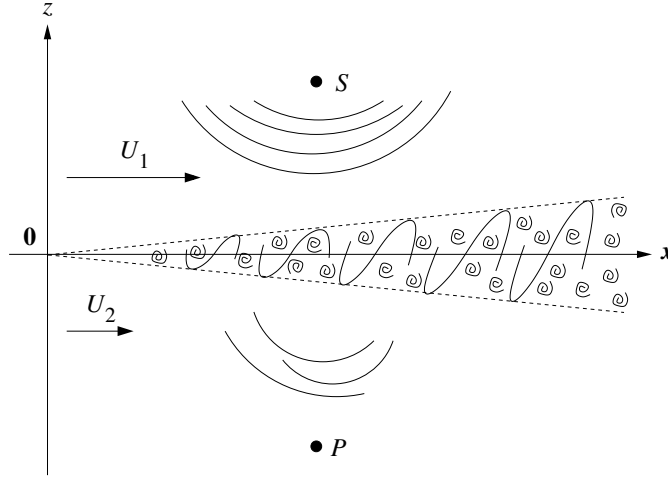


Figure 1.2 – Sketch of the experimental setup of Candel *et al.* [41]. S is the source position, and P is the microphone position.

acoustic source, placed at the center of a jet at the velocity U_1 . The scattered pressure field is measured outside the jet, at the microphone P . The microphone P is at an angle of $\theta_P = 90^\circ$ to the source. The authors measure the turbulent velocity fields with hot wires. The large turbulent structures, described by Brown and Roshko [38], are convected at the velocity v_t . The first consequence of the interaction between the acoustic wave and the turbulent flow lies in the modulation of the amplitude of the scattered pressure field extracted from the work of Candel *et al.* [41]. This modulation is low frequency, compared to the "carrier" frequency, *i.e.* the emission frequency $f_0 = \omega_0/2\pi$. The power spectral density of the pressure fluctuations, received by the microphone P , extracted from [41], is plotted on Fig. 1.3, as a function of the frequency centered on f_0 , $f - f_0$. In their works, the authors used an incident monochromatic source that emits between 4 kHz and 20 kHz, plunging in a jet between 20 and 60 m/s. This limit is explained by the fact that the energy scattered is equal to the total energy when one exceeds $f_0 \simeq 20$ kHz [81]. Furthermore the travel time between the source and the microphone is independent of the carrier frequency for $1 \text{ kHz} \leq f_0 \leq 20 \text{ kHz}$ and in these conditions for a central frequency greater than 6kHz more than half of the acoustic power is carried by the scattered field [41].

A large part of the acoustic energy remains contained in a "main peak", corresponding to the emission frequency, but we also observe the presence of two "secondary lobes" on each side of the peak. As the transmission frequency increases, the energy contained in the main peak decreases in favor of the side lobes. It is interesting to note that the frequencies for which the lobes reach their maximum, are identical to the sign and independent of the emission frequency. Candel *et al.* [41] also studied the influence of the velocity of the jet on the position of the maximum lobes. They showed that the frequency shift is proportional to the convection velocity of the turbulent structures v_t . The energy distribution on frequencies adjacent to the transmit frequency is attributed to a Doppler effect. Candel *et*

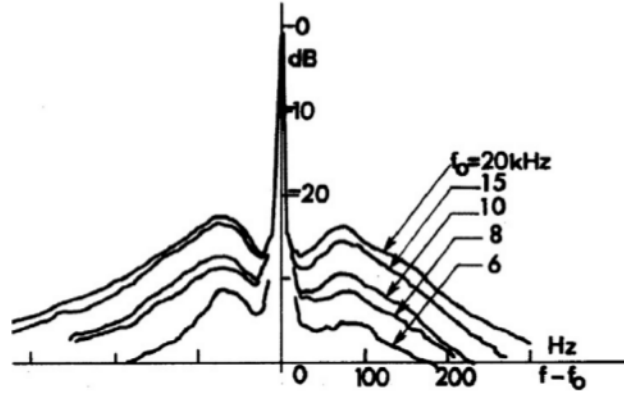


Figure 1.3 – Power spectral density of pressure fluctuations as a function of the centered frequency $f - f_0$ for a jet velocity $U_1 = 60$ m/s. Figure is taken from [41].

al. [46] show in particular that the diffusion process selects the low frequencies of the shear layer. This makes it possible to isolate the quasi-periodic nature of the passage of large turbulent structures. Schlinker and Amiet [116] studied the refraction and also the effects of acoustic diffusion. The authors explain that the spatial and spectral distribution of scattered energy is a consequence of the Doppler effect. The ray emitted by the source would be absorbed then re-emitted by the turbulent structure. This induces a double Doppler effect; At first, the ray is absorbed by a moving receiver and in a second time, re-emitted by a moving source. Schlinker and Amiet [116] carried out a series of measurements on the United Technologies Research Center’s Acoustic Research Tunnel to study the influence of the observation angle θ_P , the position and frequency of the source, the thickness of the shear layer and the Mach number of the jet on the attenuation of the main peak. Their conclusions are in agreement with those of Candel *et al.* [41]: the main peak is attenuated when the emission frequency, the thickness of the layer traversed and the Mach number increase. They also estimated that scattering effects become significant, *i.e.* when more than half of the incident energy is scattered, if $\frac{M_1 L}{\lambda_0}$ is almost greater than 0.5, with L the thickness of the shear layer, M_1 the Mach number of the jet based on the velocity U_1 , and λ_0 the wavelength of the acoustic wave emitted by the source.

The characteristics of the scattered pressure field as well as the acoustic diffusion interaction mechanisms previously described have been validated by ”simplistic” analytical models. These models are often based on a Born approximation applied to the linear equations retained to describe the acoustic wave propagation phenomena, namely the linearized Euler equations of Sect. 1.1.1 in [54, 55], or the Lighthill equation of Sect. 1.1.2 in [41, 81], or the Lilley equation of Sect. 1.1.3 in [64–66, 104], or the wave equation in a layered medium of Sect. 1.1.4 in [2, 72, 74].

1.3.2 The Born approximation

The different models of acoustic wave propagation in quiescent and moving media outlined in Sect. 1.1 read:

$$L(p'; \mathbf{w}_0) = S(\mathbf{w}_0), \quad (\text{or } L(\varrho'; \mathbf{w}_0) = S(\mathbf{w}_0)), \quad (1.42)$$

where L is a linear operator with respect to p' (or ρ'), and S is the right-hand side playing the role of a source to p' (or ρ'). From now on in this section we drop the primes $(\cdot)'$ and consider (see Eq. (1.35)) $\mathbf{v}_0(\mathbf{r}, t) = \underline{\mathbf{v}} + \varepsilon \mathbf{V}(\mathbf{r}, t)$, where again $\underline{\mathbf{v}}$ is the mean velocity field of the flow, \mathbf{V} is its turbulent (random) fluctuations, and ε is a small parameter. Then the foregoing equation is further linearized about $\underline{\mathbf{v}}$ as (the same holds for equations in ρ):

$$\begin{aligned} L(p; \mathbf{w}_0) &= S(\mathbf{w}_0), \\ L(p; \underline{\mathbf{v}} + \varepsilon \mathbf{V}, \rho_0, c_0) &= S(\underline{\mathbf{v}} + \varepsilon \mathbf{V}, \rho_0, c_0), \\ L(p; \underline{\mathbf{w}}) + \varepsilon \underline{L}(p; \mathbf{W}) &= S(\underline{\mathbf{w}}) + \varepsilon \underline{S}(\mathbf{W}), \end{aligned} \quad (1.43)$$

where \underline{L} and \underline{S} are the linearized parts of L and S , respectively, with respect to $\underline{\mathbf{v}}$, $\underline{\mathbf{w}} = (\underline{\mathbf{v}}, \rho_0, c_0)$, and $\mathbf{W} = (\mathbf{V}, \rho_0, c_0)$. The strategy is to formulate (1.43) as:

$$L(p; \underline{\mathbf{w}}) = S(\underline{\mathbf{w}}) + \varepsilon (\underline{S}(\mathbf{W}) - \underline{L}(p; \mathbf{W})). \quad (1.44)$$

Now introduce the Green's function $G_0(\mathbf{r}, \mathbf{r}', t)$ satisfying:

$$L(G_0; \underline{\mathbf{w}}) = \delta(t)\delta(\mathbf{r} - \mathbf{r}'); \quad (1.45)$$

then:

$$p = G_0 * (S(\underline{\mathbf{w}}) + \varepsilon S^{(01)}(p; \mathbf{W})), \quad (1.46)$$

where $S^{(01)}(p; \mathbf{W}) = \underline{S}(\mathbf{W}) - \underline{L}(p; \mathbf{W})$ is linear with respect to \mathbf{V} and $a*b$ is the convolution product of a and b with respect to the time t and the space \mathbf{r} . This is a so-called Lippmann-Schwinger equation [99], of which a solution can formally be constructed by mathematical induction:

$$p^{(n+1)} = p^{(0)} + \varepsilon G_0 * S^{(01)}(p^{(n)}; \mathbf{W}), \quad (1.47)$$

with $p^{(0)} = G_0 * S(\underline{\mathbf{w}})$ is the incident wave. We will only go here until the first order, so we will write p as the sum of the incident field $p^{(0)}(\mathbf{r}, t)$ and the scattered field $p^{(01)}(\mathbf{r}, t)$ as:

$$p \simeq p^{(1)}(\mathbf{r}, t) = p^{(0)}(\mathbf{r}, t) + \varepsilon p^{(01)}(\mathbf{r}, t); \quad (1.48)$$

then:

$$p^{(01)} = G_0 * S^{(01)}(p^{(0)}; \mathbf{W}). \quad (1.49)$$

We have an expression of the scattered field $p^{(01)}$, which we can see as a stochastic process because it is a function of \mathbf{V} . It is even a linear function of \mathbf{V} , G_0 is a linear operator as well as the convolution $*$, and we saw previously that $S^{(01)}$ is linear with respect to \mathbf{V} . This allows us to write $S^{(01)}(p^{(0)}; \mathbf{W}) = S_{\mathcal{O}}^{(01)}(p^{(0)}; \rho_0, c_0) \mathbf{V}$ where $S_{\mathcal{O}}^{(01)}$ is a source operator acting on \mathbf{V} , and to express the PSD of $p^{(01)}$ as a function of the PSD of \mathbf{V} . If the latter is a stationary, homogeneous stochastic process of which PSD is $\Sigma_{\mathbf{V}}$, then the PSD of the single-scattered field $p^{(01)}$, $\Sigma_{p^{(01)}}$ reads:

$$\begin{aligned} \Sigma_{p^{(01)}}(\mathbf{k}, \omega) &= \widehat{G_0} \widehat{S}(\widehat{p}^{(0)}; \mathbf{W}) \overline{\widehat{S}(\widehat{p}^{(0)}; \mathbf{W})}^{\top} \widehat{G_0}^{\top}, \\ &= \widehat{G_0} \widehat{S_{\mathcal{O}}^{(01)}}(\widehat{p}^{(0)}; \rho_0, c_0) \Sigma_{\mathbf{V}}(\mathbf{k}, \omega) \overline{\widehat{S_{\mathcal{O}}^{(01)}}(\widehat{p}^{(0)}; \rho_0, c_0)}^{\top} \widehat{G_0}^{\top}. \end{aligned} \quad (1.50)$$

This is the approach adopted in [47, 64, 81, 103, 104, 112] among others, to derive the PSD of the pressure field scattered by a turbulent jet flow for sound waves impinging it.

This is also the approach that will be followed in Chapter 2 of this thesis. A key ingredient of these analyses is a relevant choice of the PSD $\Sigma_{\mathbf{v}}$ of the turbulent velocity fluctuations which is consistent with the form imposed on the correlation function of a homogeneous isotropic turbulence field as outlined in [13, 88, 114] or axisymmetric turbulence as outlined in [12, 51, 98]; see Sect. 1.2.

1.3.3 The O’Doherty-Anstey (ODA) theory

In this section we will focus on a new approach introduced by Fouque *et al.* [71] and Garnier [74] to produce images in the context of media with random inhomogeneities. The objective of [74] is to study the cross-correlation functions of the signals recorded at a series of points located at the surface of a randomly layered medium. It is shown that this information can be processed to locate and identify an active source embedded in a randomly layered medium.

Wave propagation in a randomly layered medium

At first we will show how we can describe the propagation of a short pulse emitted by a source embedded in a random layered medium with the ODA theory. The problem is the same as in Eq. (1.27):

$$\begin{aligned} \frac{1}{K_0} \frac{\partial p'}{\partial t} + \nabla \cdot \mathbf{v}' &= 0, \\ \varrho_0 \frac{\partial \mathbf{v}'}{\partial t} + \nabla p' &= \mathbf{f}. \end{aligned} \quad (1.51)$$

In these studies the fluctuation of the medium are modeled by a random process of ϱ_0 and $K_0 = \varrho_0 c_0^2$. The model is:

$$\varrho_0(z) = \begin{cases} \underline{\varrho} [1 + \eta(z)] & \text{for } z \in [-L, 0], \\ \underline{\varrho} & \text{for } z \in (-\infty, -L) \cup (0, +\infty), \end{cases} \quad (1.52a)$$

$$\frac{1}{K_0(z)} = \begin{cases} \frac{1}{\underline{K}} [1 + \nu(z)] & \text{for } z \in [-L, 0], \\ \frac{1}{\underline{K}} & \text{for } z \in (-\infty, -L) \cup (0, +\infty), \end{cases} \quad (1.52b)$$

with η and ν described as random coefficients rapidly varying, making it possible to model the inhomogeneities of the medium. They are both zero-mean processes, furthermore the ratio between the correlation length of the fluctuations of the medium and the typical size of the medium is small. With this definition we have $\underline{c} = \sqrt{\frac{\underline{K}}{\underline{\varrho}}}$. In [2] the perturbation model is composed by (1.52a) and (1.52b), the problem is solved in one dimension. *Contrario* in [71] and [74] the perturbation model is only on the bulk modulus, (1.52b), and the problem is solved in three dimensions. This is what is presented here. This case is the one we consider in Chapter 2 before randomizing the flow. Despite the addition of two dimensions, compared to [2], the random fluctuations of the medium are still only z -dependent. The geometry of the problem is the same as the one introduced in 1.1.4, we will then use the Fourier transform introduced in Eq. (1.28a) and its inverse Eq. (1.28b). The source \mathbf{f} generate a forcing term at the point (\mathbf{x}_s, z_s) :

$$\mathbf{f}(t, \mathbf{x}, z) = \mathbf{F}(t) \delta(\mathbf{x} - \mathbf{x}_s) \delta(z - z_s). \quad (1.53)$$

$\mathbf{F}(t)$ emits a short pulse at time t_s :

$$\mathbf{F}(t) = \begin{pmatrix} \mathbf{f}_x \\ f_z \end{pmatrix} (t - t_s), \quad (1.54)$$

and is somewhere below the surface ($\mathbf{x}_s, z_s < 0$).

The front pulse emitted by the source propagates through the random medium, and its propagation is governed by the well-known ODA theory [105]. Garnier [74] explains that the front pulse is modified in two ways in this case. First, its shape spreads out in a deterministic way due to multiple scattering. Second, the wave itself is no longer deterministic, but a random time shift can be observed and described in terms of a standard Brownian motion B_z . These two effects can be described in terms of the convolution ODA kernel K_{ODA} of Eq. (1.55) [72, 105]:

$$\widehat{K}_{\text{ODA}}(\omega, \boldsymbol{\kappa}) = \exp \left(i\sqrt{\gamma(\omega, \boldsymbol{\kappa})} B_{z_s} + \frac{\gamma(\omega, \boldsymbol{\kappa}) z_s}{2} \right), \quad (1.55)$$

where:

$$\begin{aligned} \gamma(\omega, \boldsymbol{\kappa}) &= \frac{\gamma_0 \omega^2}{2c^4 \zeta(\boldsymbol{\kappa})^2}, \\ \gamma_0 &= \int_0^\infty \mathbb{E} \{ \nu(0) \nu(z) \} dz, \end{aligned} \quad (1.56)$$

with $\zeta(\boldsymbol{\kappa}) = \sqrt{\frac{1}{c^2} - |\boldsymbol{\kappa}|}$ and B_{z_s} a standard Brownian motion. To sum up, the coherent front pulse that can be recorded at the surface $z = 0$ is:

$$p'(t, \mathbf{x}, z = 0) = \frac{1}{2\pi} \int \frac{I(\boldsymbol{\kappa})}{2} e^{-i\omega(t-t_s - \boldsymbol{\kappa} \cdot (\mathbf{x} - \mathbf{x}_s) + \zeta(\boldsymbol{\kappa}) z_s)} \widehat{K}_{\text{ODA}}(\omega, \boldsymbol{\kappa}) \Sigma_a(\omega, \boldsymbol{\kappa}) \omega^2 d\omega d\boldsymbol{\kappa}, \quad (1.57)$$

where $I = \frac{\underline{g}}{\zeta(\boldsymbol{\kappa})}$ and Σ_a is the upward source contribution:

$$\Sigma_a(\omega, \boldsymbol{\kappa}) = \frac{\sqrt{I(\boldsymbol{\kappa})}}{\underline{g}} \boldsymbol{\kappa} \cdot \widehat{\mathbf{f}}_x(\omega) + \frac{1}{I(\boldsymbol{\kappa})} \widehat{f}_z(\omega). \quad (1.58)$$

K_{ODA} acts as a low-pass filter. A stationary phase argument shows that the leading-order contribution is associated with the stationary point:

$$\boldsymbol{\kappa} = \frac{\mathbf{x} - \mathbf{x}_s}{\sqrt{|\mathbf{x} - \mathbf{x}_s|^2 + z_s^2}}.$$

The pressure can be expressed in terms of the solution $p^{(0)}$ of the homogeneous problem. The random pressure field can be expressed as a convolution of $p^{(0)}$ with a Gaussian kernel:

$$p'(t, \mathbf{x}, z = 0) = \left[p^{(0)}(\cdot, \mathbf{r} = (\mathbf{x}, 0)) * \mathcal{N}_x \right] \left(t - \frac{\sqrt{\gamma_x}}{\sqrt{2c}} B_{z_s} \right), \quad (1.59)$$

where:

$$\begin{aligned} \mathcal{N}_x &= \frac{c}{\sqrt{\gamma_x |z_s| \pi}} e^{-\frac{c^2 t^2}{\gamma_x |z_s|}}, \\ \gamma_x &= \gamma_0 \frac{|\mathbf{x} - \mathbf{x}_s|^2 + z_s^2}{z_s^2}. \end{aligned} \quad (1.60)$$

Localization of a point source

The principle of inverse problems is to calculate or estimate the causes of a phenomenon from a set of observations of the effects. Here we give an example of an inverse problem: the localization of a point source in the context presented before. After that we discuss some remarks given in the literature about source identification in the context of random media.

In [74] we can see a brief review of source localization in random media resolving an inverse problem. The author says that it is important to determine how medium uncertainties transfer to uncertainties for source localization, in oceans or the Earth for example. As it is impossible to know exactly the medium properties, corrtnan efficient method of localization without knowledge of these properties has to be developed. Considering the same configuration as in the previous paragraph, the source term is assumed to be centered below the surface of the random medium at $z_s < 0$, and to emit a short pulse. The arrival times at each observation point O_j are:

$$\tau_j = t_s + \frac{1}{\underline{c}}|O_j S| + \frac{\sqrt{\gamma_{\mathbf{x}_j}}}{\sqrt{2}\underline{c}}B_{z_s}.$$

The aim is then to invert these equations to determine the source location. The situation seems complicated because of the presence of the random time shifts. However, these unknown shifts can be removed. From the expression (1.60) of $\gamma_{\mathbf{x}}$, on has [74]:

$$\tau_j = t_s + \frac{1}{\underline{c}}|O_j S|(1 + Z_s), \quad Z_s = \frac{\sqrt{\gamma_0}}{\sqrt{2}|z_s|}B_{z_s}. \quad (1.61)$$

The analysis shows that Z_s does not depend on the observation point. To find the source location signals are recorded over the time with N sensors positioned at observation points. Then we need to invert the arrival times to determine the source location $S = (\mathbf{x}_s, z_s)$, the source emission time t_s , and the random delay Z_s . We can see in [74] that it is then possible to compute the source location without error with five observation points, $N = 5$. Garnier [74] has therefore just proposed a procedure to locate the source that removes the random components introduced by the multiple scattering in the medium and thus allows an exact localization.

In this context Garnier [74] also describes the imaging of passive diffusers embedded in a random half-space and illuminated by a source located on the surface or simply by a random noise generated by a set of unknown sources. He shows that the cross-correlation function (CCF) of noisy signals recorded at two observation points on the surface can be used to retrieve information on ballistic motion. This information can be processed for imaging. Moreover, it is proved in [74] that the method is stable with respect to the statistical distribution of the medium and the statistical distribution of the noisy sources. It allows passive imaging of unknown media using only background noise. This can be put into perspective by proposing to use this kind of techniques to construct "pseudo-seismograms" in geophysics, where controlled active sources are difficult to obtain. Finally, it is hypothesized in [74] that the results can be extended to other propagation regimes where the time inversion technique is statistically stable. Qualitatively, the mechanisms responsible for the good properties of the CCF are similar to the ones that ensure efficient pulse refocusing during time-reversal experiments. Time-reversal refocusing properties are well understood mathematically not only for three-dimensional waves in randomly layered

media [70] but also, for instance, for paraxial waves [10, 22, 108] or classical waves with weak fluctuations and in the high frequency limit [11].

1.3.4 Radiative transfer theory

The incoherent wave intensity can also be calculated approximatively from a transport equation that has the form of a linear radiative transport equation [1, 67, 85, 86, 115]. The theory of radiative transport was developed to describe how light energy propagates through a turbulent atmosphere. It is based upon a linear transport equation for the angularly resolved energy density and was first derived phenomenologically during the second half of 20th century, [52, 123]. Ryzhik *et al.* [115] derive this approach to any type of waves, and particularly to acoustic wave that what we are interested in. The authors have the intuition that they need three conditions for obtaining good results with radiative transport equations:

1. The typical wavelengths λ_0 are short compared to macroscopic features of the medium: high frequency case,
2. the correlation lengths of the inhomogeneities l_c are comparable to wavelengths λ_0 ,
3. the fluctuations of the inhomogeneities are weak.

The authors insist on the second condition which allows a strong interaction between waves and inhomogeneities. This is reminiscent of what has been observed by other studies [103, 104], including the importance of this second condition. Here we consider (1.27) with the perturbation model (1.52), Ryzhik *et al.* [115] reformulates the problem as a symmetric hyperbolic system:

$$A(\mathbf{x}) \frac{\partial}{\partial t} \begin{pmatrix} \mathbf{v}' \\ p' \end{pmatrix} + \sum_{i=1}^3 D^i \frac{\partial}{\partial x^i} \begin{pmatrix} \mathbf{v}' \\ p' \end{pmatrix} = 0, \quad (1.62)$$

where

$$A(\mathbf{x}) = \begin{pmatrix} \underline{c}\mathbf{I} & 0 \\ 0 & \frac{1}{K} \end{pmatrix} \left[\begin{pmatrix} \mathbf{I} & 0 \\ 0 & 1 \end{pmatrix} + \begin{pmatrix} \eta(\mathbf{x})\mathbf{I} & 0 \\ 0 & \nu(\mathbf{x}) \end{pmatrix} \right], \quad (1.63)$$

D^i has all zero entries except for $D_{i4}^i = D_{4i}^i = 1$ and, \mathbf{v}' and p' are the velocity and the pressure disturbances respectively. Therefore the power spectral density $\Sigma_{svlw}(\mathbf{k})$ of A is:

$$\begin{aligned} \Sigma_{svlw}(\mathbf{k}) &= \delta_{sv}\delta_{lw}\delta_{s\leq 3}\delta_{l\leq 3}\Sigma_{\eta\eta}(\mathbf{k}) + \delta_{sv}\delta_{lw}\delta_{s\leq 3}\delta_{l4}\Sigma_{\eta\nu}(\mathbf{k}) \\ &+ \delta_{sv}\delta_{lw}\delta_{s4}\delta_{l4}\Sigma_{\nu\nu}(\mathbf{k}) + \delta_{sv}\delta_{lw}\delta_{s4}\delta_{l\leq 3}\Sigma_{\eta\nu}(\mathbf{k}). \end{aligned} \quad (1.64)$$

The indices s, v, l, w go from 1 to 4 and we use notation δ_{lw} which is equal to 1 if $l = w$ and equal to 0 otherwise, and $\delta_{l\leq 3}$ which is equal to 1 if $l \leq 3$ and to 0 otherwise. Here $\Sigma_{\eta\eta}$, $\Sigma_{\eta\nu}$, and $\Sigma_{\nu\nu}$ denote the Fourier transforms of the correlation functions of η with himself, η with ν , and ν with himself, respectively. Now the authors write the radiative transport equation verified by the angularly resolved, wave vector dependent, scalar energy density $a(t, \mathbf{x}, \mathbf{k})$ defined for all wave vector \mathbf{k} at each point \mathbf{x} and time t :

$$\begin{aligned} \frac{\partial a}{\partial t} + \underline{c}\hat{\mathbf{k}} \cdot \nabla_{\mathbf{x}} a &= \frac{\pi \underline{c}^2 |\mathbf{k}|^2}{2} \int \delta(\underline{c}|\mathbf{k}| - \underline{c}|\mathbf{k}'|) (a(\mathbf{k}') - a(\mathbf{k})) \\ &\times \left[(\hat{\mathbf{k}} \cdot \hat{\mathbf{k}}')^2 \Sigma_{\eta\eta}(\mathbf{k} - \mathbf{k}') + 2(\hat{\mathbf{k}} \cdot \hat{\mathbf{k}}') \Sigma_{\eta\nu}(\mathbf{k} - \mathbf{k}') + \Sigma_{\nu\nu}(\mathbf{k} - \mathbf{k}') \right] d\mathbf{k}' \end{aligned} \quad (1.65)$$

with:

$$\hat{\mathbf{k}} = \frac{\mathbf{k}}{|\mathbf{k}|} = \begin{pmatrix} \sin \theta \cos \phi \\ \sin \theta \sin \phi \\ \cos \theta \end{pmatrix}$$

in spherical coordinates, and $\underline{c} = \sqrt{K/\underline{\rho}}$ is the speed of sound. We can link a with p' and \mathbf{v}' by the expression:

$$\int a(t, \mathbf{x}, \mathbf{k}) d\mathbf{k} = \frac{1}{2} \underline{\rho}(\mathbf{x}) |\mathbf{v}'(t, \mathbf{x})|^2 + \frac{1}{2} \frac{1}{K(\mathbf{x})} p'^2(t, \mathbf{x}). \quad (1.66)$$

Time-reversal experiments in random media have also been intensively studied [68, 71, 72]. As a result the analysis and understanding of the correlation properties of incoherent wave fields have made tremendous progress in the recent years and is now the basis of many modern correlation-based imaging techniques [23, 31, 77]. We will return to these aspects at the end of this chapter. It should be noted that the work done by Fouque *et al.* [72] has focused on grouping all these types of methods, be it the propagation aspects of a wave in a random medium or the aspects of time-reversal.

There are other methods used to model the scattering of an acoustic wave by a shear layer. The general method of geometric acoustics has been developed in detail by Candel in [44, 45, 48] and has been applied in many flow configurations, notably in wind tunnel jets [41, 42]. Campos [39, 40] proposes a model, called the heuristic approach, to study the transmission of sound through turbulent shear layers which it establishes by considering three frequency regimes, $\lambda_0 \gg l_c$, $\lambda_0 \ll l_c$, and $\lambda_0 \sim l_c$, where l_c is the typical size of the inhomogeneities of the shear layer.

1.4 Numerical simulation methods of acoustic waves in random flows

In this section we will introduce different approaches to make numerical simulations of the experiments described in Sect. 1.3.1. These simulations involve the resolution of a problem of fluid dynamics (computational fluid dynamics: CFD) as well as a problem of aeroacoustics (computational aeroacoustic: CAA), which makes the implementation complicated.

Several teams have tried to find the results observed by Candel, Guédél and Julienne numerically. It was interesting, as a first approach, to study the interaction between an acoustic wave and an isolated vortex. This study was carried out by Candel [44], then by Colonius *et al.* [59] on a static vortex and more recently by Clair and Gabard [54] in the configuration of a moving vortex. A numerical scattering study that is closer to the turbulent shear layer has been performed by Ewert *et al.* [63, 64, 66] and more recently by Clair and Gabard [55]. But the study that is the closest to the observations done by Candel *et al.* [41] was made by Bennaceur during his thesis [16, 17].

Bailly *et al.* [9] computed the noise generated and radiated by turbulent flows from the linearized Euler equations with a source term induced by the turbulent velocity fluctuations and a mean flow generated by a RANS (Reynolds Averaged Navier-Stokes) simulation. The turbulent velocity fluctuations were obtained by a random Fourier series [111, 117] accounting for the convection velocity of the turbulent eddies [90]. Ewert *et al.* [64, 66] numerically simulated the propagation of an acoustic wave in a flow with a mean velocity

gradient and turbulent velocity fluctuations, using the CAA PIANO code [61]. However, the presence of a mean field gradient in the linearized Euler equations causes the appearance of hydrodynamic instabilities. This led the authors to rather solve the Pierce equation [110] which describes the propagation of sound in an unsteady and inhomogeneous flow. The turbulent velocity fluctuations are modeled by the Random Particle Mesh (RPM) method, introduced by Ewert [63, 65], which is a stochastic method that generates an unsteady turbulent field. This method consists in generating a family of either one (in two dimensions) or three (in three dimensions) fluctuating turbulent quantities ψ by filtering a white noise, connected to the turbulent velocity field by $\mathbf{V} = \nabla \times \psi$, whose tensor of spatio-temporal cross-correlations depends of the correlation length l_c , the correlation time t_c , and the variance σ_ψ^2 , of the fluctuations of ψ . It is then necessary to choose the values of σ_ψ^2 , l_c , and t_c . These quantities can be linked to the intensity of the fluctuating kinetic energy and the rate of dissipation of the kinetic energy fluctuating that can be obtained via a numerical simulation of RANS type. Furthermore they used a sponge layer as boundary conditions for the PIANO simulations [66, 73]. The authors applied this method to the experimental configuration of Candel *et al.* [41, 42]. They first performed a numerical simulation of RANS type in order to obtain the values of σ_ψ^2 , l_c , and t_c to feed the RPM model. Then they calculated, with their CAA code, the propagation of acoustic waves in the modeled turbulent shear layer and compared the power spectral densities of the scattered pressure field with those obtained by Candel *et al.* [41, 42]. Their spectra actually show the two lobes around the emission frequency but some essential characteristics of the spectra do not correspond to the experimental observations. As the convergent output velocity increases, the amount of energy scattered remains substantially the same. In addition, the position of the lobes also remains the same, whereas it is supposed to grow linearly with the convection velocity (see Sect. 1.3.1). The authors also observe a difference in level between the main peak and the secondary lobes more important than the experimental observations. They attribute this difference to the fact that their simulation does not calculate the azimuthal components of the source terms of diffusion.

More recently, Clair and Gabard [55] have performed a numerical simulation of acoustic diffusion by a turbulent layer with the same methodology as [63, 65] (RPM to generate turbulent fluctuations and CAA code PIANO to compute acoustic propagation). The stationary average flow is chosen uniform, which avoids having hydrodynamic instabilities because the average field gradients are zero. Clair and Gabard [55] study in particular the influence of the source frequency, turbulence convection velocity, and angle of observation on the shape of the spectrum of the scattered pressure. As in [66] they used a sponge layer boundary condition [54, 55]. In [55] we can see that 100 points are used to dissipate the acoustic fluctuations before they reach the boundary. The incoming sound field (monopole or plane wave) is injected in the domain through a 20 points wide sponge layer adjacent to the bottom boundary. A specific boundary condition is applied to all other boundaries: Tam's radiation boundary condition [119] is applied when the considered incident radiation is a monopole, and Thompson's 1-D characteristic condition [122] when it is a plane wave. The power spectral densities of pressure fluctuations calculated directly above the source are shown in Fig. 1.4. The spectrum goes from a form similar to that found in their previous study of acoustic diffusion by a single vortex [54], to a form closer to experimental studies, when the frequency of the source increases. It would appear that the turbulence zone is seen as a single large scale by the low frequency acoustic wave, as is the case for diffusion by a single vortex. As the frequency of the source increases, the finer turbulence plays an

increasingly important role in the acoustic diffusion mechanism.

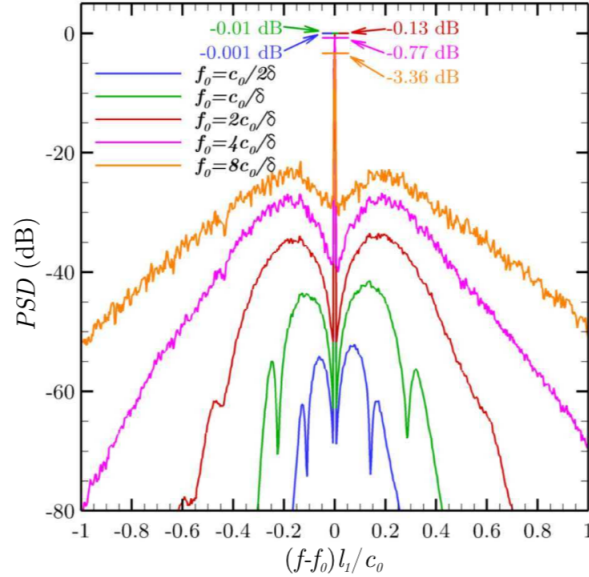


Figure 1.4 – Power spectral densities of pressure fluctuations for different frequencies f_0 of the acoustic source. Figure taken from [55]

Bennaceur *et al.* [16] study the problem of the scattering of an acoustic wave by a 3D spatially-developing plane turbulent mixing layer by means of a large eddy simulation (LES). The authors generate the turbulent layer and then introduce an acoustic source in the computational domain. The LES of the turbulent mixing layer and the acoustic field are performed, allowing the direct computation of the scattered pressure field. They use CAA methods to minimize the spurious pressure fluctuations created as the turbulent structures leave the computational domain. The calculated turbulent layer is taken with an initial Reynolds number $Re \approx 1200$ and a convective Mach number $M \approx 0.12$. LES is performed using the FUNk code; see [3,92] for previous studies using this code. A modified hybrid scheme of the second order AUSM+(P) (advance flow division method), originally proposed by Mary and Sagaut [101], is used for the discretization of Eulerian flows. It is a second order centered scheme that detects parasitic oscillations on primitive variables and activates a sensor function that modifies the Eulerian flow expression, including numerical dissipation only if oscillations are detected. Finally we can notice that the authors have added a model of random perturbations at the entry of the computational domain in order to generate a fully developed turbulent state earlier in the simulations, in the well refined zone. This mechanism aims at limiting the simulation time as well as the horizontal length of the computational domain.

A constant pressure is set for the outflow boundary condition while the constant velocities U_1 and U_2 (see Fig. 1.2) are set for the upper and lower boundaries in the cross-stream direction respectively. As the flow is statistically homogeneous span-wise, periodic boundary conditions are applied in the span-wise direction. Thus, a characteristic non-reflecting boundary condition has been implemented on both the stream-wise and transverse boundaries to minimize the spurious waves created while acoustic fluctuations leave the compu-

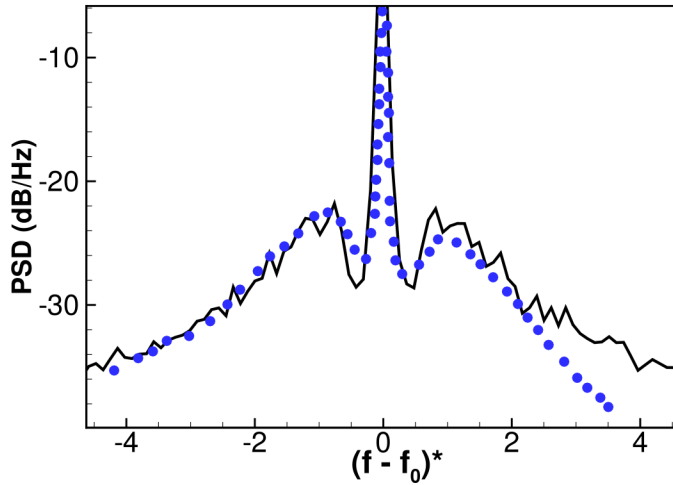


Figure 1.5 – Normalized power spectra of pressure fluctuations as functions of the normalized centered frequency $(f - f_0)^*$: (–) numerical simulation of [16] and (•) experimental observation of [41]. Figure taken from [16].

tational domain. However, Bennaceur *et al.* [16] notice that such a non-reflecting boundary condition is not sufficient when aerodynamic fluctuations reach the outflow boundary and generate small spurious waves that are not negligible compared to the acoustic fluctuations. Following Colonius *et al.* [58], two methods are combined. Firstly, the mesh is stretched in the axial direction so that the turbulent structures are no longer supported by the numerical scheme. Secondly, a damping term is added in the resolution so that the spurious reflections created by the stretching propagate upstream as less as possible.

The generated results are compared with the experimental results obtained by Candel *et al.* [41], with a wide range of parameters studied as well as the effects on the main characteristics of the scattered field. We can see an example in Fig. 1.5, where one notes the very good agreement obtained by the authors compared to the experimental observations.

Regarding the works on inverse problems, which we will discuss in detail in the next section, Borcea *et al.* [23–29, 31, 32] compute the acoustic pressure by solving the wave equation in the time domain, with a finite element method that discretizes the mixed velocity-pressure (first order system) formulation. This is done with a new family of quadrangular (2D) mixed finite elements introduced by Bécache *et al.* [14, 15]. The domain is assumed infinite so they used a perfectly matched absorbing layer (PML) to surround it, as introduced by Bérenger [19].

1.5 Source localization in random media

To finish this chapter we will talk about the aspects of the problem of localizing a source or a reflector buried in a random medium by coherent interferometry. As mentioned at the end of Sect. 1.3.4 the correlation properties of the incoherent wave field have been widely studied in order to realize correlation-based imaging. In seismic imaging the goal is to estimate the location of one or more underground sources with a passive network of receivers on the surface, or the location of reflective structures with an active network of

transducers on the surface. This is also the case in medical imaging as well as in underwater acoustics (except that receivers in underwater acoustics are also very generally immersed in the medium), and generally in all types of imaging performed in real conditions. Imaging sources or reflectors, when performed in a smooth medium, is effective with Kirchhoff migration (KM), just as when the background propagation velocity is known or can be estimated. The KM imaging technique is defined as the signal back-propagation by travel time migration, a simplified version of time-reversal imaging where we back-propagate according to a wave equation in a fictitious environment. When we speak of time-reversal we must distinguish:

- the real back-propagation in the environment which benefits from the effects of scattering of the random medium, as in [68] for the purpose of breaking up kidney stones, which is strictly speaking the time-reversal,
- and time-reversal imaging such as KM, where the signals are numerically back-propagated in a fictitious environment to image sources and reflectors, of which traces are rapidly lost in the presence of diffusion in the random medium.

Indeed, when the medium is said to be cluttered, which is generally the case in real-life imaging, travel time or KM does not work well. These methods in which sources transmit pulse are dependent on clear arrival times. When the medium is cluttered the recorded temporal traces contain long and noisy codas resulting from multiple scattering by inhomogeneities. The images obtained are then very noisy. Worse they are dependent on the medium, and for two different realizations of the same random medium with the same statistical properties we get two different images. Indeed, although it is a widely used method, KM does not use cross-correlations of the signal but the raw signals. It is known to be robust with respect to additive noise, such as measurement noise [5, 6]. This is illustrated for example in [32], where it is also shown how KM fails to image in a random (cluttered) medium. Cluttered "noise" in data and in images has a complex structure, in which correlations play an important role. By background noise in the images, we mean their random fluctuations due to fluctuations in the properties of the medium. For these reasons it is necessary to use methods that are robust with respect to fluctuations induced by the heterogeneity of the medium to make imaging when it is random. Alternative methods have been introduced in several areas, notably seismic imaging in order to define the properties of an unknown environment using coherent interferometry.

1.5.1 Coherent interferometric (CINT) imaging in random media

We will introduce here several studies [23–33, 69] which compare the Coherent INTerferometric (CINT) imaging method (1.68) with the widely used KM imaging method (1.67). The resolution and statistical fluctuations of the images are analyzed when the ambient environment is random and wave propagation can be modeled mainly by the distortion of the wavefront. KM loses statistical stability at an exponential rate with the propagation distance and leads to unreliable images that change unpredictably with the detailed features of the clutter. In KM, images are formed by overlaying the propagated array data to the domain of the image. In CINT, the local cross-correlations of the data are back-propagated into the medium. This is a denoising process that improves the signal-to-noise ratio of the images but also reduces the resolution. The tradeoff between increased stability and reduced resolution in CINT imaging was then quantified [31].

Borcea *et al.* [23, 24] as well as Chan *et al.* [53] show that imaging by interferometry, where the crosscorrelations of the signals are backpropagated and not the signals themselves, statistically stabilizes the results. Borcea *et al.* [23, 24] show this result by comparing the KM and CINT imaging methods. First we assume that we are in the case of passive imaging. In this case we are in the presence of a source (or several sources) that emits a short pulse somewhere in the medium. With a network of N receivers we record the signals emitted by the source and modulated by the medium, and then try to find its position. So we use the N temporal signals $\{p(\mathbf{r}_r, t), 1 \leq r \leq N\}$ recorded by the receivers located at $\mathbf{r}_r, 1 \leq r \leq N$, to estimate the source location by $\mathbf{r}_{\text{so}} = \arg \max_{\mathbf{r}^S \in S} \mathcal{I}(\mathbf{r}^S)$ in some search region S , where \mathcal{I} is either the KM imaging functional \mathcal{I}_{KM} or the CINT imaging functional $\mathcal{I}_{\text{CINT}}$ given below. The fictitious medium (*e.g.* homogeneous) in which the signals are back-propagated is assumed to be characterized by a Green's function $\widehat{G}_0(\mathbf{r}, \mathbf{r}', \omega) \equiv e^{i\frac{\omega}{c_0}|\mathbf{r}-\mathbf{r}'|}$, that is, a high frequency approximation of the Green's function of an homogeneous three-dimensional acoustic medium of speed of sound c_0 . Both imaging techniques use the same data to find the position of the source, but they treat them differently. Indeed in the case of KM all the signals are back-propagated for all frequencies and all receivers. In CINT imaging the crosscorrelations of the signals are taken locally in space and time and then they are back-propagated. These local properties are expressed by the two parameters X_d and Ω_d . They are the spatial and the frequency cut off parameters beyond which the data are considered to be uncorrelated. The KM imaging functional is:

$$\mathcal{I}_{\text{KM}}(\mathbf{r}^S) = \sum_{r=1}^N p\left(\mathbf{r}_r, \frac{|\mathbf{r}_r - \mathbf{r}^S|}{c_0}\right), \quad (1.67)$$

where c_0 stands for the speed of sound in the fictitious medium, and the CINT imaging functional is:

$$\mathcal{I}_{\text{CINT}}(\mathbf{r}^S; \Omega_d, X_d) = \sum_{\substack{q,r=1 \\ |\mathbf{r}_q - \mathbf{r}_r| \leq X_d}}^N \iint_{|\omega - \omega'| \leq \Omega_d} \widehat{\mathcal{C}}(\mathbf{r}_q, \mathbf{r}_r, \omega, \omega') e^{-i\frac{\omega}{c_0}|\mathbf{r}_q - \mathbf{r}^S| + i\frac{\omega'}{c_0}|\mathbf{r}_r - \mathbf{r}^S|} d\omega d\omega', \quad (1.68)$$

where:

$$\widehat{\mathcal{C}}(\mathbf{r}_q, \mathbf{r}_r, \omega, \omega') = \widehat{p}(\mathbf{r}_q, \omega) \overline{\widehat{p}(\mathbf{r}_r, \omega')}. \quad (1.69)$$

Here $\widehat{p}(\mathbf{r}_r, \omega)$ is the Fourier transform of $p(\mathbf{r}_r, t)$ in time domain, \mathbf{r}_r and \mathbf{r}_q are the positions of the receivers, and ω and ω' are the frequencies associated with the signals received by these receivers.

In the context of active imaging, one has a network of sensors that this time will serve as sources and receivers, thus we will say that we have N_s sources and N_r receivers. Indeed here the principle is that the signals are emitted with our network of sensors. The wave propagates to a reflector (or several reflectors) which we try to find, and is reflected by it. Part of the signal will go back to the sensor array which, at that moment, will record the signal. Then we try to find the position of the reflector, just as in the context of passive imaging. However the difference with the passive case is that we have N_s controlled sources at the positions $\mathbf{r}_s, 1 \leq s \leq N_s$. So in turn we have a matrix of $N_r \times N_s$ temporal signals $\{p(\mathbf{r}_r, t; \mathbf{r}_s), 1 \leq r \leq N_r, 1 \leq s \leq N_s\}$ recorded by the N_r receivers. In this case, the wave travels back and forth in the medium and will normally be modulated more strongly by

the latter. The fictitious medium is still assumed to be characterized by a Green's function $\widehat{G}_0(\mathbf{r}, \mathbf{r}', \omega) \equiv e^{i\frac{\omega}{c_0}|\mathbf{r}-\mathbf{r}'|}$. The KM imaging functional is:

$$\mathcal{I}_{\text{KM}}(\mathbf{r}^R) = \sum_{r,s=1}^N p\left(\mathbf{r}_r, \frac{|\mathbf{r}_s - \mathbf{r}^R| + |\mathbf{r}^R - \mathbf{r}_r|}{c_0}; \mathbf{r}_s\right), \quad (1.70)$$

and the CINT imaging functional is:

$$\begin{aligned} \mathcal{I}_{\text{CINT}}(\mathbf{r}^R; \Omega_d, X_d) = & \sum_{\substack{r, r'=1 \\ |\mathbf{r}_r - \mathbf{r}_{r'}| \leq X_d}}^{N_r} \sum_{\substack{s, s'=1 \\ |\mathbf{r}_s - \mathbf{r}_{s'}| \leq X_d}}^{N_s} \iint_{|\omega - \omega'| \leq \Omega_d} \widehat{p}(\mathbf{r}_r, \omega; \mathbf{r}_s) \overline{\widehat{p}(\mathbf{r}_{r'}, \omega'; \mathbf{r}_{s'})} \\ & \times e^{-i\frac{\omega}{c_0}(|\mathbf{r}_r - \mathbf{r}^R| + |\mathbf{r}^R - \mathbf{r}_s|) + i\frac{\omega'}{c_0}(|\mathbf{r}_{r'} - \mathbf{r}^R| + |\mathbf{r}^R - \mathbf{r}_{s'}|)} d\omega d\omega', \quad (1.71) \end{aligned}$$

where $\widehat{p}(\mathbf{r}_r, \omega; \mathbf{r}_s)$ is the Fourier transform in time domain of the signal $p(\mathbf{r}_r, t; \mathbf{r}_s)$ received by the sensor \mathbf{r}_r for a signal emitted by the sensor \mathbf{r}_s ; \mathbf{r}_s and $\mathbf{r}_{s'}$ denote the positions of the sensors when they are used as sources; \mathbf{r}_r and $\mathbf{r}_{r'}$ denote the positions of the sensors when they are used as receivers; and ω and ω' are the frequencies associated with the signals received by these sensors. The reflector location is estimated by $\mathbf{r}_{\text{ref}} = \arg \max_{\mathbf{r}^R \in S} \mathcal{I}(\mathbf{r}^R)$ in some search region S , where \mathcal{I} is either \mathcal{I}_{KM} or $\mathcal{I}_{\text{CINT}}$.

We can see the fundamental difference between the two imaging techniques. Again, the parameters Ω_d and X_d used by the CINT imaging functional are the frequency and spatial cut off parameters beyond which the data are considered to be uncorrelated. They appear naturally by construction of the method, however there is no rule or indication to choose them optimally. Borcea *et al* [23, 24] point out that taking all receivers over the whole frequency band is like doing a KM image. They also explain that optimal parameters Ω_d^* and X_d^* exist but give no indication of the values of these parameters nor the methods used to find them. In [25] a study is carried out in order to set up an adaptive imaging functional that can estimate these optimal parameters. A new optimization function is set up in order to automatically find the parameters Ω_d^* and X_d^* :

$$\mathcal{O}(\Omega_d, X_d) = \|\mathcal{J}(\mathbf{y}^S; \Omega_d, X_d)\|_{L^1(S)} + \alpha \|\nabla_{\mathbf{y}^S} \mathcal{J}(\mathbf{y}^S; \Omega_d, X_d)\|_{L^1(S)}, \quad (1.72)$$

where:

$$\mathcal{J}(\mathbf{y}^S; \Omega_d, X_d) = \frac{\sqrt{|\mathcal{I}_{\text{CINT}}(\mathbf{y}^S; \Omega_d, X_d)|}}{\sup_{\mathbf{y}^S \in S} \sqrt{|\mathcal{I}_{\text{CINT}}(\mathbf{y}^S; \Omega_d, X_d)|}}, \quad (1.73)$$

is the bounded variation norm [78] of the normalized square root of the image $\mathcal{I}_{\text{CINT}}$, and S is the search domain. Now we are able to find an approximation of the optimal parameters Ω_d^* and X_d^* minimizing (1.72) in Ω_d and X_d .

This search is always dependent on a user-defined $\alpha > 0$ parameter. Ω_d and X_d are always dependent on the user's choice, but the search is much more efficient than before. Indeed, for two realizations of the same medium the imaging functional may need a large Ω_d in one case and not in the other, for example. Adaptive search makes it easy to get optimal values because, from the only choice of the α parameter, it will move faster to the correct order of magnitude for Ω_d and X_d .

1.5.2 Numerical CINT experiments

The setup for the numerical experiments used by Borcea *et al.* [24] is shown in Fig. 1.6, where the dimensions of the problem are given in terms of the central wavelength λ_0 . An array of 185 transducers is used, a transducer being a device used as source and receiver. They are at a distance $h = \frac{\lambda_0}{2}$ from each other. The object to be imaged is at range $L = 90\lambda_0$ and at zero cross-range, measured with respect to the center of the array. In the passive array simulations the object is a configuration of three point sources emitting the same pulse $f(t)$ simultaneously and the distance between these points is $d = 6\lambda_0$. In the active array simulations the three sources are replaced by three disks of radius λ_0 whose centers are located at the same points. The disks are non-penetrable scatterers modeled with homogeneous Dirichlet boundary conditions (acoustic soft scatterers). A probing pulse is emitted by the central array element. The pulse $f(t)$ is the time derivative of a Gaussian with central frequency $f_0 = 1\text{kHz}$ and bandwidth $0.6 - 1.3\text{ kHz}$ (measured at 6 dB). With a propagation velocity of 3 km/s the central wavelength is $\lambda_0 = 3\text{ m}$.

To simulate imaging in a cluttered medium, the objects to be imaged (sources or scatterers) are embedded in an heterogeneous background medium. The fluctuations in the speed of sound are modeled using a random Fourier series and a Gaussian correlation function. The correlation length is $l_c = 1.5\text{ m}$ and the standard deviation σ is equal to 3%. A typical realization of the random medium is shown in Fig. 1.6, where the units in the horizontal and vertical axes are again given in terms of the central wavelength λ_0 , and the scale of the colour bar is in 10 m/s. To generate the data the acoustic wave equation, formulated as a first order velocity-pressure system in time, is solved using a mixed finite element method [14, 15]. The propagation medium is considered to be infinite in all directions and in the numerical computations a perfectly matched absorbing layer (PML) [19] surrounds the computational domain.

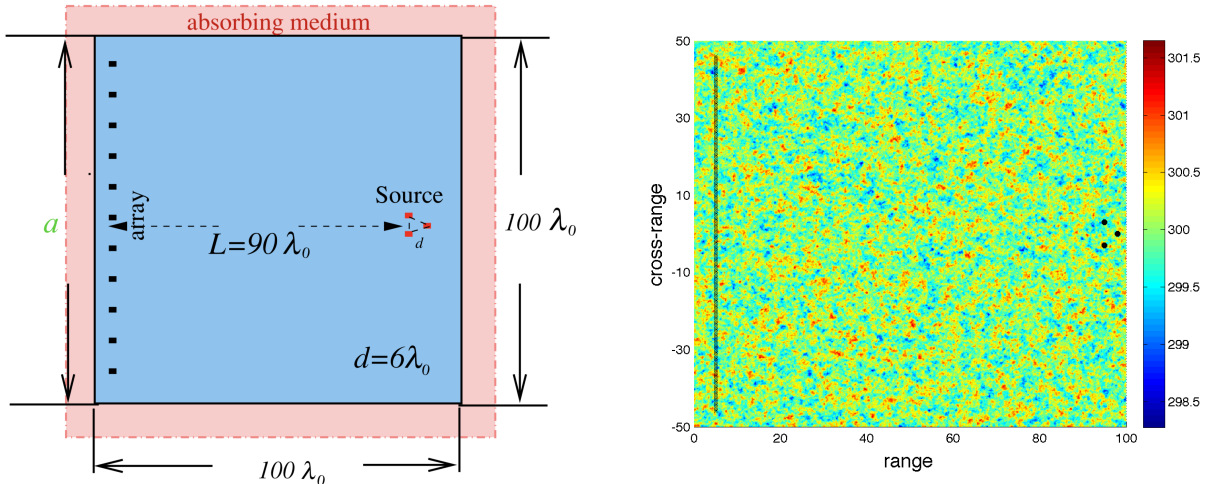


Figure 1.6 – Sketch of the computational setup used by Borcea *et al.* [24] (left) and typical realization of the random speed of sound $c_0(\mathbf{r})$ (right). The dimensions of the problem are given in terms of the central wavelength λ_0 . The locations of the sources or reflectors to be imaged are shown by dots \bullet and the locations of the transducers are shown by crosses \times .

In their work [24, 31] the authors put forward the statistical stability of CINT imaging

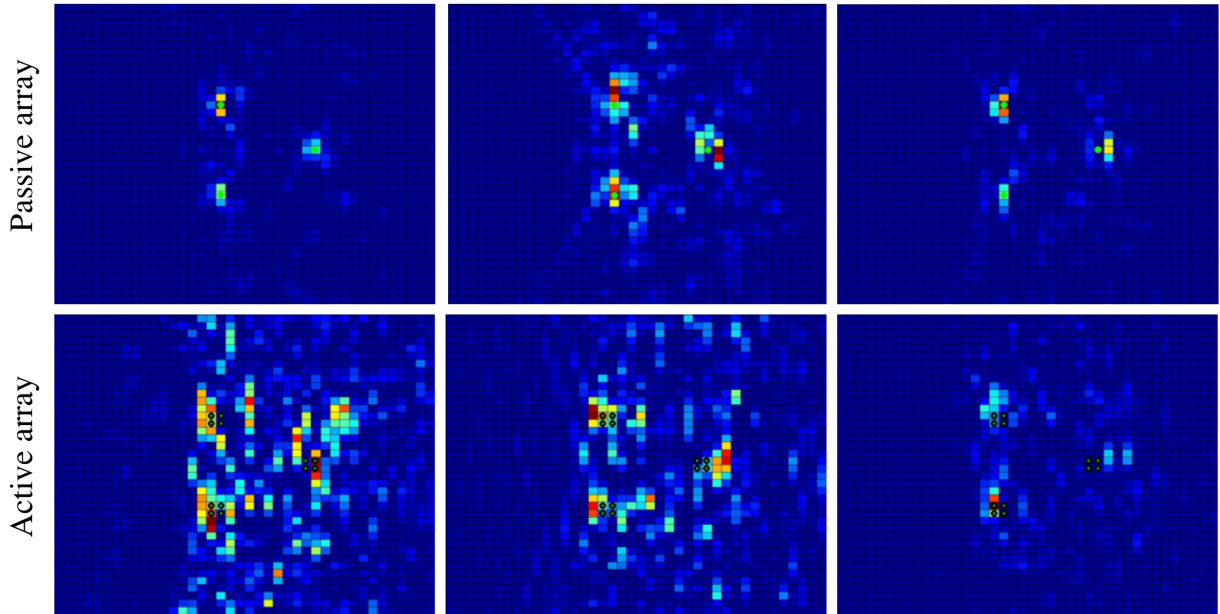


Figure 1.7 – *KM* images for three realizations of a random medium with standard deviation $\sigma = 3\%$. Figure is taken from [24].

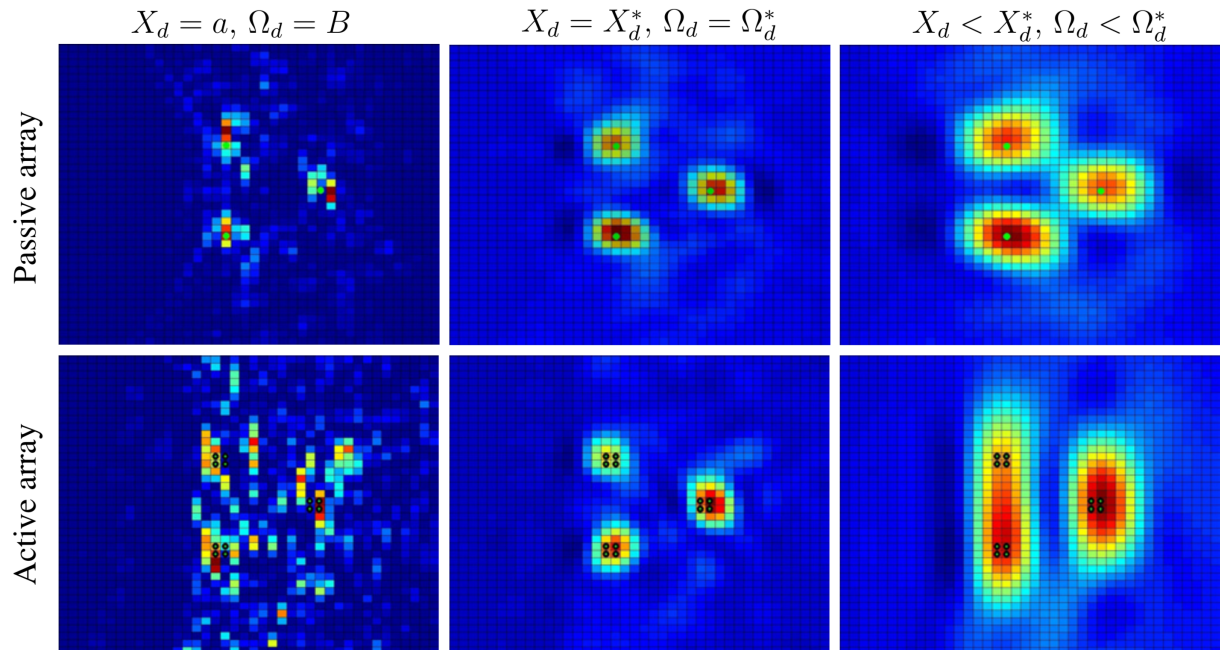


Figure 1.8 – *CINT* images for three realizations of a random medium with standard deviation $\sigma = 3\%$. Figure is taken from [24].

against KM imaging. They analyzed the KM and CINT point spread functions for passive and active arrays of sensors [31], and quantified explicitly their resolution limits and their signal-to-noise ratio (SNR). The SNR is defined as the mean point spread function at its peak divided by its standard deviation.

To carry out analytically the resolution and SNR comparative study of the KM and CINT methods, the authors used the relatively simple random travel time model for the effects of the random medium on the array data. The model is valid in the regime of geometrical optics in random media. In this regime wave diffraction, amplitude fluctuations and power delay spread due to multiple scattering are negligible, while wave front distortions are significant and well-captured by the model. A parabolic approximation model was also used [26, 29] to study CINT and KM in random media. However, an explicit analytical SNR calculation was not done, because the forward scattering model is too complicated to allow evaluation of higher order statistical moments of the array data. The results in [26, 29] agree qualitatively with those obtained in [31]. The authors are particularly interested in cases of large wave front distortions, where the random medium has a significant effect on the imaging process. It turns out that:

1. The KM and CINT imaging functions provide an unbiased estimate of the source or reflector locations. That is to say, the statistical averages of their point spread functions are maximum at the true positions of the sources or reflectors that we wish to image.
2. The SNR of the KM and CINT imaging functions near the actual positions of the sources or reflectors are radically different. The KM SNR is exponentially small with range, regardless of the bandwidth or the array aperture. This means that the KM is not statistically stable and can not be used for imaging in regimes with large wavefront distortions. The random fluctuations of the images are important and it is not possible to observe the peak of the images near the actual positions of the sources or reflectors. The CINT imaging method is significantly superior to the KM imaging method because its SNR is not weak and is improved by increasing the aperture and the bandwidth.

However, the statistical stability of the CINT comes at the detriment of some blurring of the images. The compromise between the resolution and the stability of the CINT imaging function can be explicitly quantified [31].

The results obtained so far are very encouraging and this is the reason that motivates us to extend this kind of imaging techniques to heterogeneous flows.

1.5.3 Correlation-based imaging of moving objects

More recently, correlation-based imaging used to observe fast moving objects has been studied [33, 69]. In these papers, the authors introduce a Doppler compensation parameter γ_D which is used in the imaging functional to provide the necessary correction of the movement of the object to be observed. In Chapter 3 we will consider the same compensation mechanism to extend the CINT imaging algorithm outlined above to moving heterogeneous media such as jet flows.

Borcea *et al.* [33] introduce a passive synthetic aperture radar system motivated by space surveillance radar networks for imaging small debris (the targets) in low-Earth orbit. The system proposed is a powerful transmitter on the ground with one or several flying receiver

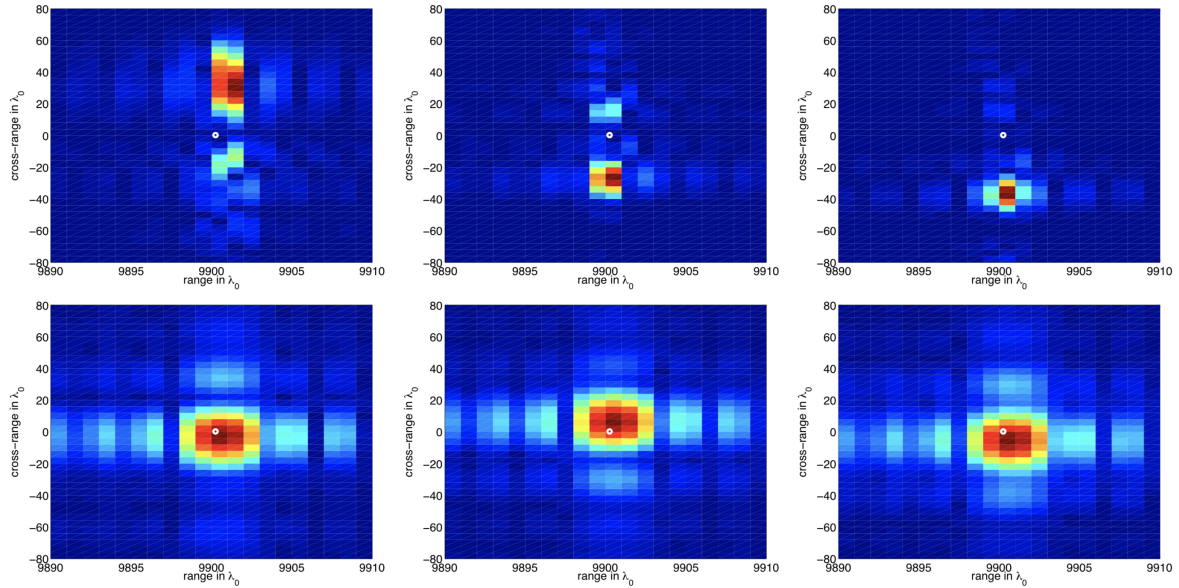


Figure 1.9 – Top row: KM images for three realizations of a random medium. Note how the peak dances around the true location of the reflector, indicated with the white dot. Bottom row: square root of the CINT images for the same three realizations of a random medium. Note that the peak is close to the true reflector location for all realizations, as predicted by the theory. The axes are range and cross-range in terms of λ_0 . Figure is taken from [31].

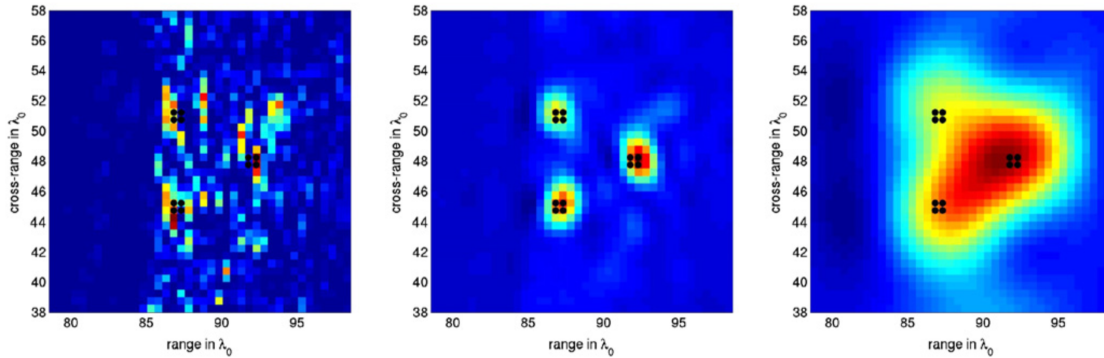


Figure 1.10 – CINT imaging function for three choices of smoothing parameters X_d and Ω_d . The left picture is with no smoothing, the middle picture is with optimal smoothing, and the right picture is with too much smoothing. The three small reflectors are indicated with black dots. Figure is taken from [25].

platforms. Each platform can separate the direct signals from the source and the reflected signals coming from below and above, respectively. Fournier *et al.* [69] also consider the problem of imaging a fast moving object. The imaging system is almost the same as in [33], except the receivers that are assumed to be located on the ground for simplicity. Indeed, it would be more interesting for the correlation-based imaging method to have high-flying airborne receivers as in [33]. However, since the velocity of the receivers is low, and much

lower than that of a satellite in low-Earth orbit, Fournier *et al.* [69] expect their theory to generalize to this case. Airborne receivers are of interest because they can fly above the turbulent atmosphere, in which case the expectation is that the correlation-based imaging method will be robust relative to atmospheric turbulence effects. Robustness of correlation-based imaging to propagation medium fluctuations was shown in [77] for stationary receiver arrays. Fournier *et al.* [69] also expect correlation-based imaging to be robust to additive measurement noise since they cross-correlate signals recorded at different receivers. Their aim is to compare the well-known matched-filter imaging method with correlation-based imaging. Imaging with correlations has the advantage of not requiring any knowledge about the probing pulse and the emitter position, both assumed known with high accuracy in the case of matched-filter imaging. But correlation-based imaging requires recording fully resolved signals without down-ramping while matched-filter imaging does not. Down-ramping consists in multiplying the signal by the inverse of the carrier frequency, to obtain a lower frequency signal easier to sample. To account for the fast moving target's velocity, Doppler compensation (taken into account through the compensation factor γ_D invoked above) is necessary for both imaging methods.

In [33] for the case of a single receiver platform, the image is formed by cross correlating the direct and reflected signals by adequately selecting the evaluation times in their imaging function and compensating for Doppler effects. In this case, the functional needs to know the arrival times from the transmitter to the antenna and from the transmitter to the search point in the image, so accurate knowledge of the transmitter location is needed. Furthermore, the one-receiver imaging modality is not capable of determining both the target location and velocity. Unique recovery can be achieved, however, by using two pairs of receivers.

For the case of multiple receiver platforms, the image is computed by cross correlating the Doppler-compensated reflected signals recorded at two of the receivers. In this case, the image formation relies on differences of travel times between the moving target and the receivers. Borcea *et al.* [33] show that we also need to know the transmitter location, but with relatively low accuracy, a result that is not without surprise. They also show that two well separated pairs of receiver platforms are sufficient for determining the target location and velocity. As the distance between the receivers increases, they find that sensitivity to knowing the transmitter location increases. Borcea *et al.* [33] anticipate that the correlation-based imaging methods that they propose are very robust with respect to additive measurement noise, because they cross-correlate signals recorded at different time windows in the one-receiver case and they cross-correlate signals recorded by different receivers in the two-receiver case. They also anticipate that the proposed methods are robust with respect to medium noise induced by the turbulent atmosphere.

In [69] it is shown that for both imaging methods, matched-filter and correlation-based, nearly optimal resolution results of the order of the wavelength are obtained. The analysis shows that even for a fast moving object such as a low-orbit satellite, the Doppler correction does not affect the resolution but needs to be taken into consideration in the imaging functions. One of the most important results is that a sparse configuration of a little number of uniformly distributed receivers over an area big enough is sufficient so as to have a point spread function with a similar shape (same maximum located at the same point and same decreasing width, which means same resolution) to the one obtained with a dense set of receivers. It is therefore possible, with a Doppler correction, to obtain an image of a fast moving object. This opens very interesting perspectives for the objective of imaging

through a random flow, which we wish to do.

1.6 Conclusion

In this chapter we have introduced the issues underlying the work that was carried out during this thesis. Indeed, there are real industrial issues requiring source localization through a random flow as well as the modeling of the associated direct problem. After a brief introduction of the equations interesting us, we have presented the work carried out on the modeling of the propagation of acoustic waves crossing a randomized/turbulent flow, and more precisely with as a point of reference the experiments carried out by Candel, Julienne and Guédel in the 70s [41–43]. We have presented several analytical models used to describe these phenomena: the Lighthill and Lilley equations solved with the Born approximation, a method using an ODA kernel, a model solving a radiative transfer equation, and a model considering a stratified medium and using a spectral approach. It is this last type of approach that interests us with the objective of achieving source localization afterwards.

Several numerical simulation methods can be used to simulate this kind of phenomena. We have shown some of the results obtained so far, more or less in agreement with the observations done in their experiments by Candel *et al.* [41–43]. The treatment of the boundary conditions is very important and we have seen that several ideas have been implemented.

Finally we have introduced some aspects of source localization in a random environment. In particular we have explained methods using coherent interferometry imaging, which is of particular interest to us. The statistical stability of this technique, unlike Kirchhoff migration, makes it a strong ally for sources or reflectors localization in a random medium. However, like any method using smoothing, it is strongly dependent on the choice of few parameters. This problem has been partially solved by the adaptive choice which, even though it still depends on a user-defined parameter, effectively finds the right smoothing parameters to use. Finally we have presented the first results obtained in the context of moving object detection using CINT imaging, which suggests us that this technique can be adapted to the case of random flows.

Chapter 2

Acoustic wave propagation in a random stratified flow

In this chapter we study the mathematical problem of the scattering of acoustic waves by a random stratified flow. Starting from Sect. 1.1.1 we consider the Euler Equations for an ideal fluid flow and linearize them around an unsteady, inhomogeneous ambient flow. Then we focus on the study of acoustic waves propagating through a random ambient flow, which is the one that interests us in order to try to explain the experiments depicted in Chapter 1. We first study in Sect. 2.2 the pressure waves transmitted by a homogeneous ambient flow to determine the Green's function of the unperturbed problem. Then in Sect. 2.3 we consider an inhomogeneous ambient flow with a randomly stratified bulk modulus and extend the results of [72] for a quiescent medium to the case of a moving medium with a uniform velocity. In Sect. 2.4 we subsequently consider an inhomogeneous ambient flow with weak perturbations of its velocity. We use a Lippmann-Schwinger approach to obtain an analytical expression of the transmitted pressure wave with those perturbations, which are modeled by a mean-square stationary process. From this expression we use a stationary-phase method to derive the power spectral density of the transmitted pressure wave. In order to get an analytical formula of the latter we assume, at the end of the calculations, that the source is time-harmonic and the turbulent layer is thin. At the end of this chapter we make different hypotheses in order to observe the influence of some source and turbulence parameters on the power spectrum and compare qualitatively our results with the literature.

2.1 Linearized Euler equations about an unsteady inhomogeneous flow

We first outline how the Euler equations (1.2) are linearized adopting here a slightly different perspective from Sect. 1.1.1 since the ambient flow is now time dependent. The full non-linear Euler equations for an ideal fluid flow in the absence of friction, heat conduction,

or heat production are (see (1.2) in Chapter 1):

$$\begin{aligned}\frac{d\varrho}{dt} + \varrho \nabla \cdot \mathbf{v} &= 0, \\ \frac{d\mathbf{v}}{dt} + \frac{1}{\varrho} \nabla p &= \mathbf{0}, \\ \frac{ds}{dt} &= 0,\end{aligned}\tag{2.1}$$

where ϱ is the fluid density, \mathbf{v} is the particle velocity, s is the specific entropy, and p is the thermodynamic pressure given by the equation of state $p = p^\#(\varrho, s)$. It arises from the thermodynamic equilibrium of the fluid so it depends on its density and temperature, or entropy. Also:

$$\frac{d}{dt} = \frac{\partial}{\partial t} + \mathbf{v} \cdot \nabla\tag{2.2}$$

is the usual convective derivative following the particle paths. This shows that the flow is isentropic (*i.e.* each fluid particle has constant entropy but different particles may have different entropy). Note that the flow is said to be homentropic if the entropy is constant and in addition the same for all particles. Besides, if the flow is incompressible then by definition $\frac{d\varrho}{dt} = 0$, which implies $\nabla \cdot \mathbf{v} = 0$ from the conservation of mass. In this situation the pressure field p can no longer be related to the density, because the latter is constant on the flow paths independently of the external loads. It becomes an independent new variable, which is not a problem since we have an additional relationship provided by the incompressibility condition. We will not impose this condition in the following analysis, though.

Linearized Euler equations arise from the previous conservation equations when their variables are expressed as sums of ambient quantities pertaining to the background flow (subscript 0), and lower-order acoustic perturbations (primed quantities):

$$\begin{aligned}\varrho(\mathbf{r}, t) &= \varrho_0(\mathbf{r}, t) + \varrho'(\mathbf{r}, t), \\ \mathbf{v}(\mathbf{r}, t) &= \mathbf{v}_0(\mathbf{r}, t) + \mathbf{v}'(\mathbf{r}, t), \\ s(\mathbf{r}, t) &= s_0(\mathbf{r}, t) + s'(\mathbf{r}, t), \\ p(\mathbf{r}, t) &= p_0(\mathbf{r}, t) + p'(\mathbf{r}, t),\end{aligned}\tag{2.3}$$

where $\mathbf{r} = (\mathbf{x}, z)$ is the position within the flow, and \mathbf{x} is the horizontal coordinates and z is the vertical coordinate. In such a manner, the ambient quantities satisfy the Euler equations (2.1):

$$\begin{aligned}\frac{d\varrho_0}{dt} + \varrho_0 \nabla \cdot \mathbf{v}_0 &= 0, \\ \frac{d\mathbf{v}_0}{dt} + \frac{1}{\varrho_0} \nabla p_0 &= \mathbf{0}, \\ \frac{ds_0}{dt} &= 0,\end{aligned}\tag{2.4}$$

together with the following relations from the equation of state applicable to the ambient flow $p_0 = p^\#(\varrho_0, s_0)$:

$$\begin{aligned}\nabla p_0 &= c_0^2 \nabla \varrho_0 + \left(\frac{\partial p^\#}{\partial s} \right)_{\varrho_0} \nabla s_0, \\ \frac{dp_0}{dt} &= c_0^2 \frac{d\varrho_0}{dt},\end{aligned}\tag{2.5}$$

where $c_0 > 0$ is the speed of sound in the ambient flow given by:

$$c_0^2 = \left(\frac{\partial p^\#}{\partial \varrho} \right)_{s_0}.$$

Here and from now on one has redefined the convective derivative as:

$$\frac{d}{dt} = \frac{\partial}{\partial t} + \mathbf{v}_0 \cdot \nabla, \quad (2.6)$$

that is, the convective derivative within the ambient flow. The primed quantities satisfy the linearized Euler equations:

$$\begin{aligned} \frac{d\varrho'}{dt} + \varrho' \nabla \cdot \mathbf{v}_0 + \nabla \cdot (\varrho_0 \mathbf{v}') &= 0, \\ \frac{d\mathbf{v}'}{dt} + \mathbf{v}' \cdot \nabla \mathbf{v}_0 + \frac{1}{\varrho_0} \nabla p' - \frac{\varrho'}{\varrho_0^2} \nabla p_0 &= \mathbf{0}, \\ \frac{ds'}{dt} + \mathbf{v}' \cdot \nabla s_0 &= 0. \end{aligned} \quad (2.7)$$

In addition, one has from the linearized equation of state:

$$p' = c_0^2 \varrho' + \left(\frac{\partial p^\#}{\partial s} \right)_{\varrho_0} s'. \quad (2.8)$$

Combining Eq. (2.4), Eq. (2.5), and Eq. (2.8) we arrive at:

$$\begin{aligned} \frac{d}{dt} \left(\frac{p'}{\varrho_0 c_0^2} \right) + \frac{1}{\varrho_0 c_0^2} \mathbf{v}' \cdot \nabla p_0 + \nabla \cdot \mathbf{v}' - s' \frac{d}{dt} \left[\frac{1}{\varrho_0 c_0^2} \left(\frac{\partial p^\#}{\partial s} \right)_{\varrho_0} \right] &= 0, \\ \frac{d\mathbf{v}'}{dt} + \mathbf{v}' \cdot \nabla \mathbf{v}_0 + \frac{1}{\varrho_0} \nabla p' - \frac{p'}{(\varrho_0 c_0)^2} \nabla p_0 - \frac{s'}{(\varrho_0 c_0)^2} \left(\frac{\partial p^\#}{\partial s} \right)_{\varrho_0} \nabla p_0 &= \mathbf{0}, \\ \frac{ds'}{dt} + \mathbf{v}' \cdot \nabla s_0 &= 0. \end{aligned} \quad (2.9)$$

Discarding the last terms in s' in these first two equations because they are of second order by the arguments devised in [110], finally yields the system [67] (the last term in the second equation below is apparently missing in [67, Eq. (2)]):

$$\begin{aligned} \frac{d}{dt} \left(\frac{p'}{K_0} \right) + \nabla \cdot \mathbf{v}' + \frac{1}{K_0} \mathbf{v}' \cdot \nabla p_0 &= 0, \\ \frac{d\mathbf{v}'}{dt} + \frac{1}{\varrho_0} \nabla p' + \mathbf{v}' \cdot \nabla \mathbf{v}_0 - \frac{p'}{\varrho_0 K_0} \nabla p_0 &= \mathbf{0}, \end{aligned} \quad (2.10)$$

where $K_0 = \varrho_0 c_0^2$ is the fluid compressibility. In terms of the unknowns $q := \frac{p'}{K_0}$ (dimensionless pressure) and $\mathbf{u} := \varrho_0 \mathbf{v}'$ (momentum) it reads:

$$\begin{aligned} \frac{dq}{dt} + \frac{1}{\varrho_0} \nabla \cdot \mathbf{u} + \frac{1}{\varrho_0 K_0} \left(\frac{\partial p^\#}{\partial s} \right)_{\varrho_0} \mathbf{u} \cdot \nabla s_0 &= 0, \\ \frac{d\mathbf{u}}{dt} + K_0 \nabla q + (\text{Tr}(\mathbf{D}\mathbf{v}_0) \mathbf{I}_3 + \mathbf{D}\mathbf{v}_0) \mathbf{u} + (\nabla K_0 - \nabla p_0) q &= \mathbf{0}. \end{aligned} \quad (2.11)$$

Here \mathbf{I}_d is the $d \times d$ identity matrix, $d \in \mathbb{N}$, $\mathbf{D}\mathbf{v}_0$ stands for the velocity strain matrix within the ambient flow, such that $(\mathbf{D}\mathbf{v}_0)_{jk} = \frac{\partial v_{0j}}{\partial r_k}$. Consequently $(\mathbf{D}\mathbf{v}_0)\mathbf{u} = \mathbf{u} \cdot \nabla \mathbf{v}_0$ as usually noted in fluid mechanics textbooks, and $\text{Tr}(\mathbf{D}\mathbf{v}_0) = \nabla \cdot \mathbf{v}_0$. In the experiments [41–43, 91, 118] depicted in Chapter 1 where no combustion occurs and temperature variations are small, the (cold) jet flow can be considered as a thermally and calorically perfect gas, whereby its heat capacities at constant volume and constant pressure c_v and c_p , respectively, are constant. Therefore by the equation of state of a perfect gas $c_0^2 = \gamma \frac{p_0}{\varrho_0}$ where $\gamma = \frac{c_p}{c_v}$ is Laplace's coefficient, and the above system reduces to:

$$\begin{aligned} \frac{dq}{dt} + \frac{1}{\varrho_0} \nabla \cdot \mathbf{u} &= 0, \\ \frac{d\mathbf{u}}{dt} + K_0 \nabla q + (\text{Tr}(\mathbf{D}\mathbf{v}_0)\mathbf{I}_3 + \mathbf{D}\mathbf{v}_0)\mathbf{u} + q(\gamma - 1)\nabla p_0 &= \mathbf{0}. \end{aligned} \quad (2.12)$$

Combining the latter with Eq. (2.4) we obtain:

$$\begin{aligned} \frac{dq}{dt} + \frac{1}{\varrho_0} \nabla \cdot \mathbf{u} &= 0, \\ \frac{d\mathbf{u}}{dt} + K_0 \nabla q + (\text{Tr}(\mathbf{D}\mathbf{v}_0)\mathbf{I}_3 + \mathbf{D}\mathbf{v}_0)\mathbf{u} - q(\gamma - 1)\varrho_0 \frac{d\mathbf{v}_0}{dt} &= \mathbf{0}. \end{aligned} \quad (2.13)$$

2.2 Acoustic waves in an homogeneous flow

Referring to the results of 1.1.4, we specialize the foregoing analysis to the situation where the ambient flow has a uniform velocity \mathbf{v}_0 , and study the acoustic waves transmitted by a layer $-L \leq z \leq 0$ of that flow. Then $\mathbf{D}\mathbf{v}_0 = \mathbf{0}$ and ϱ_0 is also a constant. The constant ambient flow velocity \mathbf{v}_0 is also parallel to the horizontal plane with coordinates \mathbf{x} , such that the convective derivative (2.6) is:

$$\frac{d}{dt} = \frac{\partial}{\partial t} + \mathbf{v}_0 \cdot \nabla_{\mathbf{x}}. \quad (2.14)$$

Here $\nabla_{\mathbf{x}}$ stands for the gradient in the horizontal plane. We more particularly address the construction of the Green's function for this problem because it has relevance to the subsequent developments where the ambient flow characteristics will be randomized. We thus add general source terms $\mathbf{s} = (h, \mathbf{f})$ on the right hand-side of (2.13) with $\mathbf{v}_0 = \text{constant}$ as follows:

$$\begin{aligned} \frac{dq}{dt} + \frac{1}{\varrho_0} \nabla \cdot \mathbf{u} &= \frac{h}{K_0}, \\ \frac{d\mathbf{u}}{dt} + K_0 \nabla q &= \varrho_0 \mathbf{f}. \end{aligned} \quad (2.15)$$

The emitting sources $\mathbf{s} = (h, \mathbf{f})$ will be specified later on; see Fig. 2.1 for the overall setting. For the time being we consider the following specific Fourier transform and its inverse with respect to the time t and the horizontal spatial coordinates \mathbf{x} :

$$\hat{\tau}(\omega, \boldsymbol{\kappa}, z) = \iint e^{i\omega(t - \boldsymbol{\kappa} \cdot \mathbf{x})} \tau(t, \mathbf{x}, z) dt d\mathbf{x}, \quad (2.16)$$

and:

$$\tau(t, \mathbf{x}, z) = \frac{1}{(2\pi)^3} \iint e^{-i\omega(t - \boldsymbol{\kappa} \cdot \mathbf{x})} \hat{\tau}(\omega, \boldsymbol{\kappa}, z) \omega^2 d\omega d\boldsymbol{\kappa}. \quad (2.17)$$

We note from this definition that $\boldsymbol{\kappa}$ is thus homogeneous to an inverse speed, or slowness. Therefore it is referred to as the (horizontal) slowness vector. Also the inverse Fourier transform with respect to that slowness vector solely will be considered in the subsequent analysis:

$$\check{\tau}(\omega, \mathbf{x}, z) = \frac{1}{(2\pi)^2} \iint e^{i\omega\boldsymbol{\kappa}\cdot\mathbf{x}} \widehat{\tau}(\omega, \boldsymbol{\kappa}, z) \omega^2 d\boldsymbol{\kappa}. \quad (2.18)$$

Taking the Fourier transform (2.16) in Eq. (2.15) yields the following system for $\widehat{\mathbf{u}} = (\widehat{\mathbf{u}}_{\mathbf{x}}, \widehat{u}_z)$ and \widehat{q} :

$$\begin{aligned} -i\omega\beta\widehat{q} + \frac{i\omega}{\varrho_0}\boldsymbol{\kappa}\cdot\widehat{\mathbf{u}}_{\mathbf{x}} + \frac{1}{\varrho_0}\frac{\partial\widehat{u}_z}{\partial z} &= \frac{\widehat{h}}{K_0}, \\ -i\omega\beta\widehat{\mathbf{u}}_{\mathbf{x}} + i\omega K_0\widehat{q}\boldsymbol{\kappa} &= \varrho_0\widehat{\mathbf{f}}_{\mathbf{x}}, \\ -i\omega\widehat{u}_z + K_0\frac{\partial\widehat{q}}{\partial z} &= \varrho_0\widehat{f}_z, \end{aligned} \quad (2.19)$$

with the definition:

$$\beta(\boldsymbol{\kappa}) := 1 - \boldsymbol{\kappa}\cdot\mathbf{v}_0 \quad (2.20)$$

and $\widehat{\mathbf{f}} = (\widehat{\mathbf{f}}_{\mathbf{x}}, \widehat{f}_z)$. Eliminating $\widehat{\mathbf{u}}_{\mathbf{x}}$ in the above finally yields:

$$\begin{aligned} \frac{\partial\widehat{u}_z}{\partial z} &= i\omega K_0 \left(\frac{\beta(\boldsymbol{\kappa})}{c_0^2} - \frac{\kappa^2}{\beta(\boldsymbol{\kappa})} \right) \widehat{q} + \frac{1}{c_0^2}\widehat{h} + \frac{\varrho_0}{\beta(\boldsymbol{\kappa})}\boldsymbol{\kappa}\cdot\widehat{\mathbf{f}}_{\mathbf{x}}, \\ \frac{\partial\widehat{q}}{\partial z} &= \frac{i\omega}{K_0}\widehat{u}_z + \frac{1}{c_0^2}\widehat{f}_z, \end{aligned} \quad (2.21)$$

for $\beta(\boldsymbol{\kappa}) \neq 0$ and $\kappa = |\boldsymbol{\kappa}|$.

2.2.1 Modes of wave propagation

In the following developments it is assumed that the waves propagate over distances much larger than the typical wavelength. This allows us to apply the diffusion approximation described in [72]. In this high-frequency regime only the propagating modes will contribute to the quantities of interest, and the evanescent modes will not play any role. Here we look at the conditions under which the wave modes are actually propagating. Ignoring the source terms in Eq. (2.21), $(\widehat{u}_z, \widehat{q})$ satisfy the following homogeneous system:

$$\begin{aligned} \frac{\partial\widehat{u}_z}{\partial z} &= i\omega K_0 \left(\frac{\beta(\boldsymbol{\kappa})}{c_0^2} - \frac{|\boldsymbol{\kappa}|^2}{\beta(\boldsymbol{\kappa})} \right) \widehat{q}, \\ \frac{\partial\widehat{q}}{\partial z} &= \frac{i\omega}{K_0}\widehat{u}_z. \end{aligned} \quad (2.22)$$

It can be reduced to the following second-order homogeneous differential equation for \widehat{u}_z :

$$\frac{\partial^2\widehat{u}_z}{\partial z^2} + \omega^2 D(\boldsymbol{\kappa})\widehat{u}_z = 0, \quad (2.23)$$

where we have defined the diffusion coefficient:

$$D(\boldsymbol{\kappa}) = \frac{\beta(\boldsymbol{\kappa})}{c_0^2} - \frac{|\boldsymbol{\kappa}|^2}{\beta(\boldsymbol{\kappa})}.$$

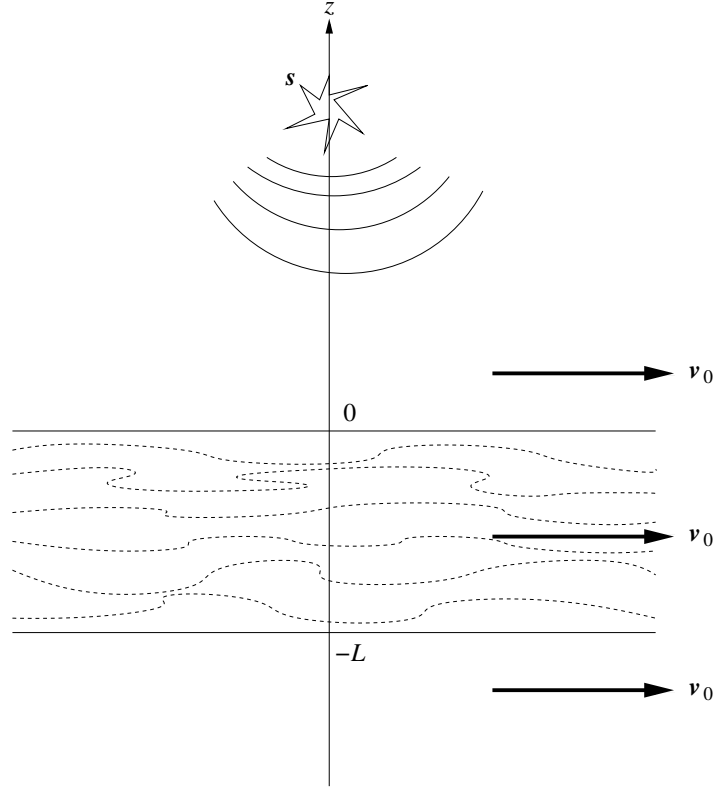


Figure 2.1 – Acoustic waves in a homogeneous flow of thickness L and flow velocity \mathbf{v}_0 .

Note that \hat{q} satisfies the same equation. The sign of $D(\boldsymbol{\kappa})$ determines whether \hat{u}_z is a propagating or an evanescent mode. Thus we want to know in which condition we have $D(\boldsymbol{\kappa}) = 0$, or $\beta(\boldsymbol{\kappa})^2 = c_0^2 |\boldsymbol{\kappa}|^2$, to deduce a condition on the sign of $D(\boldsymbol{\kappa})$. We assume here that the Mach number $M := |\mathbf{v}_0|/c_0$ for the ambient flow is $M < 1$. Then it can be deduced that $D(\boldsymbol{\kappa}) \geq 0$ provided that $c_0^2 |\boldsymbol{\kappa}|^2 \leq \beta(\boldsymbol{\kappa})^2$. Eq. (2.20) shows that when $\mathbf{v}_0 = \mathbf{0}$, this is simply $c_0 |\boldsymbol{\kappa}| \leq 1$. When $\mathbf{v}_0 \neq \mathbf{0}$ but the Mach number $M < 1$, the $\boldsymbol{\kappa}$ -domain where this condition is fulfilled is more complicated, but it contains the disk:

$$c_0 |\boldsymbol{\kappa}| \leq \frac{1}{1 + M}. \quad (2.24)$$

Both domains are displayed on Fig. 2.2 for various Mach numbers. We shall typically consider subsonic flows with low Mach numbers in the subsequent developments, thus the condition $M < 1$ will always be fulfilled.

2.2.2 Integral representation of the pressure field

The properties of the ordinary differential equations (2.21) for the scalar unknowns (\hat{q}_0, \hat{u}_z) may be first analyzed by considering the homogeneous differential system:

$$\frac{\partial}{\partial z} \begin{pmatrix} \hat{q} \\ \hat{u}_z \end{pmatrix} = i\omega\zeta \begin{bmatrix} 0 & \frac{1}{K_0\zeta} \\ K_0\zeta & 0 \end{bmatrix} \begin{pmatrix} \hat{q} \\ \hat{u}_z \end{pmatrix}, \quad (2.25)$$

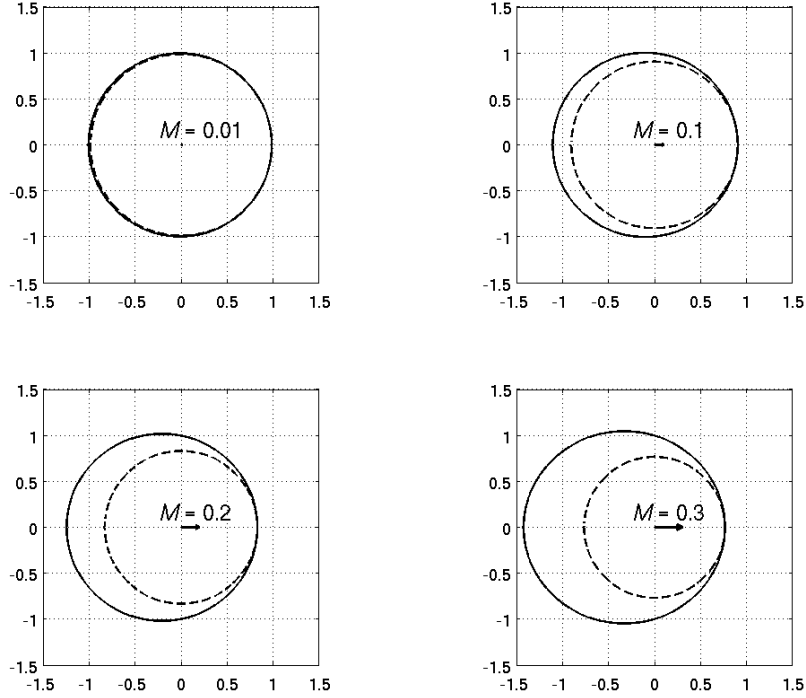


Figure 2.2 – Admissible domain for horizontal wave number $c_0 \boldsymbol{\kappa}$ of the propagating modes (solid line) and the disk $c_0 |\boldsymbol{\kappa}| \leq \frac{1}{1+M}$ (dotted line) for different Mach numbers M .

where

$$\zeta(\boldsymbol{\kappa}) := \sqrt{\frac{\beta(\boldsymbol{\kappa})}{c_0^2} - \frac{|\boldsymbol{\kappa}|^2}{\beta(\boldsymbol{\kappa})}} \quad (2.26)$$

is homogeneous to a slowness. Let $I_0(\boldsymbol{\kappa}) = K_0 \zeta(\boldsymbol{\kappa})$ be the acoustic impedance and:

$$\mathbf{M}_0 = \begin{bmatrix} I_0^{\frac{1}{2}} & I_0^{-\frac{1}{2}} \\ I_0^{\frac{1}{2}} & -I_0^{-\frac{1}{2}} \end{bmatrix}, \quad \begin{bmatrix} 0 & I_0^{-1} \\ I_0 & 0 \end{bmatrix} = \mathbf{M}_0^{-1} \begin{bmatrix} 1 & 0 \\ 0 & -1 \end{bmatrix} \mathbf{M}_0;$$

then the homogeneous system (2.25) is diagonalized as:

$$\frac{\partial}{\partial z} \mathbf{M}_0 \begin{pmatrix} \hat{q} \\ \hat{u}_z \end{pmatrix} = i\omega \zeta \begin{bmatrix} 1 & 0 \\ 0 & -1 \end{bmatrix} \mathbf{M}_0 \begin{pmatrix} \hat{q} \\ \hat{u}_z \end{pmatrix},$$

which introduces the upward and downward wave modes a and b defined such that:

$$\mathbf{M}_0 \begin{pmatrix} \hat{q} \\ \hat{u}_z \end{pmatrix} = \begin{bmatrix} e^{+i\omega\zeta(\boldsymbol{\kappa})z} & 0 \\ 0 & e^{-i\omega\zeta(\boldsymbol{\kappa})z} \end{bmatrix} \begin{pmatrix} a \\ b \end{pmatrix}. \quad (2.27)$$

The latter then satisfy:

$$\frac{\partial}{\partial z} \begin{pmatrix} a \\ b \end{pmatrix} = \mathbf{0}, \quad (2.28)$$

which means that these wave modes are independent of z away from the source position. Provided that $\boldsymbol{\kappa}$ lies in the propagating domain displayed on Fig. 2.2 such that $\zeta(\boldsymbol{\kappa})$ is real, a is the amplitude of the upward propagating mode while b is the amplitude of the downward propagating mode. When $\zeta(\boldsymbol{\kappa})$ is imaginary the wave modes are evanescent (*i.e.* they decay exponentially with the propagation distance). Here we are interested in the far-field expression of the wave so we can restrict our attention to the propagating modes.

We now add the contribution of the source. The latter is assumed to be located at the depth z_s and to generate forcing terms $\mathbf{F}(t, \mathbf{x}) = (\mathbf{F}_x(t, \mathbf{x}), F_z(t, \mathbf{x}))$ and $H(t, \mathbf{x})$ such that (see Fig. 2.3):

$$\mathbf{f}(t, \mathbf{x}, z) = \mathbf{F}(t, \mathbf{x})\delta(z - z_s), \quad h(t, \mathbf{x}, z) = H(t, \mathbf{x})\delta(z - z_s). \quad (2.29)$$

The forcing terms may either emit a short pulse at some time t_s , or a stationary random signal with Gaussian statistics, as envisaged in [74]. Both signals may also be localized spatially in the horizontal direction, such that $\mathbf{F}(t, \mathbf{x}) = \mathbf{F}_t(t)\delta(\mathbf{x} - \mathbf{x}_s)$ and $H(t, \mathbf{x}) = H_t(t)\delta(\mathbf{x} - \mathbf{x}_s)$ for example. Then the vertical momentum \hat{u}_z and pressure \hat{q} from Eq. (2.21) satisfy the jump conditions:

$$\begin{aligned} \hat{u}_z(\omega, \boldsymbol{\kappa}, z_s^+) - \hat{u}_z(\omega, \boldsymbol{\kappa}, z_s^-) &= \frac{1}{c_0^2} \hat{H}(\omega, \boldsymbol{\kappa}) + \frac{\varrho_0}{\beta(\boldsymbol{\kappa})} \boldsymbol{\kappa} \cdot \hat{\mathbf{F}}_x(\omega, \boldsymbol{\kappa}), \\ \hat{q}(\omega, \boldsymbol{\kappa}, z_s^+) - \hat{q}(\omega, \boldsymbol{\kappa}, z_s^-) &= \frac{1}{c_0^2} \hat{F}_z(\omega, \boldsymbol{\kappa}). \end{aligned} \quad (2.30)$$

Consequently, the upward and downward propagating mode amplitudes of Eq. (2.27) satisfy the jump conditions:

$$\begin{aligned} a(\omega, \boldsymbol{\kappa}, z_s^+) - a(\omega, \boldsymbol{\kappa}, z_s^-) &= \varrho_0 e^{-i\omega\zeta(\boldsymbol{\kappa})z_s} S_a(\omega, \boldsymbol{\kappa}), \\ b(\omega, \boldsymbol{\kappa}, z_s^+) - b(\omega, \boldsymbol{\kappa}, z_s^-) &= \varrho_0 e^{+i\omega\zeta(\boldsymbol{\kappa})z_s} S_b(\omega, \boldsymbol{\kappa}), \end{aligned} \quad (2.31)$$

with the source contributions given by:

$$\begin{pmatrix} S_a(\omega, \boldsymbol{\kappa}) \\ S_b(\omega, \boldsymbol{\kappa}) \end{pmatrix} = K_0^{-1} \mathbf{M}_0 \begin{pmatrix} \hat{F}_z(\omega, \boldsymbol{\kappa}) \\ \hat{H}(\omega, \boldsymbol{\kappa}) + \frac{K_0}{\beta(\boldsymbol{\kappa})} \boldsymbol{\kappa} \cdot \hat{\mathbf{F}}_x(\omega, \boldsymbol{\kappa}) \end{pmatrix}. \quad (2.32)$$

One thus deduces that:

$$\begin{pmatrix} a \\ b \end{pmatrix}(\omega, \boldsymbol{\kappa}, z) = \varrho_0 \mathbf{H}(z - z_s) \begin{bmatrix} e^{-i\omega\zeta(\boldsymbol{\kappa})z_s} & 0 \\ 0 & e^{+i\omega\zeta(\boldsymbol{\kappa})z_s} \end{bmatrix} \begin{pmatrix} S_a \\ S_b \end{pmatrix}(\omega, \boldsymbol{\kappa}) + \begin{pmatrix} A \\ B \end{pmatrix}(\omega, \boldsymbol{\kappa}), \quad (2.33)$$

where $z \mapsto \mathbf{H}(z)$ is the Heaviside step function such that $\mathbf{H}(z) = 1$ if $z \geq 0$ and $\mathbf{H}(z) = 0$ otherwise, and A and B are functions of ω and $\boldsymbol{\kappa}$ independent of z determined by the boundary conditions imposed on the wave modes. They specify the wave forms impinging the background flow (2.70) at its boundaries $z = -L$ and $z = 0$ if the source lies within it [74], $-L < z_s < 0$, or $z = -L$ and $z = z_s \geq 0$ if the source lies outside it [72]. In agreement with the experiments we have in mind, we shall consider in the subsequent developments that the second situation rather takes place; see Fig. 2.3. However, for the construction of the Green's function pertaining to the ambient flow, let us first consider that $-L < z_s < 0$. Assuming that no energy is coming upward from $z = -\infty$ or downward from $z = +\infty$, translates into the radiation conditions:

$$a(\omega, \boldsymbol{\kappa}, -L) = b(\omega, \boldsymbol{\kappa}, 0) = 0. \quad (2.34)$$

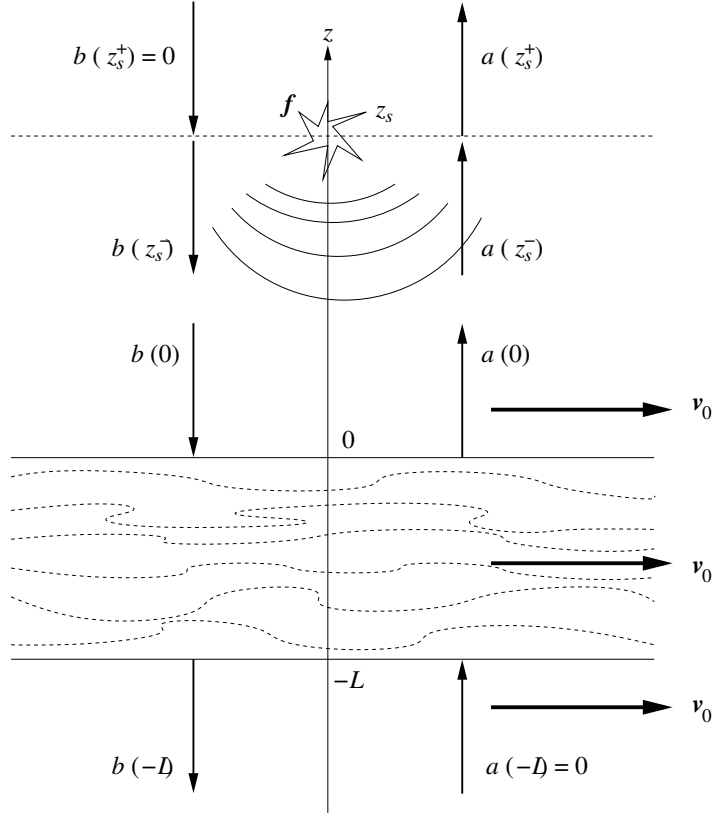


Figure 2.3 – Acoustic waves in an homogeneous flow of thickness L and flow velocity \mathbf{v}_0 . The emitting sources \mathbf{f} are centered at some $z_s \geq 0$. a is the upward wave mode amplitude and b is the downward wave mode amplitude.

Thus:

$$A = 0, \quad B = -\varrho_0 e^{+i\omega\zeta(\boldsymbol{\kappa})z_s} S_b(\omega, \boldsymbol{\kappa}), \quad (2.35)$$

and one has with Eq. (2.27):

$$\begin{aligned} \begin{pmatrix} \hat{q} \\ \hat{u}_z \end{pmatrix}(\omega, \boldsymbol{\kappa}, z) &= \frac{1}{2} e^{+i\omega\zeta(\boldsymbol{\kappa})(z-z_s)} \begin{pmatrix} \frac{\hat{H}(\omega, \boldsymbol{\kappa})}{c_0^2 I_0(\boldsymbol{\kappa})} + \frac{\varrho_0 \boldsymbol{\kappa} \cdot \hat{\mathbf{F}}_{\mathbf{x}}(\omega, \boldsymbol{\kappa})}{\beta(\boldsymbol{\kappa}) I_0(\boldsymbol{\kappa})} + \frac{\hat{F}_z(\omega, \boldsymbol{\kappa})}{c_0^2} \\ \frac{\hat{H}(\omega, \boldsymbol{\kappa})}{c_0^2} + \frac{\varrho_0 \boldsymbol{\kappa} \cdot \hat{\mathbf{F}}_{\mathbf{x}}(\omega, \boldsymbol{\kappa})}{\beta(\boldsymbol{\kappa})} + \frac{I_0(\boldsymbol{\kappa}) \hat{F}_z(\omega, \boldsymbol{\kappa})}{c_0^2} \end{pmatrix} \mathbf{H}(z - z_s) \\ &+ \frac{1}{2} e^{-i\omega\zeta(\boldsymbol{\kappa})(z-z_s)} \begin{pmatrix} \frac{\hat{H}(\omega, \boldsymbol{\kappa})}{c_0^2 I_0(\boldsymbol{\kappa})} + \frac{\varrho_0 \boldsymbol{\kappa} \cdot \hat{\mathbf{F}}_{\mathbf{x}}(\omega, \boldsymbol{\kappa})}{\beta(\boldsymbol{\kappa}) I_0(\boldsymbol{\kappa})} - \frac{\hat{F}_z(\omega, \boldsymbol{\kappa})}{c_0^2} \\ \frac{I_0(\boldsymbol{\kappa}) \hat{F}_z(\omega, \boldsymbol{\kappa})}{c_0^2} - \frac{\hat{H}(\omega, \boldsymbol{\kappa})}{c_0^2} - \frac{\varrho_0 \boldsymbol{\kappa} \cdot \hat{\mathbf{F}}_{\mathbf{x}}(\omega, \boldsymbol{\kappa})}{\beta(\boldsymbol{\kappa})} \end{pmatrix} (1 - \mathbf{H}(z - z_s)). \end{aligned} \quad (2.36)$$

From Eq. (2.19) one has $\hat{\mathbf{u}}_{\mathbf{x}} = \frac{K_0}{\beta} \hat{\mathbf{q}} \boldsymbol{\kappa}$ away from the source. As a result, after defining the four-dimensional fields:

$$\mathbf{p} = \begin{pmatrix} q \\ \mathbf{u}_{\mathbf{x}} \\ u_z \end{pmatrix}, \quad \mathbf{S} = \begin{pmatrix} H \\ \mathbf{F}_{\mathbf{x}} \\ F_z \end{pmatrix}, \quad (2.37)$$

Eq. (2.36) finally yields:

$$\begin{aligned} \widehat{\mathbf{p}}(\omega, \boldsymbol{\kappa}, z) &= \frac{1}{2} \mathbf{H}(z - z_s) e^{+i\omega\zeta(\boldsymbol{\kappa})(z-z_s)} \varrho_0 \widehat{\mathbf{g}}_0^+(\boldsymbol{\kappa}) \otimes \widehat{\mathbf{g}}_0^+(\boldsymbol{\kappa}) \widehat{\mathbf{S}}(\omega, \boldsymbol{\kappa}) \\ &\quad + \frac{1}{2} (1 - \mathbf{H}(z - z_s)) e^{-i\omega\zeta(\boldsymbol{\kappa})(z-z_s)} \varrho_0 \widehat{\mathbf{g}}_0^-(\boldsymbol{\kappa}) \otimes \widehat{\mathbf{g}}_0^-(\boldsymbol{\kappa}) \widehat{\mathbf{S}}(\omega, \boldsymbol{\kappa}), \end{aligned} \quad (2.38)$$

where:

$$\widehat{\mathbf{g}}_0^\pm(\boldsymbol{\kappa}) = \frac{1}{\sqrt{\zeta(\boldsymbol{\kappa})}} \left(\frac{1}{K_0}, \frac{\boldsymbol{\kappa}}{\beta(\boldsymbol{\kappa})}, \pm\zeta(\boldsymbol{\kappa}) \right) \quad (2.39)$$

are the so-called (generalized) eigenvectors of propagation. Here $\mathbf{a} \otimes \mathbf{b}$ stands for the usual tensor product of vectors \mathbf{a} and \mathbf{b} such that $(\mathbf{a} \otimes \mathbf{b})_{ij} = a_i b_j$ in Cartesian coordinates. This result identifies the Green's function for upward waves $\widehat{\mathbf{G}}_0^+(\omega, \boldsymbol{\kappa}, z - z_s)$, $z > z_s$, and the Green's function for downward waves $\widehat{\mathbf{G}}_0^-(\omega, \boldsymbol{\kappa}, z - z_s)$, $z < z_s$, as:

$$\widehat{\mathbf{G}}_0^\pm(\omega, \boldsymbol{\kappa}, z) = \frac{1}{2} e^{\pm i\omega\zeta(\boldsymbol{\kappa})z} \varrho_0 \widehat{\mathbf{g}}_0^\pm(\boldsymbol{\kappa}) \otimes \widehat{\mathbf{g}}_0^\pm(\boldsymbol{\kappa}). \quad (2.40)$$

Since $\mathbf{a} \otimes \mathbf{b} \mathbf{c} = (\mathbf{b} \cdot \mathbf{c})\mathbf{a}$ for any vector \mathbf{c} , $\mathbf{b} \cdot \mathbf{c}$ being the usual inner product of \mathbf{b} and \mathbf{c} , the scalars:

$$\begin{aligned} \widehat{\mathbf{S}}^\pm(\omega, \boldsymbol{\kappa}) &= \widehat{\mathbf{g}}_0^\pm(\boldsymbol{\kappa}) \cdot \widehat{\mathbf{S}}(\omega, \boldsymbol{\kappa}) \\ &= \frac{1}{\sqrt{\zeta(\boldsymbol{\kappa})}} \left(\frac{\widehat{H}(\omega, \boldsymbol{\kappa})}{K_0} + \frac{\boldsymbol{\kappa} \cdot \widehat{\mathbf{F}}_{\mathbf{x}}(\omega, \boldsymbol{\kappa})}{\beta(\boldsymbol{\kappa})} \pm \zeta(\boldsymbol{\kappa}) \widehat{F}_z(\omega, \boldsymbol{\kappa}) \right) \end{aligned} \quad (2.41)$$

then turn out to be the (generalized) coordinates of the forcing terms \mathbf{S} on the eigenvectors of propagation, in the Fourier domain.

We can now summarize the main results of this section in the following lemma.

Lemma 2.2.1 (Solution of Eq. (2.15) and Eq. (2.19)). *The solution $\mathbf{p} = (q, \mathbf{u})$ of Eq. (2.15) reads:*

$$\begin{aligned} \mathbf{p}(t, \mathbf{x}, z) &= \mathbf{G}_0 * \mathbf{s}(t, \mathbf{x}, z) \\ &= \iiint \mathbf{G}_0(t - t', \mathbf{x} - \mathbf{x}', z - z') \mathbf{s}(t', \mathbf{x}', z') dt' d\mathbf{x}' dz', \end{aligned}$$

where $\mathbf{G}_0(t, \mathbf{x}, z) = \mathbf{G}_0^+(t, \mathbf{x}, z) \mathbf{H}(z) + \mathbf{G}_0^-(t, \mathbf{x}, z) (1 - \mathbf{H}(z))$ is the Green's function computed as:

$$\mathbf{G}_0^\pm(t, \mathbf{x}, z) = \frac{\varrho_0}{2(2\pi)^3} \iint e^{+i\omega(\boldsymbol{\kappa} \cdot \mathbf{x} \pm \zeta(\boldsymbol{\kappa})z - t)} \widehat{\mathbf{g}}_0^\pm(\boldsymbol{\kappa}) \otimes \widehat{\mathbf{g}}_0^\pm(\boldsymbol{\kappa}) \omega^2 d\omega d\boldsymbol{\kappa}. \quad (2.42)$$

For point sources located at the depth $z_s \in [-L, 0]$ with forcing terms $\mathbf{S}(t, \mathbf{x})$:

$$\mathbf{s}(t, \mathbf{x}, z) = \mathbf{S}(t, \mathbf{x}) \delta(z - z_s),$$

the solution $\widehat{\mathbf{p}}$ of the system (2.19) in the Fourier domain reads for any $z \in (-L, z_s)$:

$$\begin{aligned} \widehat{\mathbf{p}}(\omega, \boldsymbol{\kappa}, z) &= \frac{1}{2} e^{-i\omega\zeta(\boldsymbol{\kappa})(z-z_s)} \varrho_0 \widehat{\mathbf{g}}_0^-(\boldsymbol{\kappa}) \otimes \widehat{\mathbf{g}}_0^-(\boldsymbol{\kappa}) \widehat{\mathbf{S}}(\omega, \boldsymbol{\kappa}) \\ &= \frac{1}{2} e^{-i\omega\zeta(\boldsymbol{\kappa})(z-z_s)} \varrho_0 \widehat{\mathbf{S}}^-(\omega, \boldsymbol{\kappa}) \widehat{\mathbf{g}}_0^-(\boldsymbol{\kappa}), \end{aligned} \quad (2.43)$$

where $\widehat{\mathbf{S}}^-(\omega, \boldsymbol{\kappa}) = \widehat{\mathbf{g}}_0^-(\boldsymbol{\kappa}) \cdot \widehat{\mathbf{S}}(\omega, \boldsymbol{\kappa})$.

Remark. In (2.42) the integral is over all $\boldsymbol{\kappa}$ in \mathbb{R}^2 . For $\boldsymbol{\kappa}$ such that $\zeta(\boldsymbol{\kappa})$ is imaginary, the sign of the square root of (2.26) which gives rise to an exponentially decaying function in (2.42) is selected. We are, however, interested only in the far-field expression, so it is possible to restrict the integral over the $\boldsymbol{\kappa}$ -domain where $\zeta(\boldsymbol{\kappa})$ is real-valued; see Fig. 2.2.

2.3 Acoustic waves in a stratified flow with random bulk modulus

We now consider the case where the bulk modulus K_0 is randomly varying about its homogenized value \underline{K} and address the diffusion approximation regime [72], whereby the scale of fluctuations ℓ of the former is much smaller than the typical wavelength λ of the waves, which in turn is typically much smaller than the thickness of the flow L . This scaling is quantified by introducing the small parameter $0 < \varepsilon \ll 1$ such that $\frac{\ell}{\lambda} = \varepsilon$ and $\frac{\ell}{L} = \varepsilon^2$. In this respect, the bulk modulus depends on the depth z in the flow $(-L, 0)$ and is constant outside:

$$\frac{1}{K_0(z)} = \begin{cases} \frac{1}{\underline{K}} [1 + \nu(\frac{z}{\varepsilon^2})] & \text{for } z \in [-L, 0], \\ \frac{1}{\underline{K}} & \text{for } z \in (-\infty, -L) \cup (0, +\infty), \end{cases}$$

where $(\nu(z), z \in \mathbb{R})$ is a zero-mean, second order stochastic process. We note from this definition that the fluctuations of the bulk modulus are not assumed to be small. Accordingly, the source term has now the form:

$$\mathbf{f}^\varepsilon(t, \mathbf{x}, z) = \varepsilon^r \mathbf{F}\left(\frac{t}{\varepsilon}, \frac{\mathbf{x}}{\varepsilon}\right) \delta(z - z_s), \quad (2.44)$$

where the multiplicative factor ε^r scales the amplitude, while the exponent r will be specified later on. In the section we assume that the source term h^ε in the mass conservation equation is zero for convenience. Then the momentum $\mathbf{u}^\varepsilon = \varrho_0 \mathbf{v}^{\varepsilon'}$ and dimensionless pressure $q^\varepsilon = \frac{p^{\varepsilon'}}{\underline{K}}$ are the solutions of the system (2.15) modified for this scaling as:

$$\begin{aligned} \left[1 + \nu\left(\frac{z}{\varepsilon^2}\right)\right] (\partial_t + \mathbf{v}_0 \cdot \nabla_{\mathbf{x}}) q^\varepsilon + \frac{1}{\varrho_0} \nabla \cdot \mathbf{u}^\varepsilon &= 0, \\ (\partial_t + \mathbf{v}_0 \cdot \nabla_{\mathbf{x}}) \mathbf{u}^\varepsilon + \underline{K} \nabla q^\varepsilon &= \varrho_0 \mathbf{f}^\varepsilon, \end{aligned} \quad (2.45)$$

provided that $-L < z < 0$. The superscript ε in these quantities stands for the fact that they depend on it because both the bulk modulus and the source do so. The scaled specific Fourier transform of the dimensionless pressure q^ε and its inverse with respect to the time t and the horizontal spatial coordinates \mathbf{x} are:

$$\widehat{q}^\varepsilon(\omega, \boldsymbol{\kappa}, z) = \iint e^{\frac{i\omega}{\varepsilon}(t - \boldsymbol{\kappa} \cdot \mathbf{x})} q^\varepsilon(t, \mathbf{x}, z) dt d\mathbf{x},$$

and:

$$q^\varepsilon(t, \mathbf{x}, z) = \frac{1}{(2\pi\varepsilon)^3} \iint e^{-\frac{i\omega}{\varepsilon}(t - \boldsymbol{\kappa} \cdot \mathbf{x})} \widehat{q}^\varepsilon(\omega, \boldsymbol{\kappa}, z) \omega^2 d\omega d\boldsymbol{\kappa},$$

with similar expressions for the momentum \mathbf{u}^ε and its transform $\widehat{\mathbf{u}}^\varepsilon$.

2.3.1 Integral representation of the pressure field

Taking the scaled Fourier transform in Eq. (2.45) yields:

$$\begin{aligned} -\frac{i\omega}{\varepsilon}\beta\left[1+\nu\left(\frac{z}{\varepsilon^2}\right)\right]\widehat{q}^\varepsilon + \frac{i\omega}{\varepsilon\varrho_0}\boldsymbol{\kappa}\cdot\widehat{\mathbf{u}}_\mathbf{x}^\varepsilon + \frac{1}{\varrho_0}\frac{\partial\widehat{u}_z^\varepsilon}{\partial z} &= 0, \\ -\frac{i\omega}{\varepsilon}\beta\widehat{\mathbf{u}}_\mathbf{x}^\varepsilon + \frac{i\omega}{\varepsilon}\underline{K}\widehat{q}^\varepsilon\boldsymbol{\kappa} &= \varrho_0\widehat{\mathbf{f}}_\mathbf{x}^\varepsilon, \\ -\frac{i\omega}{\varepsilon}\widehat{u}_z^\varepsilon + \underline{K}\frac{\partial\widehat{q}^\varepsilon}{\partial z} &= \varrho_0\widehat{f}_z^\varepsilon, \end{aligned}$$

or, after eliminating $\widehat{\mathbf{u}}_\mathbf{x}^\varepsilon$:

$$\begin{aligned} \frac{\partial\widehat{u}_z^\varepsilon}{\partial z} &= \frac{i\omega}{\varepsilon}\left[\underline{K}\underline{\zeta}^2 + \varrho_0\beta\nu\left(\frac{z}{\varepsilon^2}\right)\right]\widehat{q}^\varepsilon + \frac{\varrho_0}{\beta}\boldsymbol{\kappa}\cdot\widehat{\mathbf{f}}_\mathbf{x}^\varepsilon, \\ \frac{\partial\widehat{q}^\varepsilon}{\partial z} &= \frac{i\omega}{\varepsilon\underline{K}}\widehat{u}_z^\varepsilon + \frac{\varrho_0}{\underline{K}}\widehat{f}_z^\varepsilon, \end{aligned} \quad (2.46)$$

where:

$$\underline{\zeta}(\boldsymbol{\kappa}) := \sqrt{\frac{\beta(\boldsymbol{\kappa})}{\underline{c}^2} - \frac{|\boldsymbol{\kappa}|^2}{\beta(\boldsymbol{\kappa})}}, \quad (2.47)$$

for $\underline{c} = \sqrt{\underline{K}/\varrho_0}$ and $\beta(\boldsymbol{\kappa}) \neq 0$ given by Eq. (2.20). Along the same lines as in Sect. 2.2.1, we are interested in the propagating wave modes and consider that $\underline{\zeta}(\boldsymbol{\kappa})$ is real, which holds if $\underline{c}|\boldsymbol{\kappa}|$ lies in the admissible domain displayed on Fig. 2.2 for various Mach numbers $M = |\mathbf{v}_0|/\underline{c} < 1$. This is assumed to be the case in the following analysis.

The homogeneous differential system associated to 2.46 reads:

$$\frac{\partial}{\partial z} \begin{pmatrix} \widehat{q}^\varepsilon \\ \widehat{u}_z^\varepsilon \end{pmatrix} = \frac{i\omega}{\varepsilon}\underline{\zeta} \begin{bmatrix} 0 & \frac{1}{\underline{K}\underline{\zeta}} \\ \underline{K}\underline{\zeta} & 0 \end{bmatrix} \begin{pmatrix} \widehat{q}^\varepsilon \\ \widehat{u}_z^\varepsilon \end{pmatrix} + \frac{i\omega}{\varepsilon}\nu\left(\frac{z}{\varepsilon^2}\right) \begin{bmatrix} 0 & 0 \\ \varrho_0\beta & 0 \end{bmatrix} \begin{pmatrix} \widehat{q}^\varepsilon \\ \widehat{u}_z^\varepsilon \end{pmatrix}.$$

Let $\underline{I}(\boldsymbol{\kappa}) = \underline{K}\underline{\zeta}(\boldsymbol{\kappa})$ be the homogenized acoustic impedance and:

$$\mathbf{M} = \begin{bmatrix} \underline{I}^{\frac{1}{2}} & \underline{I}^{-\frac{1}{2}} \\ \underline{I}^{\frac{1}{2}} & -\underline{I}^{-\frac{1}{2}} \end{bmatrix}, \quad \begin{bmatrix} 0 & \underline{I}^{-1} \\ \underline{I} & 0 \end{bmatrix} = \mathbf{M}^{-1} \begin{bmatrix} 1 & 0 \\ 0 & -1 \end{bmatrix} \mathbf{M};$$

in addition, let us introduce the upward and downward propagating mode amplitudes a^ε and b^ε defined such that:

$$\mathbf{M} \begin{pmatrix} \widehat{q}^\varepsilon \\ \widehat{u}_z^\varepsilon \end{pmatrix} = \begin{bmatrix} e^{+\frac{i\omega}{\varepsilon}\underline{\zeta}(\boldsymbol{\kappa})z} & 0 \\ 0 & e^{-\frac{i\omega}{\varepsilon}\underline{\zeta}(\boldsymbol{\kappa})z} \end{bmatrix} \begin{pmatrix} a^\varepsilon \\ b^\varepsilon \end{pmatrix}. \quad (2.48)$$

The latter then satisfy:

$$\frac{\partial}{\partial z} \begin{pmatrix} a^\varepsilon \\ b^\varepsilon \end{pmatrix} = \frac{i\omega\beta(\boldsymbol{\kappa})}{2\varepsilon\underline{\zeta}(\boldsymbol{\kappa})\underline{c}^2}\nu\left(\frac{z}{\varepsilon^2}\right) \begin{bmatrix} 1 & e^{-\frac{2i\omega}{\varepsilon}\underline{\zeta}(\boldsymbol{\kappa})z} \\ -e^{+\frac{2i\omega}{\varepsilon}\underline{\zeta}(\boldsymbol{\kappa})z} & -1 \end{bmatrix} \begin{pmatrix} a^\varepsilon \\ b^\varepsilon \end{pmatrix}, \quad (2.49)$$

together with the rescaled counterparts of the jump conditions (2.31):

$$\begin{aligned} a^\varepsilon(\omega, \boldsymbol{\kappa}, z_s^+) - a^\varepsilon(\omega, \boldsymbol{\kappa}, z_s^-) &= \varrho_0\varepsilon^{r+3} e^{-\frac{i\omega}{\varepsilon}\underline{\zeta}(\boldsymbol{\kappa})z_s} \underline{S}_a(\omega, \boldsymbol{\kappa}), \\ b^\varepsilon(\omega, \boldsymbol{\kappa}, z_s^+) - b^\varepsilon(\omega, \boldsymbol{\kappa}, z_s^-) &= \varrho_0\varepsilon^{r+3} e^{+\frac{i\omega}{\varepsilon}\underline{\zeta}(\boldsymbol{\kappa})z_s} \underline{S}_b(\omega, \boldsymbol{\kappa}), \end{aligned} \quad (2.50)$$

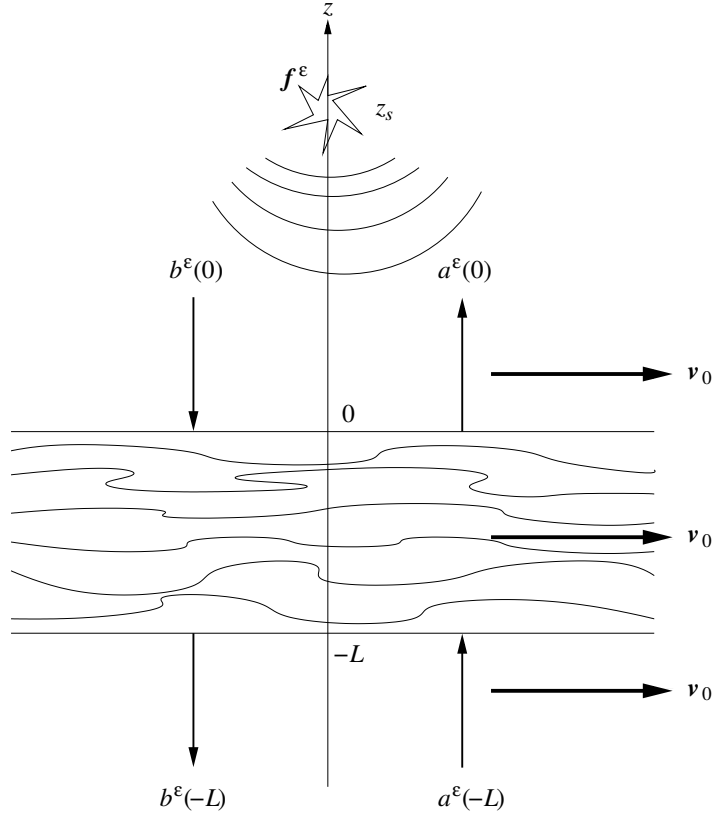


Figure 2.4 – Acoustic waves in a stratified random flow of thickness L and flow velocity \mathbf{v}_0 . The emitting sources \mathbf{f}^ε are centered at some $z_s \geq 0$. a^ε is the upward wave mode amplitude and b^ε is the downward wave mode amplitude.

where the source contributions are given by:

$$\begin{aligned} \underline{S}_a(\omega, \boldsymbol{\kappa}) &= \frac{\sqrt{\underline{I}(\boldsymbol{\kappa})}}{K} \widehat{F}_z(\omega, \boldsymbol{\kappa}) + \frac{\boldsymbol{\kappa} \cdot \widehat{\mathbf{F}}_x(\omega, \boldsymbol{\kappa})}{\beta(\boldsymbol{\kappa})\sqrt{\underline{I}(\boldsymbol{\kappa})}}, \\ \underline{S}_b(\omega, \boldsymbol{\kappa}) &= \frac{\sqrt{\underline{I}(\boldsymbol{\kappa})}}{K} \widehat{F}_z(\omega, \boldsymbol{\kappa}) - \frac{\boldsymbol{\kappa} \cdot \widehat{\mathbf{F}}_x(\omega, \boldsymbol{\kappa})}{\beta(\boldsymbol{\kappa})\sqrt{\underline{I}(\boldsymbol{\kappa})}}. \end{aligned}$$

Assuming like in the homogeneous case of Sect. 2.2 that no energy is coming upward from $z = -\infty$ or downward from $z = +\infty$, and that the source is located at the surface $z_s = 0$, the upward and downward wave components impinging the flow are:

$$\begin{aligned} a^\varepsilon(\omega, \boldsymbol{\kappa}, -L) &= 0, \\ b^\varepsilon(\omega, \boldsymbol{\kappa}, 0) &= -\varepsilon^{r+3} \underline{S}_b(\omega, \boldsymbol{\kappa}), \end{aligned} \tag{2.51}$$

see Fig. 2.4. The system (2.49) may be analyzed as in [72, Chap. 8] by introducing the propagator matrix $\mathbf{P}^\varepsilon(\omega, \boldsymbol{\kappa}, -L, z)$ such that:

$$\frac{d}{dz} \mathbf{P}^\varepsilon(\omega, \boldsymbol{\kappa}, -L, z) = \frac{1}{\varepsilon} \mathbf{H} \left(\omega, \boldsymbol{\kappa}, \frac{z}{\varepsilon}, \nu \left(\frac{z}{\varepsilon^2} \right) \right) \mathbf{P}^\varepsilon(\omega, \boldsymbol{\kappa}, -L, z) \tag{2.52}$$

with the initial condition $\mathbf{P}^\varepsilon(\omega, \boldsymbol{\kappa}, -L, -L) = \mathbf{I}_2$, and:

$$\mathbf{H}(\omega, \boldsymbol{\kappa}, z, \nu) = \frac{i\omega\beta(\boldsymbol{\kappa})\nu}{2\underline{\zeta}(\boldsymbol{\kappa})\underline{c}^2} \begin{bmatrix} 1 & e^{-2i\omega\underline{\zeta}(\boldsymbol{\kappa})z} \\ -e^{+2i\omega\underline{\zeta}(\boldsymbol{\kappa})z} & -1 \end{bmatrix}. \quad (2.53)$$

Ordinary differential equations of the form (2.52) have been extensively studied in [72]. The propagator is a frequency-dependent symplectic matrix which has the form:

$$\mathbf{P}^\varepsilon(\omega, \boldsymbol{\kappa}, -L, 0) = \begin{bmatrix} \tau^\varepsilon(\omega, \boldsymbol{\kappa}, -L, 0) & \overline{\rho^\varepsilon(\omega, \boldsymbol{\kappa}, -L, 0)} \\ \rho^\varepsilon(\omega, \boldsymbol{\kappa}, -L, 0) & \overline{\tau^\varepsilon(\omega, \boldsymbol{\kappa}, -L, 0)} \end{bmatrix},$$

with

$$|\tau^\varepsilon|^2 - |\rho^\varepsilon|^2 = 1 \quad (2.54)$$

owing to $\text{Tr } \mathbf{H}(\omega, \boldsymbol{\kappa}, z, \nu) = 0$. From Eq. (2.49) it is deduced that:

$$\mathbf{P}^\varepsilon(\omega, \boldsymbol{\kappa}, -L, z) \begin{pmatrix} a^\varepsilon(\omega, \boldsymbol{\kappa}, -L) \\ b^\varepsilon(\omega, \boldsymbol{\kappa}, -L) \end{pmatrix} = \begin{pmatrix} a^\varepsilon(\omega, \boldsymbol{\kappa}, z) \\ b^\varepsilon(\omega, \boldsymbol{\kappa}, z) \end{pmatrix}, \quad -L \leq z \leq 0;$$

thus, the boundary conditions (2.51) imply that:

$$\mathbf{P}^\varepsilon(\omega, \boldsymbol{\kappa}, -L, 0) \begin{pmatrix} 0 \\ b^\varepsilon(\omega, \boldsymbol{\kappa}, -L) \end{pmatrix} = \begin{pmatrix} a^\varepsilon(\omega, \boldsymbol{\kappa}, 0) \\ -\varepsilon^{r+3}\underline{S}_b(\omega, \boldsymbol{\kappa}) \end{pmatrix},$$

and consequently:

$$b^\varepsilon(\omega, \boldsymbol{\kappa}, -L) = -\varepsilon^{r+3}T^\varepsilon(\omega, \boldsymbol{\kappa}, -L, 0)\underline{S}_b(\omega, \boldsymbol{\kappa}),$$

where:

$$T^\varepsilon(\omega, \boldsymbol{\kappa}, -L, 0) = \overline{\tau^\varepsilon(\omega, \boldsymbol{\kappa}, -L, 0)}^{-1} \quad (2.55)$$

is the transmission coefficient of the slab $(-L, 0)$. From (2.54) we get that $T^\varepsilon(\omega, \boldsymbol{\kappa}, -L, 0)$ is uniformly bounded by one. Using the same result we also obtain the mode-energy-conservation equation:

$$|a^\varepsilon(\omega, \boldsymbol{\kappa}, 0^-)|^2 - |b^\varepsilon(\omega, \boldsymbol{\kappa}, -L)|^2 = |\varepsilon^{r+3}\underline{S}_b(\omega, \boldsymbol{\kappa})|^2. \quad (2.56)$$

It follows that the dimensionless pressure \widehat{q}^ε at the surface of the flow reads:

$$\widehat{q}^\varepsilon(\omega, \boldsymbol{\kappa}, -L) = -\frac{\varepsilon^{r+3}\varrho_0}{2\sqrt{\underline{I}(\boldsymbol{\kappa})}} e^{+i\omega\underline{\zeta}(\boldsymbol{\kappa})\frac{L}{\varepsilon}} T^\varepsilon(\omega, \boldsymbol{\kappa}, -L, 0)\underline{S}_b(\omega, \boldsymbol{\kappa}),$$

and therefore the acoustic pressure admits the following integral representation:

$$p^{\varepsilon'}(t, \mathbf{x}, -L) = \frac{\varepsilon^r}{16\pi^3} \iint e^{-\frac{i\omega}{\varepsilon}(t-\boldsymbol{\kappa}\cdot\mathbf{x}-L\underline{\zeta}(\boldsymbol{\kappa}))} T^\varepsilon(\omega, \boldsymbol{\kappa}, -L, 0) \left(\frac{\boldsymbol{\kappa} \cdot \varrho_0 \widehat{\mathbf{F}}_{\mathbf{x}}(\omega, \boldsymbol{\kappa})}{\beta(\boldsymbol{\kappa})\underline{\zeta}(\boldsymbol{\kappa})} - \varrho_0 \widehat{\mathbf{F}}_z(\omega, \boldsymbol{\kappa}) \right) \omega^2 d\omega d\boldsymbol{\kappa}. \quad (2.57)$$

Here the integral is over all frequencies ω and over slowness vectors $\boldsymbol{\kappa}$ such that $\underline{\zeta}(\boldsymbol{\kappa})$ is real-valued. The contributions of the slowness vectors $\boldsymbol{\kappa}$ that do not satisfy this condition are negligible when the propagation distance L is large (far-field acoustic pressure).

2.3.2 Characterization of moments

From the integral representation (2.57) we see that the transmission coefficients T^ε of Eq. (2.55) fully determine the transmitted wave field. From the energy conservation relationship (2.56) the moduli of these coefficients are bounded by one. Now from Eq. (2.57) again it is seen that the distribution of waves in time and space depends on the joint distribution of the integrand over all frequencies ω and horizontal slowness vectors $\boldsymbol{\kappa}$. We next illustrate that the knowledge of the joint moments of the transmission coefficient for all finite combinations of different frequencies and slowness vectors is enough to characterize the distribution of the transmitted waves in time and space. This follows from the fact that the expectations in Eq. (2.58) below have arguments that involve a finite number of frequencies and slowness vectors. In view of the form of the transmitted pressure (2.57), the subsequent analysis is a direct extension of the results of [72, Sec. 14.2] with an adapted phase accounting for the ambient flow velocity \mathbf{v}_0 .

2.3.2.1 Transmission coefficient

A convenient way to characterize the finite-dimensional distributions of the scalar wave is to compute the joint moments of order m_1, \dots, m_n :

$$\mathbb{E} \left\{ p^{\varepsilon l}(t_{0,1} + \varepsilon s_1, \mathbf{x}_1, -L)^{m_1} \cdots p^{\varepsilon l}(t_{0,n} + \varepsilon s_n, \mathbf{x}_n, -L)^{m_n} \right\},$$

which, using (2.57), can be written in an integral form with respect to the variables $\omega_{j,l}$ and $\boldsymbol{\kappa}_{j,l}$, $1 \leq l \leq n$, $1 \leq j \leq m_l$:

$$\begin{aligned} & \frac{1}{(2\pi\varepsilon)^{3m}} \int \cdots \int e^{-i\sum \omega_{j,l} s_l} e^{i\sum \frac{\omega_{j,l} \phi_{j,l}}{\varepsilon}} \mathbb{E} \left\{ \prod T^\varepsilon(\omega_{j,l}, \boldsymbol{\kappa}_{j,l}, -L, 0) \right\} \\ & \times \frac{\varepsilon^{(r+3)m}}{2^m} \prod \left[\left(\frac{\boldsymbol{\kappa}_{j,l} \cdot \varrho_0 \widehat{\mathbf{F}} \mathbf{x}(\omega_{j,l}, \boldsymbol{\kappa}_{j,l})}{\beta(\boldsymbol{\kappa}_{j,l}) \zeta(\boldsymbol{\kappa}_{j,l})} - \varrho_0 \widehat{\mathbf{F}}_z(\omega_{j,l}, \boldsymbol{\kappa}_{j,l}) \right) \right] \prod \omega_{j,l}^2 d\omega_{j,l} d\boldsymbol{\kappa}_{j,l}, \end{aligned} \quad (2.58)$$

where $m = \sum_{l=1}^n m_l$ and we have defined:

$$\phi_{j,l} = \phi(t_{0,l}, \boldsymbol{\kappa}_{j,l}, \mathbf{x}_l) = -t_{0,l} + \boldsymbol{\kappa}_{j,l} \cdot \mathbf{x}_l + L \zeta(\boldsymbol{\kappa}_{j,l}).$$

In the above expression the sum of exponents and the products are taken over all the distinct frequencies and slowness vectors, that is, over l and j such that $1 \leq l \leq n$ and $1 \leq j \leq m_l$. Therefore, we are led to study the joint distribution of the transmission coefficients for a finite number of frequencies and slowness vectors. We now relabel these by $(\omega_1, \boldsymbol{\kappa}_1), \dots, (\omega_m, \boldsymbol{\kappa}_m)$. First, consider the situation where the phase vanishes $\phi_{j,l} = 0$. Then, if we could obtain the limits:

$$\lim_{\varepsilon \rightarrow 0} \mathbb{E} \left\{ T^\varepsilon(\omega_1, \boldsymbol{\kappa}_1, -L, 0) \cdots T^\varepsilon(\omega_m, \boldsymbol{\kappa}_m, -L, 0) \right\} \quad (2.59)$$

of all these finite-dimensional problems, we would have characterized all the finite-dimensional distributions of the transmitted wave front in space and time. The argument presented in [72, Sec 8.2.5] in the one-dimensional case can be directly applied to the present situation. The limits (2.59) are given by:

$$\mathbb{E} \left\{ \tilde{T}(\omega_1, \boldsymbol{\kappa}_1, -L, 0) \cdots \tilde{T}(\omega_m, \boldsymbol{\kappa}_m, -L, 0) \right\}, \quad (2.60)$$

where the coefficients $\tilde{T}(\omega, \boldsymbol{\kappa}, -L, 0)$ are solutions of the system of stochastic differential equations:

$$\begin{aligned} d\tilde{T}(\omega, \boldsymbol{\kappa}, -L, z) = & -\omega^2 \frac{\varrho_0^2 \beta(\boldsymbol{\kappa})^2 \gamma}{4\underline{\zeta}(\boldsymbol{\kappa})^2} \tilde{T}(\omega, \boldsymbol{\kappa}, -L, z) dz \\ & + i\omega \frac{\varrho_0 \beta(\boldsymbol{\kappa}) \sqrt{\gamma}}{2\underline{\zeta}(\boldsymbol{\kappa})} \tilde{T}(\omega, \boldsymbol{\kappa}, -L, z) dW_0(L+z), \end{aligned} \quad (2.61)$$

driven by a single standard Brownian motion W_0 . The initial condition is given at $z = -L$ by:

$$\tilde{T}(\omega, \boldsymbol{\kappa}, -L, z = -L) = 1,$$

and the correlation length coefficient γ is given by:

$$\gamma = \frac{1}{\underline{K}^2} \int_{-\infty}^{+\infty} \mathbb{E} \{ \nu(0) \nu(z) \} dz. \quad (2.62)$$

This physical parameter is discussed in detail in [72, Sec. 6.3.6]. It is the Fourier transform of the autocorrelation function of ν/\underline{K} at zero frequency, hence it is non negative. An application of Itô's formula shows that Eq. (2.61) can be transformed to the Stratonovich stochastic differential equation:

$$\begin{aligned} d\tilde{T}(\omega, \boldsymbol{\kappa}, -L, z) = & -\omega^2 \frac{\varrho_0^2 \beta(\boldsymbol{\kappa})^2 \gamma}{8\underline{\zeta}(\boldsymbol{\kappa})^2} \tilde{T}(\omega, \boldsymbol{\kappa}, -L, z) dz \\ & + i\omega \frac{\varrho_0 \beta(\boldsymbol{\kappa}) \sqrt{\gamma}}{2\underline{\zeta}(\boldsymbol{\kappa})} \tilde{T}(\omega, \boldsymbol{\kappa}, -L, z) \circ dW_0(L+z), \end{aligned}$$

which admits the following explicit solution:

$$\tilde{T}(\omega, \boldsymbol{\kappa}, -L, 0) = \exp \left(i\omega \frac{\varrho_0 \beta(\boldsymbol{\kappa}) \sqrt{\gamma}}{2\underline{\zeta}(\boldsymbol{\kappa})} W_0(L) - \omega^2 \frac{\varrho_0^2 \beta(\boldsymbol{\kappa})^2 \gamma}{8\underline{\zeta}(\boldsymbol{\kappa})^2} L \right). \quad (2.63)$$

Therefore, if we substitute \tilde{T} for T^ε in Eq. (2.57), we obtain a characterization of the distribution for the wave front through its moments. This substitution leads to the correct asymptotic limit expression for the wave front also in the case with a fast phase, that is, when $\phi_{j,l}$ is nonzero. The small ε limit for the front is then obtained via a subsequent stationary-phase argument elaborated in the following Sect. 2.3.2.2. We denote by \tilde{p} the limit for the pressure that follows from such a stationary-phase (sp) evaluation, so that:

$$\begin{aligned} \tilde{p}(s, \mathbf{x}, -L) & := (\text{sp}) \lim_{\varepsilon \rightarrow 0} p^{\varepsilon'}(t_0 + \varepsilon s, \mathbf{x}, -L) \\ & = (\text{sp}) \lim_{\varepsilon \rightarrow 0} \frac{\varepsilon^r}{16\pi^3} \iint e^{-i\omega s} e^{\frac{i\omega}{\varepsilon} \phi(t_0, \boldsymbol{\kappa}, \mathbf{x})} \tilde{T}(\omega, \boldsymbol{\kappa}, -L, 0) \\ & \quad \left(\frac{\boldsymbol{\kappa} \cdot \varrho_0 \widehat{\mathbf{F}}_{\mathbf{x}}(\omega, \boldsymbol{\kappa})}{\beta(\boldsymbol{\kappa}) \underline{\zeta}(\boldsymbol{\kappa})} - \varrho_0 \widehat{F}_z(\omega, \boldsymbol{\kappa}) \right) \omega^2 d\omega d\boldsymbol{\kappa}, \end{aligned} \quad (2.64)$$

where the phase ϕ is given by:

$$\phi(t_0, \boldsymbol{\kappa}, \mathbf{x}) = -t_0 + \boldsymbol{\kappa} \cdot \mathbf{x} + L \underline{\zeta}(\boldsymbol{\kappa}). \quad (2.65)$$

2.3.2.2 Stationary-phase method

It remains to evaluate the foregoing integral (2.64) by the stationary-phase method. The analysis is a direct application of [72, Prop. 14.4] in two dimensions. First, it follows from the scaling of the stationary-phase limit in two dimensions and Eq. (2.64) that the transmitted pressure field is of order 1 if $r = -1$. Second, we search for the stationary horizontal slowness vector $\boldsymbol{\kappa}_{\text{sp}}$ that solves $\nabla_{\boldsymbol{\kappa}}\phi(\boldsymbol{\kappa}_{\text{sp}}) = \mathbf{0}$ because it is the one that gives rise to the main contribution to the integral (2.64); see Fig. 2.5 for an illustration. In view of Eq. (2.65) and Eq. (2.47) we have:

$$\nabla_{\boldsymbol{\kappa}}\phi = \boldsymbol{x} + L\nabla_{\boldsymbol{\kappa}}\underline{\zeta} = \boldsymbol{x} - \frac{L}{2\underline{\zeta}(\boldsymbol{\kappa})} \left[\left(\frac{1}{\underline{c}^2} + \frac{\kappa^2}{\beta(\boldsymbol{\kappa})^2} \right) \boldsymbol{v}_0 + \frac{2}{\beta(\boldsymbol{\kappa})} \boldsymbol{\kappa} \right],$$

where $\kappa = |\boldsymbol{\kappa}|$. The Hessian $\mathbf{H}_{\boldsymbol{\kappa}}\phi := \nabla_{\boldsymbol{\kappa}} \otimes \nabla_{\boldsymbol{\kappa}}\phi$ (used in the asymptotic computation of the integral by the stationary-phase method) is:

$$\begin{aligned} \mathbf{H}_{\boldsymbol{\kappa}}\phi &= L\nabla_{\boldsymbol{\kappa}} \otimes \nabla_{\boldsymbol{\kappa}}\underline{\zeta} \\ &= -\frac{L}{4\underline{\zeta}^3(\boldsymbol{\kappa})} \left[\left(\frac{1}{\underline{c}^2} + \frac{\kappa^2}{\beta(\boldsymbol{\kappa})^2} \right) \boldsymbol{v}_0 + \frac{2}{\beta(\boldsymbol{\kappa})} \boldsymbol{\kappa} \right] \otimes \left[\left(\frac{1}{\underline{c}^2} + \frac{\kappa^2}{\beta(\boldsymbol{\kappa})^2} \right) \boldsymbol{v}_0 + \frac{2}{\beta(\boldsymbol{\kappa})} \boldsymbol{\kappa} \right] \\ &\quad - \frac{L}{\underline{\zeta}(\boldsymbol{\kappa})\beta(\boldsymbol{\kappa})} \left[\mathbf{I}_2 + \frac{\kappa^2}{\beta(\boldsymbol{\kappa})^2} \boldsymbol{v}_0 \otimes \boldsymbol{v}_0 + \frac{2}{\beta(\boldsymbol{\kappa})} \boldsymbol{\kappa} \otimes_s \boldsymbol{v}_0 \right], \end{aligned}$$

where $\boldsymbol{a} \otimes_s \boldsymbol{b} = \frac{1}{2}(\boldsymbol{a} \otimes \boldsymbol{b} + \boldsymbol{b} \otimes \boldsymbol{a})$. Here the equation $\nabla_{\boldsymbol{\kappa}}\phi = \mathbf{0}$ does not admit a trivial solution so we cannot find an explicit formulation of $\boldsymbol{\kappa}_{\text{sp}}$ as in [72]. To work around this problem we use a Taylor expansion of ϕ . We assume now and for the rest of this section that the flow Mach number (a vector here) $\boldsymbol{M} = \boldsymbol{v}_0/\underline{c}$ has small amplitude $M = |\boldsymbol{M}| \ll 1$, and consider that the horizontal slowness vector is such that $|\boldsymbol{\kappa}| < 1/\underline{c}$ in view of (2.24). At first, the Taylor expansion of $\underline{\zeta}(\boldsymbol{\kappa})$ yields:

$$\underline{\zeta}(\boldsymbol{\kappa}) = \frac{1}{c(\boldsymbol{\kappa})} - \frac{c(\boldsymbol{\kappa})}{2\underline{c}}(1 + \underline{c}^2|\boldsymbol{\kappa}|^2)\boldsymbol{M} \cdot \boldsymbol{\kappa} + o(M), \quad c(\boldsymbol{\kappa}) = \frac{\underline{c}}{\sqrt{1 - \underline{c}^2|\boldsymbol{\kappa}|^2}}.$$

Then the phase $\phi(t, \boldsymbol{\kappa}, \boldsymbol{x})$ reads $\phi(t, \boldsymbol{\kappa}, \boldsymbol{x}) = \phi_0(t, \boldsymbol{\kappa}, \boldsymbol{x}) + M\phi_1(\boldsymbol{\kappa}) + o(M)$ where:

$$\begin{aligned} \phi_0(t, \boldsymbol{\kappa}, \boldsymbol{x}) &= -t + \boldsymbol{\kappa} \cdot \boldsymbol{x} + \frac{L}{c(\boldsymbol{\kappa})}, \\ \phi_1(\boldsymbol{\kappa}) &= -\frac{Lc(\boldsymbol{\kappa})}{2\underline{c}}(1 + \underline{c}^2|\boldsymbol{\kappa}|^2)\hat{\boldsymbol{v}}_0 \cdot \boldsymbol{\kappa}, \end{aligned}$$

for $\hat{\boldsymbol{v}}_0 = \boldsymbol{v}_0/|\boldsymbol{v}_0|$ being the direction of the flow. Likewise, the gradient of the phase is expanded as:

$$\nabla_{\boldsymbol{\kappa}}\phi(t, \boldsymbol{\kappa}, \boldsymbol{x}) = \nabla_{\boldsymbol{\kappa}}\phi_0(t, \boldsymbol{\kappa}, \boldsymbol{x}) + M\nabla_{\boldsymbol{\kappa}}\phi_1(\boldsymbol{\kappa}) + o(M)$$

where:

$$\begin{aligned} \nabla_{\boldsymbol{\kappa}}\phi_0(t, \boldsymbol{\kappa}, \boldsymbol{x}) &= \boldsymbol{x} - Lc(\boldsymbol{\kappa})\boldsymbol{\kappa}, \\ \nabla_{\boldsymbol{\kappa}}\phi_1(\boldsymbol{\kappa}) &= -\frac{Lc(\boldsymbol{\kappa})}{2\underline{c}} \left[(1 + \underline{c}^2|\boldsymbol{\kappa}|^2)\mathbf{I}_2 + \left(\frac{3 - \underline{c}^2|\boldsymbol{\kappa}|^2}{1 - \underline{c}^2|\boldsymbol{\kappa}|^2} \right) \underline{c}^2 \boldsymbol{\kappa} \otimes \boldsymbol{\kappa} \right] \hat{\boldsymbol{v}}_0. \end{aligned}$$

The equation $\nabla_{\boldsymbol{\kappa}}\phi_0(t, \boldsymbol{\kappa}, \mathbf{x}) = \mathbf{0}$ is exactly the stationary-phase equation solved in [72, Sec. 14.2.2] for a quiescent medium, so we know that:

$$\boldsymbol{\kappa}_0 = \frac{\mathbf{x}}{\underline{c}\sqrt{|\mathbf{x}|^2 + L^2}} \quad (2.66)$$

is its unique solution. Invoking the implicit function theorem, the equation $\nabla_{\boldsymbol{\kappa}}\phi(t, \boldsymbol{\kappa}, \mathbf{x}) = \mathbf{0}$ has a unique solution $\boldsymbol{\kappa}_{\text{sp}}$ in a neighborhood of $\boldsymbol{\kappa}_0$ and the function $M \mapsto \boldsymbol{\kappa}_{\text{sp}}(M)$ is differentiable in a neighborhood of $M = 0$, such that expanding it as $\boldsymbol{\kappa}_{\text{sp}}(M) = \boldsymbol{\kappa}_0 + M\boldsymbol{\kappa}_1 + o(M)$ one has:

$$\boldsymbol{\kappa}_1 = \boldsymbol{\kappa}'_{\text{sp}}(0) = -(\mathbf{H}_{\boldsymbol{\kappa}}\phi_0(\boldsymbol{\kappa}_0))^{-1}\nabla_{\boldsymbol{\kappa}}\phi_1(\boldsymbol{\kappa}_0). \quad (2.67)$$

Indeed the Hessian of ϕ_0 :

$$\mathbf{H}_{\boldsymbol{\kappa}}\phi_0(\boldsymbol{\kappa}_0) = -Lc(\boldsymbol{\kappa}_0) (\mathbf{I}_2 + c(\boldsymbol{\kappa}_0)^2\boldsymbol{\kappa}_0 \otimes \boldsymbol{\kappa}_0),$$

is invertible provided that $\boldsymbol{\kappa}_0$ is in the propagating domain such that $\underline{\zeta}(\boldsymbol{\kappa}_0)$ is real, and its inverse is:

$$(\mathbf{H}_{\boldsymbol{\kappa}}\phi_0(\boldsymbol{\kappa}_0))^{-1} = -\frac{1}{Lc(\boldsymbol{\kappa}_0)} (\mathbf{I}_2 - \underline{c}^2\boldsymbol{\kappa}_0 \otimes \boldsymbol{\kappa}_0).$$

Then the stationary horizontal slowness vector reads:

$$\boldsymbol{\kappa}_{\text{sp}} = \frac{1}{\underline{c}} \left[\frac{\mathbf{x}}{\sqrt{|\mathbf{x}|^2 + L^2}} + \frac{1}{2} \left(\frac{2|\mathbf{x}|^2 + L^2}{|\mathbf{x}|^2 + L^2} \right) \mathbf{M} + \frac{L^2}{(|\mathbf{x}|^2 + L^2)^2} (\mathbf{M} \cdot \mathbf{x}) \mathbf{x} \right] + o(M), \quad (2.68)$$

and the vertical slowness vector at the stationary point is:

$$\underline{\zeta}(\boldsymbol{\kappa}_{\text{sp}}) = \frac{1}{\underline{c}} \left[\frac{L}{\sqrt{|\mathbf{x}|^2 + L^2}} - \frac{1}{L} \left(\frac{2|\mathbf{x}|^4 + 4|\mathbf{x}|^2L^2 + L^4}{(|\mathbf{x}|^2 + L^2)^2} \right) (\mathbf{M} \cdot \mathbf{x}) \right] + o(M).$$

This corresponds to a plane-wave mode that is traveling in the direction of the observation point $(\mathbf{x}, -L)$, as seen on Fig. 2.5.

We can use now this expression to compute $\tilde{p}(s, \mathbf{x}, -L)$ from Eq. (2.64) by the stationary-phase method and have an idea of the solution of the transmission problem in the limit of small Mach numbers. The phase at the stationary point is:

$$\phi(t, \boldsymbol{\kappa}_{\text{sp}}, \mathbf{x}) = -t + \frac{\sqrt{|\mathbf{x}|^2 + L^2}}{\underline{c}} - \frac{1}{2\underline{c}} \left(\frac{2|\mathbf{x}|^2 + L^2}{|\mathbf{x}|^2 + L^2} \right) (\mathbf{M} \cdot \mathbf{x}) + o(M).$$

In view of Eq. (2.64) and [72, Prop. 14.4] we choose t_0 such that it cancels the phase at the stationary point, since otherwise this integral goes to 0 as $\varepsilon \rightarrow 0$ by Riemann-Lebesgue's lemma. At first order in the Mach number M we thus have:

$$t_0 = \frac{\sqrt{|\mathbf{x}|^2 + L^2}}{\underline{c}} - \frac{1}{2\underline{c}} \left(\frac{2|\mathbf{x}|^2 + L^2}{|\mathbf{x}|^2 + L^2} \right) (\mathbf{M} \cdot \mathbf{x}) + o(M).$$

Applying [72, Prop. 14.4] for $n = 2$ we obtain:

$$\begin{aligned} \tilde{p}(s, \mathbf{x}, -L) &= \frac{e^{i(n^*-1)\frac{\pi}{2}}}{8\pi^2 \sqrt{|\det \mathbf{H}_{\boldsymbol{\kappa}}\phi(\boldsymbol{\kappa}_{\text{sp}})|}} \\ &\times \int_{\mathbb{R}} e^{-i\omega s} \tilde{T}(\omega, \boldsymbol{\kappa}_{\text{sp}}, -L, 0) \left(\frac{\boldsymbol{\kappa}_{\text{sp}} \cdot \varrho_0 \widehat{\mathbf{F}}_{\mathbf{x}}(\omega, \boldsymbol{\kappa}_{\text{sp}})}{\beta(\boldsymbol{\kappa}_{\text{sp}})\underline{\zeta}(\boldsymbol{\kappa}_{\text{sp}})} - \varrho_0 \widehat{F}_z(\omega, \boldsymbol{\kappa}_{\text{sp}}) \right) \omega d\omega, \end{aligned}$$

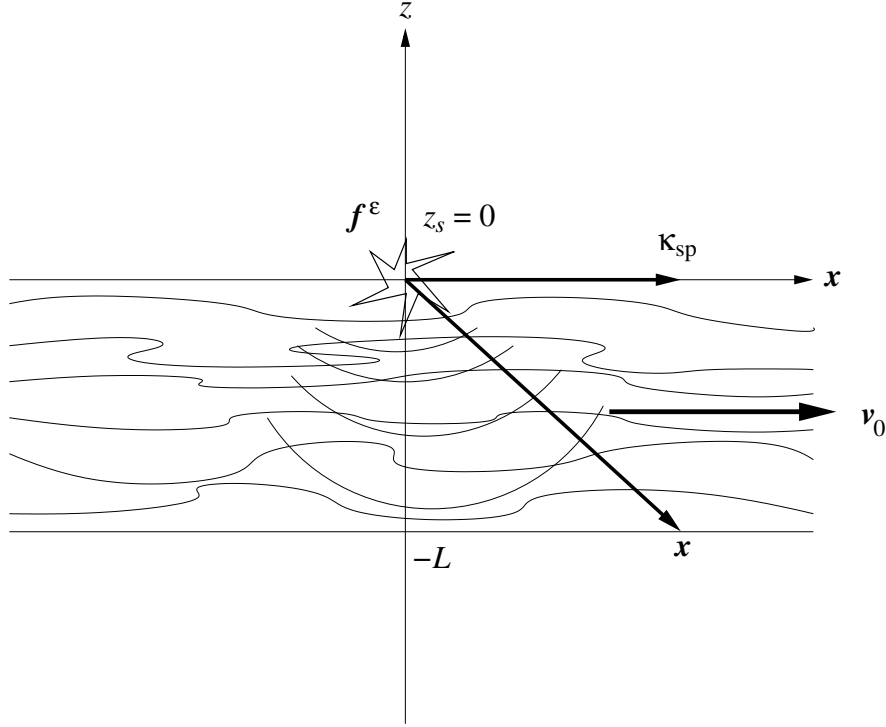


Figure 2.5 – Acoustic waves in a stratified random flow of thickness L and flow velocity \mathbf{v}_0 . The source position at $(\mathbf{x}_s, z_s) = \mathbf{0}$, the observation point at $(\mathbf{x}, -L)$, and the stationary slowness vector $\boldsymbol{\kappa}_{\text{sp}}$.

where n^* is the number of positive eigenvalues of $\mathbf{H}_{\boldsymbol{\kappa}}\phi(\boldsymbol{\kappa}_{\text{sp}})$ and $\tilde{T}(\omega, \boldsymbol{\kappa}, -L, 0)$ is given by Eq. (2.63). Since $n^* = 0$ one has therefore:

$$\begin{aligned} \tilde{p}(s, \mathbf{x}, -L) &= \frac{1}{8\pi^2 \sqrt{|\det \mathbf{H}_{\boldsymbol{\kappa}}\phi(\boldsymbol{\kappa}_{\text{sp}})|}} \\ &\times \int_{\mathbb{R}} e^{-i\omega s} e^{i\omega \frac{\varrho_0 \beta(\boldsymbol{\kappa}_{\text{sp}}) \sqrt{\gamma}}{2\zeta(\boldsymbol{\kappa}_{\text{sp}})}} W_0(L) e^{-\omega^2 \frac{\varrho_0^2 \beta(\boldsymbol{\kappa}_{\text{sp}})^2 \gamma}{8\zeta(\boldsymbol{\kappa}_{\text{sp}})^2} L} i\omega \left(\varrho_0 \widehat{F}_z(\omega, \boldsymbol{\kappa}_{\text{sp}}) - \frac{\boldsymbol{\kappa}_{\text{sp}} \cdot \varrho_0 \widehat{\mathbf{F}}_{\mathbf{x}}(\omega, \boldsymbol{\kappa}_{\text{sp}})}{\beta(\boldsymbol{\kappa}_{\text{sp}})\zeta(\boldsymbol{\kappa}_{\text{sp}})} \right) d\omega. \end{aligned} \quad (2.69)$$

The corresponding limit expression for the transmitted pressure field \tilde{p}_0 in an ambient flow with constant bulk modulus \underline{K} is obtained from the above expression with $\gamma = 0$, that is:

$$\tilde{p}_0(s, \mathbf{x}, -L) = \frac{1}{8\pi^2 \sqrt{|\det \mathbf{H}_{\boldsymbol{\kappa}}\phi(\boldsymbol{\kappa}_{\text{sp}})|}} \int_{\mathbb{R}} e^{-i\omega s} i\omega \left(\varrho_0 \widehat{F}_z(\omega, \boldsymbol{\kappa}_{\text{sp}}) - \frac{\boldsymbol{\kappa}_{\text{sp}} \cdot \varrho_0 \widehat{\mathbf{F}}_{\mathbf{x}}(\omega, \boldsymbol{\kappa}_{\text{sp}})}{\beta(\boldsymbol{\kappa}_{\text{sp}})\zeta(\boldsymbol{\kappa}_{\text{sp}})} \right) d\omega.$$

For the particular case of sources (2.44) located at the origin:

$$\mathbf{f}^\epsilon(t, \mathbf{x}, z) = \frac{1}{\epsilon} \mathbf{F}_t \left(\frac{t}{\epsilon} \right) \delta \left(\frac{\mathbf{x}}{\epsilon} \right) \delta(z) = \epsilon \mathbf{F}_t \left(\frac{t}{\epsilon} \right) \delta(\mathbf{x}) \delta(z),$$

the latter equation yields:

$$\tilde{p}_0(s, \mathbf{x}, -L) = \frac{1}{4\pi \sqrt{|\det \mathbf{H}_{\boldsymbol{\kappa}}\phi(\boldsymbol{\kappa}_{\text{sp}})|}} \left(\varrho_0 F'_{t,z}(s) - \frac{\boldsymbol{\kappa}_{\text{sp}} \cdot \varrho_0 \mathbf{F}'_{t,\mathbf{x}}(s)}{\beta(\boldsymbol{\kappa}_{\text{sp}})\zeta(\boldsymbol{\kappa}_{\text{sp}})} \right),$$

where $\kappa_{\text{sp}}(\mathbf{x})$ is given by Eq. (2.68). Eq. (2.69) thus shows that as in [72, Chap. 14], the transmitted pressure field through a stratified random flow is a simple modification of the pressure field transmitted through the constant flow. We summarize this results in the following proposition, which is the counterpart of [72, Prop. 14.3] for a random medium moving at the (small) Mach number M ; see also Sect. 1.3.3.

Proposition 2.3.1. *In distribution the transmitted pressure field is characterized by:*

$$\lim_{\varepsilon \rightarrow 0} p^{\varepsilon'} \left(\frac{\sqrt{|\mathbf{x}|^2 + L^2}}{\underline{c}} - \frac{1}{2\underline{c}} \left(\frac{2|\mathbf{x}|^2 + L^2}{|\mathbf{x}|^2 + L^2} \right) (\mathbf{M} \cdot \mathbf{x}) + \varepsilon s, \mathbf{x}, -L \right) = \tilde{p}(s, \mathbf{x}, -L),$$

where:

$$\tilde{p}(s, \mathbf{x}, -L) = [\mathcal{N}_{D(\mathbf{x}, L, M)} * \tilde{p}_0(\cdot, \mathbf{x}, -L)](s - D(\mathbf{x}, L, M)G),$$

having set:

$$D(\mathbf{x}, L, M) = \frac{\varrho_0 \beta(\kappa_{\text{sp}})}{2\underline{\zeta}(\kappa_{\text{sp}})} \sqrt{\gamma L},$$

$$\mathcal{N}_D(s) = \frac{1}{\sqrt{2\pi D}} e^{-\frac{s^2}{2D^2}},$$

and G is a Gaussian random variable with mean zero and unit variance.

The shape of the transmitted pressure wave front is thus given by the convolution of a Gaussian kernel with the shape of the pressure wave front transmitted through the constant flow. It is deterministic, whereas the travel time shift $D(\mathbf{x}, L, M)G$ is a random delay proportional to a Gaussian random variable with mean zero and unit variance. This phenomenon is referred to as stabilization of the front, as discussed again in [72, Chap. 14]. Consequently, the proposed model of a stratified flow with a random bulk modulus is not able to explain the spectral broadening effects outlined in Chapter 1 and observed in experiments. Thus we turn to the study of an alternative model where the flow velocity is now considered as a random field. The analysis is outlined in the subsequent Sect. 2.4.

2.4 Acoustic waves in a stratified flow with random velocity

We define a fluctuation model of the ambient flow velocity as follows:

$$\mathbf{v}_0(t, \mathbf{r}) = \begin{cases} \underline{\mathbf{v}} + \varepsilon \mathbf{V}(t, \mathbf{x}, z) & z \in [-L, 0], \\ \underline{\mathbf{v}} & \text{elsewhere.} \end{cases} \quad (2.70)$$

Here $0 < L$ is the width of the random flow, $\underline{\mathbf{v}}$ is the constant ambient flow velocity which is also parallel to the horizontal coordinates \mathbf{x} of $\mathbf{r} = (\mathbf{x}, z)$, and $0 \leq \varepsilon \ll 1$ is a small parameter which scales the amplitude of its fluctuations \mathbf{V} . This parameter is often called turbulence intensity in the dedicated literature, as it is related to the components of the turbulent kinetic energy. The latter are generally different for each direction [41], but it is assumed in the above model that such intensities are comparable for all directions. The fluctuations of the constant ambient flow velocity in Eq. (2.70) are given by the mean-square stationary random vector $(\mathbf{V}(t, \mathbf{r}); t \in \mathbb{R}, \mathbf{r} \in \mathbb{R}^3)$ with zero mean:

$$\mathbb{E} \{ \mathbf{V}(t, \mathbf{x}, z) \} = \mathbf{0}. \quad (2.71)$$

Its auto-correlation matrix function reads:

$$\begin{aligned} \mathbb{E}\{\mathbf{V}(t_1, \mathbf{r}_1) \otimes \mathbf{V}(t_2, \mathbf{r}_2)\} &= \mathbf{R}_V(t_1 - t_2, \mathbf{r}_1 - \mathbf{r}_2) \\ &= \mathbf{R}(t_1 - t_2) \delta(\mathbf{x}_1 - \mathbf{x}_2 - (t_1 - t_2) \mathbf{v}_t) \delta(z_1 - z_2) \frac{\mathbb{1}_{[-L_1, -L_0]}(z_1)}{L_1 - L_0}, \end{aligned} \quad (2.72)$$

where \mathbf{v}_t is the convection velocity of the turbulent structures (eddies) in the shear layer, and $t \mapsto \mathbf{R}(t)$ is a 3×3 matrix function which describes the auto-correlation in time. Here $z \mapsto \mathbb{1}_I(z)$ is the characteristic function of the set I such that $\mathbb{1}_I(z) = 1$ if $z \in I$, and 0 otherwise. L_0 and L_1 are lengths characterizing the depth of the flow ($-L_1, -L_0$) ultimately chosen as $L_0 = 0$ and $L_1 = L$. This model means that the fluctuations \mathbf{V} are delta-correlated in the local frame moving at the turbulent velocity \mathbf{v}_t .

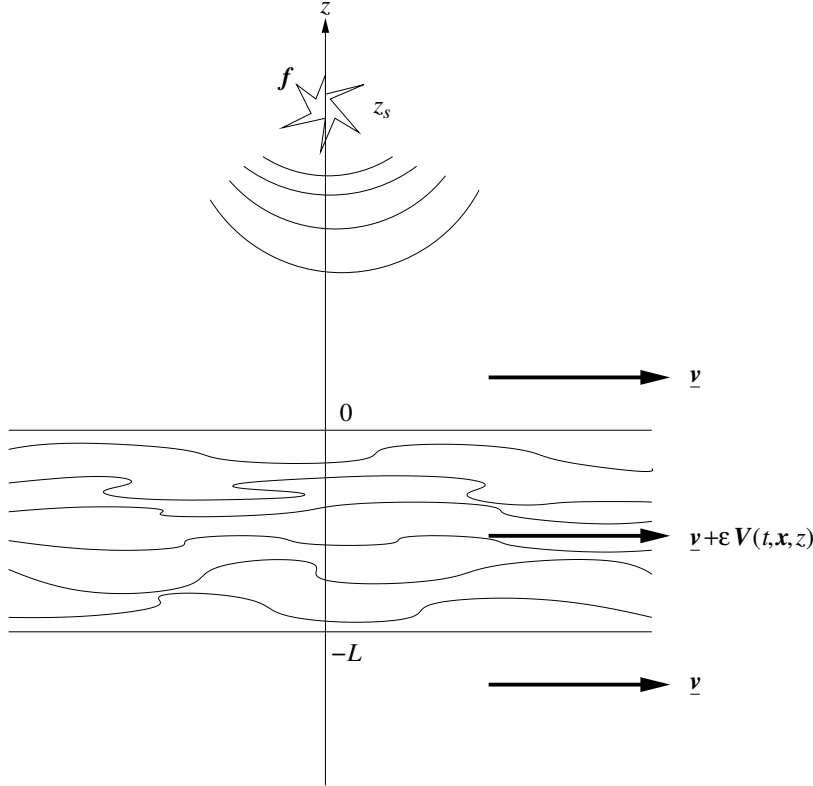


Figure 2.6 – Acoustic waves in a random flow of thickness L and average ambient flow velocity \underline{v} . The emitting sources \mathbf{f} are centered at some $z_s \geq 0$.

2.4.1 Transmitted fields with fluctuations of the ambient flow velocity

We now turn to the case of an ambient flow with a fluctuating velocity, namely Eq. (2.70) with $\varepsilon \neq 0$. The system (2.13) reads in this case:

$$\begin{aligned} \frac{dq}{dt} + \frac{1}{\varrho_0} \nabla \cdot \mathbf{u} &= \frac{h}{K_0} - \varepsilon \mathbf{V} \cdot \nabla q, \\ \frac{d\mathbf{u}}{dt} + K_0 \nabla q &= \varrho_0 \mathbf{f} - \varepsilon \mathbf{V} \cdot \nabla \mathbf{u} + \varepsilon \varrho_0 (\gamma - 1) \frac{d\mathbf{V}}{dt} q - \varepsilon ((\nabla \cdot \mathbf{V}) \mathbf{I}_3 + \mathbf{D}\mathbf{V}) \mathbf{u}, \end{aligned} \quad (2.73)$$

where:

$$\frac{d}{dt} = \frac{\partial}{\partial t} + \underline{\mathbf{v}} \cdot \nabla_{\mathbf{x}}$$

is the convective derivative. In view of Lemma 2.2.1 its solution can be written as:

$$\mathbf{p} = \mathbf{G}_0 * (\mathbf{s} - \varepsilon \mathbf{K} \mathbf{p}), \quad (2.74)$$

where:

$$\mathbf{K} = \begin{bmatrix} K_0 \mathbf{V} \cdot \nabla & \mathbf{0} \\ (1 - \gamma) \frac{d\mathbf{V}}{dt} & \frac{1}{\varrho_0} (\nabla \cdot \mathbf{V} + \mathbf{V} \cdot \nabla) \mathbf{I}_3 + \frac{1}{\varrho_0} \mathbf{D}\mathbf{V} \end{bmatrix}. \quad (2.75)$$

This is a so-called Lippmann-Schwinger equation [99], of which a solution can formally be constructed by induction:

$$\begin{aligned} \mathbf{p}^{(n+1)} &= \mathbf{p}^{(0)} - \varepsilon \mathbf{G}_0 * \mathbf{K} \mathbf{p}^{(n)} \\ &= \left(\mathbf{I}_4 + \sum_{j=1}^n (-\varepsilon \mathbf{G}_0 * \mathbf{K})^j \right) \mathbf{p}^{(0)}, \end{aligned} \quad (2.76)$$

with $\mathbf{p}^{(0)} := \mathbf{G}_0 * \mathbf{s}$. We will focus on the power spectral density (PSD) of \mathbf{p} in the subsequent developments, and more particularly the corrections to the PSD of $\mathbf{p}^{(0)}$ induced by the random fluctuations $\varepsilon \mathbf{V}(t, \mathbf{r})$ of the constant ambient flow velocity $\underline{\mathbf{v}}$. The leading correction term is proportional to ε^2 . Therefore, the above expansion is truncated at order 2 because it is anticipated that higher order terms will be negligible:

$$\mathbf{p} \simeq \mathbf{p}^{(2)} = \mathbf{p}^{(0)} - \varepsilon \mathbf{G}_0 * \mathbf{K} \mathbf{p}^{(0)} + \varepsilon^2 (\mathbf{G}_0 * \mathbf{K})^2 \mathbf{p}^{(0)}. \quad (2.77)$$

We note for convenience:

$$\mathbf{p}^{(01)} = \mathbf{G}_0 * \mathbf{K} \mathbf{p}^{(0)}, \quad \mathbf{p}^{(02)} = (\mathbf{G}_0 * \mathbf{K})^2 \mathbf{p}^{(0)},$$

the first-order and second-order terms, respectively, in the expansion of \mathbf{p} about the unperturbed, or ballistic pressure/momentum fields $\mathbf{p}^{(0)}$ solving Eq. (2.15). Fig. 2.7 sketches the zeroth, first, and second order contributions to the perturbative expansion (2.77), where $\mathbf{p}^{(01)}$ corresponds to the waves that have been scattered once by the random heterogeneities of the ambient flow velocity $\underline{\mathbf{v}}$, and $\mathbf{p}^{(02)}$ corresponds to the waves that have been scattered twice. All these quantities are the combinations of upward and downward fields. We show on Fig. 2.7 only the downward fields, *i.e.* the transmitted fields for $z \leq -L$.

Regarding the first-order perturbation $\mathbf{p}^{(01)}$, we have explicitly:

$$\mathbf{p}^{(01)}(t, \mathbf{x}, z) = \iiint \mathbf{G}_0(t - t', \mathbf{x} - \mathbf{x}', z - z') \mathbf{K} \mathbf{p}^{(0)}(t', \mathbf{x}', z') dt' d\mathbf{x}' dz'. \quad (2.78)$$

The second-order perturbation $\mathbf{p}^{(02)}$ is expressed similarly by iterating the convolution product. As will be seen in the following Sect. 2.4.2, the first-order contribution in this proposed perturbative model is responsible for the spectral broadening effect depicted in [41–43]. Therefore we will mainly focus on this term in the following analysis. In the Fourier domain (2.16), the first-order perturbation reads:

$$\begin{aligned} \widehat{\mathbf{p}}^{(01)}(\omega, \boldsymbol{\kappa}, z) &= \iint e^{i\omega(t - \boldsymbol{\kappa} \cdot \mathbf{x})} dt d\mathbf{x} \iiint \mathbf{G}_0(t - t', \mathbf{x} - \mathbf{x}', z - z') \mathbf{K} \mathbf{p}^{(0)}(t', \mathbf{x}', z') dt' d\mathbf{x}' dz' \\ &= \int \left(\iint e^{i\omega(t - \boldsymbol{\kappa} \cdot \mathbf{x})} \mathbf{G}_0(t, \mathbf{x}, z - z') dt d\mathbf{x} \right) \left(\iint e^{i\omega(t' - \boldsymbol{\kappa} \cdot \mathbf{x}')} \mathbf{K} \mathbf{p}^{(0)}(t', \mathbf{x}', z') dt' d\mathbf{x}' \right) dz' \end{aligned} \quad (2.79)$$

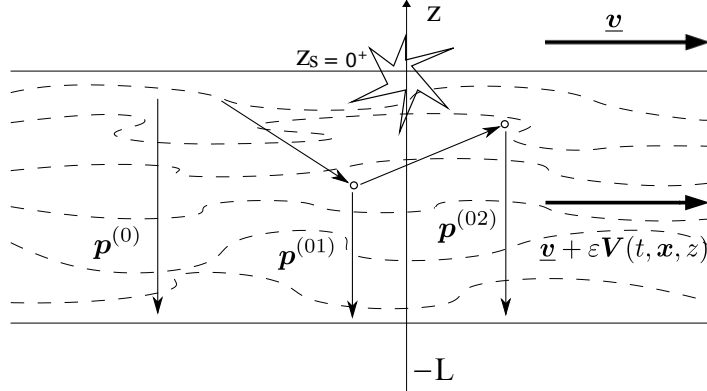


Figure 2.7 – *Acoustic waves in a random flow of thickness L and average ambient flow velocity \underline{v} . Zeroth (ballistic), first, and second order perturbations in the second-order expansion of the transmitted pressure/momentum fields.*

with the changes of variable $t - t' \rightarrow t$ and $\mathbf{x} - \mathbf{x}' \rightarrow \mathbf{x}$. The first bracketed term is nothing but $\widehat{\mathbf{G}}_0(\omega, \boldsymbol{\kappa}, z - z')$, while the second one is the Fourier transform of a product—hence a convolution product in the Fourier domain (2.16). In this setting, the Fourier transform of the product of regular functions $f(t, \mathbf{x}, z)$ and $g(t, \mathbf{x}, z)$ reads:

$$\widehat{fg}(\omega, \boldsymbol{\kappa}, z) = \frac{1}{(2\pi)^3} \iint \widehat{f}(\omega', \boldsymbol{\kappa}', z) \widehat{g}\left(\omega - \omega', \frac{\omega\boldsymbol{\kappa} - \omega'\boldsymbol{\kappa}'}{\omega - \omega'}, z\right) \omega'^2 d\omega' d\boldsymbol{\kappa}'. \quad (2.80)$$

Thus it remains to compute the Fourier transform (2.16) of \mathbf{K} , which depends on time t and the horizontal spatial coordinates \mathbf{x} through $\mathbf{V}(t, \mathbf{x}, z)$ and its various products with $\nabla = (\nabla_{\mathbf{x}}, \partial_z)$. As for the upper left term $K_{11} = K_0 \mathbf{V} \cdot \nabla$ of \mathbf{K} for instance, we have:

$$\begin{aligned} \widehat{K_{11}}f(\omega, \boldsymbol{\kappa}, z) &= \frac{K_0}{(2\pi)^3} \iint \left[i(\omega\boldsymbol{\kappa} - \omega'\boldsymbol{\kappa}') \cdot \widehat{\mathbf{V}}_{\mathbf{x}}(\omega', \boldsymbol{\kappa}', z) + \widehat{V}_z(\omega', \boldsymbol{\kappa}', z) \partial_z \right] \\ &\quad \times \widehat{f}\left(\omega - \omega', \frac{\omega\boldsymbol{\kappa} - \omega'\boldsymbol{\kappa}'}{\omega - \omega'}, z\right) \omega'^2 d\omega' d\boldsymbol{\kappa}'. \end{aligned} \quad (2.81)$$

Accordingly, the lower left term $\mathbf{K}_{21} = (1 - \gamma) \frac{d\mathbf{V}}{dt}$ yields:

$$\begin{aligned} \widehat{\mathbf{K}_{21}}f(\omega, \boldsymbol{\kappa}, z) &= \frac{1}{\rho_0 (2\pi)^3} \iint \widehat{\mathcal{K}}_{21}(\omega', \boldsymbol{\kappa}') \widehat{\mathbf{V}}(\omega', \boldsymbol{\kappa}', z) \\ &\quad \times \widehat{f}\left(\omega - \omega', \frac{\omega\boldsymbol{\kappa} - \omega'\boldsymbol{\kappa}'}{\omega - \omega'}, z\right) \omega'^2 d\omega' d\boldsymbol{\kappa}', \end{aligned} \quad (2.82)$$

where $\widehat{\mathcal{K}}_{21}(\omega, \boldsymbol{\kappa}) = i\omega\rho_0(\gamma - 1)\beta(\boldsymbol{\kappa})\mathbf{I}_3$, and the remaining lower right term:

$$\mathbf{K}_{22} = \frac{1}{\rho_0} ((\nabla \cdot \mathbf{V} + \mathbf{V} \cdot \nabla) \mathbf{I}_3 + \mathbf{D}\mathbf{V})$$

yields:

$$\begin{aligned} \widehat{\mathbf{K}}_{22}\widehat{\mathbf{f}}(\omega, \boldsymbol{\kappa}, z) &= \frac{1}{\varrho_0(2\pi)^3} \iiint \left[\left(\partial_z \widehat{V}_z(\omega', \boldsymbol{\kappa}', z) + \widehat{V}_z(\omega', \boldsymbol{\kappa}', z) \partial_z \right) \mathbf{I}_3 \right. \\ &\quad \left. + i\omega \boldsymbol{\kappa} \cdot \widehat{\mathbf{V}}_{\mathbf{x}}(\omega', \boldsymbol{\kappa}', z) \mathbf{I}_3 + \widehat{\mathbf{V}}(\omega', \boldsymbol{\kappa}', z) \otimes \begin{pmatrix} i\omega' \boldsymbol{\kappa}' \\ 0 \end{pmatrix} + \partial_z \widehat{\mathbf{V}}(\omega', \boldsymbol{\kappa}', z) \otimes \begin{pmatrix} \mathbf{0} \\ 1 \end{pmatrix} \right] \\ &\quad \times \widehat{\mathbf{f}} \left(\omega - \omega', \frac{\omega \boldsymbol{\kappa} - \omega' \boldsymbol{\kappa}'}{\omega - \omega'}, z \right) \omega'^2 d\omega' d\boldsymbol{\kappa}'. \end{aligned} \quad (2.83)$$

We finally apply the foregoing formulas to the calculation of $\widehat{\mathbf{p}}^{(01)}$ in Eq. (2.79). Here $\widehat{\mathbf{p}}^{(0)}$ is given by Lemma 2.2.1, Eq. (2.43), which is considered for the case $z_s = 0^+$ from now on in view of the application of [41–43] we have in mind. In this situation the Green's function \mathbf{G}_0 is reduced to its downward contribution \mathbf{G}_0^- in the expression of $\widehat{\mathbf{p}}^{(0)}$ and $\widehat{\mathbf{p}}^{(01)}$, as one can see on Fig. 2.7, and $\widehat{\mathbf{p}}^{(0)}$ is such that:

$$\partial_z \widehat{\mathbf{p}}^{(0)}(\omega, \boldsymbol{\kappa}, z) = -i\omega \zeta(\boldsymbol{\kappa}) \widehat{\mathbf{p}}^{(0)}(\omega, \boldsymbol{\kappa}, z).$$

This allows us to replace ∂_z by $-i(\omega - \omega') \zeta(\frac{\omega \boldsymbol{\kappa} - \omega' \boldsymbol{\kappa}'}{\omega - \omega'})$ in the expressions of the Fourier transforms of $K_{11}\mathbf{p}^{(0)}$ and $\mathbf{K}_{22}\mathbf{p}^{(0)}$ obtained with the above formulas. We summarize these results in the following proposition.

Proposition 2.4.1. *Assume the forcing terms are point sources as in Lemma 2.2.1 with $z_s = 0^+$. Then the first-order transmitted perturbations $\mathbf{p}^{(01)}$ in the perturbative expansion (2.76) are given by:*

$$\begin{aligned} \widehat{\mathbf{p}}^{(01)}(\omega, \boldsymbol{\kappa}, z) &= \frac{\varrho_0^2 e^{-i\omega \zeta(\boldsymbol{\kappa})z}}{4(2\pi)^3} \left(\iiint e^{i\omega \sigma(\omega, \boldsymbol{\kappa}, \omega', \boldsymbol{\kappa}')z'} \widehat{\mathbf{c}}(\omega, \boldsymbol{\kappa}, \omega', \boldsymbol{\kappa}') \cdot \widehat{\mathbf{V}}(\omega', \boldsymbol{\kappa}', z') \right. \\ &\quad \left. \times \widehat{\mathcal{S}}^- \left(\omega - \omega', \frac{\omega \boldsymbol{\kappa} - \omega' \boldsymbol{\kappa}'}{\omega - \omega'} \right) \omega'^2 d\omega' d\boldsymbol{\kappa}' dz' \right) \widehat{\mathbf{g}}_0^-(\boldsymbol{\kappa}), \end{aligned} \quad (2.84)$$

where $\widehat{\mathcal{S}}^-$ is the generalized coordinate given by Eq. (2.41), and the slowness σ is given by:

$$\sigma(\omega, \boldsymbol{\kappa}, \omega', \boldsymbol{\kappa}') = \zeta(\boldsymbol{\kappa}) - \left(1 - \frac{\omega'}{\omega} \right) \zeta \left(\frac{\omega \boldsymbol{\kappa} - \omega' \boldsymbol{\kappa}'}{\omega - \omega'} \right). \quad (2.85)$$

The vector $\widehat{\mathbf{c}}(\omega, \boldsymbol{\kappa}, \omega', \boldsymbol{\kappa}')$ is:

$$\widehat{\mathbf{c}}(\omega, \boldsymbol{\kappa}, \omega', \boldsymbol{\kappa}') = \widehat{\mathbf{k}}(\omega, \boldsymbol{\kappa}, \omega', \boldsymbol{\kappa}') - i\omega \sigma(\omega, \boldsymbol{\kappa}, \omega', \boldsymbol{\kappa}') \widehat{\mathbf{d}}(\omega, \boldsymbol{\kappa}, \omega', \boldsymbol{\kappa}')$$

where $\mathbf{K}_0 = \text{diag}(K_0, \frac{1}{\varrho_0}, \frac{1}{\varrho_0}, \frac{1}{\varrho_0})$, and $\widehat{\mathbf{k}}(\omega, \boldsymbol{\kappa}, \omega', \boldsymbol{\kappa}')$ and $\widehat{\mathbf{d}}(\omega, \boldsymbol{\kappa}, \omega', \boldsymbol{\kappa}')$ are given by:

$$\begin{aligned} \widehat{\mathbf{k}}(\omega, \boldsymbol{\kappa}, \omega', \boldsymbol{\kappa}') &= \frac{1}{\varrho_0 K_0} \zeta \left(\frac{\omega \boldsymbol{\kappa} - \omega' \boldsymbol{\kappa}'}{\omega - \omega'} \right)^{-\frac{1}{2}} \widehat{\mathcal{K}}_{21}(\omega', \boldsymbol{\kappa}') \widehat{\mathbf{g}}_1(\boldsymbol{\kappa}) \\ &\quad + \frac{1}{\varrho_0} \widehat{\mathbf{g}}_1(\boldsymbol{\kappa}) \cdot \widehat{\mathbf{g}}_1 \left(\frac{\omega \boldsymbol{\kappa} - \omega' \boldsymbol{\kappa}'}{\omega - \omega'} \right) \begin{pmatrix} i\omega' \boldsymbol{\kappa}' \\ 0 \end{pmatrix} + \frac{1}{\varrho_0} \begin{pmatrix} i\omega' \boldsymbol{\kappa}' \\ 0 \end{pmatrix} \cdot \widehat{\mathbf{g}}_1 \left(\frac{\omega \boldsymbol{\kappa} - \omega' \boldsymbol{\kappa}'}{\omega - \omega'} \right) \widehat{\mathbf{g}}_1(\boldsymbol{\kappa}) \\ &\quad + \widehat{\mathbf{g}}_0^-(\boldsymbol{\kappa})^\top \mathbf{K}_0 \widehat{\mathbf{g}}_0^- \left(\frac{\omega \boldsymbol{\kappa} - \omega' \boldsymbol{\kappa}'}{\omega - \omega'} \right) \widehat{\mathbf{k}}_d \left(\omega - \omega', \frac{\omega \boldsymbol{\kappa} - \omega' \boldsymbol{\kappa}'}{\omega - \omega'} \right), \end{aligned} \quad (2.86)$$

$$\begin{aligned} \widehat{\mathbf{d}}(\omega, \boldsymbol{\kappa}, \omega', \boldsymbol{\kappa}') &= \frac{1}{\varrho_0} \widehat{\mathbf{g}}_1(\boldsymbol{\kappa}) \cdot \widehat{\mathbf{g}}_1 \left(\frac{\omega \boldsymbol{\kappa} - \omega' \boldsymbol{\kappa}'}{\omega - \omega'} \right) \begin{pmatrix} \mathbf{0} \\ 1 \end{pmatrix} \\ &\quad + \frac{1}{\varrho_0} \begin{pmatrix} \mathbf{0} \\ 1 \end{pmatrix} \cdot \widehat{\mathbf{g}}_1 \left(\frac{\omega \boldsymbol{\kappa} - \omega' \boldsymbol{\kappa}'}{\omega - \omega'} \right) \widehat{\mathbf{g}}_1(\boldsymbol{\kappa}), \end{aligned} \quad (2.87)$$

respectively, with $\widehat{\mathbf{k}}_d(\omega, \boldsymbol{\kappa}) = i\omega(\boldsymbol{\kappa}, -\zeta(\boldsymbol{\kappa}))$ and:

$$\widehat{\mathbf{g}}_1(\boldsymbol{\kappa}) = \frac{1}{\sqrt{\zeta(\boldsymbol{\kappa})}} \begin{pmatrix} \boldsymbol{\kappa} \\ \beta(\boldsymbol{\kappa}), -\zeta(\boldsymbol{\kappa}) \end{pmatrix}. \quad (2.88)$$

Proof. Gathering the foregoing definitions of Eq. (2.81), Eq. (2.82), and Eq. (2.83) one arrives at:

$$\begin{aligned} \widehat{\mathbf{p}}^{(01)}(\omega, \boldsymbol{\kappa}, z) &= \frac{\varrho_0^2 e^{-i\omega\zeta(\boldsymbol{\kappa})z}}{4(2\pi)^3} \left(\iiint e^{i\omega\sigma(\omega, \boldsymbol{\kappa}, \omega', \boldsymbol{\kappa}')z'} (\widehat{\mathcal{K}}(\omega, \boldsymbol{\kappa}, \omega', \boldsymbol{\kappa}', z') \right. \\ &\quad \left. + \widehat{\mathcal{D}}(\omega, \boldsymbol{\kappa}, \omega', \boldsymbol{\kappa}', z')) \widehat{\mathcal{S}}^- \left(\omega - \omega', \frac{\omega \boldsymbol{\kappa} - \omega' \boldsymbol{\kappa}'}{\omega - \omega'} \right) \omega'^2 d\omega' d\boldsymbol{\kappa}' dz' \right) \widehat{\mathbf{g}}_0^-(\boldsymbol{\kappa}), \end{aligned}$$

where $\widehat{\mathcal{K}}$ and $\widehat{\mathcal{D}}$ are the scalar functions:

$$\begin{aligned} \widehat{\mathcal{K}}(\omega, \boldsymbol{\kappa}, \omega', \boldsymbol{\kappa}', z') &= \widehat{\mathbf{g}}_0^-(\boldsymbol{\kappa})^\top \mathbf{K}_0 \widehat{\mathbf{K}}(\omega, \boldsymbol{\kappa}, \omega', \boldsymbol{\kappa}', z') \widehat{\mathbf{g}}_0^- \left(\frac{\omega \boldsymbol{\kappa} - \omega' \boldsymbol{\kappa}'}{\omega - \omega'} \right), \\ \widehat{\mathcal{D}}(\omega, \boldsymbol{\kappa}, \omega', \boldsymbol{\kappa}', z') &= \widehat{\mathbf{g}}_0^-(\boldsymbol{\kappa})^\top \mathbf{K}_0 \widehat{\mathcal{D}}(\omega, \boldsymbol{\kappa}, \omega', \boldsymbol{\kappa}', z') \widehat{\mathbf{g}}_0^- \left(\frac{\omega \boldsymbol{\kappa} - \omega' \boldsymbol{\kappa}'}{\omega - \omega'} \right), \end{aligned} \quad (2.89)$$

where $\widehat{\mathbf{K}}$ and $\widehat{\mathcal{D}}$ are the 4×4 matrices:

$$\begin{aligned} \widehat{\mathbf{K}}(\omega, \boldsymbol{\kappa}, \omega', \boldsymbol{\kappa}', z') &= \left(\widehat{\mathbf{k}}_d \left(\omega - \omega', \frac{\omega \boldsymbol{\kappa} - \omega' \boldsymbol{\kappa}'}{\omega - \omega'} \right) \cdot \widehat{\mathbf{V}}(\omega', \boldsymbol{\kappa}', z') \right) \mathbf{I}_4 \\ &\quad + \begin{bmatrix} 0 & \mathbf{0} \\ \widehat{\mathcal{K}}_{21}(\omega', \boldsymbol{\kappa}') \widehat{\mathbf{V}}(\omega', \boldsymbol{\kappa}', z') & \widehat{\mathcal{K}}_{22}(\omega', \boldsymbol{\kappa}') \widehat{\mathbf{V}}(\omega', \boldsymbol{\kappa}', z') \end{bmatrix}, \\ \widehat{\mathcal{D}}(\omega, \boldsymbol{\kappa}, \omega', \boldsymbol{\kappa}', z') &= \begin{bmatrix} 0 & \mathbf{0} \\ \mathbf{0} & \widehat{\mathcal{D}}_{22}(\omega', \boldsymbol{\kappa}') \partial_{z'} \widehat{\mathbf{V}}(\omega', \boldsymbol{\kappa}', z') \end{bmatrix}, \end{aligned}$$

with:

$$\begin{aligned} \widehat{\mathcal{K}}_{22}(\omega', \boldsymbol{\kappa}') \widehat{\mathbf{V}}(\omega', \boldsymbol{\kappa}', z') &= \begin{pmatrix} i\omega' \boldsymbol{\kappa}' \\ 0 \end{pmatrix} \cdot \widehat{\mathbf{V}}(\omega', \boldsymbol{\kappa}', z') \mathbf{I}_3 + \widehat{\mathbf{V}}(\omega', \boldsymbol{\kappa}', z') \otimes \begin{pmatrix} i\omega' \boldsymbol{\kappa}' \\ 0 \end{pmatrix}, \\ \widehat{\mathcal{D}}_{22}(\omega', \boldsymbol{\kappa}') \partial_{z'} \widehat{\mathbf{V}}(\omega', \boldsymbol{\kappa}', z') &= \begin{pmatrix} \mathbf{0} \\ 1 \end{pmatrix} \cdot \partial_{z'} \widehat{\mathbf{V}}(\omega', \boldsymbol{\kappa}', z') \mathbf{I}_3 + \partial_{z'} \widehat{\mathbf{V}}(\omega', \boldsymbol{\kappa}', z') \otimes \begin{pmatrix} \mathbf{0} \\ 1 \end{pmatrix}. \end{aligned}$$

But by a straightforward computation:

$$\widehat{\mathcal{K}}(\omega, \boldsymbol{\kappa}, \omega', \boldsymbol{\kappa}', z') = \widehat{\mathbf{k}}(\omega, \boldsymbol{\kappa}, \omega', \boldsymbol{\kappa}') \cdot \widehat{\mathbf{V}}(\omega', \boldsymbol{\kappa}', z')$$

where $\widehat{\mathbf{k}}$ is given by Eq. (2.86). Likewise:

$$\widehat{\mathcal{D}}(\omega, \boldsymbol{\kappa}, \omega', \boldsymbol{\kappa}', z') = \widehat{\mathbf{d}}(\omega, \boldsymbol{\kappa}, \omega', \boldsymbol{\kappa}') \cdot \partial_{z'} \widehat{\mathbf{V}}(\omega', \boldsymbol{\kappa}', z')$$

where $\widehat{\mathbf{d}}$ is given by Eq. (2.87). Integrating by parts in z' one has:

$$\begin{aligned} \int e^{i\omega\sigma(\omega, \boldsymbol{\kappa}, \omega', \boldsymbol{\kappa}')z'} \widehat{\mathcal{D}}(\omega, \boldsymbol{\kappa}, \omega', \boldsymbol{\kappa}', z') dz' &= \\ &= -i\omega\sigma(\omega, \boldsymbol{\kappa}, \omega', \boldsymbol{\kappa}') \int e^{i\omega\sigma(\omega, \boldsymbol{\kappa}, \omega', \boldsymbol{\kappa}')z'} \widehat{\mathbf{d}}(\omega, \boldsymbol{\kappa}, \omega', \boldsymbol{\kappa}') \cdot \widehat{\mathbf{V}}(\omega', \boldsymbol{\kappa}', z') dz', \end{aligned}$$

which, when combined with the foregoing expression of $\widehat{\mathcal{K}}$, gives the claimed result. \square

2.4.2 Computation of the power spectral density

Our aim is to compare the foregoing analytical model with the measurements of [41–43]. Here the experimental results are presented in terms of the PSD or mean-square Fourier transform of the pressure field recorded at the interface of a free shear flow when an acoustic pulse is imposed at its opposite interface; see again Fig. 2.6 and Fig. 2.7. Considering the perturbative model (2.77) elaborated in the previous section, the mean-square Fourier transform of the pressure/momentum fields $\mathbf{p}^{(2)}$ is computed as:

$$\begin{aligned} \mathbb{E} \left\{ \widehat{\mathbf{p}}^{(2)}(\omega_1, \boldsymbol{\kappa}_1, z_1) \otimes \overline{\widehat{\mathbf{p}}^{(2)}(\omega_2, \boldsymbol{\kappa}_2, z_2)} \right\} &= \widehat{\mathbf{p}}^{(0)}(\omega_1, \boldsymbol{\kappa}_1, z_1) \otimes \overline{\widehat{\mathbf{p}}^{(0)}(\omega_2, \boldsymbol{\kappa}_2, z_2)} \\ &+ \varepsilon^2 \widehat{\mathbf{p}}^{(0)}(\omega_1, \boldsymbol{\kappa}_1, z_1) \otimes \mathbb{E} \left\{ \overline{\widehat{\mathbf{p}}^{(02)}(\omega_2, \boldsymbol{\kappa}_2, z_2)} \right\} + \varepsilon^2 \mathbb{E} \left\{ \widehat{\mathbf{p}}^{(02)}(\omega_1, \boldsymbol{\kappa}_1, z_1) \right\} \otimes \overline{\widehat{\mathbf{p}}^{(0)}(\omega_2, \boldsymbol{\kappa}_2, z_2)} \\ &+ \varepsilon^2 \mathbb{E} \left\{ \widehat{\mathbf{p}}^{(01)}(\omega_1, \boldsymbol{\kappa}_1, z_1) \otimes \overline{\widehat{\mathbf{p}}^{(01)}(\omega_2, \boldsymbol{\kappa}_2, z_2)} \right\}, \quad (2.90) \end{aligned}$$

where \bar{Z} stands for the complex conjugate of Z . Indeed, $\mathbf{p}^{(0)}$ is deterministic and $\mathbb{E} \{ \widehat{\mathbf{p}}^{(01)} \} = \mathbf{0}$ because by Prop. 2.4.1 $\mathbf{p}^{(01)}$ is linear with respect to \mathbf{V} , which is such that $\mathbb{E} \{ \mathbf{V} \} = \mathbf{0}$ by Eq. (2.71). Also since $\mathbf{V}(t, \mathbf{x}, z)$ is a mean-square stationary (in both time and space) random vector, the random vector $\mathbf{p}^{(01)}(t, \mathbf{x}, z)$ is also mean-square stationary in both time and space. Its PSD has the form of Eq. (1.50) as a function of the PSD of $\mathbf{V}(t, \mathbf{x}, z)$, and both the PSD of $\mathbf{V}(t, \mathbf{x}, z)$ and $\mathbf{p}^{(01)}(t, \mathbf{x}, z)$ are given in terms of their mean-square Fourier transforms by an expression of the form (1.40); see Sect. 1.2. In this section we specialize these expressions with the model (2.72) for the autocorrelation of $\mathbf{V}(t, \mathbf{x}, z)$.

From now on we assume that the sources $\mathbf{S}(t, \mathbf{x})$ are time-harmonic forcing terms emitting at the frequency ω_0 , which means that:

$$\widehat{\mathbf{S}}(\omega, \boldsymbol{\kappa}) = \widehat{\mathbf{S}}_0(\boldsymbol{\kappa}) \delta(\omega - \omega_0), \quad (2.91)$$

and therefore $\widehat{\mathbf{p}}^{(0)}(\omega, \boldsymbol{\kappa}, z) = \widehat{\mathbf{P}}^{(0)}(\boldsymbol{\kappa}, z) \delta(\omega - \omega_0)$, where $\widehat{\mathbf{P}}^{(0)}$ is deduced straightforwardly from Lemma 2.2.1:

$$\widehat{\mathbf{P}}^{(0)}(\boldsymbol{\kappa}, z) = \frac{1}{2} e^{-i\omega_0 \zeta(\boldsymbol{\kappa})z} \varrho_0 \widehat{\mathbf{g}}_0^-(\boldsymbol{\kappa}) \otimes \widehat{\mathbf{g}}_0^-(\boldsymbol{\kappa}) \widehat{\mathbf{S}}_0(\boldsymbol{\kappa}). \quad (2.92)$$

Consequently, the first, second, and third terms on the right-hand side of Eq. (2.90) are concentrated around the emission peak of the sources at ω_0 in the frequency domain. The spectral broadening effect described in [41–43] should therefore be explained by the last term on the right-hand side of Eq. (2.90). Thus this effect stems from the PSD of $\mathbf{p}^{(01)}$ with the perturbative model (2.77). The subsequent analyses are focused on the computation of this additional contribution, which is denoted by $\widehat{\Psi}^{(01)}(\omega_1, \boldsymbol{\kappa}_1, z_1, \omega_2, \boldsymbol{\kappa}_2, z_2)$ such that:

$$\widehat{\Psi}^{(01)}(\omega_1, \boldsymbol{\kappa}_1, z_1, \omega_2, \boldsymbol{\kappa}_2, z_2) = \mathbb{E} \left\{ \widehat{\mathbf{p}}^{(01)}(\omega_1, \boldsymbol{\kappa}_1, z_1) \otimes \overline{\widehat{\mathbf{p}}^{(01)}(\omega_2, \boldsymbol{\kappa}_2, z_2)} \right\}. \quad (2.93)$$

Also, we carefully isolate the "slow" part of the forcing terms $\widehat{\mathbf{S}}_0(\boldsymbol{\kappa})$, which is denoted by $\widehat{\mathbf{S}}_{0,\text{sl}}(\boldsymbol{\kappa})$, from its "fast" (highly oscillating) part, which is essentially a phase term $\exp(-i\omega_0 \boldsymbol{\kappa} \cdot \mathbf{x}_s)$ where \mathbf{x}_s is the horizontal central position of the sources and ω_0 is the emitting (high) frequency of Eq. (2.91); that is:

$$\widehat{\mathbf{S}}_0(\boldsymbol{\kappa}) = e^{-i\omega_0 \boldsymbol{\kappa} \cdot \mathbf{x}_s} \widehat{\mathbf{S}}_{0,\text{sl}}(\boldsymbol{\kappa}). \quad (2.94)$$

Such an ansatz will prove useful for the application of a stationary-phase argument in the following derivations.

From the result (2.84) of Prop. 2.4.1 one first has:

$$\begin{aligned} \widehat{\Psi}^{(01)}(\omega_1, \boldsymbol{\kappa}_1, z_1, \omega_2, \boldsymbol{\kappa}_2, z_2) &= \frac{\varrho_0^4 e^{-i\omega_1 \zeta(\boldsymbol{\kappa}_1) z_1 + i\omega_2 \zeta(\boldsymbol{\kappa}_2) z_2}}{16(2\pi)^6} \times \\ &\left[\iiint \omega_1'^2 d\omega_1' d\boldsymbol{\kappa}_1' dz_1' \iiint \omega_2'^2 d\omega_2' d\boldsymbol{\kappa}_2' dz_2' e^{i\omega_1 \sigma(\omega_1, \boldsymbol{\kappa}_1, \omega_1', \boldsymbol{\kappa}_1') z_1' - i\omega_2 \sigma(\omega_2, \boldsymbol{\kappa}_2, \omega_2', \boldsymbol{\kappa}_2') z_2'} \right. \\ &\quad \widehat{\mathbf{c}}(\omega_1, \boldsymbol{\kappa}_1, \omega_1', \boldsymbol{\kappa}_1')^\top \mathbb{E} \left\{ \widehat{\mathbf{V}}(\omega_1', \boldsymbol{\kappa}_1', z_1') \otimes \overline{\widehat{\mathbf{V}}(\omega_2', \boldsymbol{\kappa}_2', z_2')} \right\} \overline{\widehat{\mathbf{c}}(\omega_2, \boldsymbol{\kappa}_2, \omega_2', \boldsymbol{\kappa}_2')} \\ &\quad \left. \widehat{\mathcal{S}}^- \left(\omega_1 - \omega_1', \frac{\omega_1 \boldsymbol{\kappa}_1 - \omega_1' \boldsymbol{\kappa}_1'}{\omega_1 - \omega_1'} \right) \widehat{\mathcal{S}}^- \left(\omega_2 - \omega_2', \frac{\omega_2 \boldsymbol{\kappa}_2 - \omega_2' \boldsymbol{\kappa}_2'}{\omega_2 - \omega_2'} \right) \right] \widehat{\mathbf{g}}_0^-(\boldsymbol{\kappa}_1) \otimes \widehat{\mathbf{g}}_0^-(\boldsymbol{\kappa}_2), \quad (2.95) \end{aligned}$$

where the slowness function σ is given by Eq. (2.85). Because the auto-correlation matrix function of \mathbf{V} is given by Eq. (2.72), the covariance matrix of $\widehat{\mathbf{V}}$ reads:

$$\begin{aligned} \mathbb{E} \left\{ \widehat{\mathbf{V}}(\omega_1, \boldsymbol{\kappa}_1, z_1) \otimes \overline{\widehat{\mathbf{V}}(\omega_2, \boldsymbol{\kappa}_2, z_2)} \right\} &= \delta(z_1 - z_2) \frac{\mathbb{1}_{[-L_1, -L_0]}(z_1)}{L_1 - L_0} \\ &\times \iint \mathbf{R}(t_1 - t_2) \delta(\mathbf{x}_1 - \mathbf{x}_2 - (t_1 - t_2) \mathbf{v}_t) e^{i\omega_1(t_1 - \boldsymbol{\kappa}_1 \cdot \mathbf{x}_1) - i\omega_2(t_2 - \boldsymbol{\kappa}_2 \cdot \mathbf{x}_2)} dt_1 dt_2 d\mathbf{x}_1 d\mathbf{x}_2 \end{aligned}$$

which by the changes of variables $\tau = t_1 - t_2$, $t = \frac{1}{2}(t_1 + t_2)$, $\boldsymbol{\rho} = \mathbf{x}_1 - \mathbf{x}_2$, and $\mathbf{x} = \frac{1}{2}(\mathbf{x}_1 + \mathbf{x}_2)$ also reads:

$$\begin{aligned} \mathbb{E} \left\{ \widehat{\mathbf{V}}(\omega_1, \boldsymbol{\kappa}_1, z_1) \otimes \overline{\widehat{\mathbf{V}}(\omega_2, \boldsymbol{\kappa}_2, z_2)} \right\} &= \\ (2\pi)^3 \delta(\omega_1 - \omega_2) \delta(\omega_1 \boldsymbol{\kappa}_1 - \omega_2 \boldsymbol{\kappa}_2) \delta(z_1 - z_2) &\frac{\mathbb{1}_{[-L_1, -L_0]}(z_1)}{L_1 - L_0} \boldsymbol{\Sigma}(\omega_1(1 - \boldsymbol{\kappa}_1 \cdot \mathbf{v}_t)), \quad (2.96) \end{aligned}$$

where:

$$\boldsymbol{\Sigma}(\omega) = \int \mathbf{R}(\tau) e^{i\omega\tau} d\tau. \quad (2.97)$$

Inserting Eq. (2.96) into Eq. (2.95) one arrives at:

$$\begin{aligned} \widehat{\Psi}^{(01)}(\omega_1, \boldsymbol{\kappa}_1, z_1, \omega_2, \boldsymbol{\kappa}_2, z_2) &= \\ \frac{\varrho_0^4}{16(2\pi)^3} e^{-i\omega_1 \zeta(\boldsymbol{\kappa}_1) z_1 + i\omega_2 \zeta(\boldsymbol{\kappa}_2) z_2} \mathcal{I}(\omega_1, \boldsymbol{\kappa}_1, \omega_2, \boldsymbol{\kappa}_2) &\widehat{\mathbf{g}}_0^-(\boldsymbol{\kappa}_1) \otimes \widehat{\mathbf{g}}_0^-(\boldsymbol{\kappa}_2), \quad (2.98) \end{aligned}$$

where \mathcal{I} is given by:

$$\begin{aligned} \mathcal{I}(\omega_1, \boldsymbol{\kappa}_1, \omega_2, \boldsymbol{\kappa}_2) &= \\ \iiint \frac{\mathbb{1}_{[-L_1, -L_0]}(z)}{L_1 - L_0} e^{i\omega_1 \sigma(\omega_1, \boldsymbol{\kappa}_1, \omega, \boldsymbol{\kappa}) z - i\omega_2 \sigma(\omega_2, \boldsymbol{\kappa}_2, \omega, \boldsymbol{\kappa}) z} \mathcal{K}(\omega, \boldsymbol{\kappa}; \omega_1, \boldsymbol{\kappa}_1, \omega_2, \boldsymbol{\kappa}_2) & \\ \times \widehat{\mathcal{S}}^- \left(\omega_1 - \omega, \frac{\omega_1 \boldsymbol{\kappa}_1 - \omega \boldsymbol{\kappa}}{\omega_1 - \omega} \right) \overline{\widehat{\mathcal{S}}^- \left(\omega_2 - \omega, \frac{\omega_2 \boldsymbol{\kappa}_2 - \omega \boldsymbol{\kappa}}{\omega_2 - \omega} \right)} &\omega^2 d\omega d\boldsymbol{\kappa} dz, \end{aligned}$$

with the change of variable $\omega_1' \rightarrow \omega$, $\boldsymbol{\kappa}_1' \rightarrow \boldsymbol{\kappa}$ and \mathcal{K} reads:

$$\mathcal{K}(\omega, \boldsymbol{\kappa}; \omega_1, \boldsymbol{\kappa}_1, \omega_2, \boldsymbol{\kappa}_2) = \widehat{\mathbf{c}}(\omega_1, \boldsymbol{\kappa}_1, \omega, \boldsymbol{\kappa})^\top \boldsymbol{\Sigma}(\omega(1 - \boldsymbol{\kappa} \cdot \mathbf{v}_t)) \overline{\widehat{\mathbf{c}}(\omega_2, \boldsymbol{\kappa}_2, \omega, \boldsymbol{\kappa})}. \quad (2.99)$$

But $\widehat{\mathbf{S}}$ is given by Eq. (2.91), so that letting $L_1 \rightarrow L_0$ yields:

$$\begin{aligned} \mathcal{I}(\omega_1, \boldsymbol{\kappa}_1, \omega_2, \boldsymbol{\kappa}_2) &= \delta(\omega_1 - \omega_2)(\omega_1 - \omega_0)^2 \\ &\times \int e^{-i\omega_1\sigma(\omega_1, \boldsymbol{\kappa}_1, \omega_1 - \omega_0, \boldsymbol{\kappa})L_0 + i\omega_1\sigma(\omega_1, \boldsymbol{\kappa}_2, \omega_1 - \omega_0, \boldsymbol{\kappa})L_0} \mathcal{K}(\omega_1 - \omega_0, \boldsymbol{\kappa}; \omega_1, \boldsymbol{\kappa}_1, \omega_1, \boldsymbol{\kappa}_2) \\ &\times \widehat{\mathcal{S}}_0^- \left(\frac{\omega_1}{\omega_0} \boldsymbol{\kappa}_1 + \left(1 - \frac{\omega_1}{\omega_0}\right) \boldsymbol{\kappa} \right) \overline{\widehat{\mathcal{S}}_0^- \left(\frac{\omega_1}{\omega_0} \boldsymbol{\kappa}_2 + \left(1 - \frac{\omega_1}{\omega_0}\right) \boldsymbol{\kappa} \right)} d\boldsymbol{\kappa}, \end{aligned} \quad (2.100)$$

where $\widehat{\mathcal{S}}_0^-(\boldsymbol{\kappa}) = \widehat{\mathbf{g}}_0^-(\boldsymbol{\kappa}) \cdot \widehat{\mathbf{S}}_0(\boldsymbol{\kappa})$. Lastly, we apply the inverse Fourier transform (2.18) with respect to $\boldsymbol{\kappa}_1$ and $\boldsymbol{\kappa}_2$ to the foregoing result in order to get an expression of the correlation of the transmitted fields at two points (\mathbf{x}_1, z_1) and (\mathbf{x}_2, z_2) . The covariance matrix of $\check{\mathbf{p}}^{(01)}$ (remind the partial Fourier transform of Eq. (2.18)):

$$\boldsymbol{\Psi}^{(01)}(\omega_1, \mathbf{x}_1, z_1, \omega_2, \mathbf{x}_2, z_2) = \mathbb{E} \left\{ \check{\mathbf{p}}^{(01)}(\omega_1, \mathbf{x}_1, z_1) \otimes \overline{\check{\mathbf{p}}^{(01)}(\omega_2, \mathbf{x}_2, z_2)} \right\} \quad (2.101)$$

thus reads:

$$\begin{aligned} \boldsymbol{\Psi}^{(01)}(\omega_1, \mathbf{x}_1, z_1, \omega_2, \mathbf{x}_2, z_2) &= \frac{\varrho_0^4 \omega_1^2 \omega_2^2}{16(2\pi)^7} \times \\ &\iint e^{i\omega_1(\boldsymbol{\kappa}_1 \cdot \mathbf{x}_1 - \zeta(\boldsymbol{\kappa}_1)z_1) - i\omega_2(\boldsymbol{\kappa}_2 \cdot \mathbf{x}_2 - \zeta(\boldsymbol{\kappa}_2)z_2)} \mathcal{I}(\omega_1, \boldsymbol{\kappa}_1, \omega_2, \boldsymbol{\kappa}_2) \widehat{\mathbf{g}}_0^-(\boldsymbol{\kappa}_1) \otimes \widehat{\mathbf{g}}_0^-(\boldsymbol{\kappa}_2) d\boldsymbol{\kappa}_1 d\boldsymbol{\kappa}_2. \end{aligned}$$

Accounting for (2.100) together with the ansatz (2.94) and eventually considering the covariance on the vertical line $\mathbf{x}_1 = \mathbf{x}_2 = \mathbf{0}$ yields:

$$\begin{aligned} \boldsymbol{\Psi}^{(01)}(\omega_1, \mathbf{0}, z_1, \omega_2, \mathbf{0}, z_2) &= \delta(\omega_1 - \omega_2) \frac{\varrho_0^4 (\omega_1 - \omega_0)^2 \omega_1^4}{16(2\pi)^7} \\ &\times \iiint d\boldsymbol{\kappa} d\boldsymbol{\kappa}_1 d\boldsymbol{\kappa}_2 e^{i\omega_0 \phi_0(\boldsymbol{\kappa}, \boldsymbol{\kappa}_1, \boldsymbol{\kappa}_2)} \mathcal{K}(\omega_1 - \omega_0, \boldsymbol{\kappa}; \omega_1, \boldsymbol{\kappa}_1, \omega_1, \boldsymbol{\kappa}_2) \\ &\times \widehat{\mathcal{S}}_{0,\text{sl}}^- \left(\frac{\omega_1}{\omega_0} \boldsymbol{\kappa}_1 + \left(1 - \frac{\omega_1}{\omega_0}\right) \boldsymbol{\kappa} \right) \overline{\widehat{\mathcal{S}}_{0,\text{sl}}^- \left(\frac{\omega_1}{\omega_0} \boldsymbol{\kappa}_2 + \left(1 - \frac{\omega_1}{\omega_0}\right) \boldsymbol{\kappa} \right)} \widehat{\mathbf{g}}_0^-(\boldsymbol{\kappa}_1) \otimes \widehat{\mathbf{g}}_0^-(\boldsymbol{\kappa}_2), \end{aligned} \quad (2.102)$$

where ϕ_0 is the overall phase of the transmitted signals:

$$\begin{aligned} \phi_0(\boldsymbol{\kappa}, \boldsymbol{\kappa}_1, \boldsymbol{\kappa}_2) &= -\frac{\omega_1}{\omega_0}(z_1 + L_0)\zeta(\boldsymbol{\kappa}_1) + \frac{\omega_1}{\omega_0}(z_2 + L_0)\zeta(\boldsymbol{\kappa}_2) - \frac{\omega_1}{\omega_0} \mathbf{x}_s \cdot \boldsymbol{\kappa}_1 + \frac{\omega_1}{\omega_0} \mathbf{x}_s \cdot \boldsymbol{\kappa}_2 \\ &+ L_0 \zeta \left(\frac{\omega_1}{\omega_0} \boldsymbol{\kappa}_1 + \left(1 - \frac{\omega_1}{\omega_0}\right) \boldsymbol{\kappa} \right) - L_0 \zeta \left(\frac{\omega_1}{\omega_0} \boldsymbol{\kappa}_2 + \left(1 - \frac{\omega_1}{\omega_0}\right) \boldsymbol{\kappa} \right), \end{aligned} \quad (2.103)$$

and:

$$\widehat{\mathcal{S}}_{0,\text{sl}}^-(\boldsymbol{\kappa}) = \widehat{\mathbf{g}}_0^-(\boldsymbol{\kappa}) \cdot \widehat{\mathbf{S}}_{0,\text{sl}}(\boldsymbol{\kappa}) \quad (2.104)$$

is the generalized coordinate of the "slow" components of the forcing terms.

In view of Eq. (2.90), the PSD of the ballistic pressure/momentum fields $\mathbf{p}^{(0)}$ is also needed. But these quantities are, again, deterministic and time-harmonic at the frequency ω_0 , so that one simply computes:

$$\begin{aligned} \boldsymbol{\Psi}^{(0)}(\mathbf{0}, z_1, \mathbf{0}, z_2) &= \mathbf{P}^{(0)}(\mathbf{0}, z_1) \otimes \overline{\mathbf{P}^{(0)}(\mathbf{0}, z_2)} \\ &= \frac{\varrho_0^2 \omega_0^4}{4(2\pi)^4} \iint d\boldsymbol{\kappa}_1 d\boldsymbol{\kappa}_2 e^{-i\omega_0[\zeta(\boldsymbol{\kappa}_1)z_1 - \zeta(\boldsymbol{\kappa}_2)z_2 + \boldsymbol{\kappa}_1 \cdot \mathbf{x}_s - \boldsymbol{\kappa}_2 \cdot \mathbf{x}_s]} \\ &\times \widehat{\mathcal{S}}_{0,\text{sl}}^-(\boldsymbol{\kappa}_1) \overline{\widehat{\mathcal{S}}_{0,\text{sl}}^-(\boldsymbol{\kappa}_2)} \widehat{\mathbf{g}}_0^-(\boldsymbol{\kappa}_1) \otimes \widehat{\mathbf{g}}_0^-(\boldsymbol{\kappa}_2), \end{aligned} \quad (2.105)$$

reminding the definition (2.92). We finally invoke a stationary-phase argument to conclude on the derivation of the PSD of the transmitted pressure field, with the foregoing expression of the phase. This last step is detailed in the next section.

2.4.3 Stationary-phase method

In this section we start by considering the case $M = |\mathbf{v}|/c_0 \ll 1$ (Mach number of the ambient flow) and eventually choose $\mathbf{v} \simeq \mathbf{0}$ ($\beta \simeq 1$) to simplify the derivation below. The case $0 < M \ll 1$ will be addressed in subsequent developments. The first goal is to determine the stationary slowness vectors $\boldsymbol{\kappa}_{\text{sp}}$, $\boldsymbol{\kappa}_{1,\text{sp}}$, and $\boldsymbol{\kappa}_{2,\text{sp}}$ such that:

$$\nabla_{\boldsymbol{\kappa}} \phi_0(\boldsymbol{\kappa}_{\text{sp}}, \boldsymbol{\kappa}_{1,\text{sp}}, \boldsymbol{\kappa}_{2,\text{sp}}) = \nabla_{\boldsymbol{\kappa}_1} \phi_0(\boldsymbol{\kappa}_{\text{sp}}, \boldsymbol{\kappa}_{1,\text{sp}}, \boldsymbol{\kappa}_{2,\text{sp}}) = \nabla_{\boldsymbol{\kappa}_2} \phi_0(\boldsymbol{\kappa}_{\text{sp}}, \boldsymbol{\kappa}_{1,\text{sp}}, \boldsymbol{\kappa}_{2,\text{sp}}) = \mathbf{0}.$$

Lemma 2.4.1. *In the instance that ω_1 and ω_2 are equal to ω_0 at the first order, namely $1 - \frac{\omega_1}{\omega_0} = o(1)$ and $1 - \frac{\omega_2}{\omega_0} = o(1)$, one has:*

$$\begin{aligned} \boldsymbol{\kappa}_{1,\text{sp}} &\simeq \zeta(\boldsymbol{\kappa}_{1,\text{sp}}) \frac{\mathbf{x}_s}{z_1} = \frac{\mathbf{x}_s}{c_0 \sqrt{|\mathbf{x}_s|^2 + z_1^2}}, \\ \boldsymbol{\kappa}_{2,\text{sp}} &\simeq \zeta(\boldsymbol{\kappa}_{2,\text{sp}}) \frac{\mathbf{x}_s}{z_2} = \frac{\mathbf{x}_s}{c_0 \sqrt{|\mathbf{x}_s|^2 + z_2^2}}. \end{aligned} \quad (2.106)$$

Proof. $\zeta(\boldsymbol{\kappa})$ is given by Eq. (2.26) with $\beta(\boldsymbol{\kappa}) = 1$, therefore $\nabla_{\boldsymbol{\kappa}} \zeta(\boldsymbol{\kappa}) = -\boldsymbol{\kappa}/\zeta(\boldsymbol{\kappa})$. Thus:

$$\begin{aligned} \nabla_{\boldsymbol{\kappa}_1} \phi_0(\boldsymbol{\kappa}, \boldsymbol{\kappa}_1, \boldsymbol{\kappa}_2) &= + \frac{\omega_1}{\omega_0} \left[(z_1 + L_0) \frac{\boldsymbol{\kappa}_1}{\zeta(\boldsymbol{\kappa}_1)} - \mathbf{x}_s \right] - L_0 \frac{\frac{\omega_1}{\omega_0} \boldsymbol{\kappa}_1 + \left(1 - \frac{\omega_1}{\omega_0}\right) \boldsymbol{\kappa}}{\zeta\left(\frac{\omega_1}{\omega_0} \boldsymbol{\kappa}_1 + \left(1 - \frac{\omega_1}{\omega_0}\right) \boldsymbol{\kappa}\right)}, \\ \nabla_{\boldsymbol{\kappa}_2} \phi_0(\boldsymbol{\kappa}, \boldsymbol{\kappa}_1, \boldsymbol{\kappa}_2) &= - \frac{\omega_1}{\omega_0} \left[(z_2 + L_0) \frac{\boldsymbol{\kappa}_2}{\zeta(\boldsymbol{\kappa}_2)} - \mathbf{x}_s \right] + L_0 \frac{\frac{\omega_1}{\omega_0} \boldsymbol{\kappa}_2 + \left(1 - \frac{\omega_1}{\omega_0}\right) \boldsymbol{\kappa}}{\zeta\left(\frac{\omega_1}{\omega_0} \boldsymbol{\kappa}_2 + \left(1 - \frac{\omega_1}{\omega_0}\right) \boldsymbol{\kappa}\right)}, \\ \nabla_{\boldsymbol{\kappa}} \phi_0(\boldsymbol{\kappa}, \boldsymbol{\kappa}_1, \boldsymbol{\kappa}_2) &= - \left(1 - \frac{\omega_1}{\omega_0}\right) L_0 \frac{\frac{\omega_1}{\omega_0} \boldsymbol{\kappa}_1 + \left(1 - \frac{\omega_1}{\omega_0}\right) \boldsymbol{\kappa}}{\zeta\left(\frac{\omega_1}{\omega_0} \boldsymbol{\kappa}_1 + \left(1 - \frac{\omega_1}{\omega_0}\right) \boldsymbol{\kappa}\right)} \\ &\quad + \left(1 - \frac{\omega_1}{\omega_0}\right) L_0 \frac{\frac{\omega_1}{\omega_0} \boldsymbol{\kappa}_2 + \left(1 - \frac{\omega_1}{\omega_0}\right) \boldsymbol{\kappa}}{\zeta\left(\frac{\omega_1}{\omega_0} \boldsymbol{\kappa}_2 + \left(1 - \frac{\omega_1}{\omega_0}\right) \boldsymbol{\kappa}\right)}. \end{aligned} \quad (2.107)$$

Then for $\frac{\omega_1}{\omega_0} = O(1)$ one obtains the claimed result. \square

We subsequently apply the stationary-phase theorem to Eq. (2.102) to obtain the final expression of the PSD of the scattered transmitted pressure field given in Prop. 2.4.2 below.

Proposition 2.4.2. *Let $d = (|\mathbf{x}_s|^2 + z^2)^{\frac{1}{2}}$ be the distance from the time-harmonic sound source (2.91) at $(\mathbf{x}_s, 0^+)$ (with $\widehat{\mathbf{S}}_0 = (\widehat{H}_0, \widehat{\mathbf{F}}_{0\mathbf{x}}, \widehat{F}_{0z})$) to the observation point $(\mathbf{0}, z)$ at the depth z on the outer side of the flow. Then the ballistic transmitted pressure field $p^{(0)} = K_0 q^{(0)}$ has the form*

$$\overline{p^{(0)}(\omega, \mathbf{0}, z) \overline{p^{(0)}(\omega', \mathbf{0}, z)}} = \delta(\omega - \omega_0) \delta(\omega' - \omega_0) \Psi_0(\mathbf{x}_s, z, \omega_0) \quad (2.108)$$

with:

$$\Psi_0(\mathbf{x}_s, z, \omega_0) = \frac{\varrho_0^2 \omega_0^2}{4(2\pi)^2 c_0^2 d^4} \left| \frac{d}{\varrho_0 c_0} \widehat{H}_0 \left(\frac{\mathbf{x}_s}{c_0 d} \right) + \mathbf{x}_s \cdot \widehat{\mathbf{F}}_{0\mathbf{x}} \left(\frac{\mathbf{x}_s}{c_0 d} \right) - z \widehat{F}_{0z} \left(\frac{\mathbf{x}_s}{c_0 d} \right) \right|^2, \quad (2.109)$$

and for $1 - \frac{\omega}{\omega_0} = o(1)$ the mean-square Fourier transform of the scattered transmitted pressure field $p'^{(01)} = K_0 q^{(01)}$ reads:

$$\mathbb{E} \left\{ \check{p}'^{(01)}(\omega, \mathbf{0}, z) \overline{\check{p}'^{(01)}(\omega', \mathbf{0}, z)} \right\} = \delta(\omega - \omega') \Psi_{01}(\mathbf{x}_s, z, \omega_0, \omega) \quad (2.110)$$

where:

$$\Psi_{01}(\mathbf{x}_s, z, \omega_0, \omega) = \frac{\varrho_0^2 \omega_0^2}{4(2\pi)^3} \left(1 - \frac{\omega}{\omega_0} \right)^2 \left(\frac{\omega}{\omega_0} \right)^4 \Psi_1(\mathbf{x}_s, z, \omega, \omega_0) \Psi_0(\mathbf{x}_s, z, \omega_0), \quad (2.111)$$

and $\Psi_1(\mathbf{x}_s, z, \omega, \omega_0)$ is a filtered frequency spectrum responsible for the spectral broadening of the source centered about ω_0 given by:

$$\Psi_1(\mathbf{x}_s, z, \omega, \omega_0) = \int_{|\boldsymbol{\kappa}| \leq \frac{1}{c_0}} \mathcal{K} \left(\omega - \omega_0, \boldsymbol{\kappa}; \omega, \frac{\mathbf{x}_s}{c_0 d}, \omega, \frac{\mathbf{x}_s}{c_0 d} \right) d\boldsymbol{\kappa}, \quad (2.112)$$

where \mathcal{K} is defined by (2.99).

Proof. Expanding the phase (2.103) in a Taylor series about the small increment $\omega_0 - \omega_1$ yields:

$$\begin{aligned} \phi_0(\boldsymbol{\kappa}, \boldsymbol{\kappa}_1, \boldsymbol{\kappa}_2) &\simeq -\frac{\omega_1}{\omega_0} (L_0 + z_1) \zeta(\boldsymbol{\kappa}_1) + \frac{\omega_1}{\omega_0} (L_0 + z_2) \zeta(\boldsymbol{\kappa}_2) - \frac{\omega_1}{\omega_0} (\boldsymbol{\kappa}_1 - \boldsymbol{\kappa}_2) \cdot \mathbf{x}_s \\ &+ L_0 \zeta(\boldsymbol{\kappa}_1) + \left(1 - \frac{\omega_1}{\omega_0} \right) L_0 \boldsymbol{\kappa} \cdot \nabla_{\boldsymbol{\kappa}} \zeta(\boldsymbol{\kappa}_1) - L_0 \zeta(\boldsymbol{\kappa}_2) - \left(1 - \frac{\omega_1}{\omega_0} \right) L_0 \boldsymbol{\kappa} \cdot \nabla_{\boldsymbol{\kappa}} \zeta(\boldsymbol{\kappa}_2). \end{aligned}$$

We can thus identify the slow part of the phase ϕ_{sl} from its fast part ϕ_f proportional to ω_1/ω_0 as follows:

$$\begin{aligned} \phi_f(\boldsymbol{\kappa}_1, \boldsymbol{\kappa}_2) &= -\zeta(\boldsymbol{\kappa}_1) z_1 + \zeta(\boldsymbol{\kappa}_2) z_2 - (\boldsymbol{\kappa}_1 - \boldsymbol{\kappa}_2) \cdot \mathbf{x}_s, \\ \phi_{sl}(\boldsymbol{\kappa}, \boldsymbol{\kappa}_1, \boldsymbol{\kappa}_2) &= + \left(1 - \frac{\omega_1}{\omega_0} \right) \left((L_0 + z_1) \zeta(\boldsymbol{\kappa}_1) + L_0 \boldsymbol{\kappa} \cdot \nabla_{\boldsymbol{\kappa}} \zeta(\boldsymbol{\kappa}_1) + \boldsymbol{\kappa}_1 \cdot \mathbf{x}_s \right) \\ &\quad - \left(1 - \frac{\omega_1}{\omega_0} \right) \left((L_0 + z_2) \zeta(\boldsymbol{\kappa}_2) + L_0 \boldsymbol{\kappa} \cdot \nabla_{\boldsymbol{\kappa}} \zeta(\boldsymbol{\kappa}_2) + \boldsymbol{\kappa}_2 \cdot \mathbf{x}_s \right). \end{aligned} \quad (2.113)$$

Applying the stationary-phase theorem in dimension $n = 4$ (see for example [72, Eq. (14.77)]) to the auto-spectrum (2.102) of the first-order perturbations of the transmitted pressure/momentum fields yields:

$$\begin{aligned} \Psi^{(01)}(\omega_1, \mathbf{0}, z_1, \omega_2, \mathbf{0}, z_2) &= \delta(\omega_1 - \omega_2) \frac{\varrho_0^4 (\omega_1 - \omega_0)^2 \omega_1^4}{16\omega_0^2 (2\pi)^5} \frac{e^{i(n^*-2)\frac{\pi}{2}} e^{i\omega_0 \phi_f(\boldsymbol{\kappa}_{1,sp}, \boldsymbol{\kappa}_{2,sp})}}{\sqrt{|\det \mathbf{H}_{\boldsymbol{\kappa}_1, \boldsymbol{\kappa}_2} \phi_f(\boldsymbol{\kappa}_{1,sp}, \boldsymbol{\kappa}_{2,sp})|}} \\ &\quad \times \int e^{i\omega_0 \phi_{sl}(\boldsymbol{\kappa}, \boldsymbol{\kappa}_{1,sp}, \boldsymbol{\kappa}_{2,sp})} \mathcal{K}(\omega_1 - \omega_0, \boldsymbol{\kappa}; \omega_1, \boldsymbol{\kappa}_{1,sp}, \omega_1, \boldsymbol{\kappa}_{2,sp}) d\boldsymbol{\kappa} \\ &\quad \times \widehat{\mathcal{S}}_{0,sl}^-(\boldsymbol{\kappa}_{1,sp}) \overline{\widehat{\mathcal{S}}_{0,sl}^-(\boldsymbol{\kappa}_{2,sp})} \widehat{\mathbf{g}}_0^-(\boldsymbol{\kappa}_{1,sp}) \otimes \widehat{\mathbf{g}}_0^-(\boldsymbol{\kappa}_{2,sp}), \end{aligned}$$

where n^* is the number of positive eigenvalues of the Hessian $\mathbf{H}_{\boldsymbol{\kappa}_1, \boldsymbol{\kappa}_2} \phi_f(\boldsymbol{\kappa}_{1, \text{sp}}, \boldsymbol{\kappa}_{2, \text{sp}})$. The latter is block-diagonal owing to Eq. (2.107) and reads:

$$\mathbf{H}_{\boldsymbol{\kappa}_1, \boldsymbol{\kappa}_2} \phi_f(\boldsymbol{\kappa}_1, \boldsymbol{\kappa}_2) = \begin{bmatrix} \frac{z_1}{\zeta(\boldsymbol{\kappa}_1)} \left(\mathbf{I}_2 + \frac{\boldsymbol{\kappa}_1 \otimes \boldsymbol{\kappa}_1}{\zeta(\boldsymbol{\kappa}_1)^2} \right) & \mathbf{0} \\ \mathbf{0} & -\frac{z_2}{\zeta(\boldsymbol{\kappa}_2)} \left(\mathbf{I}_2 + \frac{\boldsymbol{\kappa}_2 \otimes \boldsymbol{\kappa}_2}{\zeta(\boldsymbol{\kappa}_2)^2} \right) \end{bmatrix},$$

such that:

$$\det \mathbf{H}_{\boldsymbol{\kappa}_1, \boldsymbol{\kappa}_2} \phi_f(\boldsymbol{\kappa}_1, \boldsymbol{\kappa}_2) = \left(\frac{z_1 z_2}{\zeta(\boldsymbol{\kappa}_1) \zeta(\boldsymbol{\kappa}_2)} \right)^2 \left(1 + \frac{|\boldsymbol{\kappa}_1|^2}{\zeta(\boldsymbol{\kappa}_1)^2} \right) \left(1 + \frac{|\boldsymbol{\kappa}_2|^2}{\zeta(\boldsymbol{\kappa}_2)^2} \right).$$

From this we can deduce that the eigenvalues of $\mathbf{H}_{\boldsymbol{\kappa}_1, \boldsymbol{\kappa}_2} \phi_f(\boldsymbol{\kappa}_1, \boldsymbol{\kappa}_2)$ are:

$$\begin{aligned} \lambda_1 &= \frac{z_1}{\zeta(\boldsymbol{\kappa}_1)}, & \lambda_2 &= \frac{z_1}{\zeta(\boldsymbol{\kappa}_1)} \left(1 + \frac{|\boldsymbol{\kappa}_1|^2}{\zeta(\boldsymbol{\kappa}_1)^2} \right), \\ \lambda_3 &= -\frac{z_2}{\zeta(\boldsymbol{\kappa}_2)}, & \lambda_4 &= -\frac{z_2}{\zeta(\boldsymbol{\kappa}_2)} \left(1 + \frac{|\boldsymbol{\kappa}_2|^2}{\zeta(\boldsymbol{\kappa}_2)^2} \right), \end{aligned}$$

and therefore $n^* = 2$. Besides:

$$\sqrt{|\det \mathbf{H}_{\boldsymbol{\kappa}_1, \boldsymbol{\kappa}_2} \phi_f(\boldsymbol{\kappa}_{1, \text{sp}}, \boldsymbol{\kappa}_{2, \text{sp}})|} = \frac{c_0^2 d_1^2 d_2^2}{z_1 z_2}$$

introducing $d_1 = (|\mathbf{x}_s|^2 + z_1^2)^{\frac{1}{2}}$ and $d_2 = (|\mathbf{x}_s|^2 + z_2^2)^{\frac{1}{2}}$, and:

$$\phi_f(\boldsymbol{\kappa}_{1, \text{sp}}, \boldsymbol{\kappa}_{2, \text{sp}}) = \frac{d_2 - d_1}{c_0}.$$

Indeed, owing to Lemma 2.106 one also has:

$$\zeta(\boldsymbol{\kappa}_{1, \text{sp}}) = \frac{z_1}{c_0 d_1}, \quad \zeta(\boldsymbol{\kappa}_{2, \text{sp}}) = \frac{z_2}{c_0 d_2}. \quad (2.114)$$

We can finally compute the mean-square Fourier transform of the first-order transmitted pressure field $p^{(01)} = K_0 q^{(01)}$ as the upper-left term of $\boldsymbol{\Psi}^{(01)}(\omega_1, \mathbf{0}, z_1, \omega_2, \mathbf{0}, z_2)$, and that of the ballistic transmitted pressure field $p^{(0)} = K_0 q^{(0)}$ as the upper-left term of $\boldsymbol{\Psi}^{(0)}(\mathbf{0}, z_1, \mathbf{0}, z_2)$. Using Eq. (2.39) with $\beta(\boldsymbol{\kappa}) = 1$ and Eq. (2.41) with the definition (2.94), we have:

$$\widehat{\mathcal{S}}_{0, \text{sl}}^-(\boldsymbol{\kappa}_{1, \text{sp}}) = e^{i \frac{\omega_0}{c_0} \frac{|\mathbf{x}_s|^2}{d_1}} \widehat{\mathbf{g}}_0^-(\boldsymbol{\kappa}_{1, \text{sp}}) \cdot \widehat{\mathbf{S}}_0^-(\boldsymbol{\kappa}_{1, \text{sp}})$$

with a similar expression for $\widehat{\mathcal{S}}_{0, \text{sl}}^-(\boldsymbol{\kappa}_{2, \text{sp}})$; see Eq. (2.104). We end up with:

$$\begin{aligned} \check{p}^{(0)}(\omega, \mathbf{0}, z_1) \overline{\check{p}^{(0)}(\omega', \mathbf{0}, z_2)} &= \delta(\omega - \omega_0) \delta(\omega' - \omega_0) \frac{e^{i \frac{\omega_0}{c_0} (\frac{z_2^2}{d_2} - \frac{z_1^2}{d_1})}}{4(2\pi)^2} \frac{\varrho_0^2 \omega_0^2}{d_1 d_2} \\ &\quad \times \varphi \left(\frac{\mathbf{x}_s}{c_0 d_1}, \frac{z_1}{c_0 d_1} \right) \overline{\varphi \left(\frac{\mathbf{x}_s}{c_0 d_2}, \frac{z_2}{c_0 d_2} \right)}, \end{aligned}$$

and:

$$\begin{aligned} \mathbb{E} \left\{ \check{p}^{(01)}(\omega_1, \mathbf{0}, z_1) \overline{\check{p}^{(01)}(\omega_2, \mathbf{0}, z_2)} \right\} &= \delta(\omega_1 - \omega_2) \frac{e^{i \frac{\omega_0}{c_0} (\frac{z_2^2}{d_2} - \frac{z_1^2}{d_1})}}{16(2\pi)^5} \frac{\varrho_0^4 \omega_0^4}{d_1 d_2} \\ &\quad \times \left(1 - \frac{\omega_1}{\omega_0} \right)^2 \left(\frac{\omega_1}{\omega_0} \right)^4 \Psi(\mathbf{x}_s, z_1, z_2, \omega_1, \omega_0) \varphi \left(\frac{\mathbf{x}_s}{c_0 d_1}, \frac{z_1}{c_0 d_1} \right) \overline{\varphi \left(\frac{\mathbf{x}_s}{c_0 d_2}, \frac{z_2}{c_0 d_2} \right)}, \end{aligned}$$

where:

$$\Psi(\mathbf{x}_s, z_1, z_2, \omega, \omega_0) = \int_{|\boldsymbol{\kappa}| \leq \frac{1}{c_0}} e^{i\omega_0 \phi_{\text{sl}}(\boldsymbol{\kappa}, \boldsymbol{\kappa}_{1,\text{sp}}, \boldsymbol{\kappa}_{2,\text{sp}})} \mathcal{H}(\omega - \omega_0, \boldsymbol{\kappa}; \omega, \boldsymbol{\kappa}_{1,\text{sp}}, \omega, \boldsymbol{\kappa}_{2,\text{sp}}) d\boldsymbol{\kappa}, \quad (2.115)$$

and, for $\widehat{\mathbf{S}}_0 = (\widehat{H}_0, \widehat{\mathbf{F}}_{0\mathbf{x}}, \widehat{F}_{0z})$:

$$\varphi(\boldsymbol{\kappa}, \zeta) = \frac{1}{K_0} \widehat{H}_0(\boldsymbol{\kappa}) + \boldsymbol{\kappa} \cdot \widehat{\mathbf{F}}_{0\mathbf{x}}(\boldsymbol{\kappa}) - \zeta \widehat{F}_{0z}(\boldsymbol{\kappa}).$$

We thus define:

$$\Psi_0(\mathbf{x}_s, z, \omega_0) = \frac{\varrho_0^2 \omega_0^2}{4(2\pi)^2 d^2} \left| \varphi\left(\frac{\mathbf{x}_s}{c_0 d}, \frac{z}{c_0 d}\right) \right|^2$$

for $d = (|\mathbf{x}_s|^2 + z^2)^{\frac{1}{2}}$, and:

$$\Psi_1(\mathbf{x}_s, z, \omega_1, \omega_0) = \Psi(\mathbf{x}_s, z, z, \omega_1, \omega_0) = \int_{|\boldsymbol{\kappa}| \leq \frac{1}{c_0}} \mathcal{H}(\omega_1 - \omega_0, \boldsymbol{\kappa}; \omega_1, \boldsymbol{\kappa}_{1,\text{sp}}, \omega_1, \boldsymbol{\kappa}_{1,\text{sp}}) d\boldsymbol{\kappa}, \quad (2.116)$$

then we obtain the claimed formulas (2.109) and (2.111). \square

It remains to compute the integral (2.115):

$$\Psi(\mathbf{x}_s, z_1, z_2, \omega, \omega_0) = \int_{|\boldsymbol{\kappa}| \leq \frac{1}{c_0}} e^{i\omega_0 \phi_{\text{sl}}(\boldsymbol{\kappa}, \boldsymbol{\kappa}_{1,\text{sp}}, \boldsymbol{\kappa}_{2,\text{sp}})} \mathcal{H}(\omega - \omega_0, \boldsymbol{\kappa}; \omega, \boldsymbol{\kappa}_{1,\text{sp}}, \omega, \boldsymbol{\kappa}_{2,\text{sp}}) d\boldsymbol{\kappa},$$

pertaining to the propagating waves such that $\zeta(\boldsymbol{\kappa})$ is real, reminding that $\boldsymbol{\kappa}_{j,\text{sp}} = \frac{\mathbf{x}_s}{c_0 d_j}$, $j = 1, 2$. This computation is done numerically, observing first that the slow phase is such that:

$$\phi_{\text{sl}}(\boldsymbol{\kappa}, \boldsymbol{\kappa}_{1,\text{sp}}, \boldsymbol{\kappa}_{2,\text{sp}}) = \left(1 - \frac{\omega_1}{\omega_0}\right) \left[\frac{L_0}{c_0} \left(\frac{z_1}{d_1} - \frac{z_2}{d_2}\right) + \frac{d_1 - d_2}{c_0} - \left(\frac{L_0}{z_1} - \frac{L_0}{z_2}\right) \boldsymbol{\kappa} \cdot \mathbf{x}_s \right]. \quad (2.117)$$

We thus have $\phi_{\text{sl}}(\boldsymbol{\kappa}, \boldsymbol{\kappa}_{1,\text{sp}}, \boldsymbol{\kappa}_{2,\text{sp}}) = 0$ for the auto-spectrum for which $z_1 = z_2$ and $d_1 = d_2$. Also assuming that $\mathbf{R}(\tau)$ is diagonal, namely $\mathbf{R}(\tau) = R(\tau)\mathbf{I}_3$, one has:

$$\begin{aligned} \mathcal{H}(\omega - \omega_0, \boldsymbol{\kappa}; \omega, \boldsymbol{\kappa}_{1,\text{sp}}, \omega, \boldsymbol{\kappa}_{2,\text{sp}}) = \\ \Sigma((\omega - \omega_0)(1 - \mathbf{v}_t \cdot \boldsymbol{\kappa})) \widehat{\mathbf{c}}(\omega, \boldsymbol{\kappa}_{1,\text{sp}}, \omega - \omega_0, \boldsymbol{\kappa}) \cdot \overline{\widehat{\mathbf{c}}(\omega, \boldsymbol{\kappa}_{2,\text{sp}}, \omega - \omega_0, \boldsymbol{\kappa})}. \end{aligned}$$

Corollary 2.4.1. *Assume that the time-autocorrelation function $\tau \mapsto R(\tau)\mathbf{I}_3$ of \mathbf{V} in Eq. (2.72) is diagonal, and let $\Sigma(\omega) = \int R(\tau) e^{i\omega\tau} d\tau$. Then the mean-square Fourier transform of the scattered transmitted pressure field $p^{(01)}$ is:*

$$\begin{aligned} \Psi_{01}(\mathbf{x}_s, z, \omega_0, \omega) = \frac{\varrho_0^2}{4(2\pi)^3} (\omega - \omega_0)^2 \left(\frac{\omega}{\omega_0}\right)^4 \Psi_0(\mathbf{x}_s, z, \omega_0) \\ \times \int_{|\boldsymbol{\kappa}| \leq \frac{1}{c_0}} \Sigma((\omega - \omega_0)(1 - \mathbf{v}_t \cdot \boldsymbol{\kappa})) \left| \widehat{\mathbf{c}}\left(\omega, \frac{\mathbf{x}_s}{c_0 d}, \omega - \omega_0, \boldsymbol{\kappa}\right) \right|^2 d\boldsymbol{\kappa}, \quad (2.118) \end{aligned}$$

where $\widehat{\mathbf{c}}$ is given in Prop. 2.4.1 and d in Prop. 2.4.2.

These results are illustrated in the next section for a correlation function and parameters adapted from the experiments in [41] and analytical models in [104].

2.4.4 Numerical example

At first, we choose a Gaussian model for the autocorrelation function $\tau \mapsto R(\tau)$ of Eq. (2.72):

$$R(\tau) = \sigma_V^2 \exp\left(-\pi \frac{\tau^2}{4\tau_s^2}\right). \quad (2.119)$$

Here τ_s is the correlation time, or the turbulence integral timescale in the dedicated literature, *i.e.* the typical time scale of a realization of the turbulent velocity fluctuations \mathbf{V} such that $\int_0^{+\infty} \frac{R(\tau)}{R(0)} d\tau = \tau_s$; and σ_V quantifies their standard deviation. Then from Eq. (2.97):

$$\Sigma(\omega) = 2\tau_s \sigma_V^2 \exp\left(-\frac{1}{\pi} \tau_s^2 \omega^2\right). \quad (2.120)$$

In view of Eq. (2.72) and Eq. (2.70), the variance σ_V^2 scales as a squared velocity—typically $|\mathbf{u}|^2$ the squared mean jet velocity. In order to compare our results of Prop. 2.4.2 with the experimental results in [41] and the analytical models in *e.g.* [104, 112], we plot on Fig. 2.8 and Fig. 2.9 the normalized "power spectrum" $\Psi_2(\mathbf{x}_s, z, \omega_0, \omega)$ of the transmitted pressure field defined by:

$$\Psi_2(\mathbf{x}_s, z, \omega_0, \omega) = \delta(\omega - \omega_0) + \frac{\varepsilon^2 \varrho_0^2}{4(2\pi)^3} (\omega - \omega_0)^2 \left(\frac{\omega}{\omega_0}\right)^2 \Psi_1(\mathbf{x}_s, z, \omega_0, \omega) \quad (2.121)$$

in dB ($\Psi_2^{\text{dB}} = 10 \log_{10} \Psi_2$) for the data provided in [102, 104]: $L = 0.1$ m for the thickness of the turbulent shear layer at a distance $D = 0.5$ m from the jet in the experiments of Candel *et al.* [41], $\tau_s = L/|\mathbf{v}_t|$, $\varepsilon = 12\%$ for the turbulence intensity, $|\mathbf{v}_t| = 0.5|\mathbf{u}|$ for the velocity of the turbulent eddies, and $c_0 = 340$ m/s and $\varrho_0 = 1.2$ kg/m³ for the ambient flow characteristics. More particularly, Fig. 2.8 shows $\Psi_2(\mathbf{0}, -L, \omega_0, \omega)$ as a function of $\Delta\omega = \omega - \omega_0$ for various tone frequencies $f_0 = \frac{\omega_0}{2\pi}$ in the range [6–20] kHz and the jet velocity $U_J = |\mathbf{u}| = 60$ m/s, and Fig. 2.9 shows $\Psi_2(\mathbf{0}, -L, \omega_0, \omega)$ as a function of $\Delta\omega$ for various jet velocity U_J in the range [20–60] m/s and $f_0 = 20$ kHz. The two lobes are well recovered, together with their position on the frequency axis which has been observed to be independent of the tone frequency f_0 . Indeed, from the expression of $\Psi_{01}(\mathbf{x}_s, z, \omega_0, \omega)$ in Prop. 2.4.2 the maxima of the lobes are approximately found as the maxima of $\Delta\omega^2 \exp(-\frac{1}{\pi} \tau_s^2 \Delta\omega^2 (1 - M_t)^2)$ which yields:

$$|\Delta\omega_{\max}| \simeq \sqrt{\pi} \frac{c_0}{L} M_t,$$

where $M_t = |\mathbf{v}_t|/c_0 \ll 1$ is the (small) Mach number for the turbulent eddies. This estimate is in good agreement with [16, 41–43, 55, 102, 112, 118]. Despite several simplifications, the proposed model allows to recover the main trends of the power spectrum of the transmitted pressure field already outlined in those previous works, namely:

- a linear growth in the position of the maximum of the lobes as a function of the velocity of the turbulent eddies M_t . Also the width of the lobes and thus the amount of scattered energy increases as well when M_t increases;
- energetic macro-eddies contribute to the largest part of the scattered pressure field. Spectral broadening is related to a Doppler shift due to the motion of these large structures which act as secondary sources for the scattered field.

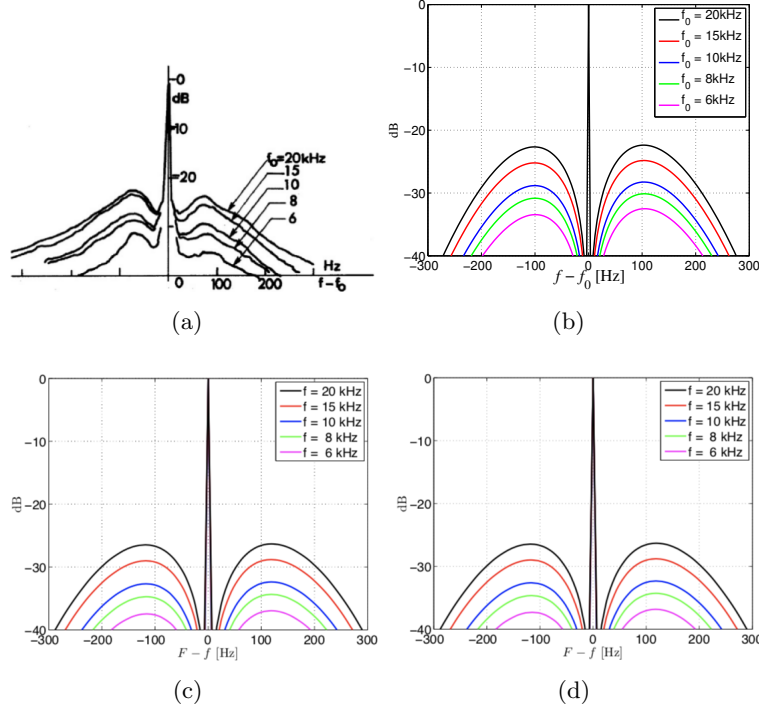


Figure 2.8 – Normalized power spectrum of the transmitted pressure field as a function of the frequency gap $f - f_0$ for various tone frequencies f_0 in the range $[6-20]$ kHz and jet velocity $U_J = |\underline{v}| = 60$ m/s: (a) experimental observations from [41]; (b) the results of Prop. 2.4.2; (c) the model of [104] for a Gaussian homogeneous axisymmetric turbulence (HAT) correlation function of the fluctuations of the ambient flow velocity; (d) the model of [104] for a Gaussian homogeneous isotropic turbulence (HIT) correlation function of the fluctuations of the ambient flow velocity. Note that in [104] the notations $\omega = 2\pi F$ and $\omega_0 = 2\pi f$ are rather used.

2.5 Conclusion

In this chapter we have first developed an analytical model of the pressure field transmitted by a plane shear layer (stratified flow) with uniform velocity and random bulk modulus (compressibility) when a point source acts above it. The analysis starts from the linearized Euler’s equations for a uniform ambient flow, for which the associated Green’s function is derived. Considering random perturbations of the bulk modulus of the ambient flow and a diffusion scaling, the transmission coefficient of the plane shear layer is constructed explicitly as the solution of an Itô stochastic differential equation. This allows to construct an integral representation of the transmitted pressure field, which exhibits the phenomenon of stabilization of the front already outlined in [72] for quiescent layered media (see also Sect. 1.3.3). This model is not able to predict the spectral broadening effect depicted in Chapter 1, though, and an alternative model had to be considered in this respect.

Consequently, we have developed an analytical model of the power spectrum of the acoustic waves transmitted by a plane turbulent shear layer of which ambient velocity is randomly perturbed by weak spatial and temporal fluctuations, when a time-harmonic

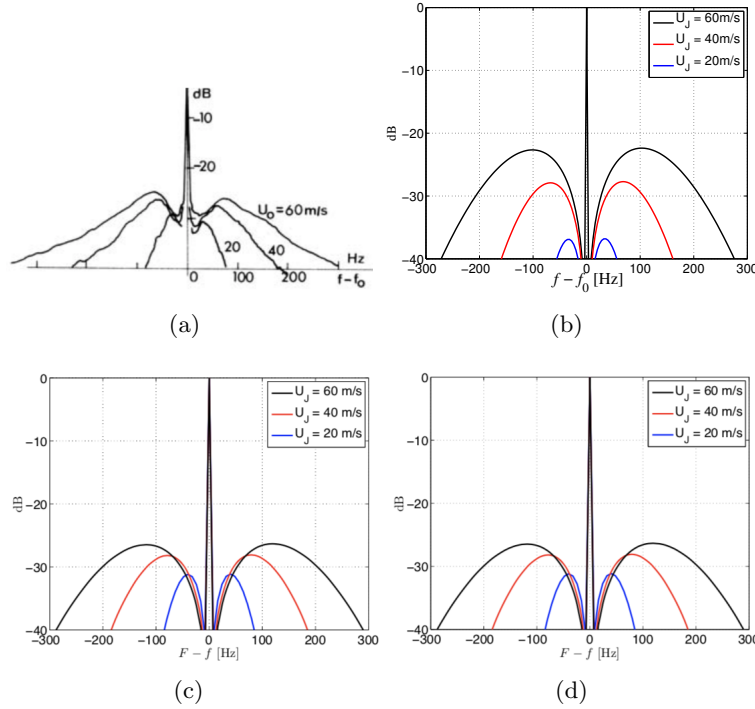


Figure 2.9 – Normalized power spectrum of the transmitted pressure field as a function of the frequency gap $f - f_0$ for various jet velocities $U_J = |\underline{v}|$ in the range $[20-60]$ m/s and tone frequency $f_0 = 20$ kHz: (a) experimental observations from [41]; (b) the results of Prop. 2.4.2; (c) the model of [104] for a Gaussian homogeneous axisymmetric turbulence (HAT) correlation function of the fluctuations of the ambient flow velocity; (d) the model of [104] for a Gaussian homogeneous isotropic turbulence (HIT) correlation function of the fluctuations of the ambient flow velocity. Note that in [104] the notations $\omega = 2\pi F$ and $\omega_0 = 2\pi f$ are rather used.

source acts above it. (2.93). The analysis again starts from the linearized Euler’s equations written as a Lippmann-Schwinger equation, considering that the fluctuations of the ambient flow velocity act as secondary sources for the transmitted acoustic waves. A Born-like approximate solution of the Lippmann-Schwinger equation has been derived to work out a first-order model of the pressure field transmitted by the shear layer. In this model, the transmitted waves are constituted by their unperturbed component formed by the waves emitted by the source which have not been scattered by the ambient velocity fluctuations, and their perturbed component formed by the waves which have typically been scattered once by those fluctuations. These scattered waves are of particular interest since they have been characterized by their PSD in the experiments reported in [41–43], which primarily motivated this work. Using various assumptions for the ambient flow (thin layer) and the (high-frequency) source, and a stationary-phase argument, a model for the PSD of the scattered waves transmitted by the shear layer has been derived. It exhibits the main properties observed for the experimental PSD in [41–43, 91, 118], and for the numerically simulated PSD and alternative analytical models in [16, 55, 64, 102, 104, 112, 118].

The PSD of the pressure field transmitted by the shear layer shows a characteristic

spectral broadening effect, whereby a reduction of the main peak at the source tone frequency in favor of more distributed spectral humps on both sides of the former, is observed. The main peak arises from the unperturbed transmitted pressure, and sidebands (lobes) arise in connection with a Doppler shift effect due to the motion of the turbulent eddies acting as secondary sources for the scattered transmitted pressure. A widening of these lobes proportional to the convection velocity of the turbulent eddies has been observed, as well as the independence of the location of their maxima with respect to the tone frequency. Increasing the latter also leads to a widening of the sidebands and higher scattered levels. The proposed analysis has used a delta-correlated model of the turbulent velocity spatial fluctuations and a Gaussian model of its temporal fluctuations, though it could be improved by considering correlation models pertaining to homogeneous isotropic turbulent (HIT) or homogeneous axisymmetric turbulence (HAT) as done in [104]. However the model retained here has been able to predict the main features outlined above.

Chapter 3

Coherent interferometry in a random flow

In this chapter, we are interested in developing imaging algorithms based on coherent interferometry (CINT) in order to localize acoustic sources or reflectors with acoustic waves that have passed through a turbulent (random) flow. We thus consider the linearized Euler equations (1.5) (LEE) about a stationary ambient flow satisfying Eq. (1.4), with the aim of localizing such defects within the actual random flow. Acoustical data will be generated by numerical simulations of the LEE and the ambient flow in idealized configurations. The proposed CINT algorithms will be tested on these configurations and compared with Kirchhoff migration (KM) algorithms.

3.1 Imaging functionals in random moving media

3.1.1 Model problem

We start by considering the model problem of computing the pressure field emitted by a point source in an ambient flow with constant velocity because it has relevance to the imaging algorithms considered in the subsequent developments. The LEE (1.5) where the specific force \mathbf{f} is ignored read:

$$\begin{aligned}(\partial_t + \mathbf{v}_0 \cdot \nabla) \varrho' + \nabla \cdot (\varrho_0 \mathbf{v}') + \varrho' \nabla \cdot \mathbf{v}_0 &= m, \\(\partial_t + \mathbf{v}_0 \cdot \nabla) \mathbf{v}' + \frac{1}{\varrho_0} \nabla p' + (\mathbf{v}' \cdot \nabla) \mathbf{v}_0 - \frac{\varrho'}{\varrho_0^2} \nabla p_0 &= \mathbf{0},\end{aligned}\tag{3.1}$$

with the barotropic assumption $p' = c_0^2 \varrho'$. Here again $c_0(\mathbf{r})$ stands for the speed of sound not influenced by the waves. The ambient flow is stationary and the ambient quantities, namely the ambient pressure $p_0(\mathbf{r})$, velocity $\mathbf{v}_0(\mathbf{r})$, and density $\varrho_0(\mathbf{r})$ satisfy Eq. (1.4):

$$\begin{aligned}\nabla \cdot (\varrho_0 \mathbf{v}_0) &= 0, \\(\mathbf{v}_0 \cdot \nabla) \mathbf{v}_0 + \frac{1}{\varrho_0} \nabla p_0 &= \mathbf{0}, \\(\mathbf{v}_0 \cdot \nabla) p_0 - c_0^2 (\mathbf{v}_0 \cdot \nabla) \varrho_0 &= 0.\end{aligned}\tag{3.2}$$

If the ambient quantities are non vanishing constant, which is consistent at least with Eq. (3.2), we obtain by taking the convective derivative $\partial_t + \mathbf{v}_0 \cdot \nabla$ of the first equation in

(3.1) and the divergence $\nabla \cdot$ of the second equation in (3.1):

$$\frac{1}{c_0^2}(\partial_t + \mathbf{v}_0 \cdot \nabla)^2 p - \Delta p = (\partial_t + \mathbf{v}_0 \cdot \nabla)m. \quad (3.3)$$

Here we have dropped the primes $(\cdot)'$ for convenience. This is the convected wave equation (1.9) first proposed by Blokhintzev [21] for steady irrotational ambient flows. If \mathbf{v}_0 is constant all over the domain Ω where the imaging procedure is performed, one can then consider a local frame moving at this velocity. The local coordinates \mathbf{R} and pressure field $P(\mathbf{R}, t)$ are defined by:

$$\mathbf{R} = \mathbf{r} - \mathbf{v}_0 t, \quad P(\mathbf{R}, t) = p(\mathbf{R} + \mathbf{v}_0 t, t).$$

With this change of variable one notices that $\partial_t P = (\partial_t + \mathbf{v}_0 \cdot \nabla)p$ and obtains that in the moving frame:

$$\frac{1}{c_0^2} \partial_t^2 P - \Delta P = \partial_t \mathcal{M}, \quad (3.4)$$

where similarly $\mathcal{M}(\mathbf{R}, t) = m(\mathbf{R} + \mathbf{v}_0 t, t)$. This is actually the acoustic wave equation (1.8) with a vanishing ambient flow.

The acoustic Green's function $G_0(\mathbf{R}, \mathbf{R}', t)$ is defined as the solution of the wave equation for a right-hand side $\partial_t \mathcal{M}(\mathbf{R}, t) \equiv F(\mathbf{R}, t) = \delta(t)\delta(\mathbf{R} - \mathbf{R}')$ with zero initial conditions and reads:

$$G_0(\mathbf{R}, \mathbf{R}', t) = \mathcal{G}_0(\mathbf{R} - \mathbf{R}', t) = \begin{cases} \frac{1}{4\pi|\mathbf{R} - \mathbf{R}'|} \delta\left(t - \frac{|\mathbf{R} - \mathbf{R}'|}{c_0}\right) & \text{if } t \geq 0, \\ 0 & \text{if } t < 0. \end{cases} \quad (3.5)$$

The solution of the wave equation (3.4) for a source \mathcal{M} with time-dependent spatial compact support $\Omega_s(t)$ is then:

$$P(\mathbf{R}, t) = \frac{1}{4\pi} \frac{\partial}{\partial t} \int dt' \int_{\Omega_s(t')} \frac{\mathcal{M}(\mathbf{R}', t')}{|\mathbf{R} - \mathbf{R}'|} \delta\left(t' - t + \frac{|\mathbf{R} - \mathbf{R}'|}{c_0}\right) d\mathbf{R}'. \quad (3.6)$$

We now assume that the source is a fixed point source in the reference frame, such that $\mathcal{M}(\mathbf{R}, t) = A(t)\delta(\mathbf{R} - \mathbf{R}_s(t))$ where $\mathbf{R}_s(t) = \mathbf{r}_s - \mathbf{v}_0 t$ and \mathbf{r}_s is the fixed location of the source in the reference frame, and A is its amplitude. Then owing to the identity $\int Y(t')\delta(X(t'))dt' = \sum_j Y(t_j)|\partial_{t'} X|_{t'=t_j}^{-1}$ where the t_j 's depend of t and are the roots of $X(t') = 0$, one obtains:

$$P(\mathbf{R}, t) = \frac{1}{4\pi} \frac{\partial}{\partial t} \sum_j \frac{A(t_j)}{||\mathbf{R} - \mathbf{R}_s(t_j)| + \mathbf{M} \cdot (\mathbf{R} - \mathbf{R}_s(t_j))|},$$

where $\mathbf{M} := \frac{\mathbf{v}_0}{c_0}$ is the Mach number (a vector in the present case) of the ambient flow. The sum is taken over the t_j 's such that $c_0(t - t_j) = |\mathbf{R} - \mathbf{R}_s(t_j)|$, which can not have more than one solution in the subsonic regime $|\mathbf{M}| = M < 1$ [107, Chapter 5]. Indeed, if one lets $\phi(z) = |\mathbf{R} - \mathbf{R}_s(z)| - c_0(t - z)$ then $\phi'(z) = c_0 + \frac{(\mathbf{R} - \mathbf{R}_s(z)) \cdot \mathbf{v}_0}{|\mathbf{R} - \mathbf{R}_s(z)|} > 0$ in the subsonic regime. Thus ϕ increases monotonically and the situation $\phi(z) = 0$ arises at most once, say $t = t_s$ the time of emission of a sound wave which arrives at the observation point \mathbf{R} at time t in the moving frame. Solving for this equation with $\mathbf{R} = \mathbf{r} - \mathbf{v}_0 t$, we arrive at:

$$t_s = t - \frac{d}{c_0} \frac{\sqrt{1 - (M \sin \alpha)^2} - M \cos \alpha}{1 - M^2},$$

where $Md \cos \alpha = \mathbf{M} \cdot (\mathbf{r} - \mathbf{r}_s)$; that is, $d = |\mathbf{r} - \mathbf{r}_s|$ is the distance between the source point \mathbf{r}_s and the observation point \mathbf{r} in the reference frame, and α is the angle between \mathbf{v}_0 and $\mathbf{r} - \mathbf{r}_s$. The acoustic pressure in the reference frame finally reads:

$$p(\mathbf{r}, t) = \frac{1}{4\pi|\mathbf{r} - \mathbf{r}_s|\sqrt{1 - (M \sin \alpha)^2}} A' \left(t - \frac{|\mathbf{r} - \mathbf{r}_s| \sqrt{1 - (M \sin \alpha)^2} - M \cos \alpha}{c_0} \right). \quad (3.7)$$

3.1.2 Reverse-time and Kirchhoff migration

We now consider the classical reverse-time (RT) and Kirchhoff migration (KM) algorithms to image sources or reflectors. We adapt them to the situation of interest for us, namely the localization of such sources or reflectors in an ambient flow. In reverse-time migration [120], one uses N fixed sensors located at \mathbf{r}_r , $1 \leq r \leq N$, to localize a source (the so-called passive case) or a reflector (the active case) at some unknown location \mathbf{r}_s in the actual (unknown) flow by back-propagating in a fictitious flow of known characteristics the pressure fields recorded by the sensors. This setup is schematized on Fig. 3.1. Let us consider the case of the wave equation in a quiescent medium, that is a flow with $\mathbf{v}_0 = \mathbf{0}$, and a constant speed of sound c_0 . Introducing the Fourier and inverse Fourier transform in the time domain:

$$\widehat{p}(\mathbf{r}, \omega) = \int_{\mathbb{R}} e^{i\omega t} p(\mathbf{r}, t) dt, \quad p(\mathbf{r}, t) = \frac{1}{2\pi} \int_{\mathbb{R}} e^{-i\omega t} \widehat{p}(\mathbf{r}, \omega) d\omega, \quad (3.8)$$

the time-harmonic Green's function $\widehat{G}_0(\mathbf{r}, \mathbf{r}', \omega)$ solves the wave equation (3.4) in the Fourier domain—the Helmholtz equation with $\widehat{F}(\mathbf{r}, \omega) = \delta(\mathbf{r} - \mathbf{r}')$:

$$\frac{\omega^2}{c_0^2} \widehat{G}_0 + \Delta \widehat{G}_0 = -\delta(\mathbf{r} - \mathbf{r}'), \quad (3.9)$$

together with the Sommerfeld radiation condition at infinity $|\mathbf{r}| \rightarrow +\infty$:

$$\left(\hat{\mathbf{r}} \cdot \nabla - i \frac{\omega}{c_0} \right) \widehat{G}_0 = \mathcal{O} \left(\frac{1}{|\mathbf{r}|^2} \right), \quad (3.10)$$

where $\hat{\mathbf{r}} := \frac{\mathbf{r}}{|\mathbf{r}|}$; that is, $\widehat{G}_0(\mathbf{r}, \mathbf{r}', \omega) \propto e^{i \frac{\omega}{c_0} |\mathbf{r}|}$ at infinity. It satisfies the reciprocity property:

$$\widehat{G}_0(\mathbf{r}, \mathbf{r}', \omega) = \widehat{G}_0(\mathbf{r}', \mathbf{r}, \omega) \quad (3.11)$$

everywhere, and since the ambient medium is homogeneous:

$$\widehat{G}_0(\mathbf{r}, \mathbf{r}', \omega) = \widehat{\mathcal{G}}_0(\mathbf{r} - \mathbf{r}', \omega) = \frac{e^{i \frac{\omega}{c_0} |\mathbf{r} - \mathbf{r}'|}}{4\pi |\mathbf{r} - \mathbf{r}'|}. \quad (3.12)$$

The passive case consists in localizing a source in a quiescent medium of which the actual speed of sound $c_0(\mathbf{r})$ is instead variable and imperfectly known. One starts by recording at the N sensors the pressure fields emitted by the source $F(\mathbf{r}, t) = f(t)\delta(\mathbf{r} - \mathbf{r}_s)$. This yields the dataset $\{p(\mathbf{r}_r, t); 1 \leq r \leq N\}$ (or its Fourier transforms $\{\widehat{p}(\mathbf{r}_r, \omega); 1 \leq r \leq N\}$) constituted by the pressure fields recorded by the sensors located at \mathbf{r}_r , $1 \leq r \leq N$. They are subsequently time reversed, which amounts of taking the conjugates of their Fourier

transforms, and back propagated in the fictitious domain of which Green's function is known, namely $\widehat{G}_0(\mathbf{r}, \mathbf{r}', \omega)$. The reverse-time imaging functional $\mathcal{I}_{\text{RT}}(\mathbf{r}^S)$ is ultimately formed by stacking all the data:

$$\mathcal{I}_{\text{RT}}(\mathbf{r}^S) = \frac{1}{2\pi} \sum_{r=1}^N \int_{\mathbb{R}} \widehat{G}_0(\mathbf{r}_r, \mathbf{r}^S, \omega) \overline{\widehat{p}(\mathbf{r}_r, \omega)} d\omega. \quad (3.13)$$

The KM algorithm [20] for passive imaging has been introduced in Sect. 1.5.1, Eq. (1.67). It considers $\widehat{G}_0(\mathbf{r}, \mathbf{r}', \omega) \equiv \exp(i\frac{\omega}{c_0}|\mathbf{r} - \mathbf{r}'|)$ and the following imaging functional, replacing the Green's function by its phase term in Eq. (3.13) above:

$$\begin{aligned} \mathcal{I}_{\text{KM}}(\mathbf{r}^S) &= \frac{1}{2\pi} \sum_{r=1}^N \int_{\mathbb{R}} e^{i\frac{\omega}{c_0}|\mathbf{r}_r - \mathbf{r}^S|} \overline{\widehat{p}(\mathbf{r}_r, \omega)} d\omega \\ &= \sum_{r=1}^N p\left(\mathbf{r}_r, \frac{|\mathbf{r}_r - \mathbf{r}^S|}{c_0}\right), \end{aligned} \quad (3.14)$$

such that the source location can be estimated by:

$$\mathbf{r}_{\text{so}} = \arg \max_{\mathbf{r}^S \in S} \overline{\mathcal{I}_{\text{KM}}(\mathbf{r}^S)} \quad \text{in some search region } S.$$

The range resolution of KM is $\frac{c_0}{B}$, where B is the source frequency bandwidth. Its cross-range resolution is $r_c = \frac{\lambda_0 L}{a}$ (Rayleigh's resolution formula), where a is the aperture of the sensor array, λ_0 is the source central wavelength, and L is the distance from the source (range); see Fig. 3.1. KM is known to work poorly when the medium is scattering, however it remains very robust with respect to additive measurement noise. In the random paraxial regime such that $\lambda_0 \ll a \ll L$ it can be shown that for N large (dense array):

$$\mathbb{E} \left\{ \widehat{\mathcal{I}}_{\text{RT}}(\mathbf{r}^S, \omega) \right\} = \text{sinc} \left(\frac{x}{r_c} \right) \text{sinc} \left(\frac{y}{r_c} \right) e^{-\eta(\omega)} \overline{\widehat{f}(\omega)}, \quad (3.15)$$

where $\eta(\omega)$ is a damping coefficient depending on the two-point statistics of the random medium, $\mathbb{E}\{X\}$ stands for the mathematical expectation (or average) of the random variable X , and $\mathbf{r}^S = (x, y, L)$. However the reverse-time pressure field is statistically unstable [22] in the sense that:

$$\text{SNR} = \frac{\mathbb{E} \{ \mathcal{I}_{\text{RT}}(\mathbf{r}^S, t) \}}{\text{Var} \{ \mathcal{I}_{\text{RT}}(\mathbf{r}^S, t) \}^{\frac{1}{2}}} \ll 1,$$

where $\text{Var}\{X\} = \mathbb{E} \{ (X - \mathbb{E}\{X\})^2 \}$ stands for the variance.

Now in view of the result (3.7), it is proposed to modify the foregoing imaging functional to include a Doppler compensation factor $\gamma_D(\mathbf{r}, \mathbf{r}', \mathbf{v}_0)$ which compensates the shift of the arrival time induced by the flow when the ambient medium moves at an average velocity $\mathbf{v}_0 \neq \mathbf{0}$:

$$\gamma_D(\mathbf{r}, \mathbf{r}', \mathbf{v}_0) = \left(1 - \left| \frac{\mathbf{v}_0}{c_0} \right|^2 \right)^{-1} \left[\sqrt{1 - \left| \frac{\mathbf{v}_0}{c_0} \right|^2 + \left(\frac{\mathbf{v}_0 \cdot (\mathbf{r} - \mathbf{r}')}{c_0 |\mathbf{r} - \mathbf{r}'|} \right)^2} - \frac{\mathbf{v}_0 \cdot (\mathbf{r} - \mathbf{r}')}{c_0 |\mathbf{r} - \mathbf{r}'|} \right]. \quad (3.16)$$

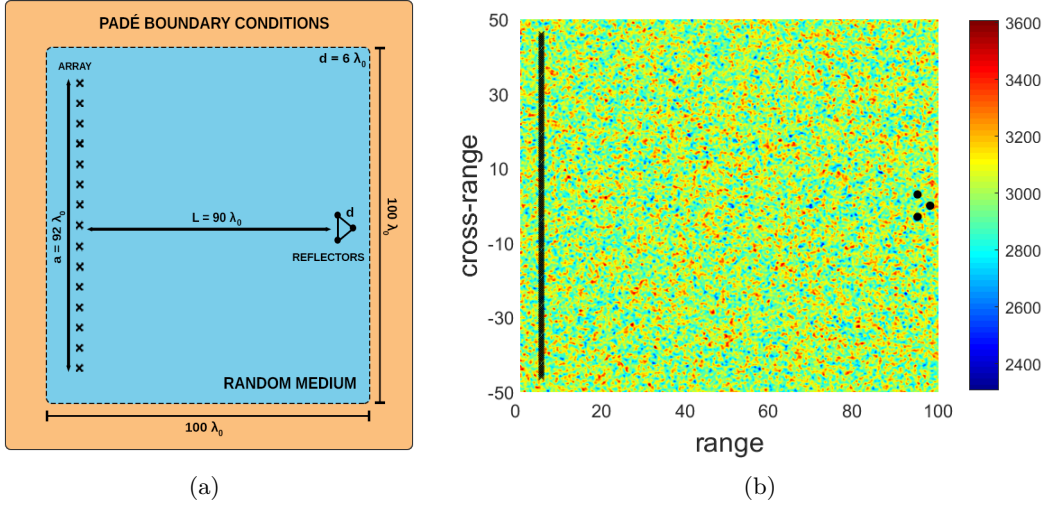


Figure 3.1 – The typical imaging configuration considered in this chapter, after [24]. Dimensions are given in terms of the central wavelength λ_0 . (a) The locations of the sources (passive case) or reflectors (active case) to be imaged is shown by dots \bullet and the locations of the transducers is shown by crosses \times . In the case of active imaging the central transducer is used as a source. (b) Typical realization of the random speed of sound $c_0(\mathbf{r})$.

The compensated KM imaging functional (3.14) thus reads:

$$\mathcal{I}_{\text{KM}}(\mathbf{r}^S) = \sum_{r=1}^N p \left(\mathbf{r}_r, \gamma_D(\mathbf{r}_r, \mathbf{r}^S, \mathbf{v}_0) \frac{|\mathbf{r}_r - \mathbf{r}^S|}{c_0} \right), \quad (3.17)$$

where one observes that $\gamma_D(\mathbf{r}, \mathbf{r}', \mathbf{0}) = 1$ and the imaging functional (3.14) for a quiescent medium is recovered.

In the active case, the network of sensors is used for detecting reflectors. One or several sensors \mathbf{r}_s , $1 \leq s \leq N_s$, emit signals which are recorded after a round trip to the reflectors. In this context the dataset $\{p(\mathbf{r}_r, t; \mathbf{r}_s); 1 \leq r \leq N, 1 \leq s \leq N_s\}$ (or its Fourier transforms $\{\hat{p}(\mathbf{r}_r, \omega; \mathbf{r}_s); 1 \leq r \leq N, 1 \leq s \leq N_s\}$) is constituted by the pressure fields recorded by the sensors located at \mathbf{r}_r , $1 \leq r \leq N$, when the sensors located at \mathbf{r}_s , $1 \leq s \leq N_s$, act as active sources. The KM algorithm for active imaging has also been introduced in Sect. 1.5.1, Eq. (1.70). The KM imaging functional in the active case is written:

$$\mathcal{I}_{\text{KM}}(\mathbf{r}^R) = \sum_{r=1}^N \sum_{s=1}^{N_s} p \left(\mathbf{r}_r, \frac{|\mathbf{r}_s - \mathbf{r}^R|}{c_0} + \frac{|\mathbf{r}^R - \mathbf{r}_r|}{c_0}; \mathbf{r}_s \right), \quad (3.18)$$

and:

$$\mathbf{r}_{\text{ref}} = \arg \max_{\mathbf{r}^R \in S} \mathcal{I}_{\text{KM}}(\mathbf{r}^R) \quad \text{in some search region } S \quad (3.19)$$

is the position of the reflector. As for the passive case, the foregoing imaging functional is modified to include a Doppler compensation factor $\gamma_D(\mathbf{r}, \mathbf{r}', \mathbf{v}_0)$ when the ambient medium moves at an average velocity $\mathbf{v}_0 \neq \mathbf{0}$. In the active case the KM imaging functional (3.18)

is written now:

$$\mathcal{I}_{\text{KM}}(\mathbf{r}^R) = \sum_{r=1}^N \sum_{s=1}^{N_s} p \left(\mathbf{r}_r, \gamma_D(\mathbf{r}_s, \mathbf{r}^R, \mathbf{v}_0) \frac{|\mathbf{r}_s - \mathbf{r}^R|}{c_0} + \gamma_D(\mathbf{r}^R, \mathbf{r}_r, \mathbf{v}_0) \frac{|\mathbf{r}^R - \mathbf{r}_r|}{c_0}; \mathbf{r}_s \right). \quad (3.20)$$

In this case the first γ_D compensates the time shift induced by the flow, for the travel between the source to the reflector. The second γ_D compensates this shift for the travel between the reflector and the receiver.

3.1.3 Coherent interferometric imaging

Coherent interferometric imaging (CINT) [23–33, 69] of sources or reflectors uses finite-aperture arrays alike, *e.g.* a square $[-\frac{a}{2}, \frac{a}{2}] \times [-\frac{a}{2}, \frac{a}{2}] \times \{0\}$ of N sensors, to localize in a cluttered medium a source $\mathbf{r}_s = (0, 0, L)$ typically at the distance L (range) from the array; see again Fig. 3.1 for the standard configuration. It consists in back propagating empirical correlations of the pressure fields, rather than the pressure fields themselves, in a fictitious medium in order to alleviate the statistical instability of KM with clutter. Indeed, forming the correlations enables to partially cancel the incoherent random phase shifts of the signals and thus enhance statistical stability. As for the RT and KM algorithms, the procedure goes in two steps described hereafter.

First step

The empirical cross-correlation of the recorded pressure fields at the sensors \mathbf{r}_q and \mathbf{r}_r reads:

$$\mathcal{C}_T(\mathbf{r}_q, \mathbf{r}_r, t) = \int p(\mathbf{r}_q, \tau) p(\mathbf{r}_r, \tau - t) d\tau.$$

Now CINT first step consists in forming the empirical cross-correlation of the recorded pressure fields in the Fourier domain:

$$\widehat{\mathcal{C}}(\mathbf{r}_q, \mathbf{r}_r, \omega, \omega') = \widehat{p}(\mathbf{r}_q, \omega) \overline{\widehat{p}(\mathbf{r}_r, \omega')}, \quad (3.21)$$

which is such that the Fourier transform in time domain of the empirical cross-correlation \mathcal{C}_T is:

$$\begin{aligned} \widehat{\mathcal{C}}_T(\mathbf{r}_q, \mathbf{r}_r, \omega) &= \int e^{i\omega t} \mathcal{C}_T(\mathbf{r}_q, \mathbf{r}_r, t) dt \\ &= \widehat{\mathcal{C}}(\mathbf{r}_q, \mathbf{r}_r, \omega, \omega). \end{aligned}$$

It is important to note that the data used in CINT imaging are the same as those used in KM imaging. The same network of receivers is used, but it is the way in which these data are post-processed which differentiates the two methods. As we have already seen, with KM the raw signals are back-propagated whereas with CINT the empirical cross-correlation that we have just introduced, (3.21), is back-propagated. Moreover this is done locally in space and frequency, as it is explained just below (see also the introduction in Sect. 1.5.1).

Second step

The second step consists in numerically back-propagating the empirical cross-correlations $\widehat{\mathcal{C}}(\mathbf{r}_q, \mathbf{r}_r, \omega, \omega')$ in a fictitious (*e.g.* homogeneous) medium, of which Green's function is again $\widehat{G}_0(\mathbf{r}, \mathbf{r}', \omega) \equiv \exp(i\frac{\omega}{c_0}|\mathbf{r} - \mathbf{r}'|)$. The cross-correlations are computed locally in frequency and space and not over the whole frequency range and for all pairs of sensors. The CINT imaging functional of a source (passive case) in a quiescent medium reads:

$$\mathcal{I}_{\text{CINT}}(\mathbf{r}^S; \Omega_d, X_d) = \sum_{\substack{q, r = 1 \\ |\mathbf{r}_q - \mathbf{r}_r| \leq X_d}}^N \iint_{|\omega - \omega'| \leq \Omega_d} \widehat{\mathcal{C}}(\mathbf{r}_q, \mathbf{r}_r, \omega, \omega') e^{-i\frac{\omega}{c_0}|\mathbf{r}_q - \mathbf{r}^S| + i\frac{\omega'}{c_0}|\mathbf{r}_r - \mathbf{r}^S|} d\omega d\omega', \quad (3.22)$$

such that the source location can be estimated by:

$$\mathbf{r}_{\text{so}} = \arg \max_{\mathbf{r}^S \in S} \mathcal{I}_{\text{CINT}}(\mathbf{r}^S; \Omega_d, X_d) \quad \text{in some search region } S.$$

Ideally the frequency window Ω_d is chosen as the so-called decoherency frequency Ω_c , *i.e.* the frequency gap beyond which the frequency components of the recorded pressure fields are no longer correlated. Likewise, the spatial window X_d is ideally chosen as the decoherency length X_c , *i.e.* the sensor gap beyond which the recorded pressure fields are no longer correlated. The range resolution of CINT is $\frac{c_0}{\Omega_d}$ (the usual range resolution formula with the effective bandwidth $\Omega_d < B$ where B is the source bandwidth), and its cross-range resolution is $\frac{\lambda_0 L}{X_d}$ (the Rayleigh's resolution formula with the effective array diameter $X_d < a$). The decoherency parameters Ω_c and X_c depend on the statistical properties of the fluctuations in the random medium. They are not known since the random medium is also unknown, so the CINT parameters Ω_d and X_d have to be determined from the data. Alternatively, they may be determined by the adaptive algorithm developed in [26], as presented in Sect. 1.5.1.

Reflector imaging

CINT imaging can be used to localize reflectors alike: a square array $[-\frac{a}{2}, \frac{a}{2}] \times [-\frac{a}{2}, \frac{a}{2}] \times \{0\}$ of N transducers is put up at a distance L from a reflector located at $\mathbf{r}_{\text{ref}} = (0, 0, L)$. Among the N transducers, N_s are used as sources located at $\{\mathbf{r}_s; 1 \leq s \leq N_s\}$, and N_r are used as receivers (sensors) located at $\{\mathbf{r}_r; 1 \leq r \leq N_r\}$. The dataset of recorded pressure fields is denoted by $\{p(\mathbf{r}_r, t; \mathbf{r}_s); 1 \leq r \leq N_r, 1 \leq s \leq N_s\}$. The CINT imaging functional of a reflector (active case) in a quiescent medium reads:

$$\mathcal{I}_{\text{CINT}}(\mathbf{r}^R; \Omega_d, X_d) = \sum_{\substack{r, r' = 1 \\ |\mathbf{r}_r - \mathbf{r}_{r'}| \leq X_d}}^{N_r} \sum_{\substack{s, s' = 1 \\ |\mathbf{r}_s - \mathbf{r}_{s'}| \leq X_d}}^{N_s} \iint_{|\omega - \omega'| \leq \Omega_d} \widehat{p}(\mathbf{r}_r, \omega; \mathbf{r}_s) \overline{\widehat{p}(\mathbf{r}_{r'}, \omega'; \mathbf{r}_{s'})} \times e^{-i\frac{\omega}{c_0}(|\mathbf{r}_r - \mathbf{r}^R| + |\mathbf{r}^R - \mathbf{r}_s|) + i\frac{\omega'}{c_0}(|\mathbf{r}_{r'} - \mathbf{r}^R| + |\mathbf{r}^R - \mathbf{r}_{s'}|)} d\omega d\omega', \quad (3.23)$$

such that the reflector location can be estimated by:

$$\mathbf{r}_{\text{ref}} = \arg \max_{\mathbf{r}^S \in S} \mathcal{I}_{\text{CINT}}(\mathbf{r}^S; \Omega_d, X_d) \quad \text{in some search region } S.$$

Full migration

The unfiltered full migration imaging functional is (in the passive case):

$$\begin{aligned} \mathcal{I}_{\text{BF}}(\mathbf{r}^S) &= \sum_{q=1}^N \sum_{r=1}^N \iint_{\mathbb{R}^2} \widehat{\mathcal{C}}(\mathbf{r}_q, \mathbf{r}_r, \omega, \omega') e^{-i\frac{\omega}{c_0}|\mathbf{r}_q - \mathbf{r}^S| + i\frac{\omega'}{c_0}|\mathbf{r}_r - \mathbf{r}^S|} d\omega d\omega' \\ &= |\mathcal{I}_{\text{KM}}(\mathbf{r}^S)|^2, \end{aligned} \quad (3.24)$$

if all pairs of sensors and frequencies are summed up in Eq. (3.22). Thus one gets the same image as with KM (3.14): the full migration of all cross-correlations does not work if the medium is scattering.

Coherent interferometric imaging in a random flow

In view of the result (3.7) of Sect. 3.1.1, it is proposed to modify the foregoing CINT imaging functional (3.22) for localizing a source to include the Doppler compensation factor (3.16). The compensated CINT imaging functional in the passive case thus reads:

$$\begin{aligned} \mathcal{I}_{\text{CINT}}(\mathbf{r}^S; \Omega_d, X_d) &= \\ &\sum_{\substack{q, r = 1 \\ |\mathbf{r}_q - \mathbf{r}_r| \leq X_d}}^N \iint_{|\omega - \omega'| \leq \Omega_d} \widehat{\mathcal{C}}(\mathbf{r}_q, \mathbf{r}_r, \omega, \omega') e^{-i\frac{\omega}{c_0}\gamma_D(\mathbf{r}_q, \mathbf{r}^S, \mathbf{v}_0)|\mathbf{r}_q - \mathbf{r}^S| + i\frac{\omega'}{c_0}\gamma_D(\mathbf{r}_r, \mathbf{r}^S, \mathbf{v}_0)|\mathbf{r}_r - \mathbf{r}^S|} d\omega d\omega'. \end{aligned} \quad (3.25)$$

Along the same lines, we modify the CINT imaging functional (3.23) in the active case as:

$$\begin{aligned} \mathcal{I}_{\text{CINT}}(\mathbf{r}^S; \Omega_d, X_d) &= \sum_{\substack{r, r' = 1 \\ |\mathbf{r}_r - \mathbf{r}_{r'}| \leq X_d}}^{N_r} \sum_{\substack{s, s' = 1 \\ |\mathbf{r}_s - \mathbf{r}_{s'}| \leq X_d}}^{N_s} \iint_{|\omega - \omega'| \leq \Omega_d} \widehat{p}(\mathbf{r}_r, \omega; \mathbf{r}_s) \overline{\widehat{p}(\mathbf{r}_{r'}, \omega'; \mathbf{r}_{s'})} \\ &\times e^{-i\frac{\omega}{c_0}(\gamma_D(\mathbf{r}_r, \mathbf{r}^S, \mathbf{v}_0)|\mathbf{r}_r - \mathbf{r}^S| + \gamma_D(\mathbf{r}^S, \mathbf{r}_s, \mathbf{v}_0)|\mathbf{r}^S - \mathbf{r}_s|)} \\ &\times e^{+i\frac{\omega'}{c_0}(\gamma_D(\mathbf{r}_{r'}, \mathbf{r}^S, \mathbf{v}_0)|\mathbf{r}_{r'} - \mathbf{r}^S| + \gamma_D(\mathbf{r}^S, \mathbf{r}_{s'}, \mathbf{v}_0)|\mathbf{r}^S - \mathbf{r}_{s'}|)} d\omega d\omega'. \end{aligned} \quad (3.26)$$

3.2 Discontinuous Galerkin method for Euler equations

In order to test the KM and CINT imaging functionals in quiescent or moving cluttered media, the dataset $\{p(\mathbf{r}_r, t); 1 \leq r \leq N\}$ of recorded pressure fields is simulated numerically using the computer code SPACE [60, 109] for computational fluid dynamics (CFD) and computational aero-acoustics (CAA). It solves the Euler equations (1.2) and linearized Euler equations (LEE) (1.5) or (3.1) by the discontinuous Galerkin (DG) finite element method and an explicit Runge-Kutta time integration scheme.

3.2.1 Euler equations DG solver (CFD)

In their conservative form, the Euler equations (1.2) for an ideal fluid read:

$$\partial_t \mathbf{w} + \nabla \cdot \mathcal{F}(\mathbf{w}) = \mathbf{g}, \quad (3.27)$$

with $\mathbf{g} = (m, \mathbf{0}, 0)$, $\mathbf{w} = (\rho, \rho\mathbf{v}, \rho E)$ the vector of conservative variables, where E is the energy density per unit mass:

$$E = e + \frac{1}{2}|\mathbf{v}|^2,$$

and e is the internal energy per unit mass, and \mathcal{F} the flux operator given by:

$$\mathcal{F}(\mathbf{w}) = \begin{pmatrix} \rho\mathbf{v} \\ \rho\mathbf{v} \otimes \mathbf{v} + p\mathbf{I}_3 \\ (p + \rho E)\mathbf{v} \end{pmatrix}.$$

Note that for a fluid following the law of perfect gas such that $p\rho^{-\gamma} = \text{constant}$ along particle paths, where $\gamma = \frac{c_p}{c_v}$ is the perfect gas constant (Laplace's coefficient), and c_v and c_p are the heat capacities at constant volume and constant pressure, respectively, one has $e(T) = c_v T$ as a function of temperature T , and $\rho e = \frac{p}{\gamma-1}$. Considering a bounded domain Ω with boundary Γ , the variational formulation of the Euler equations (3.27) reads:

$$\int_{\Omega} (\partial_t \mathbf{w} + \nabla \cdot \mathcal{F}(\mathbf{w})) \psi \, d\Omega = \int_{\Omega} \mathbf{g} \psi \, d\Omega, \quad \forall \psi \in V(\Omega),$$

where $V(\Omega)$ is a set of admissible fields in Ω . Subdividing the domain Ω into N_{Ω} non-overlapping elements or cells as $\Omega_h = \bigcup_{i=1}^{N_{\Omega}} \Omega_i$, and its boundary Γ into N_{Γ} surface elements as $\Gamma_h = \bigcup_{j=1}^{N_{\Gamma}} \Gamma_j$, one obtains after integration by parts:

$$\begin{aligned} \sum_{i=1}^{N_{\Omega}} \left(\int_{\Omega_i} \partial_t \mathbf{w} \psi \, d\Omega - \int_{\Omega_i} \mathcal{F}(\mathbf{w}) \cdot \nabla \psi \, d\Omega + \oint_{\partial\Omega_i|\Gamma} \tilde{\mathcal{F}}(\mathbf{w}, \mathbf{w}^+) \cdot \mathbf{n}_i \psi \, d\Gamma \right) \\ + \sum_{j=1}^{N_{\Gamma}} \oint_{\Gamma_j} \mathcal{F}(\mathbf{w}) \cdot \mathbf{n}_j \psi \, d\Gamma = \int_{\Omega} \mathbf{g} \psi \, d\Omega, \quad \forall \psi \in V_h(\Omega), \end{aligned} \quad (3.28)$$

where $\partial\Omega_i$ is the boundary of the geometric cell Ω_i , and \mathbf{n}_i is its outward unit normal; likewise, \mathbf{n}_j is the outward unit normal to Γ_j . Here $V_h(\Omega)$ is typically a broken set of piecewise polynomial functions on the partition Ω_h . If it is constructed such that its elements are continuous at the boundary of two adjacent elements $\Gamma_{ij} = \Omega_i \cap \Omega_j$, then the third term in the left hand-side above (the summation on the interior boundaries $\partial\Omega_i|\Gamma$) vanishes. If however it is constructed such that no continuity relation is enforced between adjacent elements, then the physical normal flux $\mathcal{F}(\mathbf{w}) \cdot \mathbf{n}_i$ on $\partial\Omega_i|\Gamma$ has to be carefully evaluated. It is actually replaced by the flux $\tilde{\mathcal{F}}(\mathbf{w}, \mathbf{w}^+) \cdot \mathbf{n}_i$ which is a numerical flux accounting for the fact that in view of this subdivision, \mathbf{w} may have different values on both sides of the edge $\partial\Omega_i$. Local Lax-Friedrichs numerical fluxes (see for example [83]) are used in SPACE, namely:

$$\tilde{\mathcal{F}}(\mathbf{w}, \mathbf{w}^+) \cdot \mathbf{n} = \frac{1}{2}(\mathcal{F}(\mathbf{w}) + \mathcal{F}(\mathbf{w}^+)) \cdot \mathbf{n} - \xi \lambda_{\max}(\mathbf{w}^+ - \mathbf{w}),$$

where \mathbf{w} (respectively \mathbf{w}^+) stands for the interior (respectively exterior) trace of \mathbf{w} in Ω_i , $\xi \in [0, 1]$, and:

$$\lambda_{\max} = \max(|\mathbf{v} \cdot \mathbf{n}|, |\mathbf{v} \cdot \mathbf{n} + c|, |\mathbf{v} \cdot \mathbf{n} - c|, |\mathbf{v}^+ \cdot \mathbf{n}^+|, |\mathbf{v}^+ \cdot \mathbf{n}^+ + c^+|, |\mathbf{v}^+ \cdot \mathbf{n}^+ - c^+|).$$

Here $c = \sqrt{\gamma p / \rho}$ is the adiabatic speed of sound.

3.2.2 Linearized Euler equations DG solver (CAA)

The LEE are established assuming a subsonic flow. An entropy equation is used rather than an energy equation. Also assuming that at initial time the entropy is spatially uniform, it remains spatially uniform at any time; see Eq. (1.2). Hence the flow is homentropic. Such an hypothesis is not essential for the method, but it is commonly done and provides with a problem of smaller size. Introducing the variable $\mathbf{w}' = (\mathbf{v}', \frac{c_0 \rho'}{\rho_0})$, Eq. (3.1) can be written:

$$\begin{bmatrix} (\partial_t + \mathbf{v}_0 \cdot \nabla) \mathbf{I}_3 & c_0 \nabla \\ c_0 \nabla^\top & \partial_t + \mathbf{v}_0 \cdot \nabla \end{bmatrix} \mathbf{w}' + \begin{bmatrix} \mathbf{D}\mathbf{v}_0 & \frac{1}{\rho_0} (\nabla(\rho_0 c_0) - \frac{1}{c_0} \nabla p_0) \\ \frac{c_0}{\rho_0} (\nabla \rho_0)^\top & -\frac{1}{c_0} \mathbf{v}_0 \cdot \nabla c_0 \end{bmatrix} \mathbf{w}' = \mathbf{g}',$$

where \mathbf{g}' is an acoustic source term, and $(\mathbf{D}\mathbf{v}_0)_{ij} = \partial_j v_{0i}$. Since the flow is homentropic and the fluid is assumed to follow the law of perfect gas, one has:

$$\frac{1}{\rho_0} \left(\nabla(\rho_0 c_0) - \frac{1}{c_0} \nabla p_0 \right) = \nabla c_0, \quad -\frac{1}{c_0} \mathbf{v}_0 \cdot \nabla c_0 = \frac{\gamma - 1}{2} \nabla \cdot \mathbf{v}_0.$$

Hence the foregoing system also reads:

$$\partial_t \mathbf{w}' + \mathcal{A}_i \partial_i \mathbf{w}' + \mathcal{B} \mathbf{w}' = \mathbf{g}',$$

where for $\mathbf{v}_0 := (u_0, v_0, w_0)$:

$$\mathcal{A}_1 = \begin{bmatrix} u_0 & 0 & 0 & c_0 \\ 0 & u_0 & 0 & 0 \\ 0 & 0 & u_0 & 0 \\ c_0 & 0 & 0 & u_0 \end{bmatrix}, \quad \mathcal{A}_2 = \begin{bmatrix} v_0 & 0 & 0 & 0 \\ 0 & v_0 & 0 & c_0 \\ 0 & 0 & v_0 & 0 \\ 0 & c_0 & 0 & v_0 \end{bmatrix}, \quad \mathcal{A}_3 = \begin{bmatrix} w_0 & 0 & 0 & 0 \\ 0 & w_0 & 0 & 0 \\ 0 & 0 & w_0 & c_0 \\ 0 & 0 & c_0 & w_0 \end{bmatrix},$$

and:

$$\mathcal{B} = \begin{bmatrix} \mathbf{D}\mathbf{v}_0 & \nabla c_0 \\ \frac{c_0}{\rho_0} (\nabla \rho_0)^\top & \frac{\gamma-1}{2} \nabla \cdot \mathbf{v}_0 \end{bmatrix}.$$

These matrices depend on the ambient flow:

$$\rho_0 = w_1, \quad u_0 = \frac{w_2}{w_1}, \quad v_0 = \frac{w_3}{w_1}, \quad w_0 = \frac{w_4}{w_1}, \quad c_0 = \sqrt{\gamma(\gamma-1)} \sqrt{\frac{w_5}{w_1} - \frac{w_2^2 + w_3^2 + w_4^2}{2w_1^2}},$$

where $\mathbf{w} = (w_1, w_2, w_3, w_4, w_5)$ is the solution of Euler equations (3.28). We note that the matrix \mathcal{B} vanishes for constant ambient quantities. For a local element Ω_i , the weak formulation of the LEE reads:

$$\int_{\Omega_i} (\partial_t \mathbf{w}' + \mathcal{A}_i \partial_i \mathbf{w}' + \mathcal{B} \mathbf{w}') \psi \, d\Omega + \oint_{\partial\Omega_i} \mathcal{M}(\mathbf{n})(\mathbf{w}'_+ - \mathbf{w}') \psi \, d\Omega = \int_{\Omega_i} \mathbf{g}' \psi \, d\Omega, \quad \forall \psi \in V(\Omega), \quad (3.29)$$

where \mathbf{w}'_+ stands for the exterior trace of \mathbf{w}' , \mathbf{w}' stands for the interior one, and \mathbf{n} is the outward unit normal. \mathcal{M} is a boundary flux operator, where the chosen flux generalizes the method of characteristics in one-dimensional media as follows. Since the matrix $\mathcal{A}_i n_i$ (with summation over the repeated index) is symmetric, it is diagonalizable and can be split into a positive part (corresponding to the set of positive eigenvalues) and a negative part (corresponding to the set of negative eigenvalues):

$$\mathcal{A}_i n_i = [\mathcal{A}_i n_i]^+ + [\mathcal{A}_i n_i]^-.$$

In our approach $\mathcal{M} = [\mathcal{A}_i n_i]^-$, that is, a fully upwind scheme. Furthermore, as matrices \mathcal{A}_j , $j = 1, 2, 3$, \mathcal{B} , and \mathcal{M} only depend on constant values of the ambient flow, a global sparse matrix is built for each computational subdomains.

3.2.3 Spatial discretization and functional basis

Both variational formulations (3.28) and (3.29) are solved with a nodal DG method [83]. The field $\boldsymbol{\psi}(\boldsymbol{\xi})$ ($\boldsymbol{\psi}$ can be \boldsymbol{w} in CFD or \boldsymbol{w}' in CAA) with coordinates $\boldsymbol{\xi}$ in the d -simplex in physical dimension d , is discretized in each cell with a set of n values $\boldsymbol{\psi}_i = \boldsymbol{\psi}(\boldsymbol{\xi}_i)$. For the linear element $[-1, 1]$ ($d = 1$), the approximation of $\boldsymbol{\psi}(\boldsymbol{\xi})$ reads:

$$\tilde{\boldsymbol{\psi}}(\boldsymbol{\xi}) = \sum_{i=0}^n \ell_i(\boldsymbol{\xi}) \boldsymbol{\psi}_i$$

where $\{\ell_i(\boldsymbol{\xi}); \boldsymbol{\xi} \in [-1, 1], 0 \leq i \leq n\}$ is a set of Lagrangian polynomials of degrees $n+1$ based on the Gauss-Lobatto points $\{\boldsymbol{\xi}_i \in [-1, 1]; 0 \leq i \leq n\}$. Indeed, the choice of Gauss-Lobatto points is required to keep a good condition number of operators with high orders [82]. Polynomials based on equidistant grid points present high amplitude oscillations near the boundaries while the polynomials based on Gauss-Lobatto points do not. The amplitude of oscillations increases with the order of polynomials and is responsible of the so-called Runge phenomenon providing severely ill-conditioned operators. The sets of Lagrangian polynomials based on equidistant and Gauss-Lobatto points are plotted in Fig. 3.2 for order $n = 30$. High order optimized bases are also available for triangles, tetrahedrons, pyramids and wedges. To evaluate nodal polynomials, the Lebesgue's function:

$$l(x) = \sum_{i=0}^n |\ell_i(x)| \quad (3.30)$$

is commonly used because it reveals the Runge phenomenon of the polynomial basis. In Fig. 3.3, the Lebesgue's function for P_{10} tetrahedrons (top) and pyramids (bottom) based on equidistant and optimized points are plotted. The reduction of the Runge phenomenon with optimized set of nodes is clearly visible.

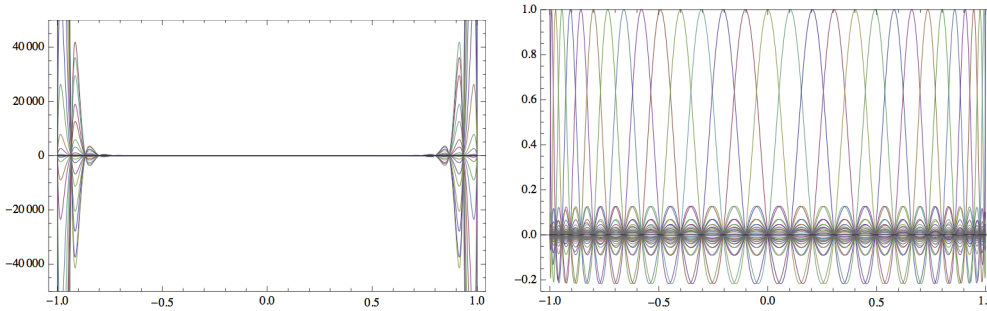


Figure 3.2 – Sets of Lagrangian basis based on equidistant (left) and Gauss-Lobatto (right) points for order 30. From [109].

Gauss quadratures are used for numerical integration over triangles, tetrahedrons, and pyramids. For edges, quadrangles (and hexahedras) the one-dimensional basis is tensorized and Gauss-Legendre-Lobatto quadratures of order $n + 1$ are used with the nodal basis of order $n + 1$ based on Gauss-Lobatto nodes. For that particular case, Gauss points and interpolation points are collocated so that $\ell_i(\boldsymbol{\xi}_j) = \delta_{ij}$, and the integration formula

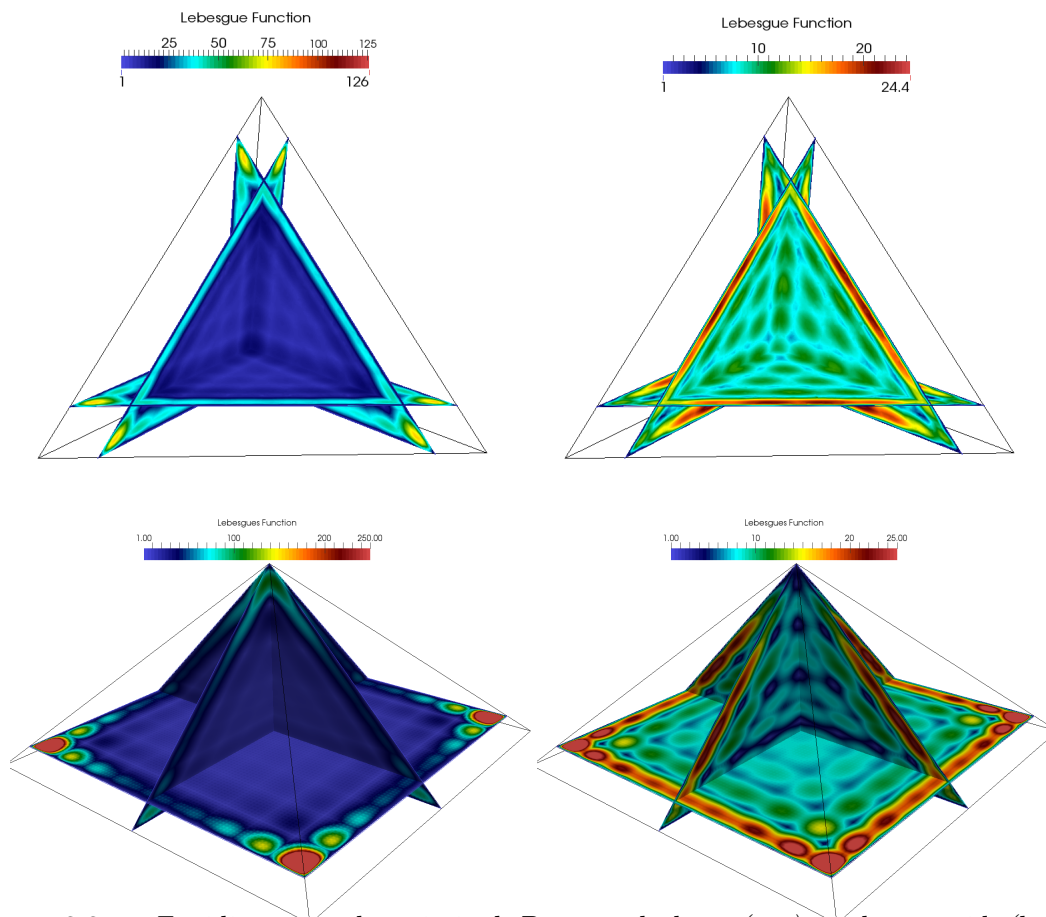


Figure 3.3 – *Equidistant and optimized P_{10} tetrahedron (top) and pyramid (bottom) Lebesgue's function. From [109].*

simplifies:

$$\int_{-1}^{+1} \psi(\xi) d\xi = \sum_{i=0}^n \psi_i \sum_{j=0}^n \omega_j l_i(\xi_j) = \sum_{i=0}^n \omega_i \psi_i, \quad (3.31)$$

where $\{\omega_i; 0 \leq i \leq n\}$ are the quadrature weights. Moreover, the mass matrix is lumped and becomes diagonal. However, the Gauss-Legendre-Lobatto quadrature of order $n + 1$ provides exact numerical integration for polynomials of which degree is lower or equal to $2n - 1$, and the degree of the formulation is $2n + 1$. Several studies [57, 62] have shown that the use of Gauss-Lobatto quadratures does not introduce a numerical error higher than the approximation error for linear problems. For CFD, the collocation of degrees and Gauss points strongly reduces the time of computation. For CAA, as global matrices are stored, it does not change anything.

3.2.4 Boundary conditions

For the boundary conditions we use non-reflective, Padé conditions [89]. These conditions allow us to limit the numerical echo. However they also limit the percentage of randomness that we can take for the perturbation of the flow, as well as the fineness of the mesh that we take.

3.2.5 Time discretization

Once the variational formulation (3.29) has been discretized in space using piecewise polynomial functions, it is discretized in time using a second-order Runge-Kutta explicit scheme [60, 109].

3.3 Imaging in a motionless random medium

In this section the imaging algorithms outlined in Sect. 3.1 are first applied to a motionless random medium. The same configuration as in [24] is considered for validation purposes; see Fig. 3.1. We seek to determine the position of three sources or reflectors buried in an inhomogeneous medium in two dimensions. The inhomogeneous medium will be modeled as a random medium. Regarding the terminology used in the remaining of this chapter, a random medium refers to a medium with a random speed of sound c_0 that can be subjected to deterministic (constant) or random ambient velocity \mathbf{v}_0 . All CFD and CAA simulations were performed using the parallel scalar cluster of ONERA [106]. This cluster has a total of 17,360 cores for a peak performance of 667 Tflop/s. The post-processing of all results was done using Matlab R2015a. All imaging functionals have been normalized and their range is between 0 and 1. In addition, to compare the results obtained by the KM and CINT imaging algorithms, the CINT imaging functional $|\mathcal{I}_{\text{CINT}}|$ and the squared KM imaging functional $|\mathcal{I}_{\text{KM}}|^2$ are formed because $|\mathcal{I}_{\text{CINT}}| \propto |\mathcal{I}_{\text{KM}}|^2$.

3.3.1 Model setup

We thus consider a quiescent ambient medium with $\mathbf{v}_0 = \mathbf{0}$, $\rho_0 = \text{constant}$, and a random speed of sound written here as $c_0(\mathbf{r}) = \underline{c}(1 + \sigma\mu(\mathbf{r}))$, where $\underline{c} = \text{constant}$, σ is the relative standard deviation, and $(\mu(\mathbf{r}), \mathbf{r} \in \mathbb{R}^3)$ is a homogeneous (stationary), mean-zero second-order random process. An exponential autocorrelation function is chosen (also

called Matern 1/2 model) corresponding to non-smooth samples of the random process. This perturbation is simulated by a random Fourier series of the stationary process $\mu(\mathbf{r})$ [111, 117]:

$$\mathcal{R}_\mu(\mathbf{r}, \mathbf{r}') := \mathbb{E} \{ \mu(\mathbf{r}) \mu(\mathbf{r}') \} = e^{-\frac{|\mathbf{r}-\mathbf{r}'|}{\ell_c}}, \quad (3.32)$$

where ℓ_c is the correlation length. The setup for numerical validation is shown in Fig. 3.1 where the dimensions of the problem are given in terms of the central wavelength λ_0 . The horizontal axis is the range and the vertical axis along which the array is aligned is the cross-range. This array contains $N = 185$ transducers at a distance $\lambda_0/2$ from each other, with an aperture $a = 92\lambda_0$. The object to be imaged is at a range $L = 90\lambda_0$ and zero cross-range, and it is either constituted by three sources $6\lambda_0$ apart from each other and emitting the same signals $t \mapsto f(t)$ (passive configuration), or three non penetrable disks of radius λ_0 with homogeneous Dirichlet boundary conditions and centered at the same points (active configuration). In this latter case, the central transducer of the array emits the probing pulse $t \mapsto f(t)$ and all other transducers and this one are used as receivers. The pulse is:

$$f(t) = -\omega_0^2(t - t_0) e^{-\frac{1}{2}\omega_0^2(t-t_0)^2}, \quad (3.33)$$

where $\omega_0 = 2\pi f_0$ is the central (circular) frequency such that $\lambda_0 = \underline{c}/f_0$. We choose $f_0 = 1$ kHz and $t_0 = 1/f_0$ as in [24]; see Fig. 3.4. For this central frequency, the bandwidth of the signal is [0.6–1.3] kHz. All pressure data in the bandwidth [0–1.5] kHz are post-processed to build the KM and CINT imaging functionals.

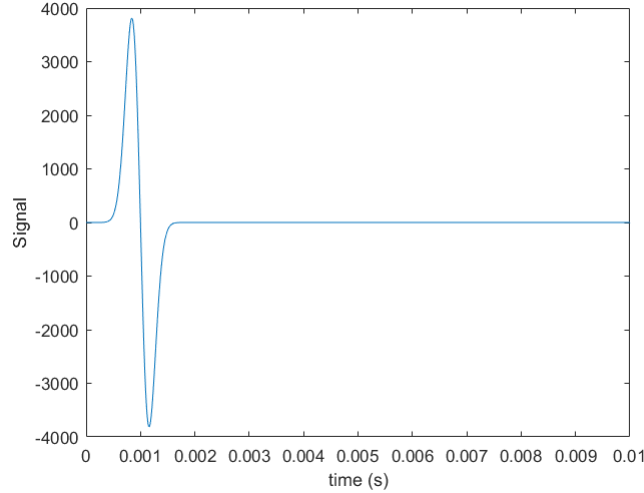


Figure 3.4 – Shape of the signal $t \rightarrow f(t)$ used for CINT imaging in a motionless ambient medium.

The cluttered medium in Fig. 3.1 and subsequent simulations correspond to an average speed of sound $\underline{c} = 3000$ m/s, standard deviation $\sigma = 3\%$, and wavelength $\lambda_0 = 0.3$ m at the central frequency $f_0 = 1$ kHz. The correlation length is $\ell_c = \lambda_0/2 = 0.15$ m. This is a delicate situation to deal with, since $\lambda_0 \simeq \ell_c$ as *a priori* required if one wants to probe objects of this size. To generate the dataset to be post-processed with the imaging functionals described above in Sect. 3.1.2 and Sect. 3.1.3, we use the DG finite element

method described in Sect. 3.2.2 and thus solve the LEE for a random speed of sound. The propagation medium is considered to be infinite in all directions. Numerically, we use non-reflective (Padé) boundary conditions all around the discretized medium in order to avoid wave reflection.

3.3.2 Mesh

The same mesh will be used for all our simulations in this section and the subsequent Sect. 3.4. It consists in triangular elements with 3 nodes, and includes about 1.1 million nodes and 2.3 million elements. Fig. 3.5 shows a zoom on the mesh around one of the three reflectors to be imaged in the active case. The DG SPACE computation code makes it very easy to increase the order of the mesh elements. We voluntarily take polynomials of degree 1 in agreement with the calculations done in [24]. For a central frequency $f_0 = 1000\text{Hz}$ and an average speed of sound $\underline{c} = 3000\text{ m/s}$, this corresponds to about 5 to 10 nodes per wavelength. Some differences will be observed in the resolution of the results obtained here compared to those obtained in [24].

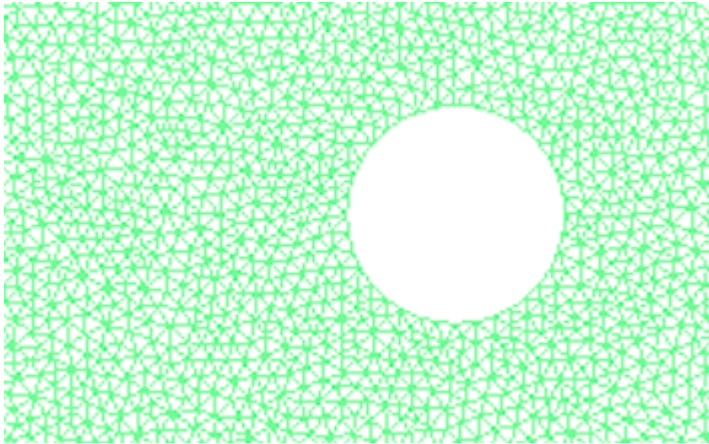


Figure 3.5 – *Mesh used for the validation of the KM and CINT imaging functionals in a motionless and moving random medium. Zoom around one of the three reflectors to be imaged in the active case.*

Indeed, the resolution we use (5-10 nodes per wavelength) is relatively far from the resolution used in [24], which is 30 nodes per wavelength. This choice to lower the accuracy of our mesh had to be done because, in addition to studying the case where the ambient medium is at rest, we also study the case where it is moving with a uniform velocity \mathbf{v}_0 . The latter case greatly deteriorates the Courant-Friedrichs-Lewy (CFL) number $\text{CFL} = \underline{c}\Delta t/\Delta x$ of the time-space discretization scheme, where Δt is the typical time increment and Δx is the typical element edge length. More precisely, we can not have both a fine mesh and a large time step because of the risk that the obtained solution may diverge. So without forgetting that we will post-process all computations with Matlab and are limited by its memory capabilities, and in order to obtain results that have been converged with a number of iterations that do not exceed the capacities of the computer, we use a coarser mesh. Mesh optimization is to be considered in future studies. On the other hand, a regular four-node quadrilateral element mesh is used in [24] as well as a mixed finite element spatial resolution

method and a second-order leapfrog temporal integration scheme [14, 15]. Thus we use a different mesh and resolution scheme.

3.3.3 Active imaging

As a first illustration of the methodology, we consider the localization of three reflectors (active configuration) using the KM imaging functional (3.14) and the CINT imaging functional (3.22). The search domain is a square of size $20\lambda_0 \times 20\lambda_0$ centered around $(90\lambda_0, 0)$.

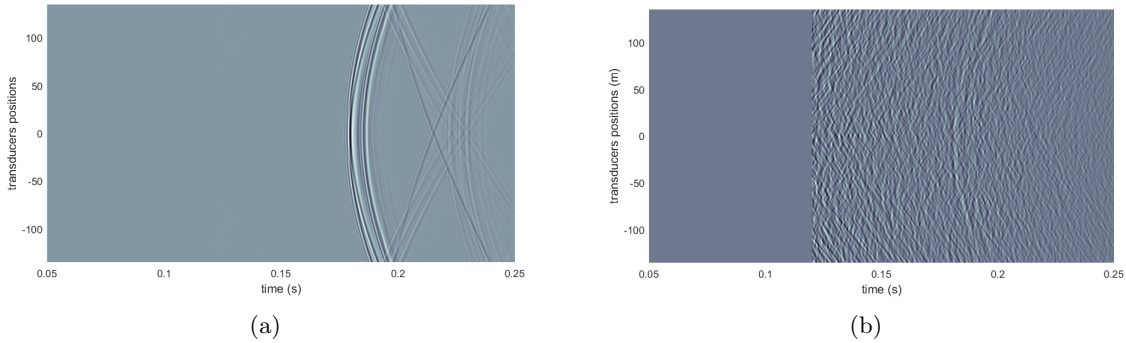


Figure 3.6 – *Imaging in a motionless medium in the configuration of Fig. 3.1. (a) Time traces recorded at the receivers in the case of a constant speed of sound $\underline{c} = 3000$ m/s. (b) Time traces recorded at the receivers in the case of a random speed of sound of mean $\underline{c} = 3000$ m/s and standard deviation $\sigma = 3\%$. The horizontal axis is time (in s) and the vertical axis is the array transducer location (in units of λ_0).*

Let us first look at the case where the motionless medium of Fig. 3.1 is homogeneous, that is, its speed of sound is constant and equal to \underline{c} . For this case, the KM imaging functional should give peaks corresponding to the positions of the reflectors. An example of the signals scattered by the reflectors is shown in Fig. 3.6(a). In the active configuration we use the central sensor as a source and all the sensors of the array as receivers. We clearly distinguish the echoes of the signal for each reflector. In addition, the signals are symmetric with respect to the central receiver which also serves as a source. Therefore, we should be able to find the position of each reflector. To be convinced of this, the results obtained with the KM imaging algorithm are given in Fig. 3.7 with a pixel size of $\lambda_0/2$. We find the three reflectors in the middle of the search region. However, the peak of the imaging functional at the position of the reflectors is not as sharp as in [24]. This spread of the peak is mainly attributed to the mesh used. This result is deemed sufficient for a first study, though. A refined mesh shall be used in future works.

In the case of the motionless medium of Fig. 3.1 with a random speed of sound, it is much more difficult to distinguish the wavefront and the echoes of the three reflectors on Fig. 3.6(b), since the signals are noisy. The causes of this noise are the multiple scattering of acoustic waves on the inhomogeneities present in the medium. In addition, the noise will be different from one realization of the medium to another. We understand very well why KM imaging algorithm is not effective. Indeed we back-propagate all the noise contained in the signals recorded by the receivers, and this noise is not canceled by the Green's function \hat{G}_0 of the homogeneous ambient medium playing the role here of a fictitious medium. This noise

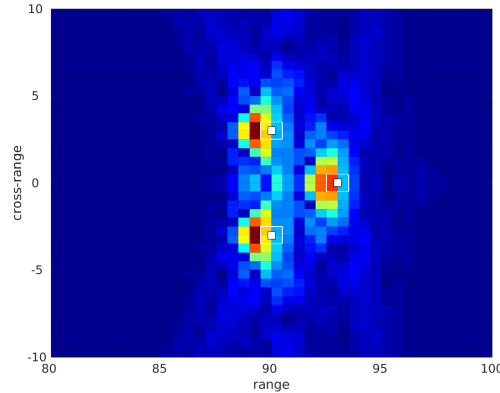


Figure 3.7 – *KM active imaging in a motionless medium in the configuration of Fig. 3.1 with constant speed of sound $\underline{c} = 3000$ m/s. The reflectors to be localized are drawn in white.*

phenomenon appears very clearly when we compute the KM imaging functional (Fig. 3.8(a) and Fig. 3.8(b)). We observe noisy images that are different from one realization of the medium to another, hence we get statistically unstable images. The random phase present in the signals is not satisfactorily canceled by back-propagation. We do not get a sharp peak around the position of the three different reflectors as in the case of the homogeneous motionless medium.

Let us now look at the results obtained with the CINT imaging algorithm. The results are displayed in Fig. 3.8(c) and Fig. 3.8(d) for respectively the first realization of the medium and the second realization of the medium with the same mean $\underline{c} = 3000$ m/s and standard deviation $\sigma = 3\%$. The squared KM imaging functional $|\mathcal{I}_{\text{KM}}|^2$ is shown because when $X_d = a$ and $\Omega_d = B$, we have $|\mathcal{I}_{\text{CINT}}| = |\mathcal{I}_{\text{KM}}|^2$. The optimal CINT parameters will be denoted by $\Omega_d = \Omega_d^*$ and $X_d = X_d^*$ in the following. They were found "by hand", however there may be a more optimal set of parameters but the adaptive algorithm [26] was not used. Indeed in our computational setup producing a CINT image takes several hours. It is therefore faster to find parameters close to the optimal parameters by hand. However we think that with the ability to produce images more quickly the adaptive choice presented in [26] is a real plus for producing images with a better resolution. Overall we can observe that the images are less noisy than those obtained by the KM imaging algorithm, as they are smoother and statistically stable. By using the CINT imaging algorithm, we can thus cancel a certain part of the random phase present in the signals acquired by the receivers and coming from the multiple scattering of the acoustic waves on the inhomogeneities of the medium. The influence of the realization of the random medium has therefore been reduced as can be seen on Fig. 3.8. For two different realizations of the medium, we obtain two different images with the KM imaging functional but CINT imaging results are relatively close. Nevertheless, as expected, the cross-range resolution and the range resolution are slightly altered. The peak centered around each reflector, which has been observed in the case of an homogeneous medium, is rather spread here. This comes from the smoothing of the image induced by the CINT imaging algorithm. Obtaining a good image is therefore based on the compromise between the smoothing necessary to compensate the noise and

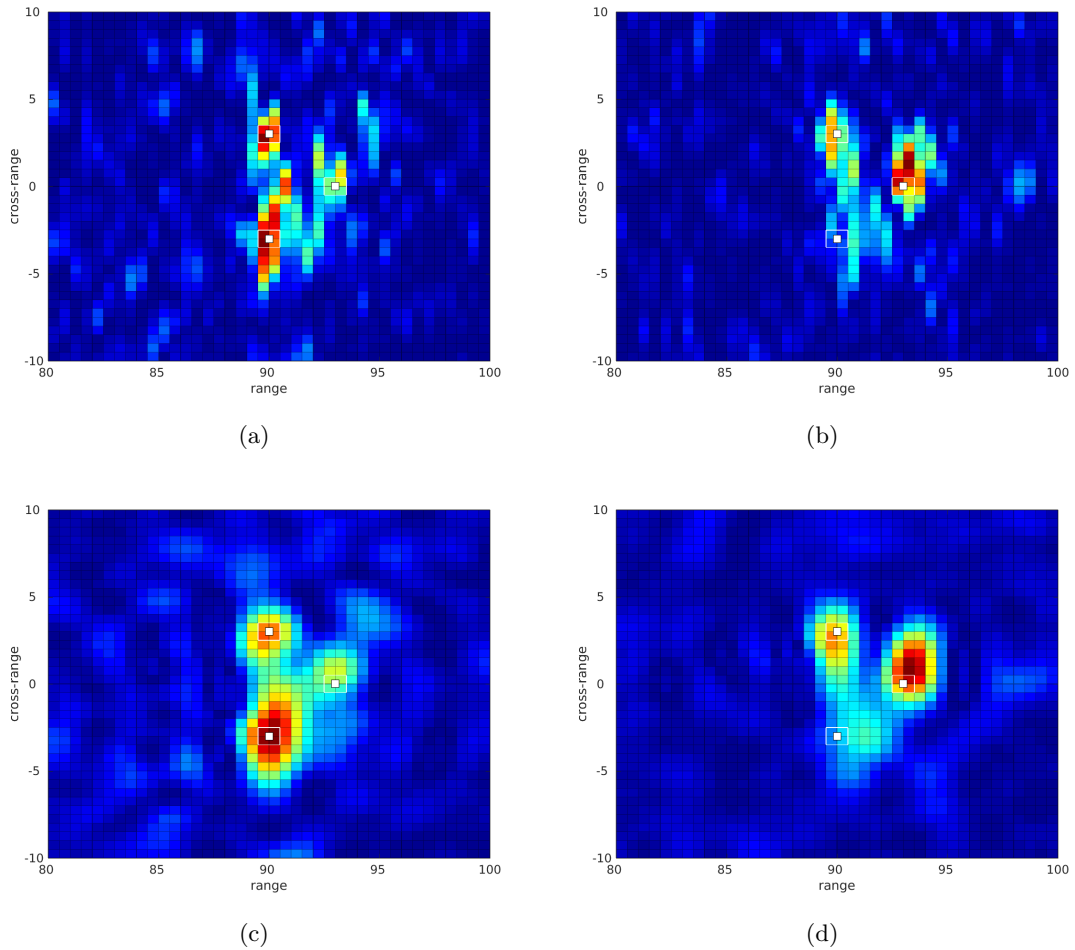


Figure 3.8 – Active imaging in a motionless medium in the configuration of Fig. 3.1 with random speed of sound with mean $\underline{c} = 3000$ m/s and standard deviation $\sigma = 3\%$. Comparison of the KM and CINT imaging functionals for two different realizations of the random medium. (a) Squared KM imaging functional for the first realization of the medium. (b) Squared KM imaging functional for the second realization of the medium. (c) CINT imaging functional for the first realization of the medium. (d) CINT imaging functional for the second realization of the medium. $\Omega_d = 0.09 \times B$ and $X_d = 0.85 \times a$ for both media. The reflectors to be localized are drawn in white.

the loss of resolution that it induces. It is the heart of the CINT imaging algorithm through the choice of parameters Ω_d and X_d . The choice of an optimal decoherency frequency Ω_d contributes to enhance range resolution, while the choice of an optimal decoherency length X_d contributes to enhance cross-range resolution.

3.3.4 Passive imaging

Some results are briefly presented now for the case of passive imaging. Here the sensors in the array are used as receivers only, and we want to localize three sources buried in a

motionless medium with a random speed of sound; see again Fig. 3.1. In this configuration we note that the KM imaging functional easily finds the sources, so there is little interest of using the CINT imaging algorithm in this configuration to the extent that much less time is required to produce an image by the KM imaging algorithm. We can see on Fig. 3.9 that the two imaging functionals find the three sources with good precision. Indeed in the passive setup the signal emitted by the sources goes through the random medium only once, which is not enough to be sufficiently scattered and put in default the KM imaging algorithm. Surely, there should be higher levels of randomness to achieve this. In the next two sections we will use an active imaging setup to show the interest of the CINT imaging algorithm compared to the KM imaging algorithm.

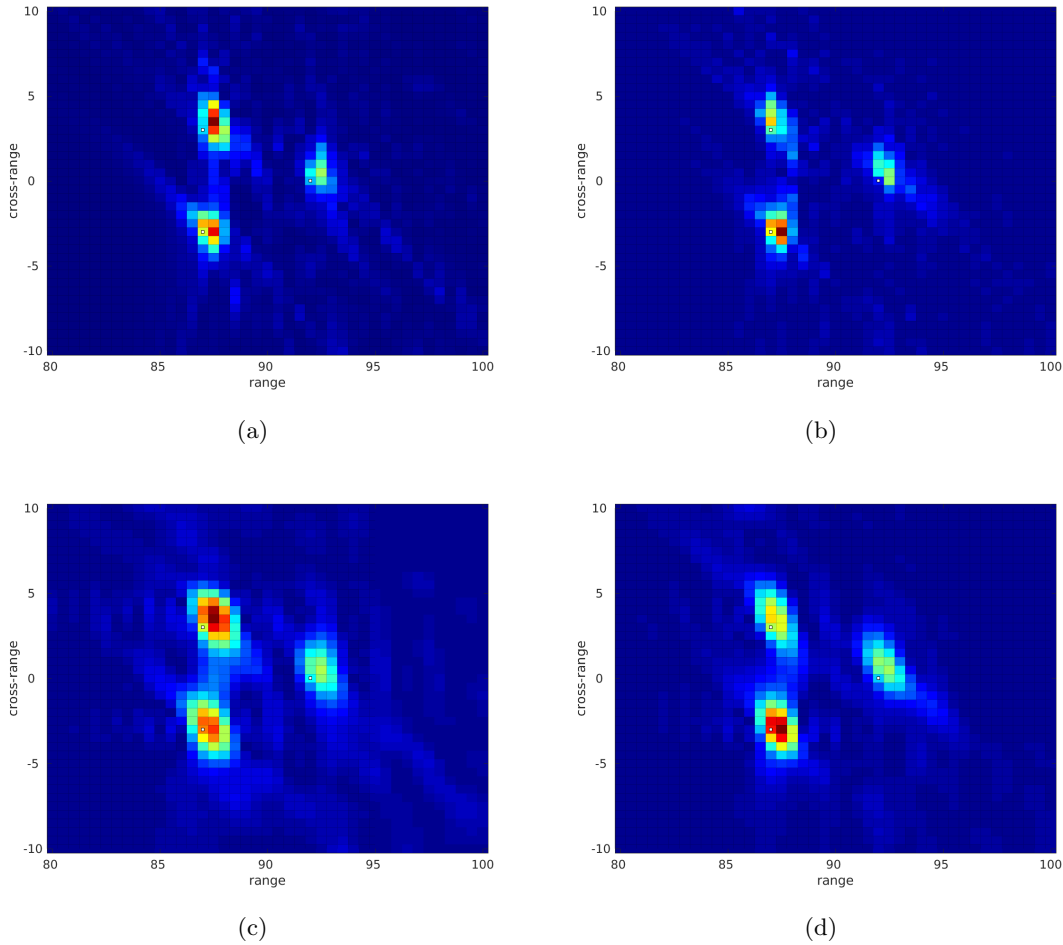


Figure 3.9 – *Passive imaging in a motionless medium in the configuration of Fig. 3.1 with random speed of sound with mean $\bar{c} = 3000$ m/s and standard deviation $\sigma = 3\%$. Comparison of the KM and CINT imaging functionals for two different realizations of the random medium. (a) Squared KM imaging functional for the first realization of the medium. (b) Squared KM imaging functional for the second realization of the medium. (c) CINT imaging functional for the first realization of the medium. (d) CINT imaging functional for the second realization of the medium. $\Omega_d = 0.09 \times B$ and $X_d = 0.85 \times a$ for both media. The sources to be localized are drawn in white.*

3.4 Imaging in a moving random medium

In this section, we consider again the configuration depicted in Fig. 3.1, except that the ambient medium is now moving at the velocity \mathbf{v}_0 which may be either uniform, or randomly perturbed around its mean uniform value. At first we will assume that the speed of sound is constant in order to highlight the role of the Doppler compensation factor (3.16) for the KM and CINT imaging algorithms in that moving ambient medium. Then the speed of sound will also be randomly perturbed around its mean value, as in the foregoing section.

3.4.1 Active imaging in a random medium moving at a uniform velocity

The ambient medium is moving at a uniform velocity \mathbf{v}_0 in the cross-range direction:

$$\mathbf{v}_0 = \begin{pmatrix} 0 \\ M \cdot \underline{c} \end{pmatrix} \quad (3.34)$$

with the Mach number $M = 0.3$ and $\underline{c} = 3000$ m/s. We use the KM imaging functional (3.20) and CINT imaging functional (3.26) to localize the three reflectors in Fig. 3.1 (active configuration). First of all, let us look at the signals recorded by all the sensors for either a constant or a random speed of sound; see Fig. 3.10. We note that the symmetry with respect to the transducer used as a source—the central sensor—is no longer respected. This is because the ambient medium is now moving in the cross-range upward direction. We thus understand that this phenomenon will have to be considered by a certain correction factor in our imaging functionals. This is the role of the Doppler compensation coefficient γ_D of Eq. (3.16). In Fig. 3.10, we still see the different echoes of the signal on the reflectors. Thus, if our coefficient is correct, we should be able to see the position of each reflector in that case of a constant speed of sound.

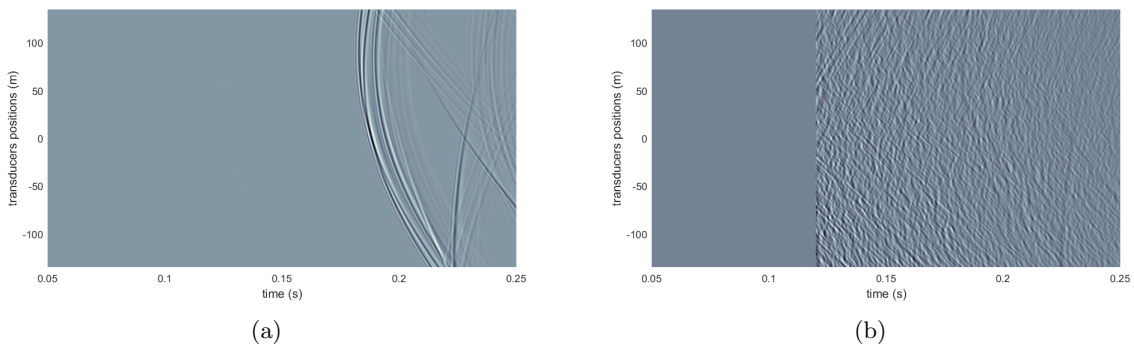


Figure 3.10 – *Imaging in a moving medium in the configuration of Fig. 3.1 with uniform velocity in the cross-range direction. (a) Time traces recorded at the receivers in the case of a constant speed of sound $\underline{c} = 3000$ m/s. (b) Time traces recorded at the receivers in the case of a random speed of sound of mean $\underline{c} = 3000$ m/s and standard deviation $\sigma = 3\%$. The horizontal axis is time (in s) and the vertical axis is the array transducer location (in units of λ_0).*

In order to highlight the role of the Doppler compensation coefficient, we show in Fig. 3.11 the KM imaging functional (3.18) without γ_D (Fig. 3.11(a)) and the KM imaging

functional (3.20) with γ_D (Fig. 3.11(b)). The speed of sound is constant and the search domain is a square of size $20\lambda_0 \times 20\lambda_0$ centered around $(90\lambda_0, 0)$. We note that when γ_D is not used, we do not find the positions of the three reflectors. Indeed, in this case, we back-propagate the signals in a medium at rest. Conversely, when γ_D is taken into account in the KM imaging functional, we get their position relatively well. Nevertheless, we notice that there is a slight shift for the top reflector. There can be several explanations: error of discretization during the resolution of the equations, imperfect reflections of the waves on the reflectors and/or imperfect absorption on the edges of the computational domain, or error induced in the model by the (first-order) corrector γ_D . Further study may lead to a better understanding of this phenomenon.

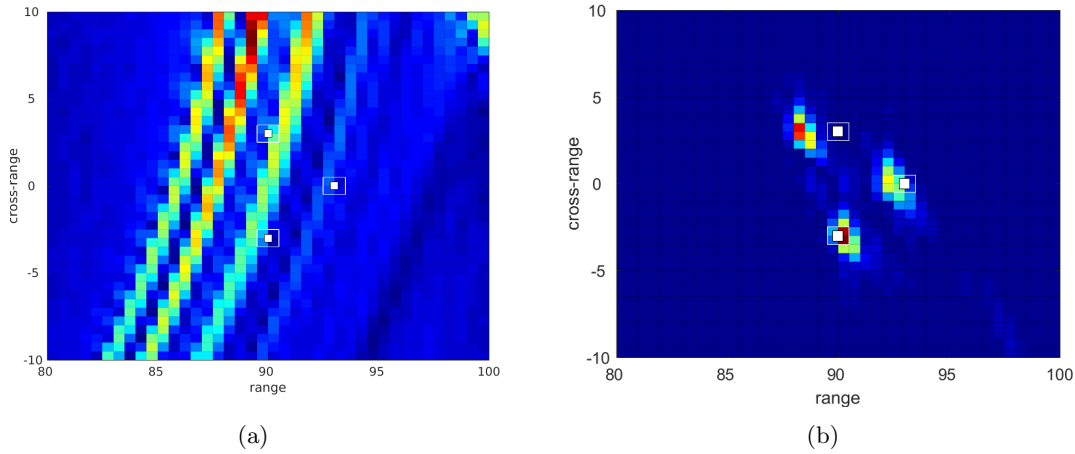


Figure 3.11 – *KM active imaging in a moving medium in the configuration of Fig. 3.1 with constant velocity \mathbf{v}_0 in the cross-range upward direction and constant speed of sound $\underline{c} = 3000$ m/s. Influence of the Doppler compensation coefficient γ_D on KM imaging functional: (a) without γ_D ; (b) with γ_D . The reflectors to be localized are drawn in white.*

Then the speed of sound of the ambient medium moving at the uniform velocity \mathbf{v}_0 of (3.34) is randomly perturbed about its mean value \underline{c} with the standard deviation $\sigma = 3\%$. From now on, the Doppler compensation factor γ_D of (3.16) will be considered for all simulations. The KM imaging functional for two realizations of the medium is shown in Fig. 3.12. As in Fig. 3.8, we observe very noisy images that differ from one realization of the medium to another. We thus apply the CINT imaging algorithm to the signals received by the receivers. The optimal setting for Ω_d and X_d is found in the same way as before. The results can be seen in Fig. 3.13. We only show one realization of the medium but we can make the same observations as in Sect. 3.3: the KM imaging algorithm is statistically unstable while the CINT imaging algorithm is statistically stable. For the KM imaging functional of Fig. 3.13(a), we have difficulties finding the positions of the three reflectors since the image is noisy. For the CINT imaging functional of Fig. 3.13(b), the positions of the three reflectors appears much more clearly. The uncertainties present on the image obtained by the KM algorithm have practically disappeared. Nevertheless, we have, as expected, a loss in resolution that comes from the smoothing phenomenon of the CINT algorithm.

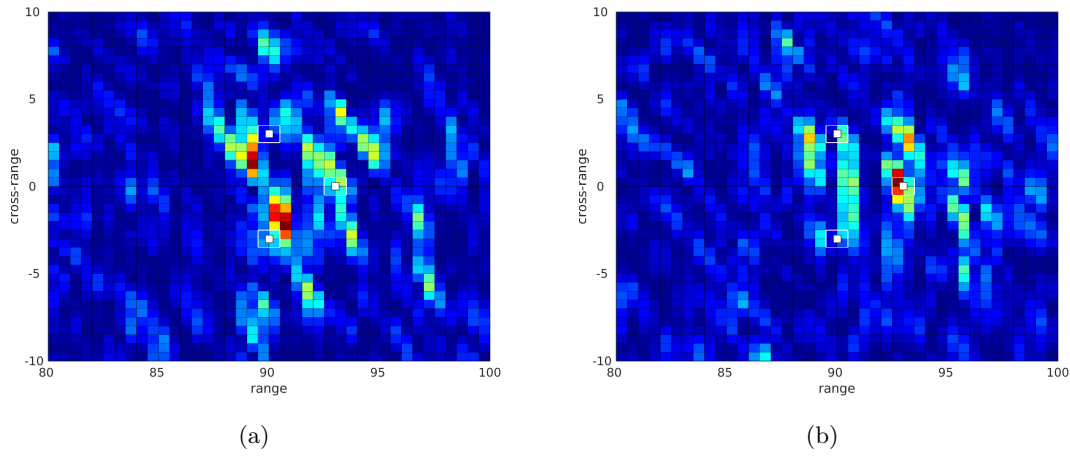


Figure 3.12 – KM active imaging in a moving medium in the configuration of Fig. 3.1 with constant velocity \mathbf{v}_0 in the cross-range upward direction and random speed of sound with mean $\underline{c} = 3000$ m/s and standard deviation $\sigma = 3\%$. (a) Squared KM imaging functional for the first realization of the medium. (b) Squared KM imaging functional for the second realization of the medium. The reflectors to be localized are drawn in white.

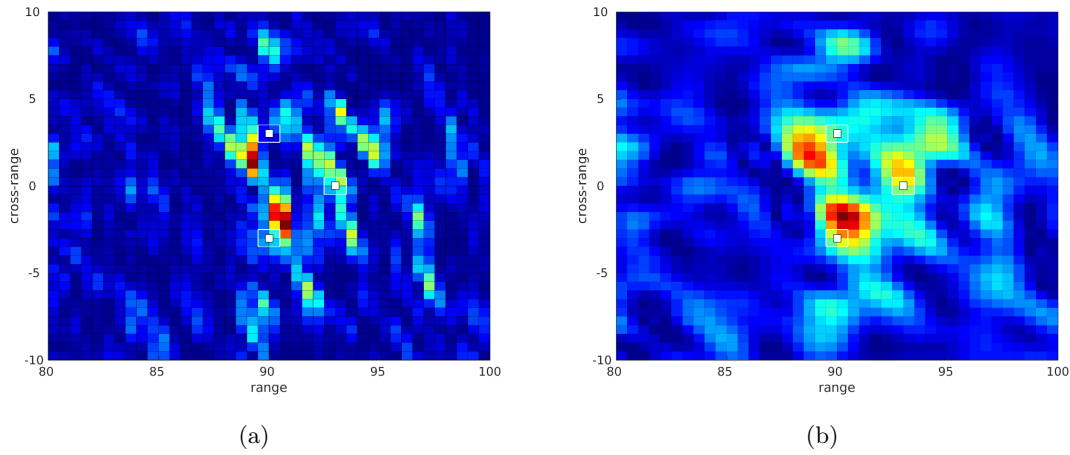


Figure 3.13 – Active imaging in a moving medium in the configuration of Fig. 3.1 with constant velocity \mathbf{v}_0 in the cross-range upward direction and random speed of sound with mean $\underline{c} = 3000$ m/s and standard deviation $\sigma = 3\%$. Comparison of the KM and CINT imaging functionals for one realization of the random medium. (a) Squared KM imaging functional. (b) CINT imaging functional with $\Omega_d = \frac{B}{12}$ and $X_d = 0.9 \times a$. The reflectors to be localized are drawn in white.

3.4.2 Active imaging in a random medium moving at a random velocity

The same configuration as in the previous sections is considered (see Fig. 3.14), but the ambient medium is now moving at a random velocity \mathbf{v}_0 :

$$\mathbf{v}_0(\mathbf{r}) = \begin{pmatrix} \sigma_1 \mu_1(\mathbf{r}) \\ M \cdot \underline{c}(1 + \sigma_2 \mu_2(\mathbf{r})) \end{pmatrix}$$

with the Mach number $M = 0.3$, $\underline{c} = 3000$ m/s, and $\sigma_1 = \sigma_2 = 3\%$. The disturbances μ_1 and μ_2 are stationary, mean-zero independent random processes. Matern 1/2 autocorrelation functions (3.32) are chosen for μ_1 and μ_2 . These perturbations are simulated by random Fourier series of stationary processes [111, 117]. One realization is shown on Fig. 3.14(c)–3.14(d) for illustration purposes. We note that this random ambient velocity \mathbf{v}_0 does not necessarily solve the ambient flow equations (3.2) and the autocorrelation functions of its turbulent components do not fulfill the necessary condition Eq. (1.37). This simplified model is a first attempt to take into account turbulent phenomena with the KM and CINT imaging algorithms. More realistic models shall be envisaged in future works.

In the same way as in the previous sections, let us first look at the signals recorded by all the sensors for either a constant or a random speed of sound; see Fig. 3.15. We note that the symmetry with respect to the transducer used as a source—the central sensor—is not respected. Compared to the moving medium with constant velocity, we observe here an echo fairly close to the echo in Fig. 3.10 but noisier. This is induced by the velocity of the ambient medium which is now random. Thus, the waves propagating in this medium will also be noisy. However, even in the presence of this noise, we always see the different fronts representing the echoes of the signal on the three reflectors. The role of the Doppler compensation coefficient γ_D is also highlighted in Fig. 3.16. Here we show the KM imaging functional (3.18) without γ_D and the KM imaging functional (3.20) with γ_D for one realization of the random velocity \mathbf{v}_0 of the ambient medium. The compensation coefficient is computed for the mean velocity of the ambient medium. The search domain is again a square of size $20\lambda_0 \times 20\lambda_0$ centered around $(90\lambda_0, 0)$. KM imaging algorithm accounting for the Doppler compensation coefficient works well in this configuration (constant speed of sound) even if the ambient flow velocity is random.

Images obtained by the KM imaging algorithm for two realizations of the ambient medium with random velocity and random speed of sound are shown in Fig. 3.17. We observe, as in the preceding cases, the statistical instability of the KM imaging functional, since we can not determine unambiguously the positions of the reflectors for any realization of the medium. We thus apply the CINT imaging algorithm to the signals received by the receivers. The optimal setting for Ω_d and X_d is found in the same way as before. The results can be seen in Fig. 3.18. We only show one realization of the medium but we can make the same observations as in Sect. 3.3. Using the KM imaging algorithm (Fig. 3.18(a)), we can not distinguish the positions of the three reflectors. On the contrary, using the CINT imaging algorithm (Fig. 3.18(b)), we can much more easily distinguish the positions of the three reflectors. However, we can notice two things. First, we still have a loss in resolution due to smoothing. Second, we can observe that there are slight offsets of the positions of the reflectors (of the order of a few pixels). This phenomenon can be explained by the fact that the mesh step is not sufficiently reduced, discretization errors are therefore present and not negligible. It could also be explained by the fact that the Doppler compensation coefficient γ_D is a first order correction.

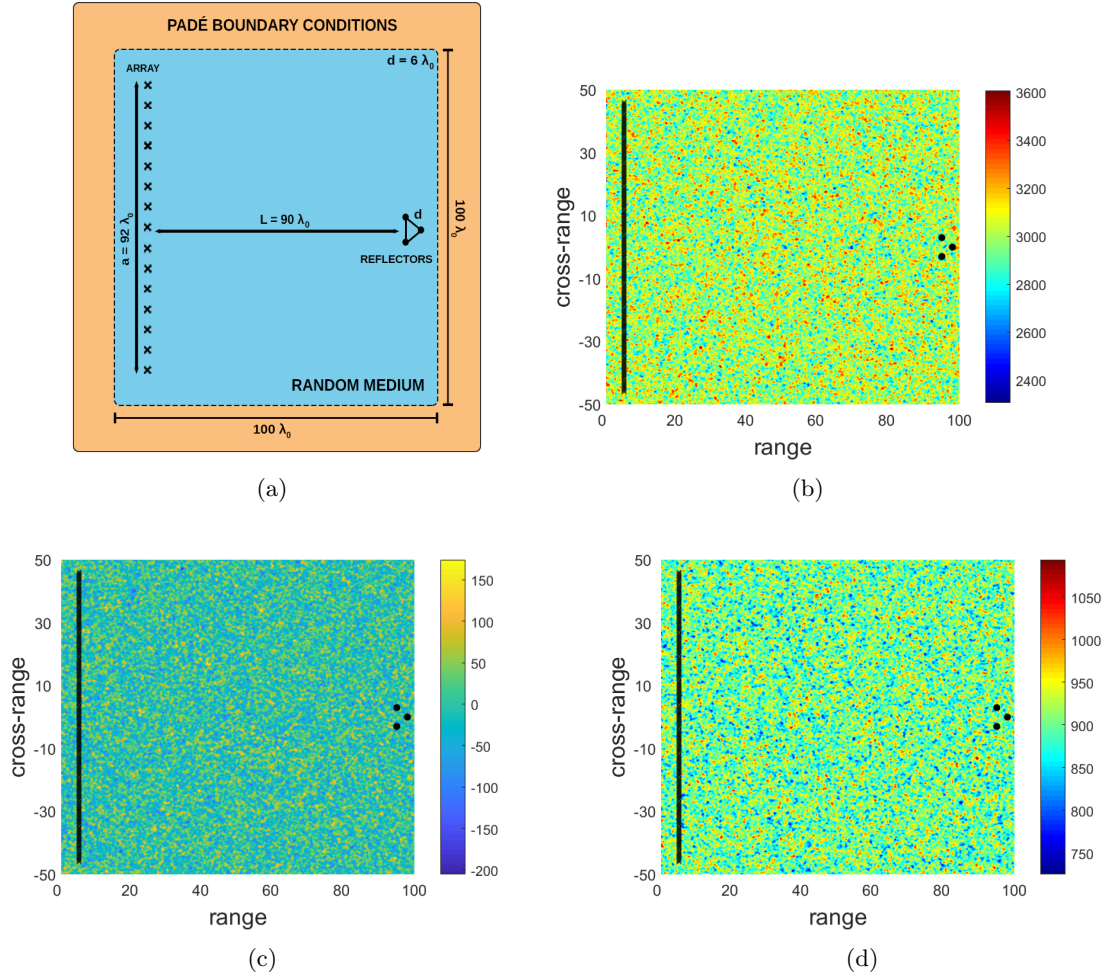


Figure 3.14 – Active imaging in a moving medium with random velocity \mathbf{v}_0 and random speed of sound with mean $\underline{c} = 3000$ m/s and standard deviation $\sigma = 3\%$. The locations of the reflectors to be imaged is shown by dots \bullet and the locations of the transducers is shown by crosses \times . (a) Computational setup with dimensions in terms of the central wavelength λ_0 . (b) Typical realization of the random speed of sound $c_0(\mathbf{r})$. (c) Typical realization of the random ambient flow velocity in the range direction. (d) Typical realization of the random ambient flow velocity in the cross-range direction.

3.5 Passive imaging through a synthetic turbulent jet flow

In this section we finally aim at getting closer to a real flow configuration by trying to build images through a synthetic turbulent jet flow. Indeed, until now, the medium in which the imaging algorithms were tested does not really have any physical relevance, contrary to the framework in which this section fits.

3.5.1 Model setup

A sketch of the configuration considered here is shown in Fig. 3.19. This case study is inspired by the experiments conducted by Candel *et al.* in the 70's [41–43] at the Von

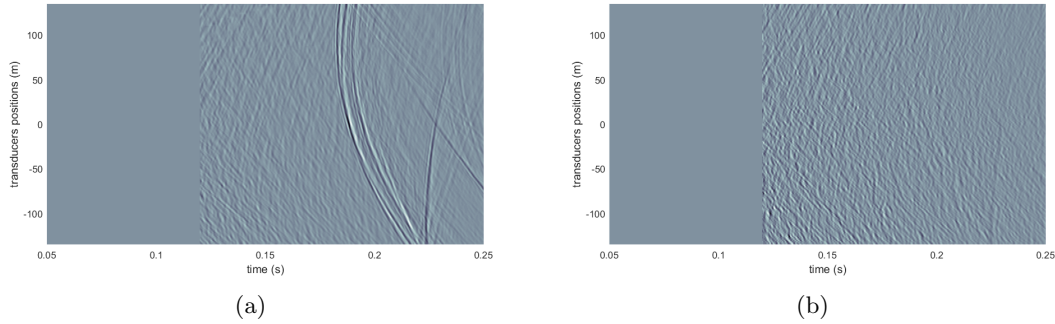


Figure 3.15 – *Imaging in a moving medium in the configuration of Fig. 3.14 with random velocity. (a) Time traces recorded at the receivers in the case of a constant speed of sound $\underline{c} = 3000$ m/s. (b) Time traces recorded at the receivers in the case of a random speed of sound of mean $\underline{c} = 3000$ m/s and standard deviation $\sigma = 3\%$. The horizontal axis is time (in s) and the vertical axis is the array transducer location (in units of λ_0).*

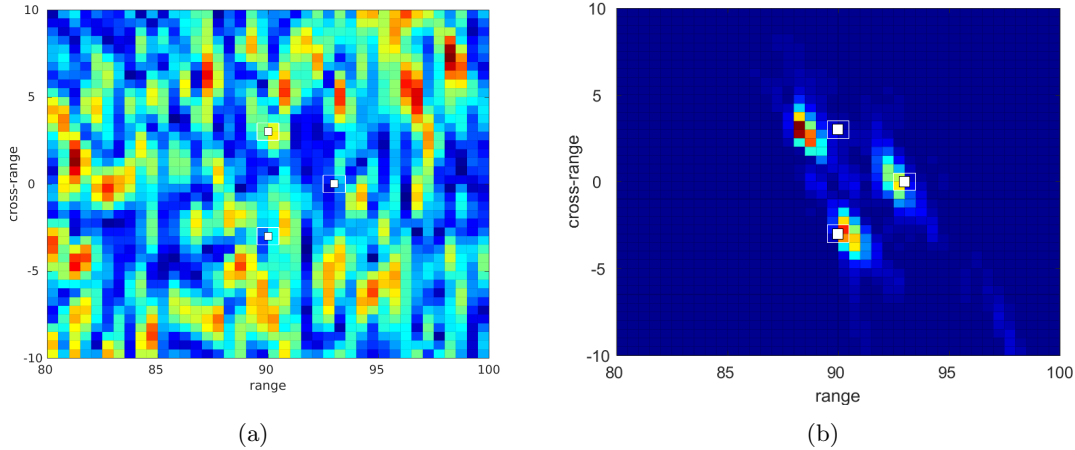


Figure 3.16 – *KM active imaging in a moving medium in the configuration of Fig. 3.14 with random velocity \mathbf{v}_0 and constant speed of sound $\underline{c} = 3000$ m/s. Influence of the Doppler compensation coefficient γ_D on KM imaging functional: (a) without γ_D ; (b) with γ_D . The reflectors to be localized are drawn in white.*

Kármán institute, and more recently by Kröber *et al.* [91] at the Aeroacoustic Wind Tunnel Braunschweig (AWB) facility, and by Sijtsma *et al.* [118] at the DNW (the German-Dutch Wind Tunnels) PLST wind tunnel. The jet inflow boundary conditions (left side of Fig. 3.19) yield two sub-domains with average ambient flow velocities $U_1 = 100$ m/s and $U_2 = 50$ m/s, respectively, with turbulent shear layers in between. Our goal is to image point sources lying in the first medium with an array of sensors placed in the second medium—that is, a passive imaging setup in the terminology used in the foregoing sections.

The data for this generic jet configuration are synthesized numerically in two steps as follows:

- First, we simulate the ambient shear flow by solving the Euler equations using the

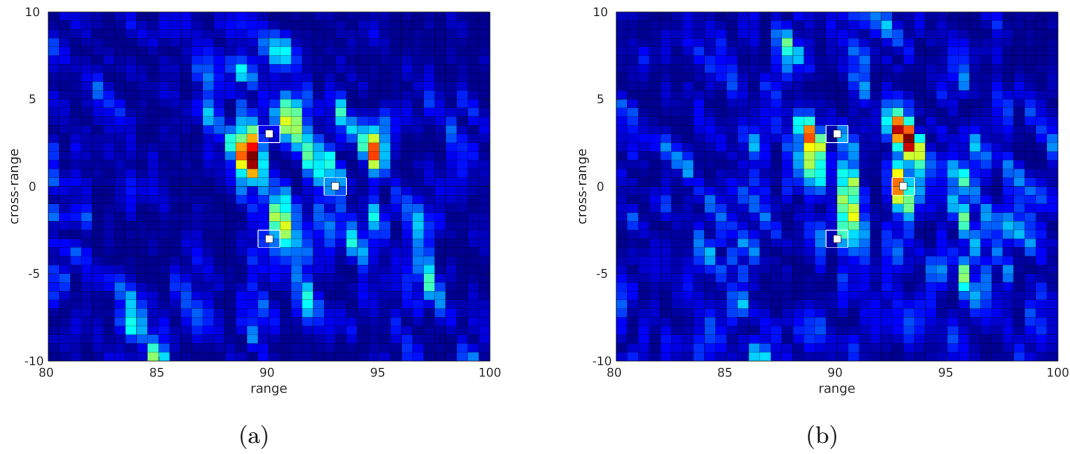


Figure 3.17 – *KM active imaging in a moving medium in the configuration of Fig. 3.14 with random velocity \mathbf{v}_0 and random speed of sound with mean $\underline{c} = 3000$ m/s and standard deviation $\sigma = 3\%$. (a) Squared KM imaging functional for the first realization of the medium. (b) Squared KM imaging functional for the second realization of the medium. The reflectors to be localized are drawn in white.*

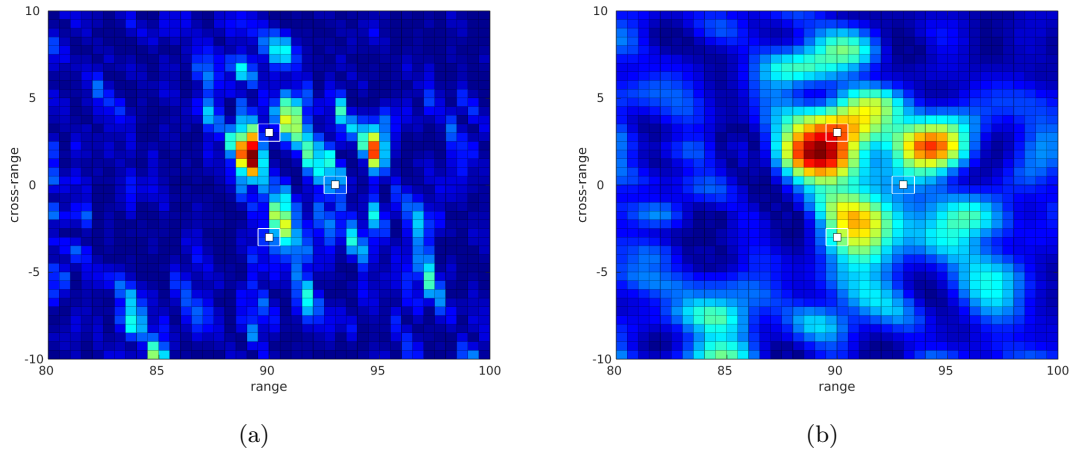


Figure 3.18 – *Active imaging in a moving medium in the configuration of Fig. 3.14 with random velocity \mathbf{v}_0 and random speed of sound with mean $\underline{c} = 3000$ m/s and standard deviation $\sigma = 3\%$. Comparison of the KM and CINT imaging functionals for one realization of the random medium. (a) Squared KM imaging functional. (b) CINT imaging functional with $\Omega_d = \frac{B}{15}$ and $X_d = 0.9 \times a$. The reflectors to be localized are drawn in white.*

DG solver outlined in Sect. 3.2.1. This is the CFD step. In order to generate turbulence, viscosity phenomenon must be present. By definition, Euler equations are theoretically only used to solve perfect fluids, *i.e.* without viscosity. Nevertheless, some viscosity is actually generated by the numerical scheme. At first, we will use this numerical viscosity to simulate the turbulent shear layers.

— Second, we simulate the propagation of acoustic waves in the ambient flow obtained in

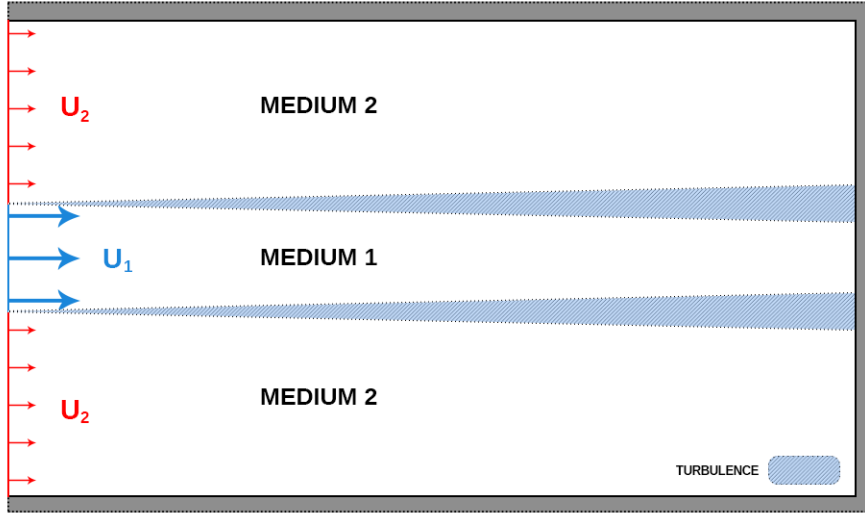


Figure 3.19 – *Synthetic jet flow configuration: ■ non-reflection Padé boundary conditions; — jet inflow boundary condition for the central zone with $U_1 = 100$ m/s; — jet inflow boundary condition outside the central zone with $U_2 = 50$ m/s.*

the CFD step by solving the linearized Euler equations using the DG solver outlined in Sect. 3.2.2. This is the CAA step. In a first approximation, we will consider that the acoustic phenomena are much faster than the fluidic phenomena. As a result, the ambient flow will be considered as "frozen". The flow obtained at the last time increment of the CFD step will be used as the carrier (ambient) flow for the CAA step.

3.5.2 Imaging setup

A parameterization of the imaging setup for the synthetic jet flow of Fig. 3.19 is shown in Fig. 3.20. We seek to determine the positions of three point sources whose emitted signals pass through a turbulent shear layer. All sources emit the same signal given by Eq. (3.33). The central frequency is here $f_0 = 50$ kHz. The fluid studied is the air defined by a speed of sound $\underline{c} = 340$ m/s at the temperature $T = 20^\circ\text{C}$. This corresponds to a wavelength $\lambda_0 = 6.8 \times 10^{-3}$ m. The remote array contains 45 sensors at a distance $\frac{\lambda_0}{2}$ from each other.

3.5.3 Mesh for the CFD and CAA computations

The same mesh is used for both the CFD and CAA steps. It is constructed so that there are 30 elements per wavelength λ_0 (the typical wave length of the source) for a mesh size of $100\lambda_0 \times 100\lambda_0$. We thus have 3000×3000 elements, that is a total of 9 million elements. The mesh is regular and composed of quadrilateral elements with four nodes each.

3.5.4 Flow calculation

The base flow computed in the CFD step is shown in Fig. 3.21. As a first approximation, we will consider it as frozen and use it as the ambient flow for testing the KM and CINT

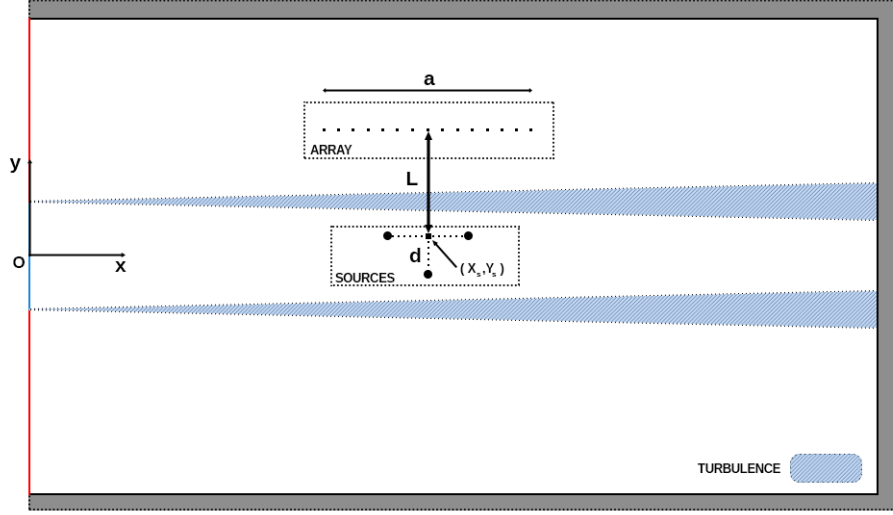


Figure 3.20 – *Synthetic jet flow configuration: imaging setup.* a is the aperture of the sensors array, L is the distance between the central sensor and the barycenter of the two upper sources, and d is the distance between this barycenter and the lower source.

imaging algorithms. We can already notice that we will observe the development of a turbulent shear layer at the interfaces between the parts of the jet having different inflow velocities. This turbulent layer arises from the inflow velocity difference: 100 m/s for the first medium located between $-10\lambda_0$ and $10\lambda_0$ along the range axis (y), and 50 m/s elsewhere (the second medium). It should be noted at this stage that we are not interested in computing precisely the turbulent structures for this jet configuration. Our aim is rather to test the imaging algorithms in such a heterogeneous medium. The turbulent layers as resolved by the present numerical scheme are sufficient to exhibit and discuss their main features.

3.5.5 Refraction compensation mechanism

In addition to the Doppler compensation coefficient γ_D of Eq. (3.16) which accounts for the convection effects, we must consider the fact that the acoustic waves generated by the source in the first medium will pass through media subjected to different velocities; see Fig. 3.22. Thus, we introduce a refraction compensation mechanism in the imaging functionals introduced in Sect. 3.1. In this context the KM passive imaging functional (3.17) and CINT passive imaging functional (3.25) take the form:

$$\mathcal{I}_{\text{KM}}(\mathbf{r}^S) = \sum_{r=1}^N p(\mathbf{r}_r, \gamma_{D_1}(\mathbf{r}^S, \mathbf{r}_O, U_1 \hat{\mathbf{e}}_x) T_1 + \gamma_{D_2}(\mathbf{r}_O, \mathbf{r}_r, U_2 \hat{\mathbf{e}}_x) T_2), \quad (3.35)$$

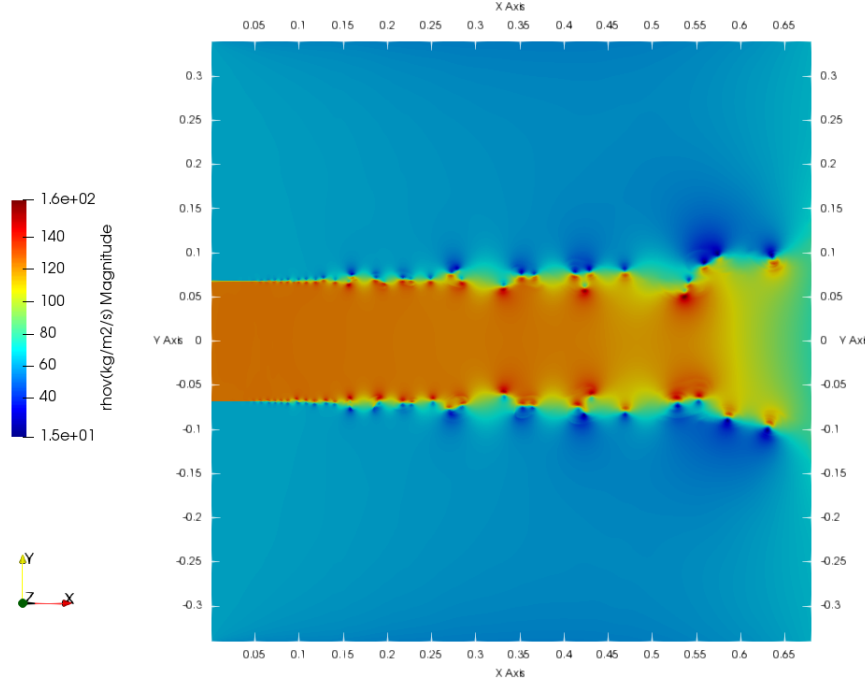


Figure 3.21 – Base flow obtained by solving Euler equations (CFD step) using a DG finite element method for space discretization and Runge-Kutta method for time discretization for the synthetic jet configuration of Fig. 3.19. The color gradient represents the norm of the momentum $|\rho\mathbf{v}|$.

and:

$$\begin{aligned} \mathcal{I}_{\text{CINT}}(\mathbf{r}^S; \Omega_d, X_d) = & \sum_{\substack{q, r = 1 \\ |\mathbf{r}_q - \mathbf{r}_r| \leq X_d}}^N \iint_{|\omega - \omega'| \leq \Omega_d} \widehat{\mathcal{C}}(\mathbf{r}_q, \mathbf{r}_r, \omega, \omega') e^{-i\omega(\gamma_{D_1}(\mathbf{r}^S, \mathbf{r}_O, U_1 \hat{\mathbf{e}}_x)T_1 + \gamma_{D_2}(\mathbf{r}_O, \mathbf{r}_q, U_2 \hat{\mathbf{e}}_x)T_2)} \\ & \times e^{i\omega'(\gamma_{D_1}(\mathbf{r}^S, \mathbf{r}_{O'}, U_1 \hat{\mathbf{e}}_x)T'_1 + \gamma_{D_2}(\mathbf{r}_{O'}, \mathbf{r}_r, U_2 \hat{\mathbf{e}}_x)T'_2)} d\omega d\omega', \quad (3.36) \end{aligned}$$

respectively, where $\hat{\mathbf{e}}_x$ is the unit vector along the (horizontal) direction of the ambient flow. The Doppler compensation coefficients γ_{D_1} and γ_{D_2} are calculated as in (3.16) with the velocities of sound c_1 and c_2 of the two media. Referring to Fig. 3.22 where α is the angle of the incident wave, β the angle of the refracted wave, and \mathcal{O} is the point of the interface between both media where the wave is refracted, then the travel times within the first and second media are $T_1 = a_1/c_1$ and $T_2 = a_2/c_2$, respectively, where $a_1 = l_1/\cos\alpha = |\mathbf{r}^S - \mathbf{r}_O|$ and $a_2 = l_2/\cos\beta = |\mathbf{r}_O - \mathbf{r}_q|$, respectively (likewise, $T'_1 = a'_1/c_1$ and $T'_2 = a'_2/c_2$ with $a'_1 = |\mathbf{r}^S - \mathbf{r}_{O'}|$ and $a'_2 = |\mathbf{r}_{O'} - \mathbf{r}_r|$). It is important to note that in this refraction compensation mechanism only the phase (travel times) is significant for localizing the source, and not the amplitude. This is the reason why no amplitude reflection/transmission coefficient is required in the imaging functionals.

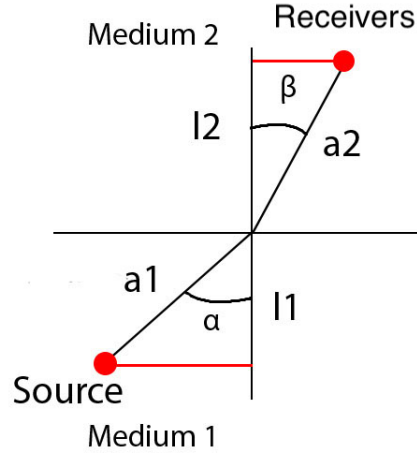


Figure 3.22 – *Refracted acoustic wave at the interface between two media with speeds of sound c_1 and c_2 : α is the angle of the incident wave, β is the angle of the refracted wave. The interface is taken as the mean shear layer between the first and second media in Fig. 3.19.*

One source case	
f_0	50 kHz
X_s	$12\lambda_0$
Y_s	0
d	0
L	$20\lambda_0$
a	$22\lambda_0$

Table 3.1 – *Imaging setup parameters for a single source through a synthetic turbulent jet.*

3.5.6 Imaging of the sources

We will first focus on determining the position of a single source. The distance d between the upper sources is set to zero in this case. The size of the search window is $10\lambda_0 \times 10\lambda_0$ centered around the source point (X_s, Y_s) . A pixel being of size $\frac{2\lambda_0}{5}$, this corresponds to a window of 25×25 pixels. The parameters defining this case are gathered in Tab. 3.1. The results obtained with the KM imaging algorithm are shown in Fig. 3.23 and those obtained with the CINT imaging algorithm are shown in Fig. 3.24. We know that the jet flow used is ideal and does not reflect reality but we obtain the desired mechanisms. We can see the influence of the Doppler compensation coefficient γ_D . Without this coefficient we have a shift of the position of the source, however if we use it in our imaging functionals we observe that they find with satisfactory precision the position of the source. We can also see that the refraction compensation mechanism does not really have any influence on the result. This was predictable because the speeds of sound of the two media are identical. Furthermore the distance between the source and the receivers is low, which leads to low refraction of the waves. However in a more favorable configuration for refraction we put forward the assumption that this mechanism will become of prime importance.

Second, we aim at determining the positions of three sources. The parameters defining

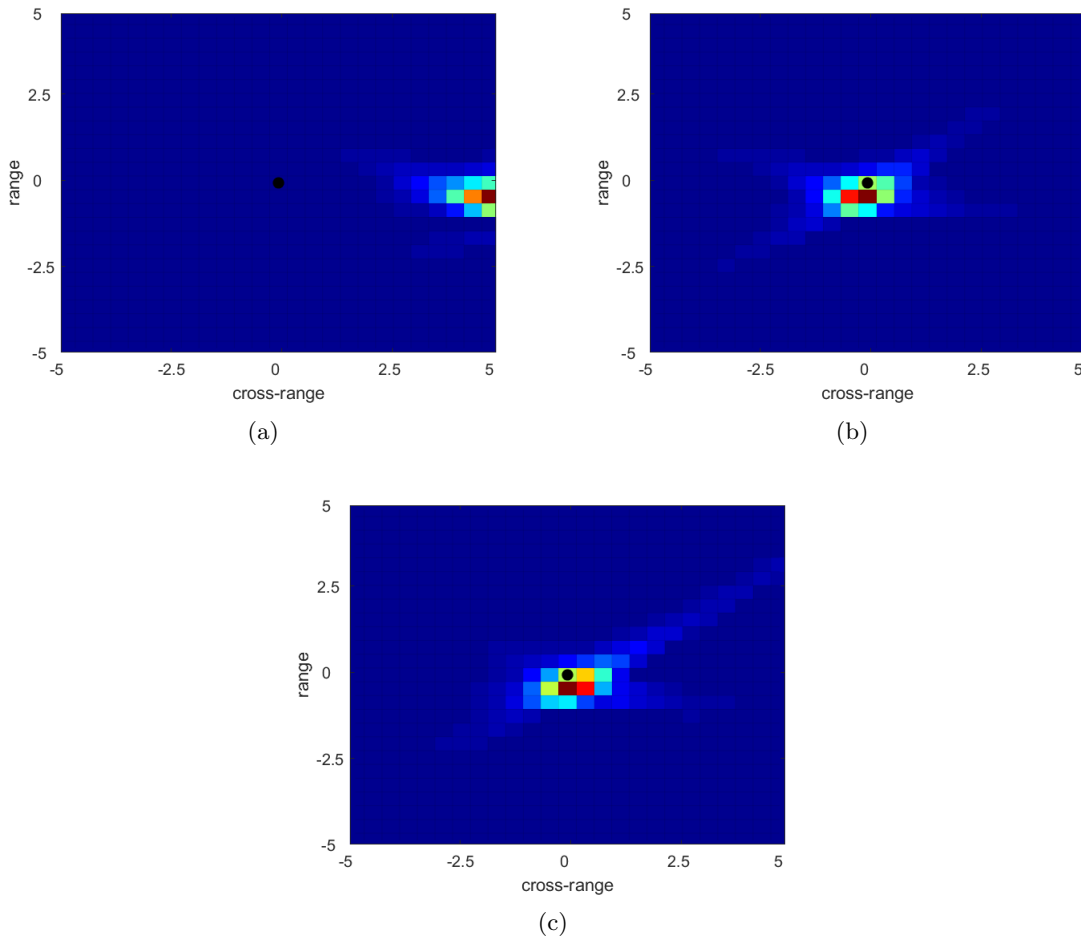


Figure 3.23 – *KM passive imaging of a single source through a synthetic turbulent jet flow. Influence of the Doppler compensation coefficient γ_D and refraction compensation mechanism on KM imaging functional: (a) without any compensation; (b) with Doppler compensation coefficient γ_D ; (c) with Doppler compensation coefficient γ_D and refraction compensation mechanism. The source location is shown by a dot \bullet .*

this case are gathered in Tab. 3.2. The search window is the same as the case with one source. The results obtained with the KM imaging algorithm are shown in Fig. 3.25 and those obtained with the CINT imaging algorithm are shown in Fig. 3.26. The same conclusions can be drawn as for the case with a single source.

3.6 Conclusion

After introducing the model problem and recalling the principles of the two imaging functionals we use, namely Kirchhoff migration (KM) in Sect. 3.1.2 and Coherent Interferometry (CINT) in Sect. 3.1.3, we proposed a suitable form of these functionals by introducing the Doppler compensation coefficient γ_D of Eq. (3.16). This parameter makes it possible to perform imaging through a random flow. Indeed we first back-propagated our

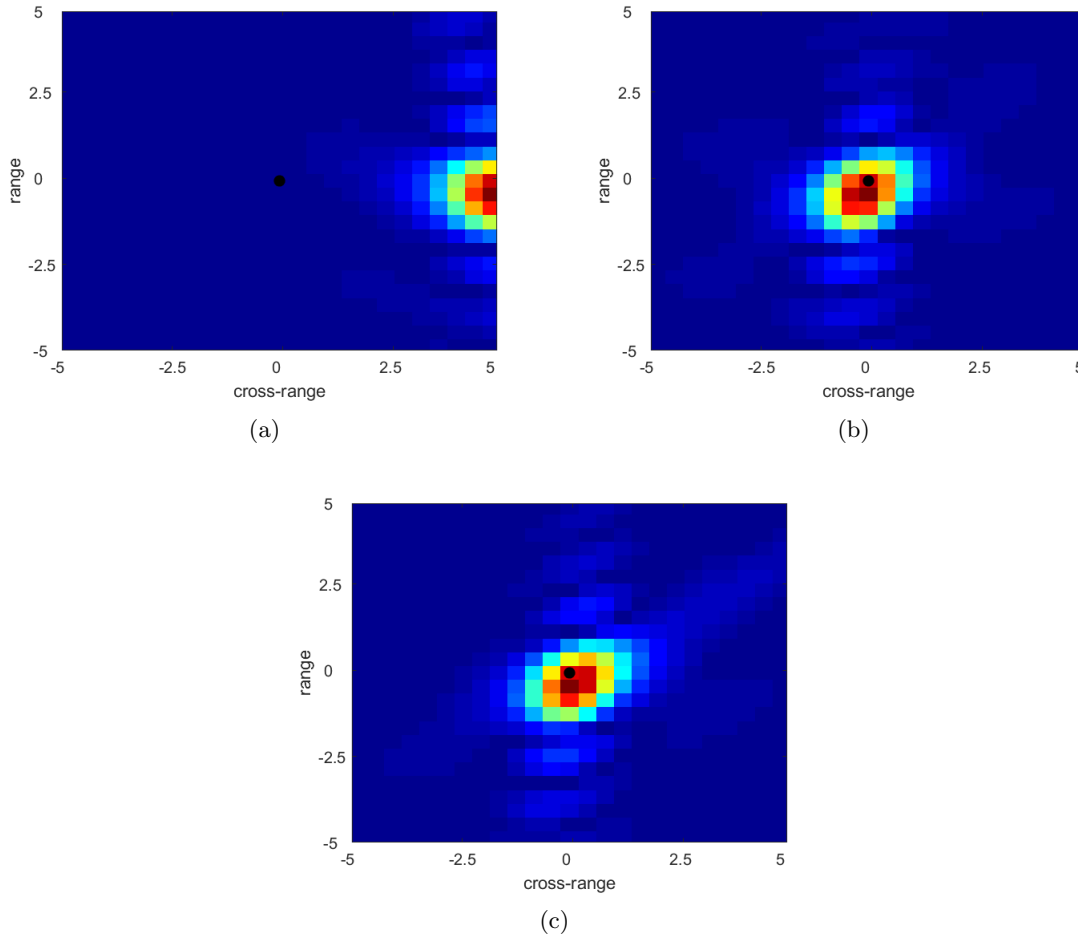


Figure 3.24 – *CINT passive imaging of a single source through a synthetic turbulent jet flow. Influence of the Doppler compensation coefficient γ_D and refraction compensation mechanism on CINT imaging functional: (a) without any compensation; (b) with Doppler compensation coefficient γ_D ; (c) with Doppler compensation coefficient γ_D and refraction compensation mechanism. The source location is shown by a dot \bullet .*

signals in a homogeneous medium at rest, which does not cancel out the effects that the signals have undergone when passing through a moving ambient medium. The factor γ_D allows us to compensate these effects and perform imaging efficiently.

In a first step we validated our solver, SPACE, in a homogeneous medium at rest then in a random medium at rest in Sect. 3.3.1. It has been seen that in the context of passive imaging the levels of medium disturbances considered are too low to see an interest in CINT imaging. Indeed, in this context, the signals pass one time in the medium and are not sufficiently scattered by the latter to put KM in default. That is why we focused on the context of active imaging.

In active imaging, the signals first go to the reflectors and then go back to the receivers thus propagating back and forth in a random medium. They are therefore much more modulated. The difference is easily seen when comparing the figures 3.9 and 3.12 which

Three sources case	
f_0	50 kHz
X_s	$12\lambda_0$
Y_s	0
d	$3\lambda_0$
L	$20\lambda_0$
a	$22\lambda_0$

Table 3.2 – *Imaging setup parameters for three sources through a synthetic turbulent jet.*

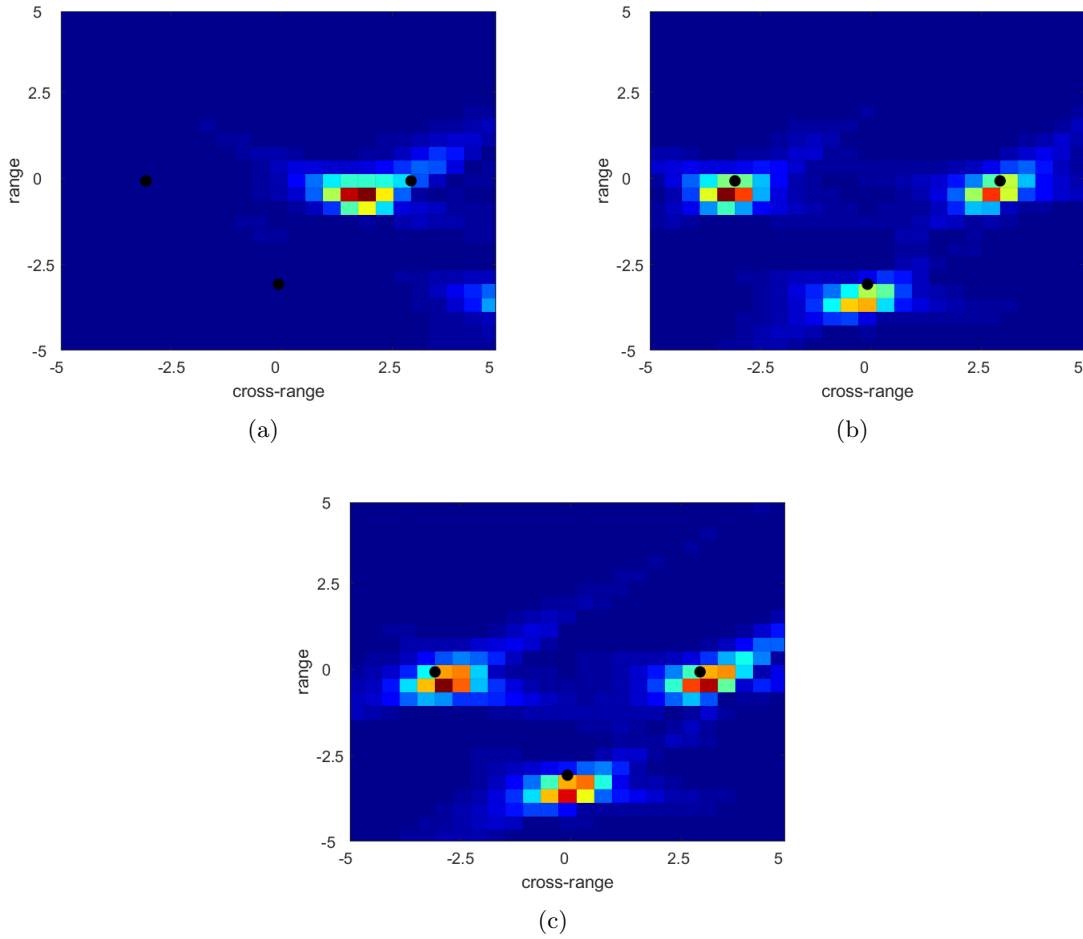


Figure 3.25 – *KM passive imaging of three sources through a synthetic turbulent jet flow. Influence of the Doppler compensation coefficient γ_D and refraction compensation mechanism on KM imaging functional: (a) without any compensation; (b) with Doppler compensation coefficient γ_D ; (c) with Doppler compensation coefficient γ_D and refraction compensation mechanism. The source locations are shown by dots \bullet .*

show KM in both contexts for a random medium with the same characteristics. The strength of CINT imaging lies mainly in the fact that it is statistically stable, which is not the case for

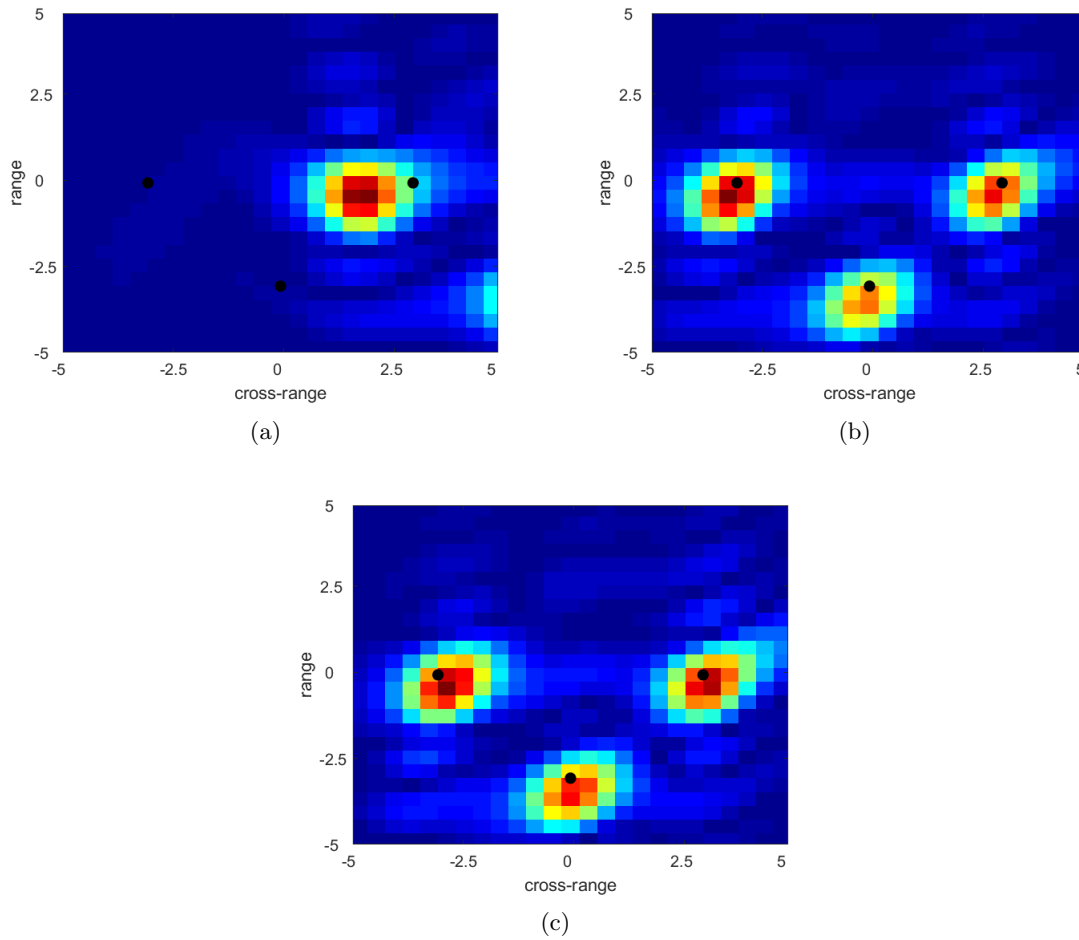


Figure 3.26 – *CINT passive imaging of three sources through a synthetic turbulent jet flow. Influence of the Doppler compensation coefficient γ_D and refraction compensation mechanism on CINT imaging functional: (a) without any compensation; (b) with Doppler compensation coefficient γ_D ; (c) with Doppler compensation coefficient γ_D and refraction compensation mechanism. The source locations are shown by dots \bullet .*

KM imaging. One of the counterparts lies in the smoothing of the CINT imaging that must be set in order to have satisfactory results. The other main counterpart is the time required to make an image that is a few hours for the CINT while KM is almost instantaneous, with Matlab on a standard computer.

Both imaging methods in a moving ambient medium were tested in two configurations:

- the ambient medium has a random speed of sound and is moving with a uniform velocity,
- the ambient medium has a random speed of sound and is moving with a random velocity.

We could see the importance of the Doppler compensation coefficient γ_D . These two configurations that put KM imaging algorithm in default did not affect the CINT imaging algorithm, which was able to localize the three sources quite efficiently each time; see

Fig. 3.13 and Fig. 3.18.

Finally, we performed some tests of the KM and CINT imaging algorithms through a synthetic turbulent jet calculated by CFD. We placed ourselves in the case of passive imaging because of technical constraints, and added a refraction compensation mechanism. In this context we saw that the KM algorithm, under the conditions implemented in these tests, works relatively well if we use the Doppler compensation coefficient γ_D . We also saw the tiny influence of the refraction compensation mechanism, which is explained by the configuration considered. This mechanism could be of prime importance if a configuration more favorable for refraction is considered.

Conclusions and perspectives

In this thesis we have analyzed some models of propagation of acoustic waves in inhomogeneous quiescent media, as essentially developed in [72], and we have extended these results to inhomogeneous moving media. We have obtained in Sect. 2.2 and Sect. 2.3 explicit integral representations of the pressure fields that have been transmitted by an homogeneous ambient flow and a cluttered ambient flow with a random bulk modulus, namely Lemma 2.2.1 and Prop. 2.3.1 respectively. More precisely, in Sect. 2.3 we have adapted to moving random media the approach of [72, Chap. 14] for quiescent random media. We have also derived in Sect. 2.4 an explicit expression of the power spectral density of the pressure field transmitted by a cluttered ambient flow with a random velocity for various simplifications of the flow features; see Prop. 2.4.2. More particularly, we have obtained an integral representation of the pressure field for this case in Prop. 2.4.1, using various assumptions for the ambient flow (thin layer) and the (high-frequency) source, and a Born approximation. We have also developed a solution for finding the stationary-phase point for this problem in Lemma 2.4.1. These are the main results of Chapter 2 of the thesis. We have compared our results with the literature in Sect. 2.4.4 and we have seen that our model gives the same tendencies as others models [54, 55, 64, 66, 103, 104, 112] or experimental observations [41–43, 91, 118]. Our model managed to highlight a characteristic spectral broadening effect, whereby a reduction of the main peak at the source tone frequency in favor of more distributed spectral humps on both sides of this peak is observed. We have seen that the main peak is directly related to the unperturbed transmitted pressure while sidebands (lobes) arise in connection with a Doppler shift effect due to the motion of the turbulent eddies acting as secondary sources for the scattered transmitted pressure. We have observed a widening of these lobes proportional to the convection velocity of the turbulent eddies, as well as the independence of the locations of their maxima with respect to the tone frequency. Increasing the latter also leads to a widening of the sidebands and higher scattered levels.

It would be interesting in future works to relax some hypotheses such as the thickness of the layer, which is supposed to be infinitely thin, or the velocity of the flow, for which the Mach number is assumed to be much smaller than 1. Moreover, the flow has always been assumed to be z -dependent in order to obtain a stratified configuration as described in [72]. Axisymmetric flow geometries should be studied in future works for aerospace applications. Our model of delta-correlated turbulent velocity fluctuations in Sect. 2.4 could also be improved by considering more general auto-correlation functions of the form (1.37) imposed by the assumption of homogeneous isotropic turbulence, or homogeneous axisymmetric turbulence as in [104]. Finally, we have considered that the source-microphone axis was perpendicular to the flow. Studying the influence of the angle of illumination as in [40, 55, 103, 112] should bring interesting information. Measurements and models of the

cross power spectra between two microphones have been reported in [41–43, 81], and our model could also be compared to these results.

Then we have introduced in Chapter 3 two imaging methods, Kirchhoff’s migration (KM) and coherent interferometry (CINT), which we have adapted to the flow imaging context with a Doppler compensation factor (3.16). The same idea has been implemented in [33, 69] to characterize fast moving objects. The Doppler compensation factor must compensate the shift of the arrival time induced by the flow when the ambient medium moves at an average velocity. We have compared these two methods in several contexts in Sect. 3.4.1 (random medium moving at a uniform velocity) and Sect. 3.4.2 (random medium moving at a random velocity), after validating our discontinuous Galerkin finite element solver in Sect. 3.3.1. We have highlighted the fact that in a passive imaging context, at the considered noise levels, the KM imaging technique was more interesting than the CINT imaging technique because the images made with KM are satisfactory and the computation time is much lower. However, in the context of active imaging, the results are very different since KM can not effectively find the positions of the reflectors that we want to image, unlike CINT. The CINT imaging technique also gives statistically stable results unlike the KM imaging technique, *i.e.* in two different realizations of the random medium we get the same results with CINT imaging which is not the case with KM imaging. It seems interesting then to optimize the CINT imaging technique in order to reduce its computation time since it works in a broader context than the KM imaging technique. Moreover this will make the CINT parameter adaptive choice algorithm introduced in [26] interesting to use, which is not the case today because of the computation time necessary to produce an image. Finally some results of imaging through a turbulent jet were presented in Sect. 3.5. Indeed, the main objective of this work was to be able to characterize (*i.e.* to detect and to localize) a source in a real jet configuration. In this context we have seen that we could not fail the KM technique because we could not generate enough turbulence with our CFD calculation, and we were in a passive imaging configuration.

It would be interesting in future works to generate more turbulence ”artificially”, as done in [16], or to consider an active imaging configuration with such a low level of turbulence. It would also be necessary to modify the configuration of the sensors, the distance separating them, their distances from the source, or the permeability of the reflectors in the active setting in order to see the influence of these parameters on our results. Moreover the computing power having limited us in term of mesh refinement, but also the source-reflectors distance, it would be interesting to be able to perform simulations on large computers in order to go further with these questions. It would also be possible, in this case, to propagate the waves in a CFD-solved jet and get closer to the work of [16]. Finally, as we have seen for the theoretical considerations, it will be interesting to study the effects induced by a higher Mach number, especially on the Doppler compensation mechanism, and to see the influence of a non-perpendicular illumination.

Bibliography

- [1] J.-L. Akian, É. Savin. Kinetic modeling of multiple scattering of acoustic waves in randomly heterogeneous flows. <http://arXiv.org/abs/1710.03621>.
- [2] D. G. Alfaro Vigo, J.-P. Fouque, J. Garnier, A. Nachbin. Robustness of time reversal for waves in time-dependent random media. *Stochastic Process. Appl.* **113**(2), 289-313 (2004).
- [3] N. Alferéz, I. Mary, E. Lamballais. Study of stall development around an airfoil by means of high fidelity large eddy simulation. *Flow Turbul. Combust.* **91**(3), 623-641 (2013).
- [4] K. K. Ahuja, H. K. Tanna, B. J. Tester. An experimental study of transmission, reflection and scattering of sound in a free jet flight simulation facility and comparison with theory. *J. Sound Vib.* **75**(1), 51-85 (1981).
- [5] H. Ammari, J. Garnier, H. Kang, W. K. Park, K. Sølna. Imaging schemes for perfectly conducting cracks. *SIAM J. Appl. Math.* **71**(1), 68-91 (2011).
- [6] H. Ammari, J. Garnier, K. Sølna. A statistical approach to target detection and localization in the presence of noise. *Waves Random Complex Media* **22**, 40-65 (2012).
- [7] R. K. Amiet. Correction of open jet wind tunnel measurement for shear layer refraction. In *Proc. 2nd AIAA Aeroacoustics Conf., 24-26 March 1975, Hampton VA*. AIAA Paper #1975-532 (1975).
- [8] M. Asch, W. Kohler, G. Papanicolaou, M. Postel, B. White. Frequency content of randomly scattered signals. *SIAM Rev.* **33**(4), 519-625 (1991).
- [9] C. Bailly, P. Lafon, S. Candel. A stochastic approach to compute noise generation and radiation of free turbulent flows. In *Proc. 1st CEAS/AIAA Aeroacoustics Conf., 12-15 June, München*. AIAA Paper #1995-092 (1995).
- [10] G. Bal, G. Papanicolaou, L. Ryzhik. Self-averaging in time reversal for the parabolic wave equation. *Stoch. Dyn.* **2**(4), 507-531 (2002).
- [11] G. Bal, L. Ryzhik. Time reversal and refocusing in random media. *SIAM J. Appl. Math.* **63**(5), 1475-1498 (2003).
- [12] G. K. Batchelor. The theory of axisymmetric turbulence. *Proc. R. Soc. Lond. A* **186**, 480-502 (1946).
- [13] G. K. Batchelor. *The Theory of Homogeneous Turbulence*. Cambridge University Press, Cambridge (1953).
- [14] E. Bécache, P. Joly, C. Tsogka. Étude d'un nouvel élément fini mixte permettant la condensation de masse. *C. R. Acad. Sci. Séries I* **324**(11), 1281-1286 (1997).

- [15] E. Bécache, P. Joly, C. Tsogka. An analysis of new mixed finite elements for the approximation of wave propagation problems. *SIAM J. Numer. Anal.* **37**(4), 1053-1084 (2000).
- [16] I. Bennaceur, D. C. Mincu, I. Mary, M. Terracol, L. Larchevêque, P. Dupont. Numerical simulation of acoustic scattering by a plane turbulent shear layer: Spectral broadening study. *Comput. Fluids* **138**, 83-98 (2016).
- [17] I. Bennaceur. *Étude numérique de la diffusion d'une onde acoustique par une couche de cisaillement turbulente à l'aide d'une simulation aux grandes échelles*. PhD Thesis, Université Aix-Marseille (2017).
- [18] P. G. Bergmann. The wave equation in a medium with a variable index of refraction. *J. Acoust. Soc. Am.* **17**(4), 329-333 (1946).
- [19] J.-P. Bérenger. A perfectly matched layer for the absorption of electromagnetic waves. *J. Comput. Phys.* **114**(2), 185-200 (1994).
- [20] N. Bleistein, J. K. Cohen, J. W. Stockwell, Jr. *Mathematics of Multidimensional Seismic Imaging, Migration, and Inversion*. Springer-Verlag, New York NY (2001).
- [21] D. Blokhintzev. The propagation of sound in a inhomogeneous and moving medium I. *J. Acoust. Soc. Am.* **18**(2), 322-328 (1946); II. *J. Acoust. Soc. Am.* **18**(2), 329-334 (1946).
- [22] P. Blomgren, G. Papanicolaou, H. Zhao. Super-resolution in time-reversal acoustics. *J. Acoust. Soc. Am.* **111**(1), 230-248 (2002).
- [23] L. Borcea, G. Papanicolaou, C. Tsogka. Theory and applications of time reversal and interferometric imaging. *Inverse Problems* **19**(6), S139-S164 (2003).
- [24] L. Borcea, G. Papanicolaou, C. Tsogka. Interferometric array imaging in clutter. *Inverse Problems* **21**(4), 1419-1460 (2005).
- [25] L. Borcea, G. Papanicolaou, C. Tsogka. Coherent interferometry in finely layered random media. *Multiscale Model. Simul.* **5**(1), 62-83 (2006).
- [26] L. Borcea, G. Papanicolaou, C. Tsogka. Adaptive interferometric imaging in clutter and optimal illumination. *Inverse Problems* **22**(4), 1405-1436 (2006).
- [27] L. Borcea, G. Papanicolaou, C. Tsogka. Coherent interferometric imaging in clutter. *Geophys.* **71**(4), SI165-SI175 (2006).
- [28] L. Borcea, G. Papanicolaou, C. Tsogka. Optimal illumination and wave form design for imaging in random media. *J. Acoust. Soc. Am.* **122**(6), 3507-3518 (2007).
- [29] L. Borcea, G. Papanicolaou, C. Tsogka. Asymptotics for the space-time Wigner transform with applications to imaging. In *Stochastic Differential Equations: Theory and Applications* (P. H. Baxendale, S. V. Lototsky, eds.), pp. 91-111. World Scientific, Singapore (2007).
- [30] L. Borcea, J. Garnier, G. Papanicolaou, C. Tsogka. Coherent interferometric imaging, time gating and beamforming. *Inverse Problems* **27**(6), 065008 (2011).
- [31] L. Borcea, J. Garnier, G. Papanicolaou, C. Tsogka. Enhanced statistical stability in coherent interferometric imaging. *Inverse Problems* **27**(8), 085004 (2011).
- [32] L. Borcea, G. Papanicolaou, C. Tsogka. Adaptive time-frequency detection and filtering for imaging in heavy clutter. *SIAM J. Imaging Sci* **4**(3), 827-849 (2011).

- [33] L. Borcea, J. Garnier, G. Papanicolaou, K. Sølna, C. Tsogka. Resolution analysis of passive synthetic aperture imaging of fast moving objects. *SIAM J. Imaging Sci.* **10**(2), 665-710 (2017).
- [34] R. Burridge, G. Papanicolaou, P. Sheng, B. White. Probing a random medium with a pulse. *SIAM J. Appl. Math.* **49**(2), 582-607 (1989).
- [35] L. M. Brekhovskikh, O. A. Godin. *Acoustics of Layered Media I. Plane and Quasi-Plane Waves*. Springer-Verlag, Berlin (1990).
- [36] L. M. Brekhovskikh, O. A. Godin. *Acoustics of Layered Media II. Point Sources and Bounded Beams*. Springer-Verlag, Berlin (1999).
- [37] E. H. Brown, S. F. Clifford. Spectral broadening of an acoustic pulse propagating through turbulence. *J. Acoust. Soc. Am.* **54**(1), 36-39 (1973).
- [38] G. L. Brown, A. Roshko. On density effects and large structure in turbulent mixing layers. *J. Fluid Mech.* **64**(4), 755-816 (1974).
- [39] L. M. B. C. Campos. The spectral broadening of sound by turbulent shear layers. Part 1. The transmission of sound through turbulent shear layers. *J. Fluid Mech.* **89**(4), 723-749 (1978).
- [40] L. M. B. C. Campos. The spectral broadening of sound by turbulent shear layers. Part 2. The spectral broadening of sound and aircraft noise. *J. Fluid Mech.* **89**(4), 751-783 (1978).
- [41] S. Candel, A. Guédel, A. Julienne. Refraction and scattering in an open wind tunnel flow. In *Proc. 6th Int. Congress on Instrumentation in Aerospace Simulation Facilities ICIASF'75, Ottawa ON*, pp. 288-300 (1975).
- [42] S. Candel, A. Guédel, A. Julienne. Radiation, refraction and scattering of acoustic waves in a free shear flow. In *Proc. 3rd AIAA Aeroacoustics Conf., 20-23 July 1976, Palo Alto CA*. AIAA paper #1976-544 (1976).
- [43] S. Candel, A. Guédel, A. Julienne. Résultats préliminaires sur la diffusion d'une onde acoustique par écoulement turbulent. *J. Phys. Colloques* **37**(C1), C1-153-C1-160 (1976).
- [44] S. Candel. Numerical solution of conservation equations arising in linear wave theory: application to aeroacoustics. *J. Fluid Mech.* **83**(3), 465-493 (1977).
- [45] S. Candel. *Études théoriques et expérimentales de la propagation acoustique en milieu inhomogène et en mouvement*. PhD thesis, Université de Paris VI (1977).
- [46] S. Candel, A. Guédel, A. Julienne. Diffusion d'une onde monochromatique par un écoulement turbulent IV. In *Colloque Euromech 94 sur la Propagation des Ondes dans les Milieux Inhomogènes, septembre 1977, Marseille, France*. English version: Scattering of a monochromatic wave by a turbulent flow IV. Royal Aircraft Establishment Translation 1991 (1979).
- [47] S. Candel. Numerical solution of wave scattering problems in the parabolic approximation. *J. Fluid Mech.* **90**(3), 465-507 (1979).
- [48] S. Candel. A review of numerical methods in acoustic wave propagation. In *Recent Advances in Aeroacoustics (A. Krothapalli, C. A. Smith, eds.)*, pp. 339-410. Springer, New York NY (1986).

- [49] A. Cargill. Sound propagation through fluctuating flows—Its significance in aeroacoustics. In *Proc. 8th AIAA Aeroacoustics Conf., 11-13 April 1983, Atlanta GA*. AIAA Paper #1983-697 (1983).
- [50] <https://windtunnel.onera.fr/cepra-19-large-scale-anechoic-wind-tunnel-noise-research-facility>.
- [51] S. Chandrasekhar. The theory of axisymmetric turbulence. *Philos. Trans. R. Soc. Lond. Ser. A* **242**(855), 557-577 (1950).
- [52] S. Chandrasekhar. *Radiative Transfer*. Dover publications, New York NY (1960).
- [53] T. K. Chan, Y. Kuga, A. Ishimaru. Experimental studies on circular SAR imaging in clutter using angular correlation function technique. *IEEE Trans. Geosci. Remote Sens.* **37**(5), 2192-2197 (1999).
- [54] V. Clair, G. Gabard. Numerical assessment of the scattering of acoustic waves by turbulent structures. In *Proc. 21st AIAA/CEAS Aeroacoustics Conf., 22-26 June 2015, Dallas TX*. AIAA Paper #2015-2680 (2015).
- [55] V. Clair, G. Gabard. Numerical investigation on the spectral broadening of acoustic waves by a turbulent layer. In *Proc. 22nd AIAA/CEAS Aeroacoustics Conf., 30 May - 1 June 2016, Lyon, France*. AIAA paper #2016-2701 (2016).
- [56] J.-F. Clouet, J.-P. Fouque. Spreading of a pulse travelling in random media. *Ann. Appl. Prob.* **4**(4), 1083-1097 (1994).
- [57] G. Cohen, P. Joly, N. Tordjman, Éléments finis d'ordre élevé avec condensation de masse pour l'équation des ondes en dimension 1, *INRIA Technical Report RR-2323*, Le Chesnay (1994).
- [58] T. Colonius, S. K. Lele, P. Moin. Boundary conditions for computation of aerodynamic sound generation. *AIAA J.* **31**(9), 1574-1582 (1993).
- [59] T. Colonius, S. K. Lele, P. Moin. The scattering of sound waves by a vortex: numerical simulations and analytical solutions. *J. Fluid Mech.* **260**, 271-298 (1994).
- [60] Ph. Delorme, P. Mazet, C. Peyret, Y. Ventribout, Computational aeroacoustics applications based on a discontinuous Galerkin method. *Comptes Rendus Mécanique* **333**(9), 676-682 (2005).
- [61] J. Delfs, M. Bauer, R. Ewert, H. Grogger, M. Lummer, T. Lauke. *Numerical Simulation of Aerodynamic Noise with DLR's Aeroacoustics code PIANO*. PIANO manual for version 5.2, DLR, Braunschweig (2008).
- [62] M. Duruflé. *Intégration numérique et éléments finis d'ordre élevé appliqués aux équations de Maxwell en régime harmonique*. PhD Thesis, Paris-Dauphine University (2006).
- [63] R. Ewert. RPM - the fast random particle-mesh method to realize unsteady turbulent sound sources and velocity fields for CAA applications. In *Proc. 13th AIAA/CEAS Aeroacoustics Conf., 21-23 May 2007, Rome, Italy*. AIAA Paper #2007-3506, (2007).
- [64] R. Ewert, O. Kornow, B. J. Tester, C. J. Powles, J. W. Delfs, M. Rose. Spectral broadening of jet engine turbine tones. In *Proc. 14th AIAA/CEAS Aeroacoustics Conf., 5-7 May 2008, Vancouver BC*. AIAA paper #2008-2940 (2008).
- [65] R. Ewert. Broadband slat noise prediction based on CAA and stochastic sound sources from a fast random particle-mesh (RPM) method. *Comput. Fluids* **37**(4), 369-387 (2008).

- [66] R. Ewert, O. Kornow, J. W. Delfs, J. Yin, T. Röber, M. Rose. A CAA based approach to tone haystacking. In *Proc. 15th AIAA/CEAS Aeroacoustics Conf., 11-13 May 2009, Miami FL*. AIAA Paper #2009-3217 (2009).
- [67] A. Fannjiang, L. Ryzhik. Radiative transfer of sound waves in a random flow: turbulent scattering, straining, and mode-coupling. *SIAM J. Appl. Math.* **61**(5), 1545-1577 (2001).
- [68] M. Fink. Time-reversed acoustics. *Scientific American* **281**(5), 91-97 (1999).
- [69] J. Fournier, J. Garnier, G. Papanicolaou, C. Tsogka. Matched-filter and correlation-based imaging for fast moving objects using a sparse network of receivers. *SIAM J. Imaging Sci.* **10**(4), 2165-2216 (2017).
- [70] J.-P. Fouque, K. Sølna. Time-reversal aperture enhancement. *Multiscale Model. Simul.* **1**(2), 239-259 (2003).
- [71] J.-P. Fouque, J. Garnier, A. Nachbin, K. Sølna. Time reversal refocusing for point source in randomly layered media. *Wave Motion* **42**(3), 238-260 (2005).
- [72] J.-P. Fouque, J. Garnier, G. Papanicolaou, K. Sølna, *Wave Propagation and Time Reversal in Randomly Layered Media*, Springer-Verlag, New York NY (2007).
- [73] J. Freund. A simple method for computing far-field sound in aeroacoustic computations. *J. Comput. Phys.* **157**(2), 796-800 (2000).
- [74] J. Garnier. Imaging in randomly layered media by cross-correlating noisy signals. *Multiscale Model. Simul.* **4**(2), 610-640 (2005).
- [75] J. Garnier, G. Papanicolaou. Passive sensor imaging using cross correlations of noisy signals in a scattering medium. *SIAM J. Imaging Sciences* **2**(2), 396-437 (2009).
- [76] J. Garnier, K. Sølna. Cross correlation and deconvolution of noise signals in randomly layered media. *SIAM J. Imaging Sciences* **3**(4), 809-834 (2010).
- [77] J. Garnier, G. Papanicolaou. *Passive Imaging with Ambient Noise*. Cambridge University Press, Cambridge (2016).
- [78] E. Giusti. *Minimal Surfaces and Functions of Bounded Variation*. Birkhäuser, Basel (1984).
- [79] M. E. Goldstein. *Aeroacoustics*. McGraw-Hill, New York NY (1976).
- [80] M. E. Goldstein. An exact form of the Lilley's equation with a velocity quadrupole/temperature dipole source term. *J. Fluid Mech.* **443**, 231-236 (2001).
- [81] A. Guédel. Scattering of an acoustic field by a free jet shear layer. *J. Sound Vib.* **100**(2), 285-304 (1985).
- [82] J. S. Hesthaven. From electrostatics to almost optimal nodal sets for polynomial interpolation in a simplex. *SIAM J. Numer. Anal.* **35**(2), 655-676 (1998).
- [83] J. S. Hesthaven, T. Warburton, *Nodal Discontinuous Galerkin Methods*, Springer, New York NY (2008).
- [84] M. S. Howe. Multiple scattering of sound by turbulence and other inhomogeneities. *J. Sound Vib.* **27**(4), 455-476 (1973).
- [85] A. Ishimaru. *Wave Propagation and Scattering in Random Media, Vol. 1: Single Scattering and Transport Theory*. Academic Press, San Diego CA (1978).

- [86] A. Ishimaru. *Wave Propagation and Scattering in Random Media, Vol. 2: Multiple Scattering, Turbulence, Rough Surfaces, and Remote Sensing*. Academic Press, San Diego CA (1978).
- [87] Th. von Karman. The fundamentals of the statistical theory of turbulence. *J. Aero. Sci.* **4**(4), 131-138 (1937).
- [88] Th. von Karman, L. Howarth. On the statistical theory of isotropic turbulence. *Proc. R. Soc. Lond. A* 1938 **164**, 192-215 (1938).
- [89] R. Kechroud, X. Antoine, A. Soulaïmani. Numerical accuracy of a Padé-type non-reflecting boundary condition for the finite element solution of acoustic scattering problems at high-frequency. *Int. J. Numer. Methods Engng.* **64**(10), 1275-1302 (2005).
- [90] R. H. Kraichnan. Diffusion by a random velocity field. *Phys. Fluids* **13**(1), 22-31 (1970).
- [91] S. Kröber, M. Hellmold, L. Koop. Experimental investigation of spectral broadening of sound waves by wind tunnel shear layers. In *Proc. 19th AIAA/CEAS Aeroacoustics Conf., 27-29 May 2013, Berlin, Germany*. AIAA paper #2013-2255 (2013).
- [92] C. Laurent, I. Mary, V. Gleize, A. Lerat, D. Arnal. DNS database of a transitional separation bubble on a flat plate application to RANS modeling validation. *Comput. Fluids* **61**, 21-30 (2012).
- [93] É. Larose. Mesoscopics of ultrasound and seismic waves: applications to passive imaging. *Ann. Phys. Fr.* **31**(3), 1-126 (2006).
- [94] M. J. Lighthill. On sound generated aerodynamically: (I) General theory. *Proc. R. Soc. Lond.* **A211**(1107), 564-587 (1952).
- [95] M. J. Lighthill. On the energy scattered from the interaction of turbulence with sound or shock waves. *Proc. Cambridge Phil. Soc.* **49**(3), 531-551 (1953).
- [96] M. J. Lighthill. On sound generated aerodynamically: (II) Turbulence as a source of sound. *Proc. R. Soc. Lond.* **A222**(1148), 1-32 (1954).
- [97] G. M. Lilley. Generation of sound in a mixing region. In *The Generation and Radiation of Supersonic Jet Noise* vol. **IV: Theory of Turbulence Generated jet Noise, Noise Radiation from Upstream Sources, and Combustion Noise**, pp. 2-69. Technical report AFAPL-TR-72-53, Air Force Aero Propulsion Laboratory, Wright-Patterson Air Force Base OH (1972).
- [98] E. Lindborg. Kinematics of homogeneous axisymmetric turbulence. *J. Fluid Mech.* **302**, 179-201(1995).
- [99] B. A. Lippmann, J. Schwinger. Variational principles for scattering processes I. *Phys. Rev.* **79**(3), 469-480 (1950).
- [100] L. Mandel, E. Wolf. *Optical Coherence and Quantum Optics*. Cambridge University Press, Cambridge (1995).
- [101] I. Mary, P. Sagaut. Large eddy simulation of flow around an airfoil near stall. *AIAA J.* **40**(6), 1139-1145 (2002).
- [102] A. McAlpine, C. J. Powles, B. J. Tester. A weak-scattering model for tone haystacking. In *Proc. 15th AIAA/CEAS Aeroacoustics Conf., 11-13 May 2009, Miami, FL*. AIAA paper #2009-3216 (2009).
- [103] A. McAlpine, C. J. Powles, B. J. Tester. A weak-scattering model for turbine-tone haystacking. *J. Sound Vib.* **332**(16), 3806-3831 (2013).

- [104] A. McAlpine, B. J. Tester. A weak-scattering model for tone haystacking caused by sound propagation through an axisymmetric turbulent shear layer. In *Proc. 22nd AIAA Aeroacoustics Conf., 30 May - 1 June 2016, Lyon, France*. AIAA paper #2016-2702 (2016).
- [105] R. F. O'Doherty, N. A. Anstey. Reflections on amplitudes. *Geophys. Prospect.* **19**(3), 430-458 (1971).
- [106] ONERA. Un nouveau super-calculateur pour la recherche aérospatiale <https://www.onera.fr/fr/actualites/un-nouveau-supercalculateur-pour-la-recherche-aerospatiale> (2018).
- [107] V. E. Ostashev, D. K. Wilson. *Acoustics in Moving Inhomogeneous Media (2nd Ed.)*. CRC Press, Boca Raton FL (2016).
- [108] G. Papanicolaou, L. Ryzhik, K. Sølna. Statistical stability in time reversal. *SIAM J. Appl. Math.* **64**(4), 1133-1155 (2004).
- [109] C. Peyret. A full high-order method for computational aeroacoustics. In *Proc. 23rd AIAA/CEAS Aeroacoustics Conference, 5-9 June 2017, Denver CO*. AIAA paper #2017-3174 (2017).
- [110] A. D. Pierce. Wave equation for sound in fluids with unsteady inhomogeneous flow. *J. Acoust. Soc. Am.* **87**(6), 2292-2299 (1990).
- [111] F. Poirion, C. Soize, Numerical simulation of homogeneous and inhomogeneous Gaussian stochastic vector fields. *La Recherche Aérospatiale (English ed.)* **1989-1**, 41-61 (1989).
- [112] C. J. Powles, B. J. Tester, A. McAlpine. A weak-scattering model for turbine-tone haystacking outside the cone of silence. *Int. J. Aeroacoustics* **10**(1), 17-50 (2011).
- [113] D. C. Pridmore-Brown. Sound propagation in a fluid flowing through an attenuating duct. *J. Fluid Mech.* **4**(4), 393-406 (1958).
- [114] H. P. Robertson. The invariant theory of isotropic turbulence. *Math. Proc. Cambridge Philos. Soc.* **36**(2), 209-223 (1940).
- [115] L. Ryzhik, G. Papanicolaou, J. B. Keller. Transport equations for elastic and other waves in random media. *Wave Motion* **24**(4), 327-370 (1996).
- [116] R. H. Schlinker, R. K. Amiet. *Refraction and scattering of sound by a shear layer*. NASA Contractor Report #3371 (1980).
- [117] M. Shinozuka, Simulation of multivariate and multidimensional random processes, *J. Acoust. Soc. Am.* **49**(1B), 357-368 (1971).
- [118] P. Sijtsma, S. Oerlemans, T. Tibbe, T. Berkefeld, C. Spehr. Spectral broadening by shear layers of open jet wind tunnels. In *Proc. 20th AIAA/CEAS Aeroacoustics Conf., 16-20 June 2014, Atlanta GA*. AIAA paper #2014-3178 (2014).
- [119] C. K. W. Tam, J. C. Webb. Dispersion-relation-preserving finite difference schemes for computational acoustics. *J. Comput. Phys.* **107**(2), 262-281 (1993).
- [120] A. Tarantola. Inversion of seismic reflection data in the acoustic approximation. *Geophys.* **49**(8), 1259-1266 (1984).
- [121] V. I. Tatarski. *Wave Propagation in a Turbulent Medium*. Dover Publications, New York NY (1961).

- [122] K. Thompson. Time dependent boundary conditions for hyperbolic systems. *J. Comput. Phys.* **68**(1), 1-24 (1987).
- [123] H. C. Van de Hulst. *Multiple Light Scattering: Tables, Formulas, and Applications*. Academic Press, New York NY (1980).